Title
Engineering Porous Silicon for a Top-Down Approach to Controlled Drug Delivery

Author
Machness, Ariella

Publication Date
2020

Peer reviewed|Thesis/dissertation

UNIVERSITY OF CALIFORNIA
Los Angeles

Engineering Porous Silicon for a Top-Down Approach to Controlled Drug Delivery

A dissertation submitted in partial satisfaction of the
requirements for the degree Doctor of Philosophy
in Materials Science and Engineering

by

Ariella Machness

2020

ABSTRACT OF THE DISSERTATION

Engineering Porous Silicon for a Top-Down Approach
to Controlled Drug Delivery

by

Ariella Machness
Doctor of Philosophy in Materials Science and Engineering
University of California, Los Angeles, 2020
Professor Mark S. Goorsky, Chair

Nanocarriers that localize a therapeutic to a disease site and release it “on-demand” via the clinician’s control will mitigate the adverse effects that reduce a patient’s quality of life while undergoing oncology treatment. Moreover, magnetically actuated drug delivery carriers are appealing platforms in next-generation targeted medicine, yet these carriers must be compatible with scalable fabrication techniques to realize their clinical translation. In this dissertation, a magnetically capped porous silicon nanocomposite (APTESPSi@Fe_3O_4), that responds to physiologically relevant temperatures, was developed using cost-effective, highly scalable methods such as electrochemical etching. Fourier transform infrared spectroscopy (FTIR), CHNS elemental analysis, and zeta potential confirmed that accelerated hydrolysis at 45 °C altered the porous silicon surface chemistry. This hydrolysis-mediated electrostatic degradation between the porous silicon and Fe_3O_4 caps translated to a thermoresponsive release behavior in dissolution studies with sorafenib (SFN), where minimal drug was released at room temperature

and 37 °C, while an enhanced release occurred at 45 °C and 50 °C. The magnetic heat dissipation capabilities with application of an alternating magnetic field (AMF) was calculated by the specific absorption rate (SAR) through calorimetry and magnetic susceptibility measurements. Comparing these two methods revealed that the electrostatic interactions between the porous silicon and Fe_3O_4 do not hinder the Brownian relaxation and heat dissipation. The nanocomposite and its components demonstrated high cytocompatibility after 24 hours with RAW 246.7, MDA-MB-231, and HepG2 cells, but not with MCF-7. High cytocompatibility was also observed when the cells incubated with particles were heated to 45 °C for 15 min followed by 37 °C for the remaining 6 hour incubation period. Porous silicon and its nanocomposite improved the SFN solubility in *in vitro* studies with MDA-MB-231 and HepG2, resulting in increased anticancer activity in comparison to the free drug. Moreover, the anticancer activity was readily controlled from the magnetic nanocomposite by modulating the amount of SFN released with temperature. Confocal microscopy and flow cytometry showed a higher uptake of the amine-modified porous silicon in comparison to the magnetic nanocomposite in MDA-MB-231 cells. The temperature increase to 45 °C showed a reduced particle uptake, yet future studies monitoring the fluorescence from the free drug rather than the nanocarrier will prove useful. This novel system has laid the groundwork for a promising tool for clinicians to lessen the burden that millions of cancer patients face as they receive treatment.

The dissertation of Ariella Machness is approved.

Bruce Dunn

Ximin He

Andrea Kasko

Mark S. Goorsky, Committee Chair

University of California, Los Angeles

2018

No matter how far I drift

Deep waters

Won’t scare me tonight

Table of Contents

List of Figures

List of Tables

Acknowledgements

In graduate school the research process does not always follow a linear trajectory. Realistically, hypotheses fail, pivots are inevitable, and you may find yourself halfway across the world frustrated over a leaking HPLC at 10 o'clock at night. Yet, with this whirlwind path I am indebted with mentorships, friendships and a true understanding of how to build to a story from the 4 pm coffee break "what if?".

Thank you Professor Goorsky for molding me into the researcher that I am today. You provided a perfect balance between rigorous guidance and trusting my judgement to take on exciting opportunities that, frankly, is non-traditional of graduate students. Thank you to my committee members Professor Dunn, Professor He, and Professor Kasko for providing mentorship and guidance at the most critical points in my graduate studies. I would like to thank the Goorsky lab members who have come and gone or are still around for always being so willing to help and to discuss research roadblocks: Jeff, Chao, Tingyu, Nachi, Andrew, Eva, Michael, Steven, and Kenny.

My graduate studies would not have been possible without generous funding from the National Science Foundation Graduate Research Fellowship Program. This fellowship opened many doors and gave me the opportunity to conduct research abroad at the University of Helsinki. Professor Santos, thank you for supporting my application for coming to Finland, for welcoming me into a not-so-Finnish family (the Santos Lab) and for your mentorship on this project. To the Santos lab: kiitos, obrigada, and grazie mille for taking me into your family and for showing me the true meaning of sisu. From the tears over Gesualda and cell contamination arguments to international dinners and karonka celebrations, you made this year both a productive and memorable one. To Alexandra aka lab mama, obrigada por me ajudar. Thank you

for your patience and quite literally holding my hand during cell passaging. But more importantly, thank you for the pajama parties, bacalhau com natas, and walks in Seurasaari. You made the winter that much more bearable. And thank you to João, my negative productivity partner in crime (think Unicafe breakfasts and chicken wing dinners). Our Finnish summer made weekend HPLC studies that much more difficult. I would also like to thank other lab members for their friendships and help both in and out of the lab: Giulia, Patricia, Joanna, Flavia, Nazanin, Sofia and so many more.

This work would not be possible without the support of family and friends, especially those who helped trivialize my failed experiments after a couple gin and tonics. Thank you, Matt, for being my escape from this for the last 10+ years. And Gloria, gracias por enseñarme fortaleza con tanta gracia. I would also like to express my gratitude to Adi and Sarit, who always keep me laughing albeit the distance. תודה לאמא ואבא על האהבה והתמיכה ללא תנאי לשוטט בעולם. You always have faith in what I am doing, even when I do not have it myself. אני אוהבת אותכם. And finally, to Orlando, who has been my solace for the last four and a half years: Gracias por tu amor, por su paciencia, para tu mente abierta y corazón abierto. Te quiero para siempre.

VITA

2014 Bachelor of Science in Chemistry, Materials Science

University of California, Los Angeles

Los Angeles, California, U.S.A.

Publications

A. Machness, A. Correia, E. Mäkilä, A. Lew, N. Shah, A. Curcio, M. Kemmell, T. Kohout, T. Bai, W. Zhang, N. Zanjanizadeh Ezazi, K. Moslova, J. Salonen, C. Wilhelm, H. A. Santos, and M. S Goorsky, "Design, Synthesis, and Characterization of Magnetic, Amide-Functionalized Porous Silicon Nanoparticles with Electrostatic-Mediated Degradation." to be submitted (2020).

A. Machness, A. Correia, G. Torrieri, E. Mäkilä, F. Fontana, J. Salonen, H. A. Santos, and M. S. Goorsky, "Electrostatically Bound Magnetic Capping Agents Mediate Thermoresponsive Drug Delivery in Porous Silicon Nanoparticles." to be submitted (2020).

S. Bertoni, A. Machness, M. Tiboni, R. Bártolo, and H. A. Santos, "Reactive oxygen species responsive nanoplatforms as smart drug delivery systems for gastrointestinal tract targeting." *Biopolymers,* 111(1), p.e23336 (2020).

X. Kou, A. Machness, E. Paluch, and M. S. Goorsky, "Homoepitaxial Growth of InP on Electrochemical Etched Porous InP Surface." *ECS Journal of Solid State Science and Technology*, 7(5), pp. P269-P273 (2018).

M. Gervasoni, A. Machness, and M. S. Goorsky, "Decreased Surface Porosity and Roughness of InP for Epitaxially Grown Thin-Film Devices: A Path to Integration of High Performance Electronics." *ECS Transactions*, 75(9), pp.241-245 (2016).

B. Bob, A. Machness, T.B. Song, H. Zhou, C. H. Chung, and Y. Yang, "Silver nanowires with semiconducting ligands for low-temperature transparent conductors." *Nano Research*, 9(2), pp.392-400 (2016).

Chapter 1. Introduction

According to the World Health Organization (WHO), cancer is the second leading global cause of death and accounted for an estimated 9.6 million deaths in 2018[1,2]. Chemotherapy is currently a standard treatment for a variety of cancers[3]. However, a chemotherapy dose is typically administered systemically and is indiscriminate between killing healthy and cancerous cells, resulting in a high frequency and severity of patient-reported chemotherapy side effects. For example, in a study surveying 449 chemotherapy recipients 86% of participants reported at least one side effect, 67% reported experiencing six or more side effects, and 27% reported a grade IV side effect, most commonly fatigue or dyspnea[4]. These side effects, which could often diminish a patient's quality of life, necessitates a transition from the "one-size fits all" approach in cancer therapy. As researchers and clinicians realize a patient specific, or targeted, therapeutic approach, cancer is viewed as a pathological relationship between an organism and an environment[5]. Cancer cells and host cells form an ecosystem, where, initially, the cancer cells are an invasive species to a new environment, the body, and eventually, the cell interactions modify this environment.

The new era of oncology therapy is encouraging researchers to pay more attention to the soil[5], such that the patient receives the most appropriate treatment given the environment. These efforts include the detection of genetic mutations within a patient that are a predictive factor of poor prognosis. For example, del (17p), a deletion on the short arm of chromosome 17, is a vital prognostic marker in chronic lymphocytic leukemia (CLL) that is associated with poor outcomes and rapid disease progression[6,7]. While precision medicine is typically associated with a genetic approach to patient care, it has also been noted for increasing a drug's versatility to adapt to a

cohort of patients. Researchers are turning to nanomedicine, an interdisciplinary research field that applies nanotechnology to medicine, to improve and diversify the way chemotherapy and other cancer treatments interface with the body's cancer ecosystem.

Nanomedicines are conferring an enhanced therapeutic index to existing therapies or enabling new treatment approaches (i.e., CRLX101 developed by Cerulean and AZD2811 developed by AstraZeneca) by aiming for a "right target" and "right exposure"[8]. By enhancing the therapeutic index, patient safety and tolerability can improve and enable more drug to be administered to achieve a more pronounced affect, such as anticancer activity. For instance, Abraxane™ is an albumin-bound formulation of the chemotherapeutic paclitaxel that received Food and Drug Administration (FDA) approval in 2005 as a second-line treatment for metastatic breast cancer[9]. This example utilizing nanomedicine has allowed higher doses of paclitaxel to be administered to patients in comparison to the regular formulation Taxol™, because Abraxane™ avoids the use of Cremophor™, which is associated with hypersensitivity[8]. By binding the protein albumin to paclitaxel, the total dose of paclitaxel being administered for metastatic breast cancer patients is reduced by 85%[9,10]. While the first generation of nanopharmaceuticals on the market focused on drug reformulation, the nanopharmaceutical market is expected to grow on the account of second-generation products, particularly the delivery of biotherapeutics (i.e. recombinant proteins, monoclonal antibodies, antibody fragment, and nucleic acids such as small interfering ribonucleic acid (siRNA) and gene editing constructs)[11]. Nucleic acids have emerged as promising candidates for drug therapy in various diseases and are now recognized as the third major drug discovery platform in addition to small molecules and antibodies[12]. While this new class of therapies is promising, siRNA is prone to enzymatic degradation before reaching the target site[13]. Therefore, nanomedicines will be critical in protecting the molecule during delivery

to the diseased site. The combination of nanomedicines and siRNA has made its way to the clinic, with Onpattro, a liposomal formulation of siRNA, recently gaining FDA approval for treating polyneuropathies resulting from the hereditary disease transthyretin-mediated amyloidosis (hATTR)[14].

Nanomedicines have the potential to not only increase therapeutic efficacy and promote patient quality of life, but also to enable remote-control access to delivery by clinicians. By using external stimuli (i.e. light, magnetic field, ultrasounds) to actuate the therapeutic payload in the vicinity of the tumor microenvironment or upon tumor cellular uptake the therapeutic efficacy can further improve. Moreover, a remotely actuated drug delivery system could inherently tailor the patient's dose regimen. For example, a clinician can tune remotely controlled parameters such as magnetic field frequency and amplitude to modulate the amount of drug released. Therefore, the same formulation can possess varying pharmacokinetics based on the desired response for a patient. Progressing nanomedicine therapeutics to the clinic has been slow, as was the case for early antibody therapeutics[8]. One underlying reason for the limited clinical translation is the technical and cost challenges in scale-up and manufacturing[15]. These nanocarriers tend to consist of multiple components that are either costly or tedious to synthesize, and therefore cannot readily scale for mass commercialization. In academic laboratories, micrograms or milligrams of product are usually produced, while grams or kilograms are necessary for preclinical screening, clinical trials, and, ultimately, clinical use[11]. Therefore, a material that can be readily scaled for clinical use should be considered in drug delivery research.

Porous Silicon (PSi) is a promising drug delivery carrier due to its biocompatibility, high surface area (up to 700-1,000 m^2/g), tunable pore structure with pore volumes > 0.9 cm^3/g, and

versatile surface chemistry[16]. Moreover, this material is compatible with microfabrication techniques commonly used in the electronics industry. Thus, PSi can potentially overcome challenges associated with scaling-up nanomaterial synthesis and formulation from the lab to industrial scale while maintaining control over their diverse properties. In this work, PSi was used to engineer magnetically actuated drug delivery nanocarriers that are compatible with scalable fabrication techniques to realize their clinical translation. Moreover, encapsulating poorly water-soluble or degradation-prone therapeutics inside the PSi nanocarrier can revive promising therapeutics that previously failed in clinical trials due to the their poor solubility.

Overall, this dissertation aims to:

1. Develop a magnetic PSi nanocarrier system comprised of cost-effective, highly scalable materials to overcome fabrication challenges typically associated with clinical translation of nanomedicines
2. Investigate the biocompatibility and cellular interaction of the magnetic PSi nanocarrier system with various cancer cell and macrophage lines.
3. Utilize the magnetic PSi nanocarrier system to improve the delivery of poorly water-soluble drugs in a controlled, thermoresponsive manner.

Chapter 2 provides an extensive literature review on the field of nanomedicine, PSi fabrication, magnetic NPs application in drug delivery, and the combination of PSi and magnetic NPs to form localized, thermoresponsive nanocomposites. Chapter 3 discusses the fabrication and optimization of magnetic PSi nanocomposites and its components. The magnetic and thermoresponsive behavior is investigated for amine-modified PSi nanoparticles (NPs) capped with electrostatically bound Fe_3O_4 NPs in Chapter 4. Chapter 5 observes the biocompatibility and cellular interaction of the magnetic PSi nanocomposite with cancer and macrophage cell

lines. Moreover, the anticancer activity of a poorly water-soluble drug encapsulated in the nanocomposite is investigated. In Chapter 6, a physical encapsulation method, nanoprecipitation, is used to fabricate thermoresponsive PSi NPs in a facile, highly scalable manner in comparison to typical chemical conjugation methods. Future experiments and conclusions are finalized in Chapter 7. Overall, this work provides a proof-of-concept of an on-command drug delivery system using cost-effective, highly scalable fabrication processes. This establishes an opportunity for the clinical translation of a nanocarrier that can potentially localize the therapeutic and trigger its release “on demand” once it has been endocytosed by the target cell to mitigate systemic exposure and reduce clinical side effects.

Chapter 2. Background and Literature Review

2.1 Field of Nanomedicine

With nearly 90% of therapeutics in the drug development pipeline possessing poor solubility[17] and clinical translations hindered by adverse effects that outweigh therapeutic benefit[18], the search remains for a "magic bullet" in the pharmaceutical industry. Nanotechnology has the potential to overcome some of the challenges that allow only 5% of therapeutics in the clinical pipeline to reach the market[19]. More specifically, the field of nanomedicine, defined by Nature publishing group as "a branch of medicine that applies the knowledge and tools of nanotechnology to the prevention and treatment of disease," has precisely engineered nanoscale materials to develop novel therapeutic and diagnostic modalities[20]. The concepts of nanomedicine were posited as early as 1908, with Paul Ehrlich's "magic bullet", or drugs that go straight to their intended cell-structural targets, to specifically destroy invading microbes or tumor cells[21]. Moreover, in 1959 Richard Feynman's lecture "There's plenty of room at the bottom" encouraged researchers to develop nanodevices that interact with the body at the cellular level[22]. The combination of designing advanced nanoscale materials and increasing the molecular understanding of diseases has deepened the field's knowledge on how to exploit nanotherapeutics in the clinic. This knowledge has led to the development of nanopharmaceuticals, nanodiagnostics, nanotheranostics and nanobiomaterials[11].

The growing interest in these applications is evident through the increasing number of publications and FDA-approved products[11,23,24]. A query of research publications in the PubMed database from 198'0 to 2017 containing the terms "NP" and "implant" or "NP" and "drug

delivery" are shown in Figure 2.1a, along with the number of FDA-approved products[23]. A PubMed query for the terms "NP" and "drug delivery" from 1995-2018 are shown on a complete scale in Figure 2.1b.

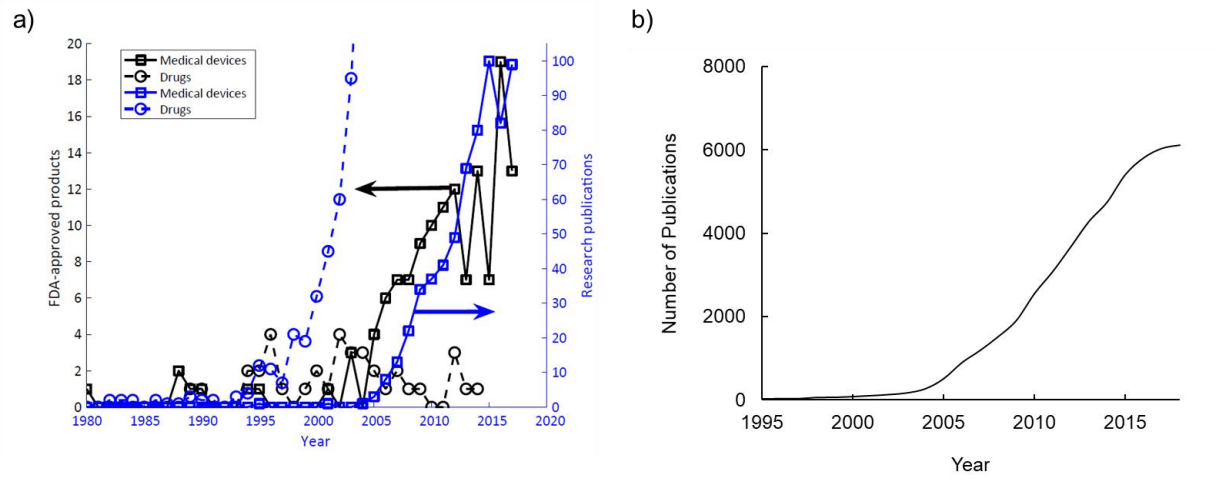

Figure 2.1 a) FDA-approved medical devices (black squares) and drugs (black circles) containing nanostructures. The blue squares and blue circles correspond to the number of research publications for nanostructure-containing medical devices and drugs. b) Number of publications containing the terms 'nanoparticle' and 'drug delivery' from 1995-2018 obtained from a PubMed query. Fig. 2.1a adapted from ref 8.

NP drug delivery publications surged in the early 2000's and greatly surpass the number of publications on NP-containing medical devices. However, the market of FDA-approved products has been dominated by the latter, probably due to the lower cost and regulatory hurdles associated with medical devices[25]. Nonetheless, NPs for drug delivery applications continues to generate interest in the clinic, with more than 200 companies across the world currently developing nanopharmaceuticals and market reports anticipating that 15% of the total pharamaceutical market would be dominated by nanopharmaceuticals in 2019[11]. The first generation of nanopharmaceuticals on the market focused on drug reformulation, with the most successful example being Doxil, a liposomal formulation of the chemotherapeutic doxorubicin. The nanopharmaceutical market is expected to grow on the account of second-generation products, particularly the delivery of biotherapeutics (i.e. recombinant proteins, monoclonal

antibodies, antibody fragment, and nucleic acids such as siRNA and gene editing constructs)[11,26]. Encapsulation of next-generation therapeutics into NPs will be critical to stabilizing and protecting sensitive biomolecules from degradation, such as nucleic acids that readily degrade in biological fluids [13,27]. Recently, Onpattro, a liposomal formulation of siRNA, was approved for treating polyneuropathies resulting from the hereditary disease transthyretin-mediated amyloidosis (hATTR)[14].

The oncology sector has generated the highest research and clinical translation interest in nanopharmaceuticals. According to WHO, cancer is the second leading cause of death and is responsible for about 1 in 6 deaths globally[1,2]. Cancers are often treated with chemotherapeutics[3], which are administered systemically and result in adverse effects such as weakened immune system, increased bruising and bleeding, nausea and vomiting[4]. Thus, there is a need to improve cancer treatment regimens while improving the patient quality of life during treatment[28]. Around 60.1% of nanomedicine articles published between 2013 and 2019 investigated oncology applications[24]. Moreover, oncological therapeutics comprised the highest fraction of annual sales of NP-based drug delivery systems in 2015[11]. Nanomedicine has gained the highest attention in oncology, because these nanocarriers can deliver hydrophobic molecules, protect the free drug from premature degradation[13], enhance absorption into a selected tissue (i.e. a solid tumor), improve intracellular penetration[29–31], control the pharmacokinetics[32], and improve the biodistribution profile through an extended circulating half-life[33,34]. Overall, these advantages yield nanocarriers that increase local drug concentration and reduce the systemic toxicities that result in patients discontinuing use of the therapeutic.

Although conventional chemotherapy has shown some success, its main drawbacks include poor bioavailability, non-specific targeting and high-dose requirements that result in

adverse side effects, and the development of multiple drug resistance[35]. As previously mentioned, nearly 90% of drugs in the development pipeline and 40% of approved drugs are poorly water soluble[17], including chemotherapeutics such as paclitaxel, doxetacel, and methotrexate. This hydrophobicity is problematic, because any drug to be absorbed must be present in the form of an aqueous solution at the site of absorption[36]. Therefore, higher doses will be required to reach therapeutic plasma concentrations for a pharmacological response[35]. Consequently, higher doses of chemotherapy may result in serious complications, such as cardiac toxicity[37], peripheral neurotoxicity[38], and bone marrow[39]. One example of a nanocarrier that increased the solubility and decreased the administered dose of paclitaxel is Abraxane, an albumin-bound paclitaxel drug that was approved by the FDA in 2005 as a second-line treatment for metastatic breast cancer[9]. Conventional paclitaxel preparations are dissolved in Cremophor® EL* (polyoxyethylated castor oil) due to its poor aqueous solubility, but this solvent-based paclitaxel is associated with risk of hypersensitivity and requires premedication with steroids and antihistamines[8]. By binding the protein albumin to paclitaxel the total dose of paclitaxel being administered for metastatic breast cancer patients is reduced by 85% [9,10]. Nanocarriers are also utilized to diminish the vulnerability of a therapeutic to premature degradation and clearance.

Nanoparticle Administration and Biodistribution

There are several routes of NP administration into the body, including intraosseous (IO, injection into the marrow bone), intraperitoneal (IP, injection into the abdomen), subcutaneous (SC, injection under the skin), intravenous (IV, injection into the veins), and intramuscular (IM, injection into the muscles). IV injection has been the most common method of administration in cancer-related publications[40]. Once the NPs are introduced into systemic circulation, they immediately face a biological barrier: the mononuclear phagocyte system (MPS)[15,41,42]. The MPS

consists of phagocytic cells that reside within the liver, spleen, lymph nodes and bone marrow, and sequesters the NPs typically into the liver and spleen before being able to reach the therapeutic site of interest[43,44]. Figure 2.2 shows how NPs are cleared from the bloodstream and accumulate in the MPS-related tissues or organs before entering the tumor.

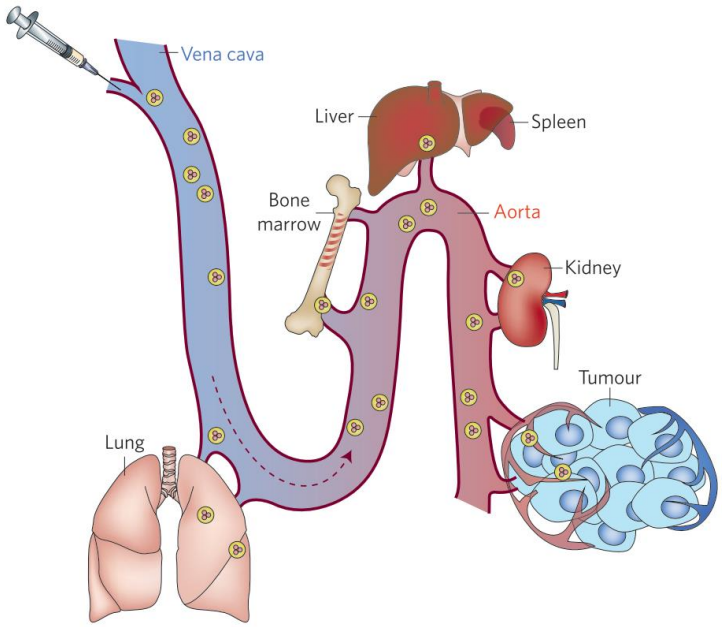

Figure 2.2 Systemically delivered nanoparticles are cleared from the bloodstream and accumulate in several tissues or organs comprising mononuclear phagocytic system (i.e. liver, spleen) before entering the tumor. The liver and spleen, and to a certain extent the bone marrow, can entrap large amounts of blood-borne nanoparticles as they enter systemic circulation. Nanoparticles less than 6 nm in diameter may be filtered from the blood by the kidneys and excreted in the urine. Image adapted from ref 37.

Moreover, materials <6 nm are filtered by the kidneys and excreted renally in urine or feces[45–47]. Materials in the 20- 200 nm size range can avoid renal filtration, allowing prolonged residence time in the bloodstream and a higher chance of reaching the diseased tissue[46]. Encapsulating therapeutics into nanocarriers mitigates renal filtration upon introduction into the bloodstream. Moreover, therapeutics have widely been conjugated with poly (ethylene glycol) (PEG) to improve the pharmacokinetics (i.e. increasing the therapeutics' half-life circulation in the bloodstream)[33,48,49].

Tumors have the tendency to preferentially take up and retain macromolecules, in part due to physiological abnormalities in the blood and lymphatic vessels. Tumor vessels possess leaky blood vessels resulting from large interendothelial cell junctions, as shown in Figure 2.3[42].

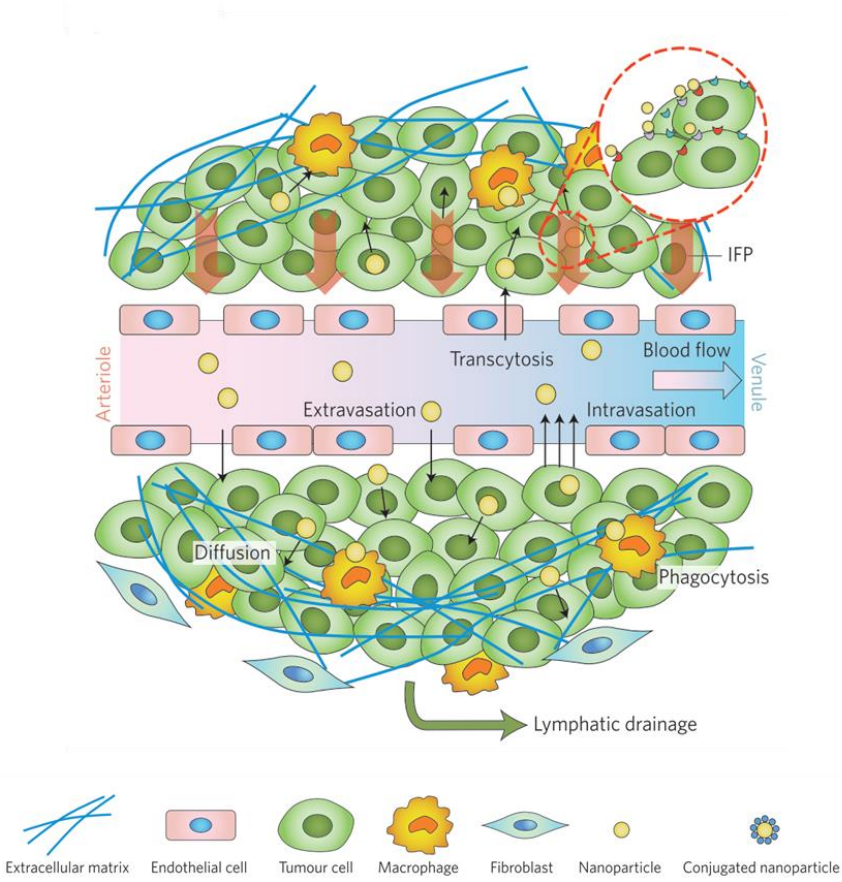

Figure 2.3 Unlike normal tissues, tumors have leaky vasculatures and dysfunctional lymphatics. This allows nanoparticles to passively extravasate and be retained within the tumor interstitium, also termed the enhanced permeation and retention (EPR) effect. With passive targeting NPs can interact non-specifically with different cell-membrane receptors to extravasate into the tumor microenvironment. Image adapted from reference 37.

Histologic evaluations have shown that pores between interendothelial junctions in some tumours were as large as a few micrometres in diameter, resulting in significantly higher vascular permeability relative to normal tissues[50,51]. This leaky vasculature allows NPs to passively extravasate between the endothelial cells and has been the mechanistic basis for the enhanced permeation and retention (EPR) effect that is commonly attributed to passively delivering nanomedicines into tumors[52–54]. Once the NPs are introduced into the tumor cells via

endocytosis, NPs are degraded by lysosomes and then soluble products are released back into the bloodstream for renal filtration (when products are < 6 nm) and subsequent excretion by urine[55,56]. Considering the biological barriers NPs face during IV administration before reaching a tumor, potential premature drug degradation and release can result in unintended off-targeting, toxic effects. Clinical interventions or changes in the tumor microenvironment can be exploited to localize and control the therapeutic release at the site of interest.

Stimuli Responsive Nanocarriers

Localized and controlled release can be monitored through internal stimuli (i.e. changes in environmental pH[57–60]) or external stimuli (i.e. light[61–63], magnetic field[64–66]). Internal stimuli include variation in physiological parameters that often characterize the disease to be targeted. With cancer, local changes in the tumor region such as acidic pH[67] and increased concentration of specific enzymes and reactive oxygen species (ROS)[68] is observed. With local acidification at the tumor site, polymers polymerized from acrylic acid, methacrylic acid, maleic anhydride and N,N-dimethylaminoethyl methacrylate are widely used to dissolve the nanocarrier upon exposure to acidic pH[69]. Moreover, the FDA-approved cationic polymer aminoalkyl methacrylate copolymer (Eudragit E) has increased solubility in acidic environments and has been used for suppressing a burst drug release profile in the oral cavity[70]. Overexpression of enzymes such as matrix metalloproteinases (MMPs) and hyaluronidase (HAase) are closely associated with tumor invasion and metastasis[71–73]. For example, a cell-penetrating peptide-modified liposome core with a hyaluronic acid-based crosslinked shell encapsulated a tumor necrosis factor-related apoptosis inducing ligand (TRAIL), or a cytokine that binds to death receptors on the plasma membrane[74]. In the tumor microenvironment, the hyaluronic acid shell was dissolved by the over expressed HAase, resulting in the TRAIL release. Higher ROS concentrations in tumors versus

normal tissue is due to the presence of reducing agents such as glutathione[75]. The redox-sensitive diselenide linkage and disulfide conversion into thiols have been incorporated into material systems for ROS-targeted drug delivery[76].

Drug delivery systems that can actuate a payload release by external stimuli remain largely experimental but are particularly promising because of their potential to control drug localization and release "on demand"[69,72]. More specifically, activation by external stimuli can remotely localize and actuate the carrier, improving the biodistribution while mitigating toxicity in a highly controlled, remote manner. Some examples of external stimuli include light[61,63], radio frequencies (RF)[77], ultrasound[78,79], and magnetic field[65,80,81]. One way in which external stimuli induce carrier release is by modulating the temperature of thermoresponsive carriers. For example, alternating magnetic fields (AMFs) generate heat in magnetic materials as a result of Neel relaxation, Brownian relaxation and hysteresis losses[82–84] that result in nanocarrier phase transitions or the breaking of thermally labile bonds. Gold–gold sulfide nanoshells incorporated into poly(N-isopropylacrylamide-co-acrylamide) (PNIPAM-AAM) hydrogels initiated temperature changes with application of near-infrared light that resulted in the burst release of methylene blue and proteins of varying molecular weight[85]. While most commercialization and research efforts in nanomedicine have focused on polymer-based nanocarriers, inorganic materials have also gained attention as promising targeted drug delivery vectors.

2.2 PSi in the Field of Nanomedicine

Although silicon (Si) has been more commonly associated with computer chips than drug delivery, it has gained attention in nanomedicine applications since the discovery of PSi as a biocompatible material[86,87]. PSi was initially discovered by Uhlir at Bell Laboratories in the mid 1950's[88] when he attempted to electrochemically machine Si wafers for their use in

microelectronic circuits. However, it was not until the discovery of PSi's photoluminescent properties by Canham in the early 1990s[89,90] where the material's interest resurfaced. Subsequently, with the discovery of PSi's biocompatibility and biodegradability in the mid-1990s[86,87,91], a surge of PSi-related publications emerged in the early 2000s (Figure 2.4a). The increase in PSi publications with drug delivery applications emerged a few years later (Figure 2.4b) and currently constitutes around 20% of PSi-related publications.

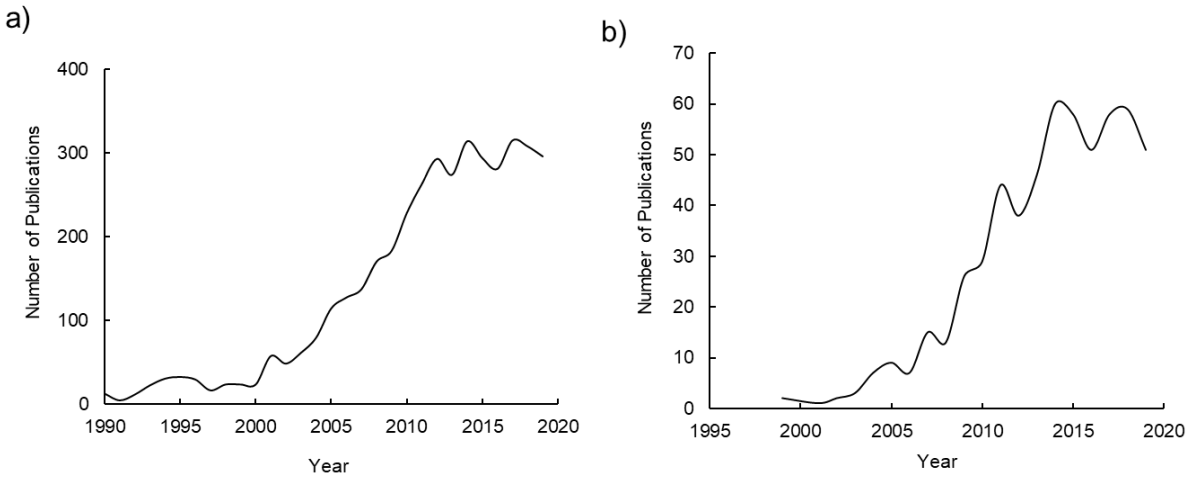

Figure 2.4 A query of research publications in the PubMed database was used to determine a) the number of publications containing the term 'porous silicon' from 1990-2019 and b) the number of publications containing the term 'porous silicon' and 'drug delivery' from 1999-2019.

The material has also found other biomedical-related applications such as optical biosensors, biomolecular screening, and tissue engineering[92]. PSi exhibits attractive properties for controlled drug delivery applications, including a large surface area (up to 700-1,000 m^2/g) for surface functionalization, tunable pore structure with pore volumes > 0.9 cm^3/g, luminescence, and convenient surface chemistry[93–95]. The PSi surfaces can be readily modified to control and monitor the release rate of drug payloads, or to increase intracellular concentration through targeting moieties such as tumor-specific ligands[96–98]. One way of forming PSi is by

electrochemical etching of single crystalline silicon wafers in a hydrofluoric acid (HF) electrolyte solution. The wafer is anodically biased in the fluoride- based electrolyte solution.

PSi Electrochemical Etching

PSi formed by electrochemical etching in HF is highly controlled, allowing the tailoring of pore sizes and volumes from the scale of microns to nanometers. Dissolution of the Si wafer requires the presence of a hole for the initial oxidation steps. Lehmann and Gohele proposed that a divalent Si oxidation state is formed when the hole is captured, and an electron is subsequently injected. The Si surface continuously switches between a hydride and fluoride during the electron/ hole exchanges. Moreover, Lehmann proposed that silicon hydride bonds passivate the surface unless a hole is available [99]. Figure 2.5 shows the mechanism for the dissolution occurring on the silicon surface. The final products for Si in an aqueous HF solution are hexafluorosilicic acid, H_2SiF_6, and H_2 gas.

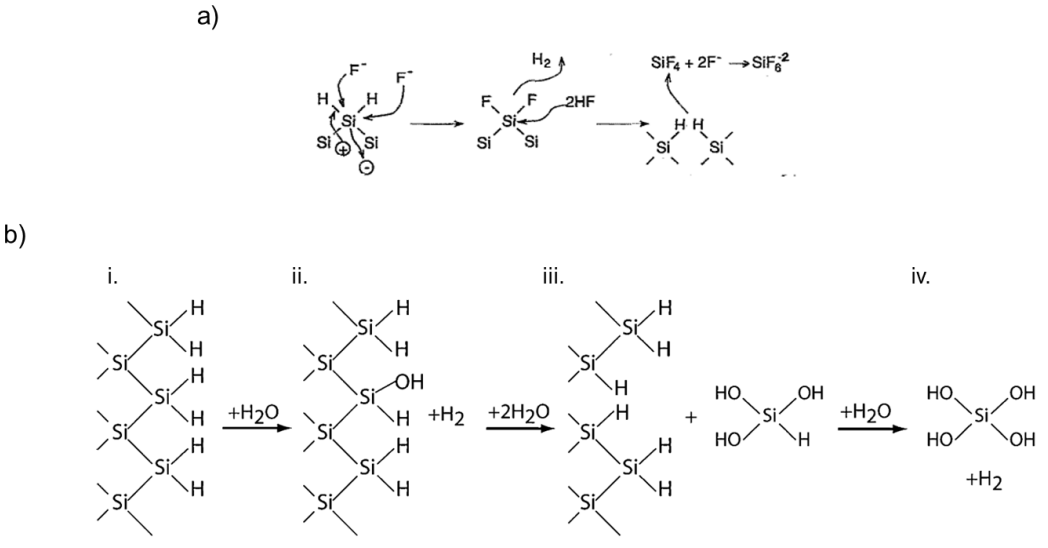

Figure 2.5 Proposed reaction mechanism for the a) formation of PSi through electrochemical etching b) and degradation in aqueous solutions, adapted from reference 107 (i) A Si-H-terminated surface immersed in H_2O. (ii) The Si-H bond undergoes hydrolytic attack and is converted to Si-OH, producing a hydrogen molecule. (iii) The Si-OH at the surface polarizes and weakens the Si-Si backbonds, which are then attacked by H_2O, producing $HSi(OH)_3$. (iv) In solution, the $HSi(OH)_3$ molecule is converted to $Si(OH)_4$ releasing a second hydrogen molecule

Characteristic dimensions governing pore geometry and morphology, such as average pore diameter, distance between pores, and spacing between branches, are modelled by the width of the space charge region (L_{SCR}), pore tip radius (L_{AV}), and diffusion instabilities [100].

The etching parameters typically used to vary the PSi morphology include electrolyte concentration, etching current, etching time, dopant, and dopant concentration. The electrolyte concentration and etching current play a role in pore sizes, porosity and layer thicknesses while the dopant and dopant concentration determine the pore geometry. The composition of the HF electrolyte solution influences the final porosity of the PSi because it determines the number of fluoride and hydrogen ions available for the dissolution reaction. While an increase in HF provides more fluoride ions to participate in the PSi formation, more hydrogen ions are present to effectively passivate the surface Si atoms. Therefore, fluoride ions are less likely to bond with Si to form the final dissolution product resulting in an inverse relationship between electrolyte concentration and porosity [101]. In addition, hydrogen gas is a byproduct of the reaction, and surface wetting agents such as ethanol are used to prevent hydrogen gas bubbles from adhering onto the silicon surface which would lead to non-uniform films.

Etching current varies the pore size, porosity, and layer thickness. There is a current threshold for the current density above which electropolishing will occur. This critical etching current is dependent on the electrolyte concentration and temperature of the etching solution as described by Equation 2.1 below.

$$J_{PSi} = A\ exp\left(-\frac{E_a}{kT}\right) C_{HF}^{3/2} \qquad \text{Eq. 2.1}$$

A is a constant of 3300 (wt% HF)$^{3/2}$ A cm^{-2}, E_a is the activation energy for pores formation (0.345 eV), k is Boltzmann's constant, T is temperature, and C_{HF} is the concentration of the

electrolyte solution[102,103]. Above this current density, for a given C_{HF} and T, the reaction is limited by ion diffusion in the electrolyte, which causes a buildup of charges at the surface, leading to uniform removal of material on the surface, also known as electropolishing. Thus, to fabricate PSi films, the etching current must be below this current threshold, where preferential etching (vs. uniform) occurs and charge supply at the electrode is the limiting factor. At low current densities, the charge carriers are confined to a smaller area and the Si dissolves along the current path, resulting in smaller pore sizes and lower porosities. At high current densities, the charge carriers spread over a larger area around the pore tip to accommodate for the increased current to minimize the interfacial impedance, resulting in larger pore sizes and higher porosities[104]. In addition, increased etching current densities increase the dissolution reaction rate because more charge is present to initiate the reaction.

Etching time affects the overall PSi layer thickness. Higher etching times allow the dissolution reaction to take place over a longer time, leading to larger pore channels. Moreover, pore branching (horizontal growth of pore channels) begins to occur after certain time periods. This pore branching tends to be problematic as it reduces the mechanical stability of the porous layer, particularly when it is a freestanding layer that has been lifted off from the substrate.

PSi is highly susceptible to oxidation with its high surface area. Upon oxidation, the nanophase silica readily dissolves in water, which is a requirement for drug delivery applications where a vector travels through an aqueous medium. Moreover, oxidation is an intermediate step for further surface functionalization to increase biocompatibility, bioavailability, and tumor targeting as previously mentioned. The oxide has been previously formed by thermal, ozone, and chemical oxidation[90].

Micron- or nano-sized particles are then achieved through ultrasonic fracture or ball milling. Conventional lithography techniques have also been used for obtaining particles with more uniform shapes[105,106]. PSi tends to have an irregular pore structure with heavily branched pores that resemble a "fir tree"-like configuration[94]. PSi's hydrogen-terminated surface is not stable and subsequent surface treatments are crucial. It is commonly oxidized to form PSi oxide because the oxide increases stability, slows degradation, and is widely accepted as a biocompatible material[107–109]. Thermal oxidation in air readily forms a stable oxide, especially at temperatures > 600°C[110]. Chemical oxidants, such as dimethyl sulfoxide (DMSO), are also used to achieve PSi oxide, and expand pores when coupled with HF[111]. Aside from PSi's formation and oxidation, its biodistribution and biodegradation has been widely studied.

PSi Biodegradation and Biodistribution

The biodegradability of PSi via a hydrolysis reaction has been confirmed[87,91,112–115] . The reactions below demonstrate PSi oxidation in the presence of an aqueous environment along with its degradation into orthosilicic acid, $Si(OH)_4$, through the hydrolysis of Si-O bonds.

$$SiH_4 + 2H_2O \rightarrow SiO_2 + 4H_2$$

$$Si + O_2 \rightarrow SiO_2$$

$$SiO_2 + H_2O \rightarrow Si(OH)_4$$

Orthosilicic acid is a form of Si that is predominantly absorbed by humans and naturally found in various tissues[114]. Silicic acid is also efficiently excreted from the human body through urine [56]. In vitro studies demonstrated that 100% of PSi NPs incubated in phosphate buffer solution (PBS) degraded within 8 hours[56]. In BALB/c mice (an albino, laboratory-bred strain of the house mouse), the PSi NPs were noticeably cleared from the body within a period of 1 week and

completely cleared in 4 weeks[56]. It has been proposed that upon cellular uptake the PSi degrade in the lysosomes via enzymes that promote hydrolysis, and once the particles are degraded to <6 nm they are readily removed via renal filtration[114]. PSi has also demonstrated enhanced degradation in tumor microenvironments due to the upregulation of ROS in the tumor vicinity that results in Si oxidation that catalyzes its degradation[92].

Extensive *in vitro* and *in vivo* studies have established the relatively low toxicity of PSi[116–118]. However, most of the reported PSi particles fabricated via this top-down approach are micron-sized[119]. Microparticles are unlikely to cross most biological barriers due to their size, which is problematic for tumor accumulation via passive targeting (i.e. EPR effect)[120]. Their dimensions may also be unsuitable for IV delivery. The smallest capillaries in the body are 5-6 μm, and therefore particles being distributed in the bloodstream must be significantly smaller to ensure that particles or aggregated particles do not cause an embolism[121]. Moreover, for particles that are functionalized with targeting moieties, NPs tend to have better binding to a unit of mass than microparticles due to their higher surface area. Therefore, NPs are of interest for intracellular delivery of therapeutics with increased efficacy. While top-down PSi formation has been extensively studied, another approach for fabricating PSi-based nanomaterials is prevalent in the field of drug delivery.

Mesoporous Silica: A Bottom-up Approach

As described above, PSi oxide micro- and NPs are synthesized via a top-down approach, whereas mesoporous silica is produced through a bottom-up approach where the fabrication is typically controlled through sol-gel chemistry techniques. Mobil Corporation Laboratories first introduced hexagonal ordered mesoporous silica NPs in 1992, which are commonly known as MCM-41 (Mobile Crystalline Materials)[122]. Through a liquid crystal templating mechanism

(LCT), the ionic surfactant, cetyltrimethylammonium bromide (CTAB), forms a micelle in an aqueous solution. The silica precursor, tetraethyl orthosilicate (TEOS), undergoes hydrolysis and condensation reactions in the presence of a base catalyst as the micelles self-assemble into NPs. Both hydrolysis and condensation reactions are shown below.

$$\text{Hydrolysis: } OH^- + Si(OR)_4 \rightarrow Si(OR)_3OH + RO^-$$

$$\text{Condensation: } SiO^- + Si(OH)_4 \rightarrow Si\text{-}O\text{-}Si + OH^-$$

Varying ratios between the surfactant, base catalyst, and silica source has resulted in varied ordering structures, including cubic and lamellar. Typical pore sizes average around 2 nm, although micelle swelling agents (typically small hydrophobic molecules) and lower temperatures resulted in larger pore sizes of around 3-6 nm[123]. These mesoporous silica NPs tend to be mesoscopically ordered yet overall possess an amorphous structure with unidirectional, 2-dimensional pores[95]. Another common form of hexagonal- ordered mesoporous silica structures is SBA-15, which has larger pore sizes up to ~ 30 nm. These larger pore sizes are obtained by using amphiphilic block copolymers as organic-structure directing agents[124]. They tend to have thicker silica walls (3.1 to 6.4 nm) in comparison to MCM-41 structures, which leads to greater hydrothermal stability. An abundance of literature exists for targeted drug delivery systems based on mesoporous silica NPs synthesized through a bottom-up approach due in part to their high surface area (>900 m^2/g), large pore volume (>0.9 cm^3/g), tunable pore size with a narrow distribution, and good chemical and thermal stability[16]. However, the bottom-up approach has several disadvantages that hinders its successful translation to the clinic as a drug delivery vector. For example, the density of silanol groups on the NP surface over a certain threshold had a high affinity for red blood cell membranes which resulted in hemolysis (red blood cell rupture or destruction)[125]. Ionic surfactants not completely removed from the NPs after synthesis can

also cause severe cytotoxicity[126,127]. Further extraction methods are used to remove the ionic surfactants, but this additional step makes the fabrication process for tedious. Overall, top-down fabrication approaches are advantageous because of their low cost and high scalability. Although nonuniformity in the porosity and thickness of PSi layers has been observed, these gradients are easily avoided by having the Si substrate in direct contact with a conductive anode material[109]. Top-down approaches also yield larger pore sizes, which is a requirement for vectors delivering siRNA or microRNA (miRNA). siRNA molecules have a rigid cylindrical shape with a length of ~5 nm and a diameter of ~2.3 nm; these dimensions are too large to readily infiltrate into MCM-41 mesoporous silica NPs which have typical pore diameters of 2 nm[128]. Therefore, a top-down approach for fabricating porous silica NPs is promising for clinical translation, particularly as a vector in the delivery of gene therapies.

Gene Therapy Delivery with PSi-Based Materials

Gene silencing therapeutics have witnessed a growing interest in cancer treatments because of their sophisticated approach to disease eradication. For example, siRNA can silence gene expressions that translate to cancerous cell growth. Since its discovery in 1999[129], siRNA has seen growth in the literature and clinical translation with four RNAi-based drugs evaluated in early clinical trials for cancer therapy as of 2016[130]. Because siRNA is subject to enzymatic degradation, rapid renal filtration, and incompatibility with the cell membrane due to their negative charge, a delivery vector is required for efficient transport and uptake by target cells. Both bottom-up and top-down Si-based vectors were demonstrated for siRNA delivery in the literature. siRNA delivery systems using bottom-up mesoporous silica NPs have been more prominent. For example, siRNA was co-delivered with the chemotherapeutic doxorubicin in mesoporous silica NPs to overcome drug resistance in breast cancer *in vitro* and *in vivo*[131,132].

However, the siRNA was bound to the porous surface which could lead to degradation before reaching the targeted site. More recently, cyclodextrin polyethylenimine (CP) was grafted to encapsulate doxorubicin and increase siRNA loading through electrostatic interactions, but the siRNA was not encapsulated and, therefore, not protected from degradation[133]. siRNA has been infiltrated into core-shell hierarchical mesostructured silica NPs but no encapsulation or capping system was used to avoid premature therapeutic release[134]. Stimuli-responsive mesoporous silica nanocarriers (i.e. pH responsive) were also demonstrated for the delivery of siRNA[135]. While siRNA delivery using magnetic mesoporous silica was demonstrated, an external stimuli (i.e. magnetic field) was not implemented to localize or control drug release [136]. Much of literature utilizing mesoporous silica fabricated from a bottom-up approach adsorb siRNA onto the surface because pore sizes are probably too small for infiltration. Therefore, a top-down fabrication approach can potentially increase siRNA encapsulation in the delivery vector while protecting it from degradation.

siRNA delivery by top-down (i.e. electrochemical etching) PSi particles is less prevalent in the literature but has nonetheless been demonstrated. Giant liposomes containing siRNA, doxorubicin loaded PSi NPs, gold nanorods, and magnetite NPs showed the potential to deliver multiple drugs with localization and controlled release capabilities[137]. However, no external magnetic fields are utilized to determine the vector's heating capabilities or how the liposome reacts to the external stimuli. Moreover, graphene oxide nanosheets encapsulated PSi NPs which in turn delayed siRNA release by a factor of 3 while increasing cellular uptake 2-folds[138]. High concentrations of siRNA were simultaneously loaded and protected while slowing its release in PSi NPs by capping the pores with an insoluble shell of calcium silicate[139]. siRNA therapeutics were also encapsulated in PSi microparticles, but as previously discussed, microparticles have

several disadvantages that render their widespread use in IV administration[140]. Overall, there is no indication of top-down PSi NPs for siRNA delivery that utilize an externally controlled magnetic field to localize the therapeutic to a targeted site and release it "on demand" through a thermosensitive encapsulate. Using a top-down fabrication approach can yield higher siRNA concentrations reaching a targeted cell while maintaining a process that is cost effective and commercially scalable. Moreover, incorporating magnetic NPs and a thermosensitive encapsulate into a $PSiO_2$ system can localize the therapeutic and trigger its release "on demand" once it has been endocytosed by the target cell, which mitigates systemic exposure that results in reduced clinical side effects.

2.3 Iron Oxide NP Synthesis, Characterization, and Application

Superparamagnetic iron oxide NPs (SPION) such as magnetite (Fe_3O_4) are used in various biomedical applications, including contrast agents in magnetic resonance imaging (MRI)[141,142], tissue repair[143,144], hyperthermia[145–147], and targeted drug delivery[148,149]. SPIONs can externally control cancerous cell death by hyperthermia and avoid systemic toxicity by therapeutic localization. *In vivo* applications require that SPION have high magnetization values, particle sizes >100 nm, a narrow particle size distribution, and biocompatibility[150]. Iron oxide particles were used for *in vitro* diagnostics 60 years ago, and have generated increasing research interest in the last two decades as a versatile biomaterial[151]. They have shown translation to the clinic as Ferumoxytol, an FDA approved treatment for iron deficiency anemia and MRI contrast agent for various cancers[152]. Another product currently in clinical trials, Magnablate, uses magnetic thermoablation to induce cancerous cell death (https://clinicaltrials.gov/ct2/show/NCT02033447). Moreover, SPIONs can externally control cancerous cell death by hyperthermia and avoid systemic toxicity by therapeutic localization.

Since localization by an external magnetic field was first demonstrated in the early 1960s, a variety of magnetic NP and microparticle carriers were subsequently used to target drugs to a specific site *in vivo*[153–156]. Magnetic manipulation is controlled by direct current (DC) magnetic fields while magnetic heating is in response to alternating current (AC) magnetic fields[81]. Once the magnetic particles reach the target site magnetic heating can be used for hyperthermia or drug release by magnetic actuation of a temperature-sensitive capped system[157].

SPION Heat Generation with Application of an AMF

This heat dissipation by SPIONs is caused by delay in the changing direction of the magnetic moment as the magnetic field polarity changes through rotation within the particle (Neel relaxation) or rotation of the particle itself (Brownian relaxation)[82]. Brownian relaxation is influenced by the local environment (i.e. viscosity of the medium) and therefore particles dissipating heat through Neel relaxation are preferred in clinical trials[83].

τ is the effective relaxation associated with Brown and Neel relaxation shown in Equation 2.2[82].

$$\frac{1}{\tau} = \frac{1}{\tau_B} + \frac{1}{\tau_N} \qquad \text{Eq. 2.2}$$

Brownian relaxation, τ_B, is related with particle rotation as the field polarity changes [158]

$$\tau_B = \frac{3\eta V_H}{k_B T} \qquad \text{Eq. 2.3}$$

and Neel relaxation, τ_N, is related with the magnetic moment aligning inside the particle [159] with field polarity changes

$$\tau_N = \tau_0 \exp\left(\frac{KV}{k_B T}\right) \qquad \text{Eq. 2.4}$$

where η is the carrier liquid viscosity (in this case water), V_H is the hydrodynamic volume $V_H = \left(\pi/6\right) d_H^3$, d_H is the hydrodynamic diameter, which has been previously estimated as three times

the magnetic core[160], K is the effective magnetic anisotropy constant for Fe_3O_4 (10^4 J m^{-3})[161], V is the particle volume $V = (\pi/6)d_3$ where d is the Fe_3O_4 diameter, τ_0 is assumed to be 10^{-9} s[161], k_B is the Boltzmann constant, and T is the temperature. Clinical translations, particularly for SPION's application in drug delivery vectors, have motivated studies related to particle sizes, NP stability, magnetic properties, and heating properties.

The heating capability of magnetic NPs is expressed by the specific absorption rate (SAR), which is a measure of the rate at which energy is absorbed per unit mass of the magnetic material when exposed to an AMF[80]. The SAR has been widely measured via two routes: through 1) magnetic susceptibility and 2) calorimetry experiments. Magnetic susceptibility, χ, is a dimensionless proportionality constant, as shown in Equation 2.5, that measures a material's degree of magnetization in response to an applied magnetic field.

$$M = H\chi \qquad \text{Eq. 2.5}$$

M is the degree of magnetization, or the magnetic moment, and H is the applied magnetic field. When an AMF is applied a magnetic moment is induced as shown in Equation 2.6.

$$M_{AMF} = \frac{dM}{dH} H_{AMF} \sin \omega t \qquad \text{Eq. 2.6}$$

M_{AMF} is the induced magnetic moment under an AMF, $\chi = \frac{dM}{dH}$, H_{AMF} is the magnetic field amplitude, and ω is the driving frequency. Equation 2.6 is only valid at lower AMF frequencies, where the magnetic moment remains in phase with the driving frequency. At higher frequencies, the magnetic moment lags behind the driving frequency which results in the susceptibility having an in-phase, or real, component χ' and an out-of-phase, or imaginary, component χ". This out-of-phase or imaginary component, χ", is associated with heat dissipation of the magnetic particle. From χ", the SAR is estimated by Equation 2.7[82]

$$SAR = \frac{\mu_0 \pi \chi''}{\rho_{particle}} f H_{applied}^2 \quad \text{Eq. 2.7}$$

where μ_0 is the permeability of free space, $H_{applied}$ and f is the magnetic field amplitude and frequency, and $\rho_{particle}$ is the density of Fe_3O_4.

Calorimetry experiments, on the other hand, directly measure temperature changes of a solution as a function of time with application of an AMF. The measurements are typically carried out in nonadiabatic conditions. SAR is calculated using Equation 2.8.

$$SAR = \frac{CV_s}{m}\frac{dT}{dt} \quad \text{Eq. 2.8}$$

where m is the total mass of Fe in the sample, C is the specific heat capacity of the suspension water (C_{water} = 4185 J L^{-1} K^{-1}), V_s is the sample volume, and $\frac{dT}{dt}$ is the temperature profile slope. The slope of the curve is considered linear and, therefore, only the first few to thirty seconds of the temperature profile is considered. Magnetic targeting and heating of nanocarriers has been widely used to localize and promote the release of the therapeutic at the disease site.

In vitro and In Vivo Magnetic Localization and Heating

Magnetic localization has been demonstrated *in vitro* and *in vivo* with magnetic fields ranging from 0.025 to 1.7 T. Figure 2.6 shows typical experimental setups for *in vitro*[162] (Fig. 2.6a) and *in vivo* (Fig. 2.6b)[163] experiments. Magnetic manipulation within the body is possible when the magnetic forces exceed the linear blood flow rates in arteries (10 cm/s) or capillaries (0.05 cm/s)[164]. *In vitro* studies have flowed SPION solutions using a peristaltic pump through slides with micron-sized channels (μ-slides, 0.4 mm)[162] and umbilical arteries[165] to investigate the magnetic NP accumulation with application of a magnetic field under dynamic conditions. Older studies conducted *in vitro* studies with syringe pumps and polyethylene tubing (inner

diameter of 1-2 mm), which can model veins (~10 mm in diameter) but not capillaries (~5-6 µm)[155].

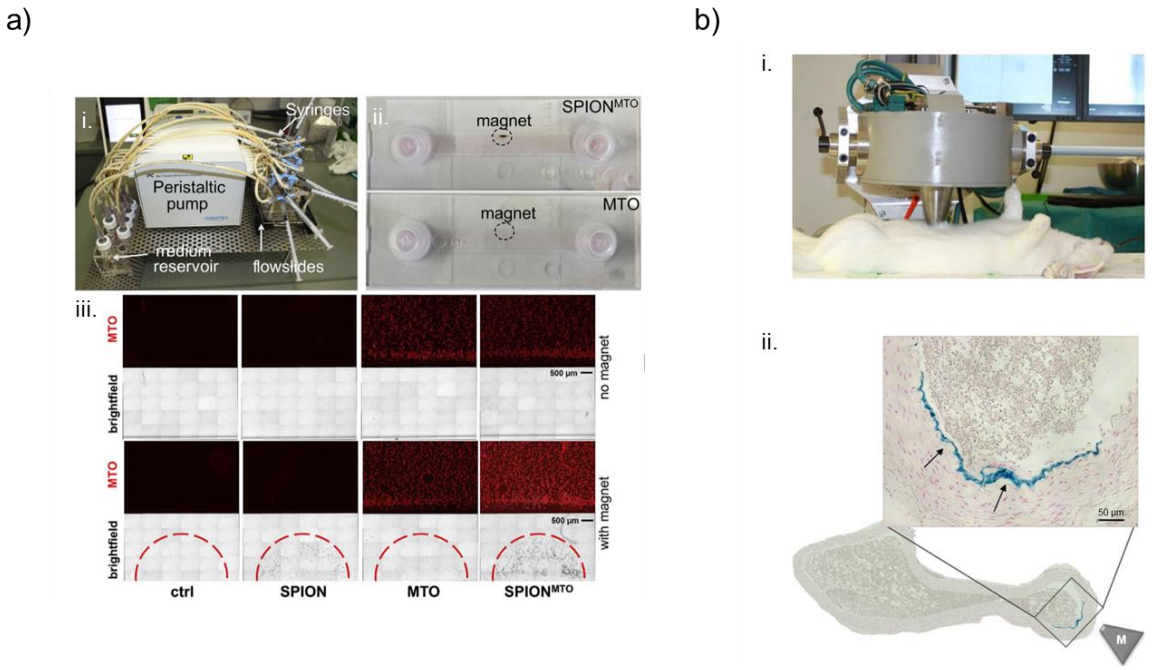

Figure 2.6 a) In vitro magnetic accumulation i. Experimental setup where a peristaltic pump perfused HT-29 cells with medium for 1 h after bolus injection of Fe_3O_4 NPs. ii. Fe_3O_4 NP accumulation in the middle of the slide after magnet removal. iii. Upper row: Mitoxantrone (MTO) distribution after 1 h incubation (6×5 tiles); lower row: Fe_3O_4 NP distribution in brightfield images with and without magnet application. b) in vivo magnetic accumulation i. Experimental setup and placement of magnetic tip on mouse for magnetic NP localization. ii. Iron in the targeted region was visualized by Prussian blue staining (arrows). Fig. 2.6 a) adapted from ref 154 and Fig. 2.6 b) adapted from ref 155.

In vivo studies have focused more on shallow tumors (i.e. <0.5 cm from the surface) as the magnetic field gradient decreases with increasing targeting tumor depth[166]. Magnetic targeting has been investigated in breast, skin (histiocytoma), and cartilage (chondrosarcoma) tumors[166]. Targeting was also observed in VX-2 squamous cell carcinoma implanted in the hind limb of rabbits[156]. Histological evaluations showed that iron oxide NPs were distributed throughout the tumor in comparison to rabbits not treated with a magnetic field, where the presence of iron oxide NPs were not observed. Moreover, iron oxide NPs were concentrated at the endothelium closest to the applied magnetic field. Although magnetic targeting is ideal for shallow tumors, as

most fields are only strong enough to manipulate particles over a few cm, studies have also localized magnetic NPs to the liver and lungs, which have an 8-12 cm targeting depth[167]. Table 2.1 summarize various *in vitro* and *in vivo* examples of magnetic NP localization.

Table 2.1 Summary of in vitro and in vivo magnetic localization studies.

	Targeted Cell Line/ Organ	Magnetic Field Applied	Particle Size	Reference
In Vitro	HT-29 (colorectal cancer)	72 T/m	53-56 nm	Alexiou et al. 2018[163]
	Umbilical arteries	72 T/m	NA	Alexiou et al. 2017. 2019[165,168]
	NA, magnetic accumulation in dynamic environment	0.024- 1.15	1 µm	Senyei et al. 1978[155]
		0.1- 1.5	1.2 µm	Viroonchaptan et al. 1995[169]
	Brain tumor	NA	Microsphere	Pulfer et al. 1997[170]
	Fibrinolysis for thrombosis prevention	0.025	NA	Inada et al. 1987[171]
	Head and neck squamous cell carcinoma	~0.001	0.5-2 µm	Allen et al. 1997[172]
In vivo	Atherosclerosis (lower abdominal aorta)	72 T/m	63-64 nm	Cicha et al. 2018[163]
	Liver, lung swine model	0.025- 0.1 T	0.5-5 µm	Goodwin et al. 1999[167]
	VX-2 squamous cell carcinoma	1.7 T	100 nm	Alexiou et al. 2000[156]
	Breast, histiocytoma, chondrosarcoma, Ewing sarcoma	0.8 T	100 nm	Lübbe et al. 1996[166]

Actuating temperature changes in a nanocarrier system by application of an AMF has been widely studied both *in vitro* and *in vivo* because therapeutic release is triggered on-demand by the clinician once it reaches the disease site. Consequently, toxicity is strongly localized and

side effects are dramatically reduced. Moreover, thermal treatments are particularly promising in oncology since the tumor tissues dissipate heat less effectively than healthy tissues, resulting in preferential damage to tumor tissues at elevated temperatures (i.e. 45 °C)[173]. Previous studies have also used an external magnetic field to temporarily disrupt and increase the permeability of vascular endothelium junctions, resulting in an increase in the amount of iron oxide NPs internalized[174]. A magnetic field of 0.5 T generated an intracellular magnetic force on the same order of magnitude compared to the shear force on vascular endothelium in capillaries in the body[175]. Magnetic heating has been reported for both hyperthermia and thermoresponsive drug release applications. Under application of an AMF, *in vitro* temperature increases up to 50 °C were observed within 4 min for Fe_3O_4 NPs encapsulated in a PNIPAM microgel[176]. Table 2.2 shows various magnetic nanocarriers with *in vitro* temperature-mediated drug release upon application of an AMF.

When moving from *in vitro* to *in vivo* experiments, the magnetic NP heating capabilities become even more stringent because a larger amount of NPs are needed to generate relevant temperatures as the magnetic field strength decreases for deeper tumors. One way to increase the magnetic heating rate is by increasing the AMF frequency (f) and magnetic field amplitude (H). However, these parameters are limited by a biocompatible value for the product of H and f. Brezovich found that for $H*f = 6.7 \times 10^9$ A/ m s given a loop diameter of about 30 cm, patients withstood treatment for more than one hour without major discomfort [177]. This field amplitude and frequency product has been widely accepted as the biocompatibility limit for patient exposure [146,147,178,179] and may exceed for smaller diameter exposures and for patients with less severe illnesses. From a material synthesis perspective, varying the magnetic NP shape and doping with transition metals has increased the SAR value and enabled hyperthermia-relevant

temperature increases *in vivo*. Nanocubes with an average diameter of 19 nm reached SAR values up to 2452 W/g_{Fe} at 520 kHz and 29 kA m^{-1} [180] in comparison to commercially available spherical iron oxide NPs[181] (SAR: 145.9 W/g_{Fe} at 420 kHz and 10.6 kA m^{-1}). Although the frequency and magnetic field amplitude are lower for the latter which contributes to the lower SAR value, the increase in these parameters tends to be linearly proportional to the SAR. Therefore, extrapolating the SAR to the higher field frequency and amplitude would not yield a 17 times difference. Moreover, magnetic nanoclusters doped with manganese (Mn) and cobalt (Co) demonstrated a temperature increase *in vivo* to 44 °C within 30 min application of an AMF[181]. The nanoclusters reached this temperature with a 6 mg Fe/ kg dose, which is comparable to a dose of Ferumoxytol.

Table 2.2 Summary of in vitro and in vivo magnetic heating studies.

	Nanosystem	Targeted Cell Line/ Organ	AFM Parameters	ΔT	Drug Release	Reference
In Vitro	Fe_2O_3 Nanocubes, PNIPAM-co-PEGMA[a]	NA	220 kHz; 20 kA m^{-1}	25- 80 °C, 15 min	3 x 10^{-1} mg/mL, 4h at 80 °C	Pellegrino et al. 2015[182]
	Fe_2O_3 P(OEGMAs-co-MAA)[b]	PC-3 (Prostate cancer)	335 kHz; 12 kA m^{-1}, (4x30min)	37- 65 °C ,30 min	100% at pH 5	Wilhelm et al. 2017[183]
	Fe_3O_4 PNIPAM	NA	380 kHz;10.3 kA m^{-1}	50 °C, 4 min	1% of drug/min	Lawes et al. 2010[176]
	$Zn_{0.9}Fe_{2.1}O_4$	U87-MG (Malignant glioma)	700 kHz, 2.7 kA m^{-1}, 1h	41 °C, 6 min	78% viability	Ammar et al. 2016[184]

	Nanocubes	KB (Human epidermoid carcinoma)	110 kHz and 20 kA m^{-1}, 1h	62 °C, 1h	0% viability	Pellegrino et al. 2012[80]
In vivo	$Zn_{0.47}Mn_{0.53}Fe_2O_4$ PZC[c]	U87-MG (Malignant glioma)	366 kHz; 13.3 kA m^{-1} (2 × 1h)	43 °C, 8 min	80% release in 20 days	Zhang et al. 2017[185]
	Co, Mn-doped, hexagon-shaped Fe_3O_4	ES-2 (Ovarian cancer)	420 kHz, 26.9 kA m^{-1}, 30 min	42 °C, 30 min	Tumor volume reduced >20x	Taratula et al. 2019[181]

[a]PNIPAM-co-PEGMA: poly(N-isopropylacrylamide)/PEGMA: polyethylene glycolmethyl ether acrylate
[b]OEGMAs-co-MMA: oligo-(ethylene glycol)methyl ether methacrylatemonomers /MMA: methyl methacrylate
[c]PZC: poly(organophosphazene)

Iron Oxide Nanoparticle Synthesis

Various approaches have been described to synthesize iron oxide NPs, including high-temperature reactions, sol-gel reactions, and by decomposition of organometallic precursors. While these synthesis routes yield NPs with a narrow size distribution, the co-precipitation method has been most widely used because of its high scalability. In this method, Fe^{2+} and Fe^{3+} ions are precipitated in alkaline solutions such as ammonium hydroxide. The chemical reaction for magnetite (Fe_3O_4) formation is shown below.

$$Fe^{2+} + Fe^{3+} + OH^- \rightarrow Fe_3O_4 + H_2O$$

Complete precipitation of Fe_3O_4 from an aqueous solution is typically expected at a pH between 8 and 14, and at a Fe^{3+}/Fe^{2+} stoichiometric ratio of 2:1. Magnetite may oxidize into maghemite (Υ-Fe_2O_3) in air, which is undesirable because bulk maghemite has a lower saturation

magnetization value than bulk magnetite (60-80 emu/g vs. 92-100 emu/g) [186]. The oxidation reaction is shown below.

$$Fe_3O_4 + 2H^+ \rightarrow \Upsilon\text{-}Fe_2O_3 + Fe^{2+} + H_2O$$

Various Fe_3O_4 synthesis parameters have been adjusted to control particle size, shape, magnetic properties, and surface properties. Increasing the Fe^{2+}/Fe^{3+} precursor injection rate into a tetramethylammonium hydroxide (TMAOH) solution from 1 to 5 mL/min found no significant variation in mean size except for the 1 mL/min rate which had a slightly larger size [141]. Moreover, decreasing the Fe^{2+}/Fe^{3+} ratio yielded a decrease in particle size [187] and established a range of ratios in which magnetite formation occurs. An increase in the hydroxide concentration resulted in a significant increase in NP size [188]. Temperature and surfactant coatings were other parameters used to vary the size, shape, and surface properties [189]. Overall, tuning Fe_3O_4 NP sizes, particularly with a narrow size distribution, is relevant because magnetic properties are size dependent. For example, theoretical estimates of heat dissipation (considering Neel and Brownian relaxation) as a function of NP size showed the highest dissipation at a size of around 12 nm [83]. There is motivation to achieve optimal heating properties by tailoring the NP size so that during clinical translation, the applied magnetic field remains within the biocompatibility limit.

While Fe_3O_4 NPs are shown to effectively induce temperature changes under the application of an AMF [190,191], their application in targeted drug delivery as bare particles is limited because therapeutics cannot be loaded into the NPs. Instead, they are either physically adsorbed [192] or covalently conjugated [193–195] to the magnetic NP surface which can induce unintended drug release or degradation. Thus, magnetic NPs have been incorporated into PSi NPs, amongst other types of carriers, to deliver therapeutics to a site of interest.

2.4 PSi@Fe_3O_4 Composites for Magnetically Modulated Drug Release

PSi@Fe_3O_4 nanocomposites are promising materials in magnetically responsive drug delivery vectors and have been fabricated through both bottom-up and top-down approaches. Top-down PSi@ Fe_3O_4 composites have been demonstrated (Sailor[196–200] and Granitzer[201–204], for example)- but their application for targeted drug delivery systems is limited. Fe_3O_4 NPs are typically infiltrated into PSi NPs by physical adsorption into the pores[198] or by infusing the magnetic suspension into a PSi film with the guidance of a magnet followed by ultrasonic fracture[197,205].

The nanocomposites are typically prepared by infiltration of a Fe_3O_4 solution into Si's porous matrix either as a film or as micro, NPs[206,202,207]. The infiltration process was also facilitated by the application of a magnetic field under the film[208]. Energy dispersive X-ray spectroscopy (EDX) confirmed the presence of Fe_3O_4 in the PSi matrix; X-ray diffraction (XRD) also corroborated Fe_3O_4 infiltration[209]. A decrease in magnetization was observed with decreasing NP size (from 8 to 4 nm) through a superconducting quantum interference device (SQUID) magnetometer[208]. Moreover, these nanocomposite structures demonstrated biocompatibility with human embryonic kidney (HEK) 293 cells[203].

Micro-and NP composites have been fabricated by a top-down approach for a variety of applications such as microfluidic reactors, drug delivery by magnetic manipulation, and contrast agents in MRI imaging. A microreactor was designed by magnetically manipulating and combining two small volumes of composite microparticle solutions to form a chemical reaction[199]. Magnetic manipulation and heating of composite microparticles by an external magnetic field were performed subsequently for hybridization of DNA strands[197]. Magnetic manipulation was used to localize the delivery of composite microparticles with a

chemotherapeutic payload, and localized cell death was confirmed[200]. Finally, increased magnetic resonance contrast was observed in PSi NPs infiltrated with Fe_3O_4 [198,196]. The study also showed that increasing the Fe_3O_4 concentration increased saturation magnetization values until a Fe_3O_4: pSi mass ratio of 25%. For concentrations above this ratio, saturation magnetization values approached that of bulk magnetite, and for mass ratios > 50% the composite transitioned from superparamagnetic to weakly ferromagnetic. The transition was speculated to be magnetic NP aggregation as they are confined within the pores. Additionally, a majority of the top-down PSi, Fe_3O_4 composites previously mentioned were oxidized after infiltration to trap the Fe_3O_4 NPs in the PSi matrix. The magnetic properties of Fe_3O_4 NPs with optimal heating properties (i.e. around 12 nm) infiltrated into PSi has not been studied. Other PSi morphology considerations such as pore size and porosity have not been studied by SQUID to determine their effect on the nanocomposite's magnetic properties. Moreover, no studies observed how the heating capabilities vary with pore morphology, NP size, and NP concentration. Therefore, there is motivation to determine a PSi, Fe_3O_4 nanocomposite with optimal heating properties towards improved clinical translation. While these nano- and microparticle formulations were successfully demonstrated as MRI contrast agents[196,198] and in Fluorescence Resonance Energy Transfer (FRET) Assays[197], their application in magnetic controlled drug delivery remains limited, as the exposed pores would lead to premature drug release. Capping agents have been widely used to prevent premature drug release until the NPs reach the site of interest, and several examples have been demonstrated in bottom-up PSi, Fe_3O_4 composites[63,210–212].

Capping agents can be either small molecular nanovalves that block individual pores or polymer networks that encapsulate the nanocarrier. These gatekeepers possess thermally labile

covalent bonds[213], electrostatic interactions[214] or phase transitions[215–217] that can be stimulated through AMFs with the presence of magnetic materials, to release a high local concentration of the therapeutic. Extensive efforts have demonstrated the AMF-mediated release of therapeutics from magnetic mesoporous silica NPs capped with molecular nanovalves based on β-cyclodextrin that are removed by dissociation at elevated temperatures or lower pH [211,213,218,219]. Thermodegradable polymer coatings have also been widely investigated with magnetic mesoporous silica NPs[216,217,220]. Overall, bottom-up nanocomposites with capping systems controlled by "on demand" magnetic actuation and manipulation have shown promising results in localized, targeted drug delivery.

While more extensive literature exists for magnetically controlled PSi@Fe_3O_4 nanocomposites for targeted drug delivery synthesized via a bottom-up approach, top-down fabrication approaches are favorable due in part to its low cost, highly controllable and scalable fabrication that is compatible with common microfabrication techniques. Top-down approaches also yield larger pore sizes, which is a requirement for vectors delivering nucleic acids such as small interfering RNA (siRNA) or microRNA (miRNA). siRNA molecules have a rigid cylindrical shape with a length of ~5 nm and a diameter of ~2.3 nm [128]; these dimensions are difficult to readily infiltrate into MCM-41 mesoporous silica NPs which have typical pore diameters of 2 nm [123]. Much of the literature utilizing mesoporous silica fabricated from a bottom-up approach adsorb siRNA onto the surface because pore sizes are probably too small for infiltration [132,220–222]. A top-down fabrication approach can potentially increase siRNA encapsulation in the delivery vector while protecting it from degradation. Therefore, a top-down approach for fabricating magnetically responsive porous silica NPs is promising for clinical

translation, particularly as a vector in the delivery of gene therapies, which have witnessed a growth in both research interest and clinical translation [41,223].

Remaining Gaps in the Literature

In an effort to overcome synthetic challenges associated with magnetic and thermally responsive PSi NPs towards clinical translation, there is motivation to combine top-down PSi NPs with the thermosensitive capping agents previously discussed. However, combining these two components is more widely observed in sensors[224], MRI contrast agents[198,225], and fluorescence- based assays [197] and remains limited in targeted drug delivery applications. Further, many of these capping agents require complex, small scale synthesis that is incompatible with the mass commercialization techniques used to fabricate the top-down PSi NPs, which could potentially hinder clinical translatability. Moreover, the Fe_3O_4 NPs previously infiltrated into the PSi could be released from the nanocarrier during subsequent surface functionalization or encapsulation with capping agents. Thus, it would be advantageous to simplify the nanocarrier system by using the magnetic component as both a heat generator and capping agent.

Magnetic NPs have been utilized as capping agents in both top-down[225] and bottom-up PSi NPs[226–228]. Top-down PSi had ω-alkene-terminated Fe_3O_4 NPs covalently bonded to the PSi surface, but the hydrocarbon linker was not thermosensitive and therefore could not modulate drug release with temperature [225]. Incorporating a thermoresponsive linker between the PSi surface and Fe_3O_4 NP capping agents would greatly reduce the complexity in fabricating magnetic responsive PSi NPs. The following Chapters will discuss the fabrication and application of a magnetically, thermally responsive PSi NP drug delivery vector. The work

demonstrated in this thesis outlines a promising nanocarrier in externally triggered drug delivery and will be of great interest for on-command nanomedicine applications in oncological therapy.

Chapter 3. Porous Silicon, Iron Oxide and Magnetic Nanocomposite Fabrication and Optimization

Magnetic PSi nanocomposites are appealing materials in magnetically actuated drug delivery carriers, as previously discussed in Chapter 2. Yet, these carriers must be compatible with commercially-scalable fabrication techniques to realize their clinical translation. Top-down fabrication of PSi is favorable due in part to its low cost, highly controllable and scalable fabrication that is compatible with common microfabrication techniques. Moreover, top-down approaches yield larger pore sizes that can hold large molecules that are gaining attention in drug delivery applications, such as siRNA or miRNA.

In this Chapter we discuss the fabrication and optimization of magnetic PSi nanocomposites and its components. PSi layers were initially optimized to readily incorporate Fe_3O_4 NPs, and the layer fabrication scalability was investigated. We then optimized the synthesis of Fe_3O_4 NPs with typical dimensions needed for PSi infiltration with high reproducibility and stability. Initial magnetic PSi formation by Fe_3O_4 NP infusion into the layers yielded low infiltration efficiency, which was overcome by physically adsorbing the Fe_3O_4 NPs onto PSi NP surfaces through electrostatic interactions. We overcome synthetic challenges associated with magnetic and thermally responsive PSi NPs towards clinical translation by combining top-down PSi NPs with a thermosensitive capping agent.

3.1. Experimental

PSi Layer and NP Formation

PSi was formed by electrochemically anodizing silicon wafers (p++-type, diameter 100 mm, 0.01- 0.02 Ω-cm B-doped <001> oriented, University Wafer) in 140 mL of an aqueous HF (38%), ethanol electrolyte solution. Anodic etching was conducted with a homemade Teflon etcher with a rubber sealing ring that can accommodate up to 100 mm diameter wafers (~7850 mm^2 surface area). However, initial optimization experiments were conducted with an O-ring sealed aperture (around 15 mm in diameter, ~ 200 mm^2 surface area) inserted between the wafer and the electrolyte. The cathode is an Au plated mesh that evenly distributes the electric field over the etching area for a homogeneous porous layer formation. Good electrical contact between the wafer and anode was maintained by placing under the wafer an aluminum foil wrapped 100 mm Si wafer supported by an array of metal springs on the anode disk. A schematic drawing of the electrochemical etching system is shown in Figure 3.1. A Keithley 220 programmable current source in constant current mode with a set voltage compliance of 30 V was used for etching.

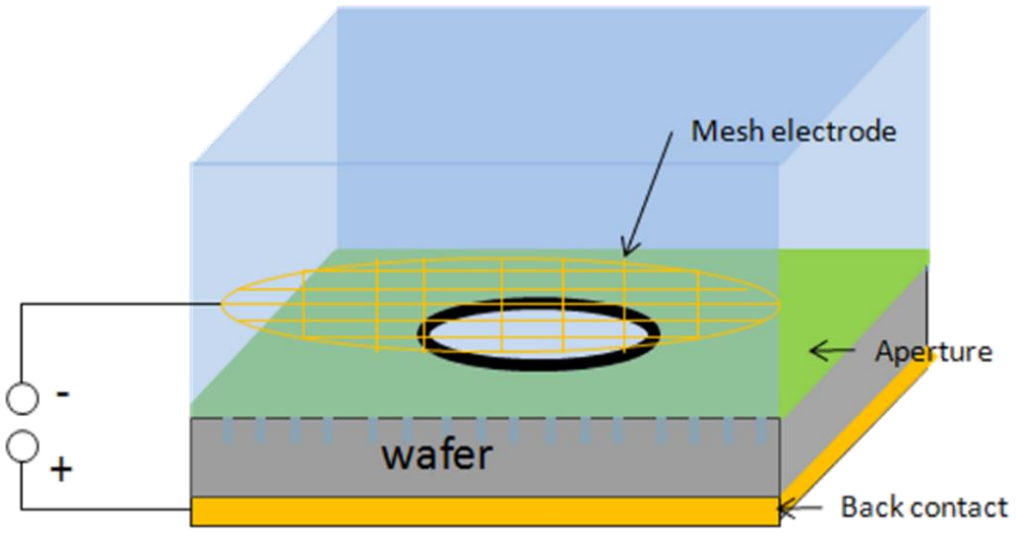

Figure 3.1 Schematic of the electrochemical etching system.

For PSi layer formations, current densities ranging from 0.3 mA/cm^2 to 50 mA/cm^2 and HF electrolyte concentrations between 5 vol% and 25 vol% were used. Etching steps were typically on the order of 5 min to 45 min. Multilayers were fabricated with subsequent etching steps that required changing the current density or HF concentration. For the multilayer structures the final current density step is within the electropolishing region, which allows for the porous layer to detach from the substrate as a film with thickness on the order of ~1-50 μm. After etching the desired porous structure, the layers were rinsed deionized (DI) water for several minutes and dried with an air flow to eliminate any remnant HF in the pores. PSi layer morphology was observed with scanning electron microscopy (Nova Nano 230, FEI Company).

PSi layers underwent surface functionalization treatments to achieve versatile surface charges and hydrophilicities. The layers were initially exposed to 49 vol% aqueous HF to eliminate any native oxide layer and resemble freshly etched films. Thermally oxidized PSi (TOPSi) layers were formed by a pre-oxidation step at 300 ° C for 1h to avoid pore coalescence at higher temps followed by oxidation at 600 ° C for 2h. Oxidation occurred in a quartz tube under ambient pressure. Amine-functionalized PSi (APTESPSi) layers were fabricated by treating thermally oxidized films with 10 vol% (3-Aminopropyl) triethoxysilane (APTES) in toluene for 1 hr at 25 °C. The layers were subsequently washed with toluene, a toluene-ethanol mixture, and ethanol to remove loosely bound APTES from the porous structure. The layers were dried in an oven at 65 °C overnight. Thermally hydrocarbonized PSi (THCPSi) layers, which possess hydrophobic characteristics, were initially washed with HF to remove any native oxide layers, as the thermal carbonization process requires a fresh hydrogen-terminated PSi surface. After drying the layers overnight the PSi layers were inserted in a quartz tube under N_2 flow (1 L/min) for 30 min at room temperature to remove oxygen and adsorbed moisture. The quartz

tube was then flushed with 1:1 N_2 and acetylene (C_2H_2) with a 1 L/min flow for 15 min at room temperature. The quartz tube was then placed in a tube furnace at 500 °C for 15 min under a 1:1 N_2−acetylene flow. After the thermal carbonization treatment, the tube furnace was cooled to room temperature under N_2 flow. Surface functionalization was confirmed by a Spectrum BX Fourier-transform infrared (FTIR) spectrometer (PerkinElmer Co.) equipped with a horizontal attenuated total reflectance accessory (MIRacle ATR, Pike Technologies Ltd.). Measurements were taken from 4000 to 450 cm^{-1} with a resolution of 2 cm^{-1} and averaging 32 scans. APTESPSi layers were further characterized for nitrogen presence through cross-section EDX.

Nitrogen sorption measurements on freshly etched and TOPSi films were conducted at 77 K with TriStar 3000 (Micromeritics Inc.) to determine the specific surface area, pore volume, and pore size distribution. The specific surface area was calculated using the Brunauer−Emmett−Teller (BET) theory, and the pore volume was determined from the isotherm using the total adsorption value at relative pressure p/p0 = 0.97. The pore size distribution was calculated from the desorption branch of the isotherm using the Barrett−Joyner−Halenda (BJH) theory.

PSi NPs were formed either by ultrasonication fracture overnight in ethanol or by milling with a high-energy ball mill (Pulverisette 7, Fritsch GmbH). Milling occurred in a 50 mL zirconia grinding jar with 18-22 zirconia 10mm grinding balls at 300 rpm in pulsed intervals overnight. The milling mediums varied for the layers with different surface functionalization. Ethanol was used as a milling medium for TOPSi. Toluene with 5 vol% APTES was used as the milling medium for APTESPSi layers and 1-decene for THCPSi. Before size-separating the particles through centrifugation, the APTESPSi layers were washed with a toluene-ethanol mixture, followed by pure ethanol. The THCPSi layers were washed in 5 w-% of succinic acid (SA) in ethanol several times to remove the 1-decene. Once the 1-decene is removed, THCPSi is

dispersed in pure ethanol for size separation. The milled NPs were size separated by repeatedly centrifuging the solution at 1500 rpm, 15 min and collecting the supernatant, which contained NPs on the order of ~200 nm as determined by dynamic light scattering (Zetasizer Nano ZS, Malvern Instruments Ltd.).

Magnetite (Fe_3O_4) Synthesis

Magnetite NPs were synthesized via the co-precipitation method similar to previous work[229]. The co-precipitation method has been most widely used because of its high scalability. In this method, Fe^{2+} and Fe^{3+} ions are precipitated in alkaline solutions such as ammonium hydroxide. The chemical reaction for magnetite (Fe_3O_4) formation is shown below.

$$Fe^{2+} + Fe^{3+} + OH^- \rightarrow Fe_3O_4 + H_2O \qquad (1)$$

Complete precipitation of Fe_3O_4 from an aqueous solution is typically expected at a pH between 8 and 14, and at a Fe^{3+}/Fe^{2+} stoichiometric ratio of 2:1.

In the original synthesis, 4.0 mL of 2M $FeCl_3$ and 1.0 mL of 1 M $FeCl_2$ were combined, and 50 mL of 0.5 M ammonium hydroxide (NH_4OH) was added to precipitate Fe_3O_4 out of the solution. The black precipitate was collected with a strong Neodymium magnet (N48, Applied Magnets) and the supernatant was decanted. The precipitate was washed with DI water twice, with the precipitate collected by the magnet each time. The magnetite NPs were stored in DI water until further use. We optimize the Fe_3O_4 synthesis by varying the NH_4OH addition rate to the $FeCl_2$ and $FeCl_3$ mixture, the NH_4OH concentration, and the $FeCl_3$ concentration.

The NPs were characterized by XRD (Parallel Beam Bede D1, Jordan Valley) and transmission electron microscope (TEM). A Jordan Valley (now Bruker) x-ray diffractometer with incident parallel beam optics, Cu Kα radiation (λ= 1.5406 Å), and scattered beam slits confirmed the magnetite phase. Williamson-Hall plots generated from the peak's full width half

maximum (FWHM) determined the NP size. The size was further corroborated by high resolution TEM (HRTEM) (Titan S/TEM 80- 300 kV, FEI). The average NP size and standard deviation was determined from 20 measurements through ImageJ.

Magnetic PSi Formation

PSi and Fe_3O_4 NPs were combined to form a magnetic composite. The composite was initially formed by infusing the magnetic suspension into the PSi layer with the guidance of a magnet followed by ultrasonic fracture [197,205]. Magnetite solutions of 1, 10, and 25 mg/mL in aqueous solution (~100 µL) were dropcasted onto the PSi trilayer with the larger pore size, porosity end facing up and a strong Neodymium magnet directly underneath the PSi layer. The magnetite suspension was left to infuse into the PSi layer until the solvent evaporated (overnight). Magnetite infusion into PSi layers was characterized by cross-section EDX (SEM Nova Nano 230, FEI Company).

Magnetic nanocomposites were also formed by physically adsorbing the negatively charges Fe_3O_4 NPs onto positively charged APTESPSi NP surfaces via electrostatic interactions. A 2mL solution containing a 1:1 ratio of APTESPsi in ethanol to Fe_3O_4 NPs in Milli-Q water was stirred at 300 rpm for 1h at room temperature. The mixture was then centrifuged at 13,200 rpm, 10 min to remove any loosely bound Fe_3O_4 NPs. The particles were subsequently washed in Milli-Q water once and stored in ethanol until further use.

The amount of Fe_3O_4 NPs electrostatically bound to the APTESPSi NPs was quantified by vibrating-sample magnetometer (VSM), which is discussed in further detail in the magnetic characterization section, and inductively coupled plasma optical emission spectrometry (ICP-OES, Atomic Emission Spectroscopy Perkin Elmer Optima 8300). The ICP-OES samples were prepared by digesting an APTESPSi@Fe_3O_4 mixture (434.8 µL APTESPSi and 9.25 µL Fe_3O_4)

in 1 mL 5M sodium hydroxide (NaOH) for 3h to initially dissolve the APTESPSi. Fe was then digested by adding 500 µL of the Si-dissolved solution to 500 µL of 37% hydrochloric acid (HCl) and stirring at 300 rpm for 3h. The solution was then diluted with 9 mL Milli-Q water to give a final HCl concentration of 1.85%.

NP size and zeta (ζ)- potential was measured in Milli-Q water using a Zetasizer Nano ZS (Malvern Instruments Ltd.). APTESPSi binding to Fe_3O_4 NPs was further confirmed by TEM (Jeol JEM-140, Jeol Ltd., Japan) and EDX. TEM samples were prepared by dropcasting 7 µL of a 100 µg/mL solution onto carbon-coated copper grids (300 mesh; Electron Microscopy Sciences, USA). Samples settled down for 5 min on the grid prior to removing excess liquid with filter paper.

3.2. PSi Layer and NP Formation

Single Layers

PSi films were fabricated by electrochemically etching highly p-doped Si wafers with various current densities and HF electrolyte concentrations. Single PSi layers formed by a single etching step were initially fabricated to investigate porous morphology changes without any influence from subsequent etching steps. While previous reports have shown that subsequent etching steps do not affect previous ones in a multilayer structure, this claim is not valid when there is a large gradient between the two layers[230]. This phenomenon is further discussed for trilayer PSi architectures later in this section.

Overall, increasing the current density increased the pore size, porosity, and layer thickness as expected and as shown in Table 3.1.

Table 3. 1 Changes in porous silicon layer morphology with current density.

Current Density (mA/cm^2)	Layer Thickness (μm)	Pore size (nm)	Porosity (%)
12.5	31.9 ± 2.5	5.1 ± 0.1	~12
25	44.4 ± 2.2	30.3 ± 5.8	~18
50	85.1 ± 8.8	25.3 ± 5.7	~38

The variation in pore morphology with increasing current density (12.5, 25, and 50 mA/cm^2) is shown in Figure 3.2.

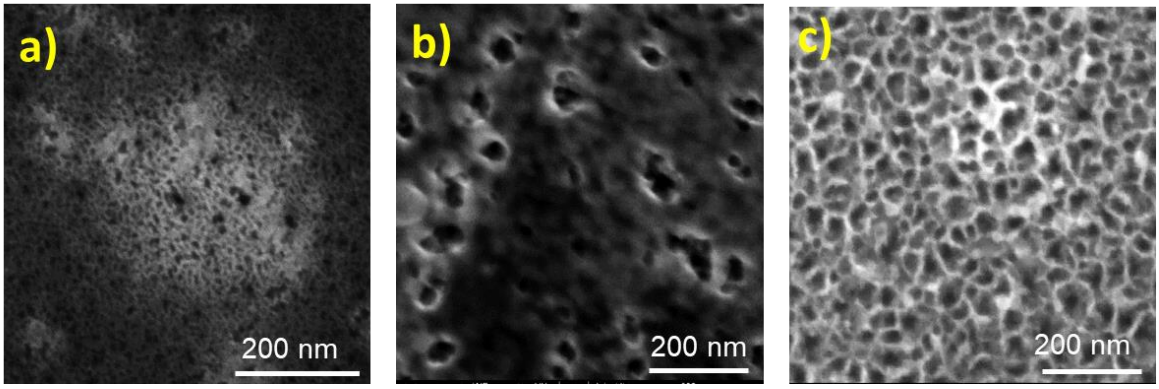

Figure 3.2 Plan-view SEM images of porous silicon layers etched at a) 12.5 b) 25 and c) 50 mA/cm^2.

The average pore size follows an exponential growth where the size increases significantly by almost 500% (from 5.1 to 30.3 nm) when the current is raised from 12.5 to 25 mA/cm^2, while there is no significant difference in pore size when the current is further raised to 50 mA/cm^2. The average pore sizes between 25 and 50 mA/cm^2 are both within their standard deviation, and therefore pore size increases significantly only up to a certain current density. The porosity changes with current density also follow a non-linear trend, where greater porosity increases (from 18% to 38%) were observed when the current was varied from 25 to 50 mA/cm^2. This suggests that at lower current densities, pore growth is the dominating process while at higher current densities a larger number of pores are formed.

The current density was not linearly proportional to the PSi layer thickness. Table 3.1 shows thickness measurements determined by cross-section optical microscope images of the PSi layers previously mentioned. All samples were etched in a 25% HF solution in ethanol for 30 minutes. In accordance with previous literature, the porous layer thickness increases with increasing current density, from 31.9 to 44.4 μm, where changes in thickness are more pronounced at higher currents. When increasing the current density from 25 to 50 mA/cm^2, the PSi layer thickness was doubled. Increasing thickness with current density is in agreement with locally enhanced dissolution rates at the pore tips as a more intense electric field is presented at the pore tip-electrolyte interface[101]. For p-type PSi the growth is determined by the direction of the current lines in the space charge region, as previously discussed in Chapter 2. The electric field enhancement, in terms of the ratio of the local field magnitude at the pore tip to the average field, increases with decreasing radius. For example, theoretical field calculations using space charge region considerations for needle-plane electrodes demonstrated a field enhancement increase from 15 to 400 when the tip radius decreased from 139 μm to 5 μm[231]. Considering that the mesopores fabricated in these instances are < 50 nm, the driving force for pore growth along the <100> direction is highly influenced by the current density. Moreover, increasing the current density can lead to a greater number of pores nucleated since it more readily overcomes the driving force for pore nucleation, and once pores are nucleated then the driving force is greater for growing down the <100> direction. Therefore, while the pore size faces a growth limit the increased current density contributes to a higher driving force to overcome more nucleation sites (leading to higher porosity) and to drive the pore growth along the current line (leading to thicker layers).

Changes in HF concentration were also investigated to confirm this parameter's effect on the PSi morphology. The HF concentration was decreased from 25% to 10% for a sample etched at 50 mA/cm^2 for 30 minutes, but no porous layer was observed. Instead, the area exposed to the electrolyte solution was in the electropolishing regime, as evident by a uniform decrease in the wafer thickness around the exposed aperture area. Upon understanding how to tune the morphology with various etching parameters, porous multilayers were investigated to remove the PSi from its substrate.

PSi Bilayers

PSi bilayers were initially fabricated with the first etching step forming the PSi layer to be utilized in further applications and the second etching step exfoliating the top layer from the substrate. With our initial design of the magnetic PSi nanocomposite, we considered a layer with a pore size gradient where one side has pore sizes large enough to fit the Fe_3O_4 NPs while the other side has pore sizes small enough where the Fe_3O_4 NPs would not infiltrate through the layer. Increasing the pore size and porosity from the top to bottom layer requires an increase in current density and/or decrease in HF concentration. The PSi bilayer fabricated by electrochemical etching in a 25% HF solution at 12.5 mA/cm^2 for 30 minutes, followed by a current density of 50 mA/cm^2 in 5% HF solution for 30 minutes. Rather than exfoliating as a film, the porous layer came off in small, millimeter and micron-sized pieces. Figure 3.3 shows cross-section images of the bilayer leftover on the substrate. Figure 3.3a shows the clear distinction between the top layer, bottom layer, and substrate. Moreover, a void between porous layers, as shown Figure 3.3b, explains the mechanical instability of the films; The two layers lack continuity, and as separate entities they are too thin to remain stable films. Interestingly, the thickness of the top porous layer in Figure 3.3b is 4.6 $\pm$ 0.1 μm, which is almost 8x thinner than

a layer etched with the first step individually. Rather, the entire porous layer thickness more closely resembles that of the first etching step when fabricated as a single step etch. Because the layer properties are claimed to not change during subsequent etching steps, this thinner layer from Figure 3.3b is probably not the entire top layer, but instead a portion of it.

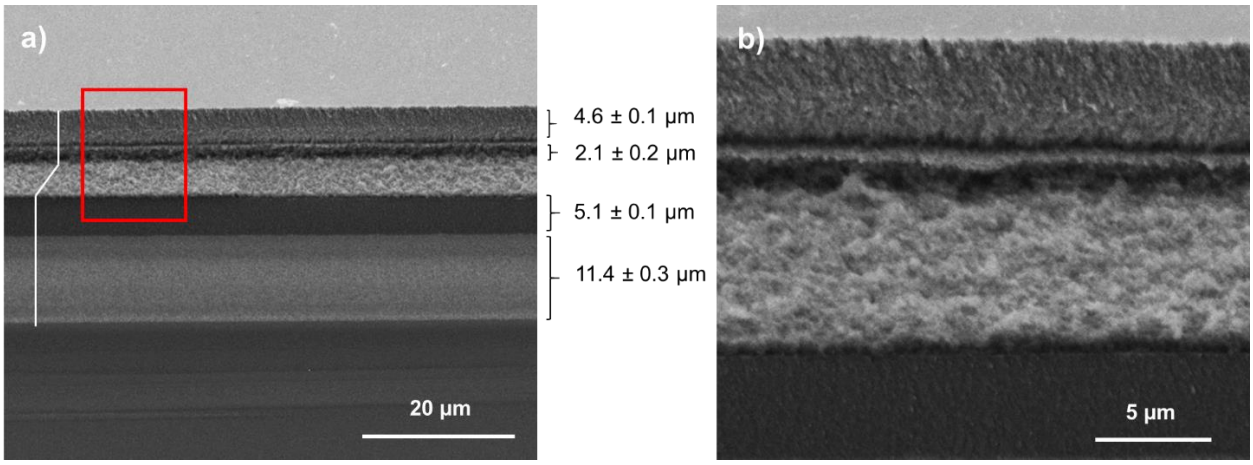

Figure 3.3 a) Cross-section SEM image of a porous silicon bilayer etched at 25% HF, 12.5 mA/cm^2, 30 min followed by 5% HF, 50 mA/cm^2, 30 min. b) Cross-section SEM image of the red inset in Figure 2a showing void formation between the etching steps.

Therefore, layer exfoliation does not necessarily occur at the second etching step and substrate interface. Rather, void formation can occur within the two layers and is not strictly limited to the layer interface. While exfoliating a powder is useful given that the end product is NPs, an intact PSi film was desired since for Fe_3O_4 NP infiltration into the PSi layers. Thus, the PSi film architecture was further modified to increase its mechanical stability. Figure 3.4 shows optical images of exfoliated bilayers with different etching conditions. Increasing the HF concentration to 10% (Figure 3.4b) and 25% (Figure 3.4d) yielded layers that exfoliated as larger pieces. However, bilayer optimizations did not exfoliate the layer as a single piece corresponding to the exposed surface area of 200 mm^2. Thus, a trilayer architecture was proposed to decrease the morphology gradient and increase the PSi mechanical stability for subsequent Fe_3O_4 NP infiltration.

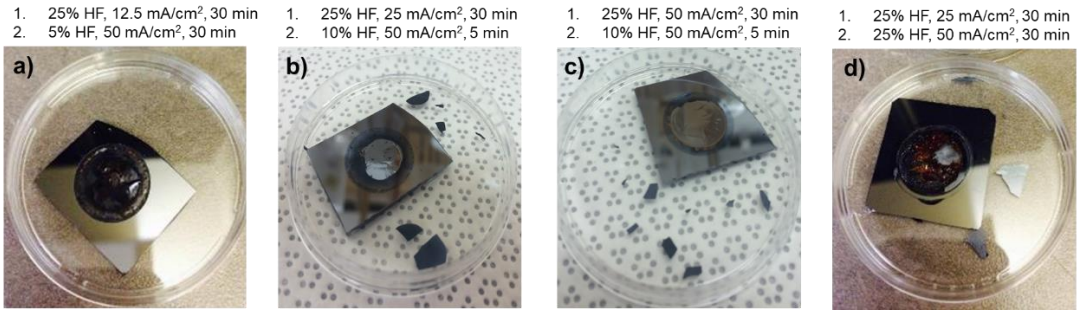

Figure 3.4 Optical images of exfoliated porous silicon bilayers optimized with different etching parameters. In all cases, the bilayer is exfoliated in several smaller pieces rather than one piece corresponding to the exposed etching area.

PSi Trilayers

PSi trilayers produce stable films due to their smaller pore morphology gradient, while remaining suitable for Fe_3O_4 NP infiltration and trapping. The film resembled an ink-bottle pore structure[232], where necks are present in the superficial layer and wider cylindrical pores are in the bulk of the layer. The first etching step (top layer) should yield a thin layer of small pores which the Fe_3O_4 NPs cannot infiltrate through. The second etching step will produce medium sized pores, large enough to host the NPs. The final etching step will remove the porous film from the substrate while also producing large pores that will readily allow the NPs to infiltrate into the film. A schematic of the trilayer is shown in Figure 3.5d. Initially, a trilayer was formed using the following conditions: 1) 12.5 mA/cm^2, 5 min 2) 25 mA/cm^2, 45 min 3) 50 mA/cm^2, 5 min all in 25% HF. However, no exfoliation from the substrate occurred. When the third etching step was increased from 5 to 30 minutes, the layer was removed from the substrate, suggesting that pore branching occurs. This final etching step also increased the pore size of the top layer by more than 3x from 5.1 + 0.1 nm to 17.2 $\pm$ 4.8 nm, which is contrary to the common observation of subsequent etching steps not influencing previous ones. Because smaller pore sizes were desired for the top layer, particularly about the same size or smaller than that of the Fe_3O_4 NPs,

the etching current density was decreased to 3 mA/cm^2 and even further to 0.15 mA/cm^2 while the subsequent etching steps were unchanged. Table 3.2 summarizes the pore morphology of this top layer as the etching current density is decreased.

Table 3.2 Changes in top layer morphology of porous silicon trilayer with current density.

First etching current (mA/cm^2)	Top layer pore size (nm)	Bottom layer pore size (nm)	Layer thickness (μm)
12.5	17.2 $\pm$ 4.8	37.3 $\pm$ 10	38.6 $\pm$ 0.3
3	12.4 $\pm$ 0.9	38.5 $\pm$ 5.7	47.6 $\pm$ 0.2
0.15	7.9 $\pm$ 1.3	24.6 $\pm$ 4.0	45.3 $\pm$ 0.8

With an initial etching current density of 0.15 mA/cm^2, the pore size decreased to 7.9 $\pm$ 1.3 nm, which is comparable in size to the Fe_3O_4 NPs. Table 3.2 also shows that the pore size of the bottom layer remains relatively unchanged and is large enough for Fe_3O_4 NPs less than 20 nm in size to infiltrate. Figure 3.5 shows plan view SEM images of the top (Figure 3.5b) and bottom (Figure 3.5a) of the PSi trilayer etched with an initial current density of 0.15 mA/cm^2, where a decrease in the pore size and porosity with decreasing current density is observed within the top layer. Figure 3.5c shows a cross-section of the porous layer, where current-line oriented pores are observed.

A mechanically stable layer was exfoliated from the substrate in one piece corresponding to that of the exposed etching area. After achieving the trilayer fabrication, scalability of the experimental conditions was investigated. The fabrication was scaled up by increasing the exposed surface area by 40x and increasing the current to maintain the same current densities, considering the higher surface areas. Scaling up this fabrication increased the amount of PSi made by more than 30x (from ~13 mg to ~400 mg per run).

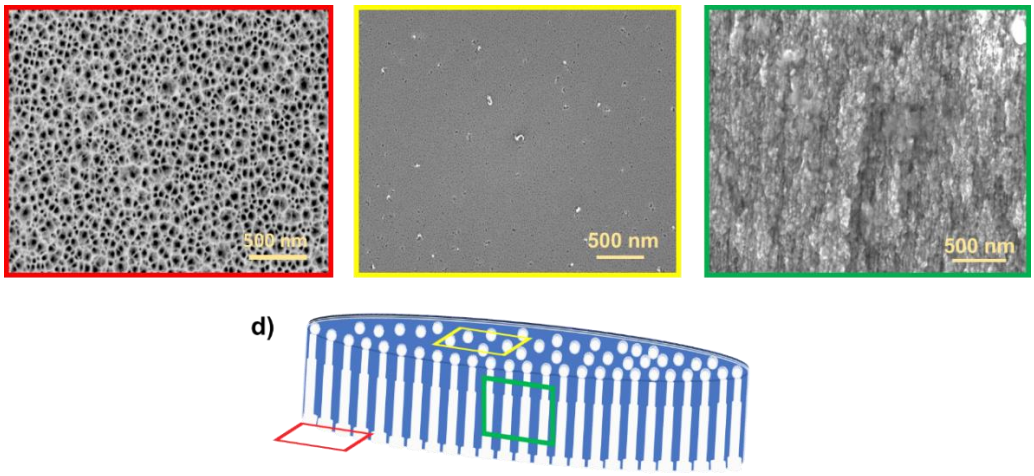

Figure 3.5 Plan view SEM images of porous silicon trilayer from the larger pore side where exfoliation from the substrate occurs (a) and from the smaller pore side resulting from the first etching step (b). A cross-section SEM image of the trilayer shows a branch-like morphology with pores growing downward in the <100> direction (c). A schematic of the trilayer shows the insets corresponding in color from where the SEM images were taken.

Figure 3.6 shows optical images of the etcher with a 200 mm^2 exposure area (Figure 3.6a), a 7850 mm^2 exposure area (Figure 3.6b), and the corresponding exfoliated layers.

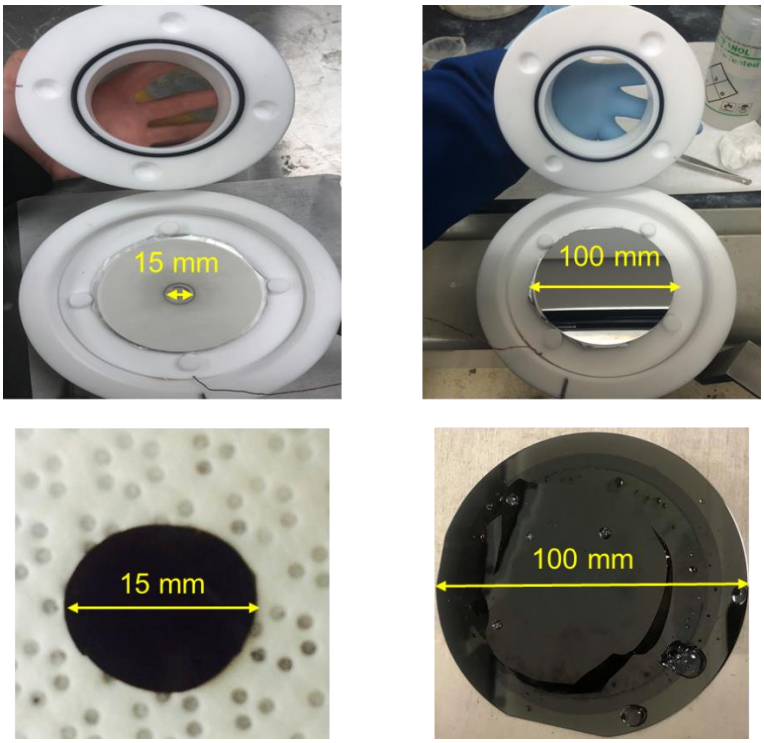

Figure 3.6 Optical images of Teflon electrochemical etcher with (a) and without (b) an aperture that varies the exposed wafer surface for porous silicon formation. The resulting layer diameter with (c) and without (d) the aperture demonstrates the scalability that is readily achieved within the same etcher.

Thus, we demonstrated a readily scalable fabrication process of PSi layers that uses minimal etching solution (140 mL) at both the optimization and scaled up level. Moreover, scalability and compatibility with common microfabrication techniques overcomes the fabrication challenges that are commonly associated with the clinical translation of nanomedicines.

The surface area, pore volume, and pore size distribution of as- anodized free-standing freshly etched and thermally oxidized PSi trilayer films before ball milling or ultrasonication fracture was determined by the BET, BJH methods. After thermally oxidizing the freshly etched PSi films the surface area decreased from 193 m^2/g to 173 m^2/g and the pore volume decreased from 0.57 cm^3/g to 0.42 cm^3/g (Figure 3.7).

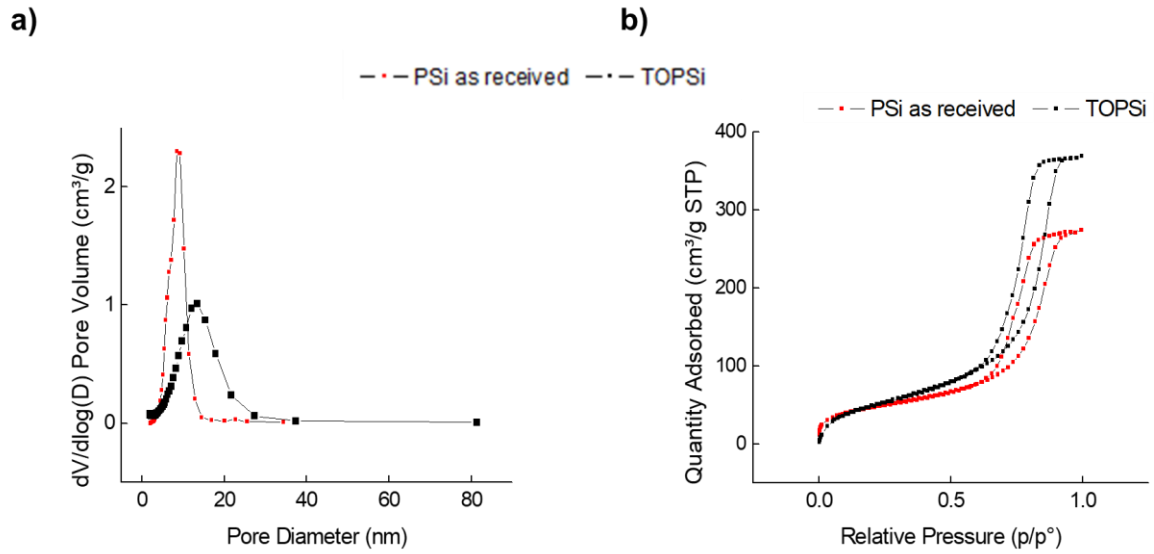

Figure 3.7 a) Pore size distribution and b) nitrogen adsorption/desorption isotherms of porous silicon and thermally oxidized porous silicon films before ball milling into nanoparticles.

Decrease in surface area and pore volume with thermal oxidation is due to the increasing molecular volume of the SiO_2 grown within the pores. Moreover, the average pore size decreased from 11.8 nm to 9.7 nm after thermal oxidation due to the SiO_2 layer grown within the pores (Figure 3.7a).

PSi Surface Chemistry

Aside from tunable morphology, the PSi films are also readily functionalized to provide versatile surface chemistries in terms of hydrophilicity and surface charge. TOPSi layers are considered hydrophilic while THCPSi is hydrophobic. Moreover, TOPSi possesses a negative surface of -26.6 $\pm$ 0.2 mV and APTESPSi has a positive surface charge of +31.7 $\pm$ 1.4 mV (Figure 3.8a).

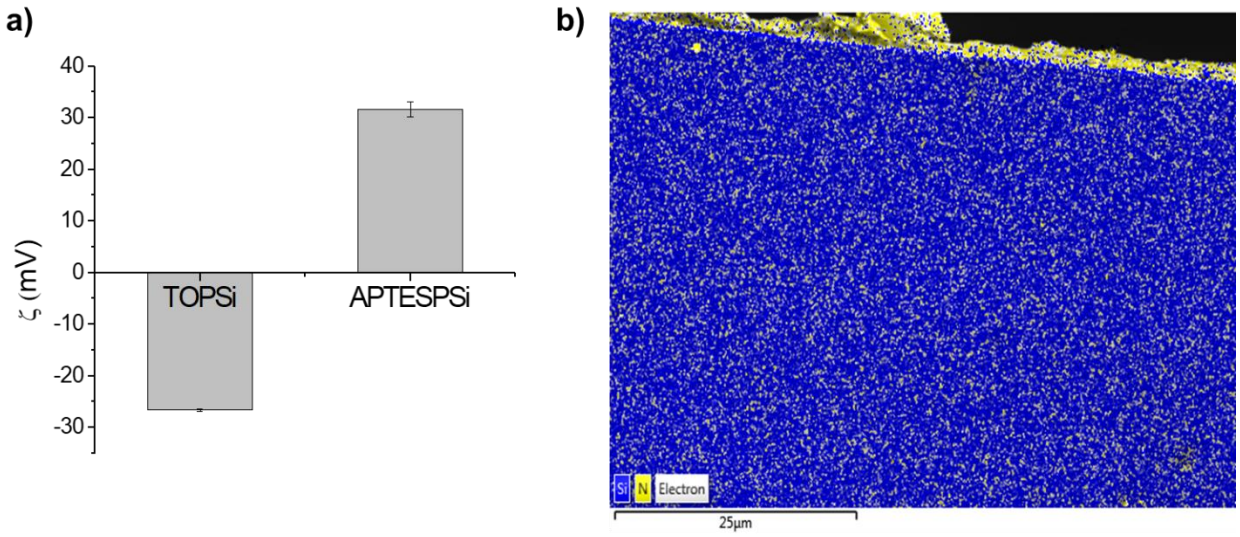

Figure 3.8 a) Zeta potential measurements of PSi nanoparticles suspended in water showing negative charges associated with hydroxyl groups from TOPSi and positively charged amine groups on APTESPSi surfaces. b) EDX elemental map analysis of APTEPSi layer cross section taken under SEM.

The surface functionalization was confirmed by FTIR (Figure 3.9). Freshly etched PSi films demonstrate transmission bands at 3600 cm^{-1} and 1100 cm^{-1} that are indicative of some oxidation due to the presence of air moisture. After dipping the film in HF the two bands disappear due to the acid dissolving SiO_2. Thermally oxidizing the films yields a broad, prominent band between 3400- 3600 cm^{-1} that indicated the presence of -OH groups. Another broad band appears at 1200 cm^{-1} associated with SiO_2. Amino functionalization that occurs after thermal oxidation is also apparent from the FTIR spectra. The appearance of bands at 1650 cm^{-1} and 1850 cm^{-1} are

assigned to the symmetric and asymmetric deformation of protonated amine groups ($-NH3^{+}$) [233,234].

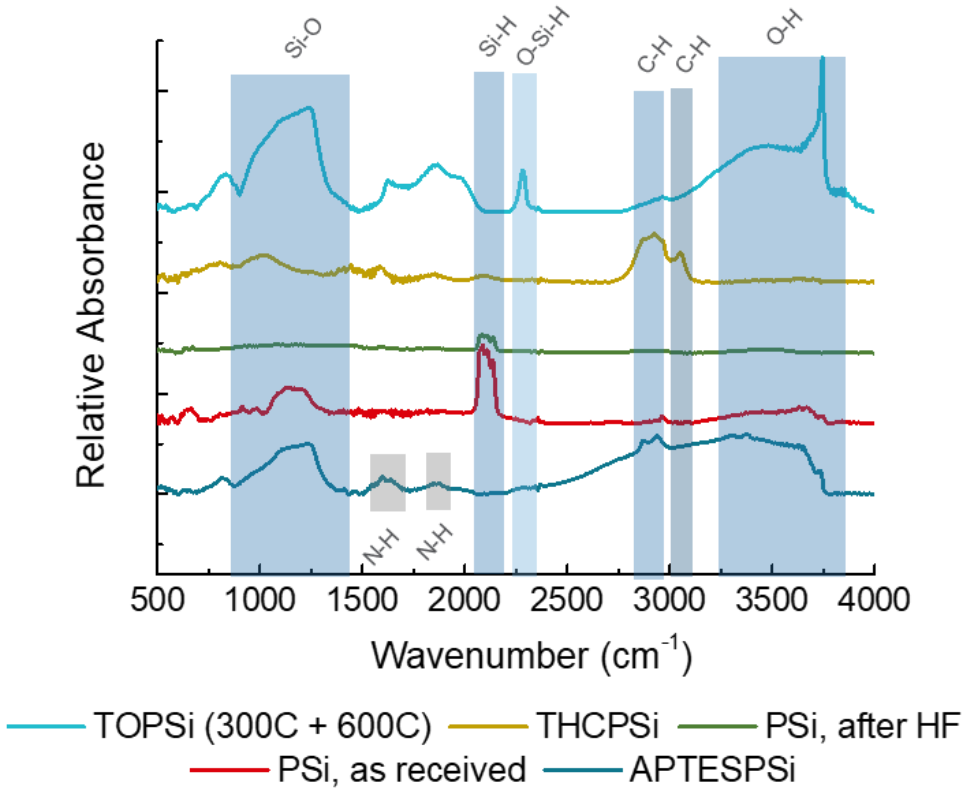

Figure 3.9 FTIR spectra for PSi films treated with different surface chemistries. PSi, as received indicates PSi films after electrochemical etching and for PSi, after HF the films were treated with HF to remove native oxide layers. For thermally oxidized PSi (TOPSi), thermal hydrocarbonized PSi (THCPSi), and amine-functionalized PSi (APTESPSi) their respective reactions are shown on the right.

The asymmetric and symmetric stretch vibration modes of $C-H_2$ and $C-H_3$ groups between 2875 cm^{-1} and 2980 cm^{-1} [235] are related to the propylsilane chains. Amine functionalization was further confirmed by cross-section EDX (Figure 3.8b). Nitrogen was observed throughout the film, indicating homogeneous distribution of the amine functionalization. Tuning the surface chemistry to have various hydrophilicities and surface charges is a pertinent consideration when encapsulating the nanocarrier within a targeting peptide, stimuli-responsive material, and pore-capping agents that localize or modulate a therapeutics' release. Electrostatic interactions and

solvent-switching precipitation techniques[57,236–238] have made it possible to encapsulate nanocarriers in a facile, efficient manner.

3.3. Magnetite (Fe_3O_4) Synthesis

Fe_3O_4 NPs were synthesized via the co-precipitation method as previously reported[229]. Initially, the NH_4OH concentration was varied from 0.375 M to 1 M. The NP sizes were determined from Williamson- Hall plots that were generated by the XRD spectra shown in Figure 3.10.

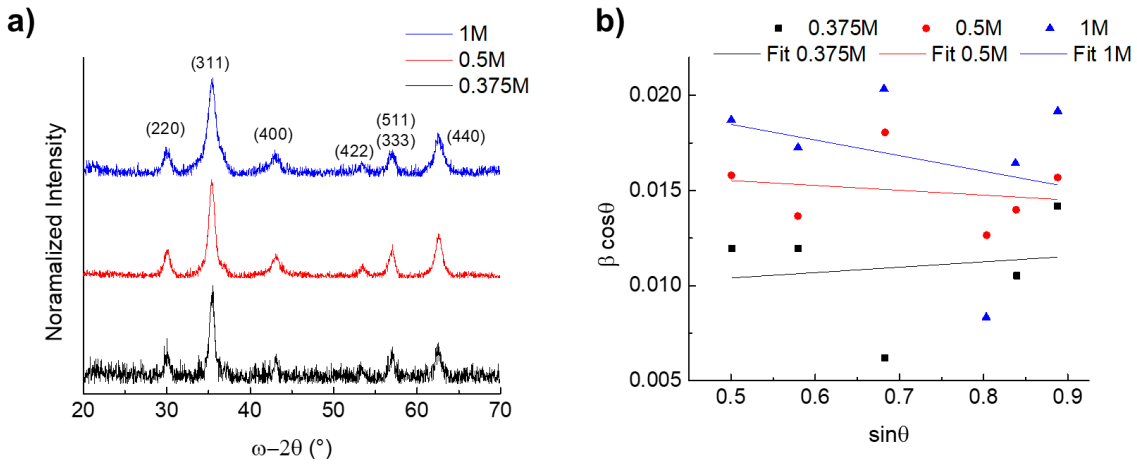

Figure 3.10 a) Powder XRD of Fe_3O_4 nanoparticles synthesized with varying NH_4OH concentrations and b) their respective Williamson-Hall plots used to determine the nanoparticle size.

Overall, the NP size increased from 6.1 nm to 15.4 nm as the NH_4OH concentration decreased from 1M to 0.375M. However, TEM measurements (not shown) revealed high aggregation in the samples, and the formation of rod-like structures for NPs synthesized with 0.375M NH_4OH. This rod shape might make it difficult for Fe_3O_4 NPs to infiltrate the Si porous structure.

The NH_4OH addition rate was also varied with nucleation and crystal growth considerations. We anticipated that faster addition rates of the NH_4OH precursor would results in a higher supersaturated solution that in turn increases the Gibbs free energy. Given that the reduction in Gibbs free energy is the driving force for crystal nucleation and growth, a larger

number of nucleation events are expected at faster precursor addition rates[239,240]. The critical radius for nucleation, r*, is dependent on the change of Gibbs free energy per unit volume of the solid phase, ΔG_v, as follows:

$$r^* = -\frac{2\gamma}{\Delta G_v} \qquad \text{Eq. 3.1}$$

where γ is the surface energy per unit area. A higher Gibbs free energy would result in smaller nuclei versus a lower Gibbs free energy from a lower precursor addition rate. With homogenous nucleation considerations, the NH_4OH addition rate was varied to 3.3 mL/hr, 10 mL/hr and 25 mL/hr. The XRD spectra and corresponding Fe_3O_4 NP sizes are shown in Figure 3.11.

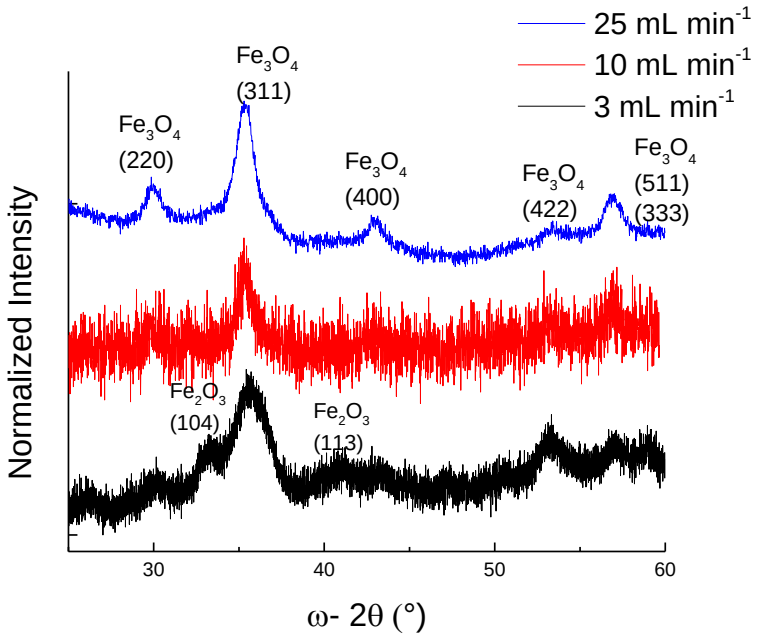

Figure 3.11 Powder XRD of Fe_3O_4 nanoparticles synthesized with varying 0.5 M NH_4OH addition rates. The presence of Fe_2O_3 at the lowest addition rate indicates oxidation.

The NP sizes were determined from the most intense diffracting plane (311) rather than Williamson-Hall plots because of the high background noise that made it difficult to determine the full-width half maximums (FWHM) for some of the diffraction peaks. Increasing the precursor addition rate from 3.3 mL/hr to 10 mL/hr doubled the NP size from ~3 nm to ~6 nm. The XRD spectrum for precursor added at 3.3 mL/hr showed an additional peak at ~33.2°, which

is typically associated with maghemite (Fe_2O_3), indicating that some oxidation is occurring at this lower addition rate. Moreover, further increasing the rate to 25 mL/hr did not result in any NP size difference. TEM images shown in Figure 3.12 confirmed that when considering the standard deviation from the size distribution, there was no significant difference in NP size within the precursor addition rate range.

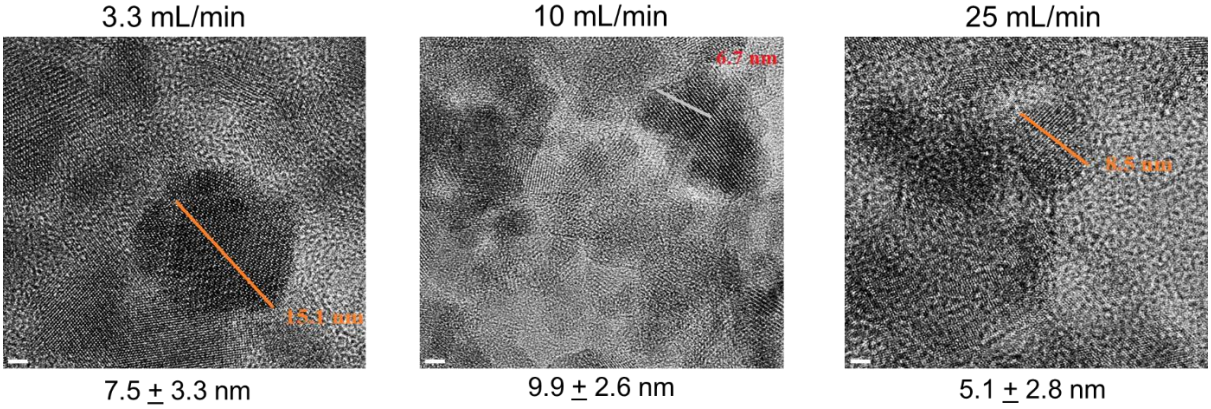

Figure 3.12 High resolution TEM images of Fe_3O_4 nanoparticles synthesized with varying 0.5 M NH_4OH addition rates with the average nanoparticle size and standard deviation below each respective image. Scale bar is 2 nm.

The NP size was also assessed by XRD at various times after the synthesis to determine the overall NP stability and whether any significant Ostwald ripening, where smaller particles within the solution redissolve and in turn allow larger particles to grow even more [239,240], is occurring. The NP spectra were collected after 2, 4, and 13 days, and the spectra are shown in Figure 3.13. Overall, there is no significant difference between the NP sizes, indicating the Fe_3O_4 NP stability.

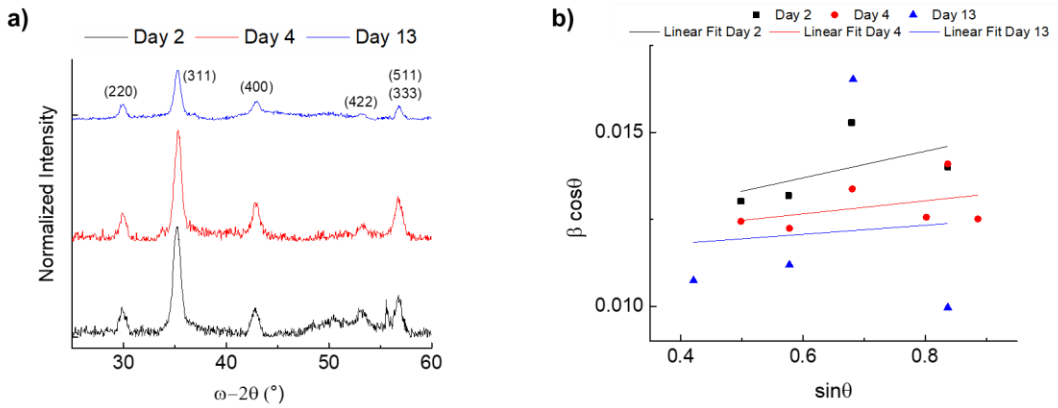

Figure 3.13 a) Powder XRD of Fe_3O_4 nanoparticles characterized after respective days of synthesis and b) their Williamson-Hall plots used to determine the nanoparticle size.

Another parameter varied in the co-precipitation synthesis was the Fe (III)/Fe (II) ratio. Previous literature has shown that varying relative concentrations of Fe^{2+} and Fe^{3+} determines the NP phase that is formed [241]. Magnetite forms between $0.60 \leq x \leq 0.66$ during alkalization, where $x = Fe^{3+}/(Fe^{3+} + Fe^{2+})$. As x reaches 1 and only Fe^{3+} ions are present, goethite formation is observed. For $x \leq 0.33$ $Fe_6(OH)_{12}SO_4$, xH_2O, also known as "Green Rust SO_4", will form. Because magnetite forms over a small range of iron precursor ratios, we varied the Fe^{3+} concentration was varied from 0.66 to 2.5 M. Figure 3.14 shows the powder XRD spectra of Fe_3O_4 NPs synthesized with different precursor concentrations and the corresponding Williamson-Hall plots that were used to determine the NP size through the y-intercept [242].

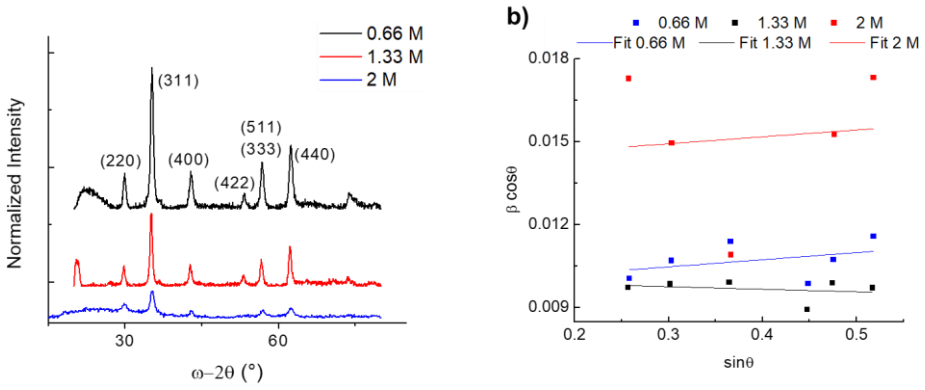

Figure 3.14 a) Powder XRD of Fe_3O_4 nanoparticles synthesized with varying Fe^{3+} concentrations and b) their respective Williamson-Hall plots used to determine the nanoparticle size.

Table 3.3 shows the resulting NP size determined from Williamson-Hall plots and a size increase with decreasing precursor concentration was observed.

Table 3.3 Y-intercepts determined from Williamson-Hall plots for Fe3O4 nanoparticles and sizes calculated using the y-intercepts.

Fe^{3+} Concentration (M)	Y-intercept	Size (nm)
0.66	0.0097	14.3
1.33	0.01	13.9
2	0.0142	9.8

TEM images of the Fe_3O_4 NPs synthesized with 2M and 1.33M Fe^{3+} further corroborated the sizes determined by the Williamson-Hall plots (Figure 3.15).

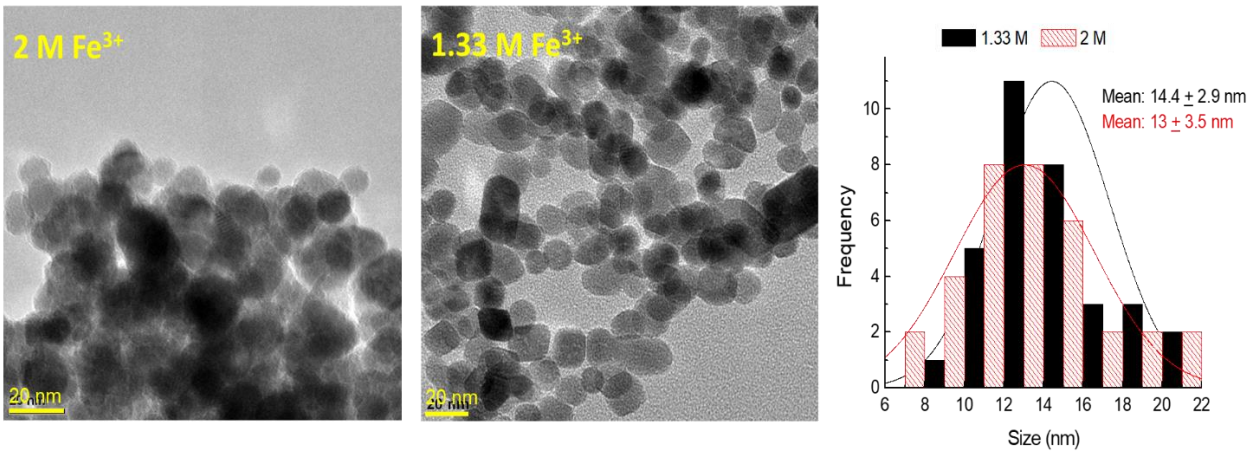

Figure 3.15 TEM images for Fe_3O_4 nanoparticles synthesized with varying Fe^{3+} concentration and their corresponding size distribution determined from 20 measurements.

However, considering the mean and standard deviation obtained from the size distribution, there is no statistically significant difference in the NP size. While there is no significant different in the size distribution, which can be difficult to determine with XRD methods, TEM allowed us to directly observe that decreasing the precursor concentration to 1.33M yielded NPs with reduced agglomeration, which is crucial in maintaining final formulation sizes that can pass through the endothelial membrane when considering the EPR effect[53,54], or in avoiding particle aggregation

in blood vessels that can lead to thrombosis[121]. Thus, Fe_3O_4 NPs synthesized with 1.33M Fe^{3+} were used to form the final APTESPSi@Fe_3O_4 nanocomposite formulation. The magnetic properties of the Fe_3O_4 NPs and APTESPSi@Fe_3O_4 nanocomposite are discussed in Chapter 4. The magnetic PSi composite was initially formed by Fe_3O_4 NP infusion into PSi layers followed by ultrasonic fracture. An alternative structure where the Fe_3O_4 NPs are bound to the PSi surface via electrostatic interactions is also proposed.

3.4. Nanocomposite Formation

The PSi layers and Fe_3O_4 NPs were subsequently combined to fabricate a magnetic PSi composite with the initial idea that Fe_3O_4 would be infiltrated inside the PSi. The Fe_3O_4 NPs were infiltrated into the PSi by an infusion method previously described[243]. A solution of Fe_3O_4 in ethanol with three different concentrations (1, 10, and 25 mg/mL) was dropcasted on top of the PSi layer with the larger pore side facing up and a magnet below the layer to magnetically guide the solution into the pores. A picture of the experimental setup is shown in Figure 3.16a.

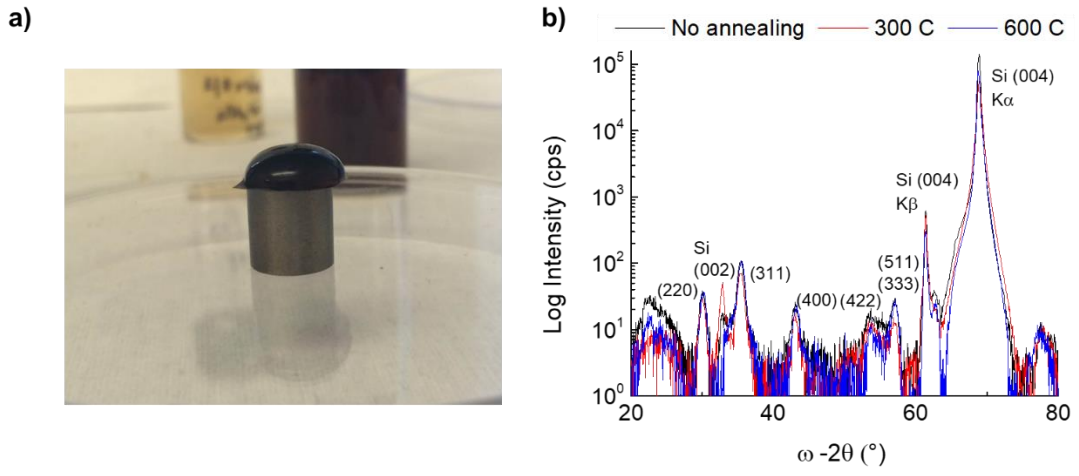

Figure 3.16 a) Optical image showing Fe_3O_4 nanoparticle (10 mg/mL) infusion into Psi layer with guidance of a magnet and b) XRD spectra of Fe_3O_4-infused Psi layers that were annealed prior to infiltration at varying temperatures.

XRD measurements of PSi layers annealed at various temperatures infused with a 10 mg/mL Fe_3O_4 solution confirmed the presence of both PSi and Fe_3O_4 phases (Figure 3.16b). After infiltration, diffraction from the (220) and (311) planes indicate that the Fe_3O_4 phase was present in the PSi. EDX measurements confirmed the presence of Fe within infiltrated PSi cross-sections. EDX spectra, linescans and elemental mapping confirmed Fe presence and its distribution throughout the cross-section (Figure 3.17).

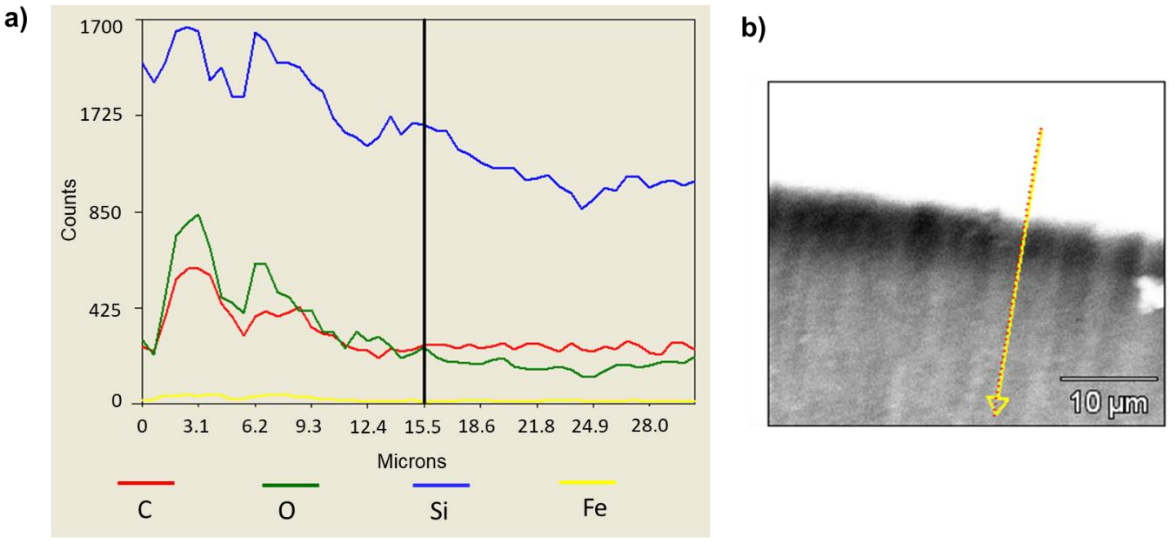

Figure 3.17 a) EDX linescan of Fe_3O_4-infiltrated PSi layer showing infiltration into the first ~10 µm of the layer and b) the corresponding x-section from which the linescan was taken of.

The decreasing intensity for Si, O, and Fe is probably due to the sample being tilted at an angle of 45°; The sample's distance from the electron beam increases and therefore its intensity decreases as the linescan progresses. A low infiltration efficiency was observed (Fig. 3.17), where the presence of Fe is only in the first ~10 µm of the sample. Despite the low infiltration efficiency, the composite was formed into NPs via ultrasonic fracture of the Fe_3O_4 infiltrated PSi layers in ethanol overnight. Larger particles were removed with a 2 µm Millipore filter and further characterized. An XRD spectrum of the nanocomposite (Figure 3.18a) shows the presence of Fe_3O_4 NPs and polycrystalline Si that is being formed as the layer is broken down by

ultrasonication. TEM images and EDX spectra of the nanocomposite are shown in Figure 3.18b and Figure 3.18d.

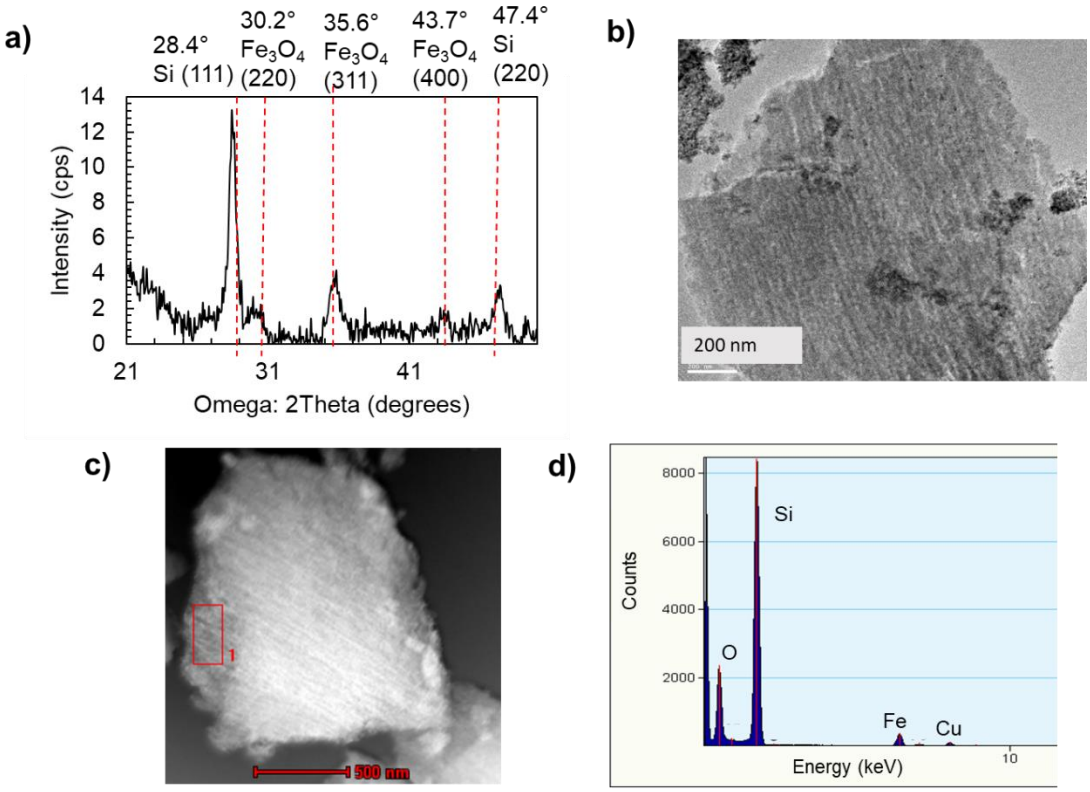

Figure 3.18 a) XRD spectra of Fe_3O_4-infiltrated PSi nanoparticles. b) TEM image of PSi nanoparticle with Fe_3O_4 nanoparticles clustered onto the surface. c) TEM image of Psi-infiltrated Fe_3O_4 nanoparticles with an EDX spectra (d) corresponding to the red inset.

Fe_3O_4 NPs are distributed through parts of the PSi NP while clusters are adsorbed on the PSi surface, as confirmed by EDX. However, the Fe_3O_4 NPs are not homogenously distributed throughout the PSi, and the overall amount of the magnetic is low. While the nanocomposite particles are formed in a simple manner that can be easily scaled for commercial applications, the nanocomposite synthesis efficiency remained low. Therefore, we proposed fabricating the nanocomposite by physically adsorbing the Fe_3O_4 NPs onto the PSi surface via electrostatic interactions.

APTESPSi@Fe_3O_4 Nanocomposite

Magnetic PSi nanocomposites were formed via electrostatic interactions between the positively charged amine-functionalized PSi surface (APTEPSi) and the negatively charged Fe_3O_4 NPs. The Fe_3O_4 NPs serve as pore capping agents that, upon degradation of the electrostatic interactions, mediate the cargo release from the PSi nanocarrier. Figure 3.19 shows a 3-dimensional schematic of the Fe_3O_4 pore-capping agents disassociating after changes in the PSi surface chemistry, as well as the proposed reaction where the propylsilane chain on the PSi surface is prone to hydrolysis and thus removal from the surface.

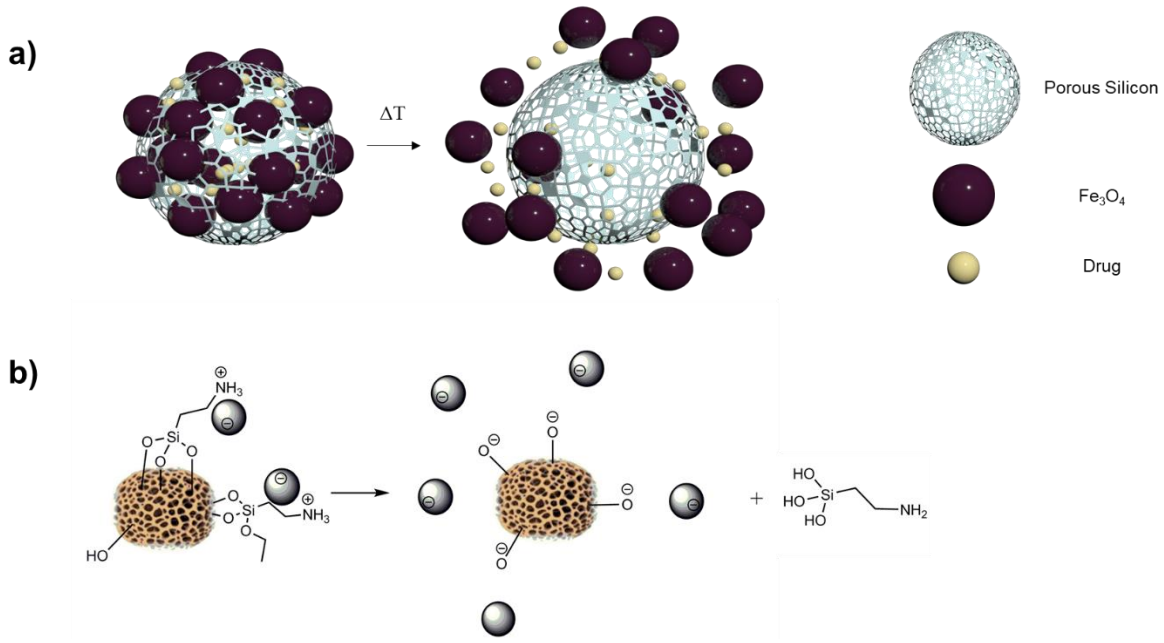

Figure 3.19 a) 3D schematic of thermally-modulated drug release from porous silicon nanoparticles capped with Fe_3O_4 nanoparticles bound to the surface by electrostatic interactions. b) The thermally-controlled surface hydrolysis reaction occurring on the porous silicon surface subsequently destroys electrostatic interactions with the Fe_3O_4 cap and promotes drug release from the pores.

Consequently, the propylsilane chain removal destroys the electrostatic interaction between the PSi and Fe_3O_4, resulting in cargo release. This hydrolysis reaction is accelerated at temperatures slightly above physiological temperature (i.e. 37 °C) and therefore the function of Fe_3O_4 NPs as pore caps can be modulated via temperature.

The APTESPSi@Fe_3O_4 nanocomposite was formed by physically mixing APTESPSi and Fe_3O_4 NPs in a 1:1 ratio at 300 rpm over 1h, with the expectation that oppositely charged surfaces would physically bind the two particles together via electrostatic interactions. The ζ-potential for APTESPSi and Fe_3O_4 was confirmed before mixing, as shown in Figure 3.20a, with APTESPSi and Fe_3O_4 exhibiting ζ -potentials of +31.7 ± 1.4 mV and -38.3 ± 1.9 mV.

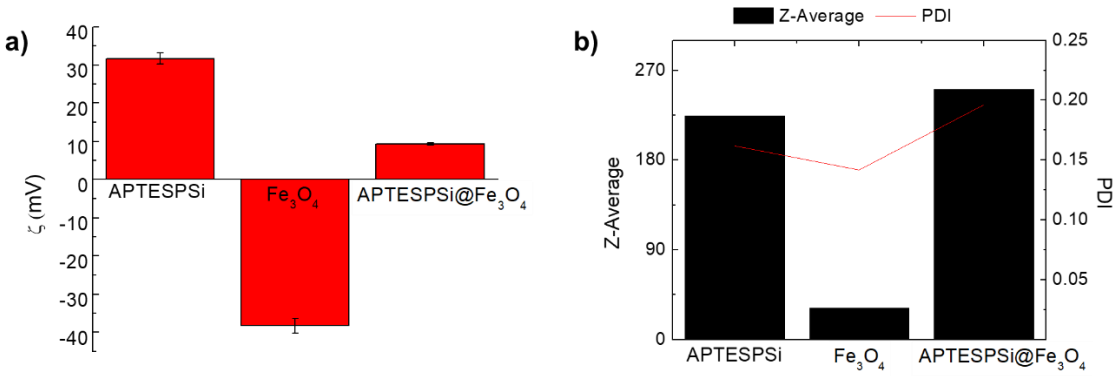

Figure 3.20 a) Zeta potential of APTESPSi, Fe_3O_4 nanoparticles, and the two combined via electrostatic interactions. Physical adsorption of Fe_3O_4 on the APTESPSi surface is confirmed by the decrease in zeta potential. b) Hydrodynamic diameter and PDI of APTESPSi, Fe_3O_4 nanoparticles, and the two combined. Changes in APTESPSi size that correspond to the size of Fe_3O_4 confirms that nanoparticle adsorption onto the surface.

After mixing the two components the ζ -potential was +9.3 ± 0.3 mV, indicating the presence of both APTESPSi and Fe_3O_4 in the solution. The final zeta potential is not exactly at the halfway point between the two initial zeta potentials because not all Fe_3O_4 NP were bound to the APTESPSi surface and were washed away during centrifugation. Changes in the hydrodynamic diameter (Z-average) were also monitored before and after the components were combined using DLS. Before mixing the APTESPSi and Fe_3O_4 NPs exhibit a Z-average of 224.6 nm and 31.6 nm with polydispersity index (PDI)s of 0.16 and 0.14, as shown in Figure 3.20b. The discrepancy in the Fe_3O_4 NP size between DLS compared to TEM or XRD is perhaps due to some Fe_3O_4 agglomeration where DLS cannot differentiate between a single particle and agglomerates in

comparison to TEM where particle sizes are determined through direct observation or XRD where Scherrer analysis is essentially calculating grain sizes. The final nanocomposite is 250.9 nm with a PDI of 0.2, which is the sum of the individual component sizes, and an indicator that the Fe_3O_4 NPs are bound to the APTEPSi surface. The Si and Fe content in the nanocomposite were determined by inductively coupled plasma optical emission spectrometry, which determined a Fe: Si ratio of 9.3: 33.4 mg/L and by dividing the two yields a Fe content of 27.9 wt%.

We also directly observed the nanocomposites under TEM to confirm that the Fe_3O_4 NPs were in fact blocking pores on the APTEPSi surface rather than agglomerating. Figure 3.21a shows a TEM image of several nanocomposites containing Fe_3O_4 on the nanocarrier surface and Figure 3.21b shows an image focused on one nanocomposite with Fe_3O_4 NPs homogeneously distributed throughout the APTESPSi surface.

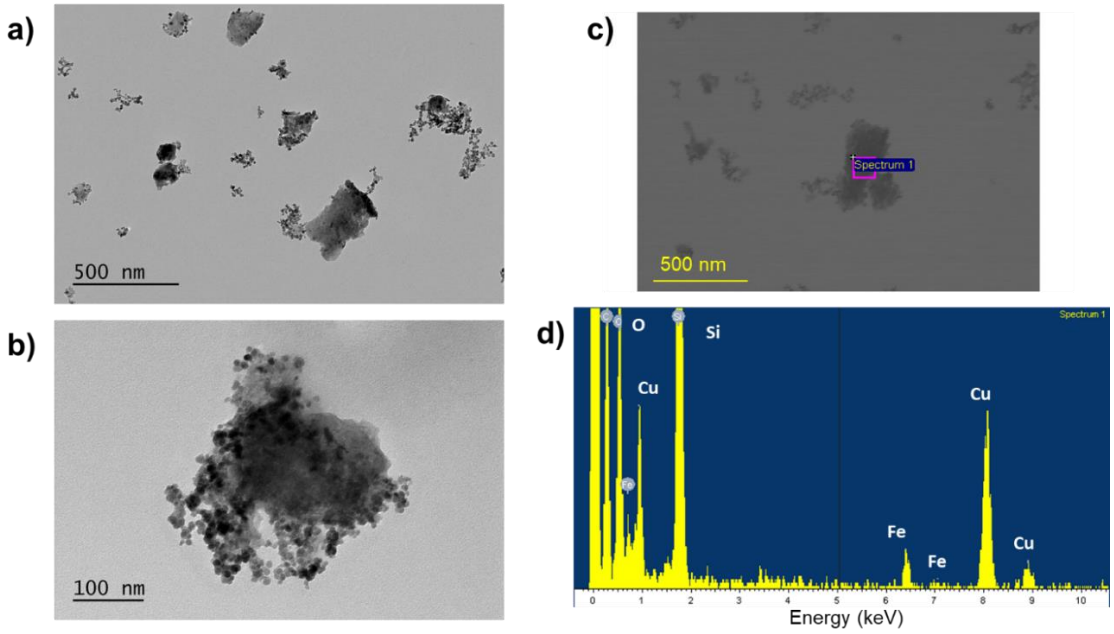

Figure 3.21 a) TEM image of APTESPSi@Fe_3O_4 nanoparticles and b) TEM image with higher magnification showing Fe_3O_4 nanoparticles covering the porous silicon surface. c) SEM image of APTESPSi@Fe_3O_4 nanoparticles and d) its EDX spectrum corresponding to the area within the purple rectangle confirming the presence of both silicon and iron elements.

This homogenous distribution is crucial to prevent premature release of therapeutics loaded into the nanocarrier pores. Moreover, the presence of Fe_3O_4 NPs on the nanocomposite was confirmed through EDX (Figure 3.21d). Such elemental analysis is crucial because the Fe_3O_4 NPs resemble the nanocarrier's porous structure and it should be confirmed that the magnetic NPs are in fact present and not an artefact observed in TEM. After successfully confirming the formation of magnetically capped- PSi NPs, we studied whether this cap could be removed at slightly elevated, physiologically relevant temperatures via the degradation of the electrostatic interactions that hold the two components together.

3.5.Conclusion

A magnetic PSi nanocomposite proposed for a remotely-controlled targeted drug delivery system was fabricated with high efficiency and scalability. The PSi is formed via a top-down approach, where the pores are formed by electrochemical etching and either sonicated or ball milled to form NPs. PSi with a three-step gradient in porosity and pore size was fabricated, with a large pore size on one end for Fe_3O_4 NP infiltration and a small pore size on the other end to keep the NPs inside the PSi. Fe_3O_4 NPs were synthesized by the co-precipitation method, and parameters such as Fe (III) concentration were varied to achieve different NPs sizes. Fe_3O_4 NPs infiltrated into the three-step gradient PSi with the guidance of a permanent magnet yielded low efficiencies of magnetic PSi NP formation. Thus, a new synthesis route was proposed for fabrication magnetic-capped PSi (APTESPSi@Fe_3O_4) NPs with high efficiency while overcoming synthetic challenges associated with scaling up in drug delivery systems. The Fe_3O_4 NPs were electrostatically bound to the APTESPSi surface and therefore blocking the pores for controlled drug delivery applications. This novel system, completely comprised of low-cost,

highly scalable components, is a promising candidate for future applications in externally triggered drug delivery

Ch. 4 Amine-Functionalized Porous Silicon Nanoparticles with Electrostatically Bound Magnetic Capping Agents Mediate Thermoresponsive Drug Delivery

Magnetically actuated drug delivery carriers are appealing platforms in next-generation precision medicine, yet these carriers must be compatible with scalable fabrication techniques to realize their clinical translation. Magnetically capped PSi NPs are promising targeted drug delivery vectors due to their low-cost, high compatibility with scalable microfabrication techniques and their ability to yield remotely triggered, on-demand therapeutic release.

This Chapter investigates whether a thermoresponsive behavior is observed in the amine-modified PSi NPs capped with electrostatically bound Fe_3O_4 NPs that were developed in Chapter 3. We determined whether the electrostatic interactions binding the PSi NPs and Fe_3O_4 capping agent are degraded through temperature changes, and whether this thermoresponsive binding translates to a controlled release profile. First, we demonstrate that as the amine modification on the PSi surface is destroyed with accelerated hydrolysis at elevated temperatures the electrostatic interactions with Fe_3O_4 are degraded, thus exposing the pores for promoting carrier release. The magnetic properties, magnetic localization and AMF heating capabilities of the nanocomposite are then discussed. This Chapter concludes with dissolution studies with a model drug (sorafenib), which show a thermoresponsive behavior that is attributed to the temperature-mediated electrostatic degradation. Overall, this proof-of-concept of an on command drug delivery system using cheap, highly scalable fabrication processes, as discussed in Chapter 3, establishes the opportunity for the clinical translation of a nanocarrier that can potentially

localize the therapeutic and trigger its release “on demand” near a disease site to mitigate systemic exposure and reduce clinical side effects.

4.1. Experimental Methods

Surface Hydrolysis on APTESPSi Surface

Temperature-mediated surface hydrolysis of APTESPSi was monitored by ζ-potential measurements taken at different times and temperatures. 20 mL solutions of 10 µg/mL APTESPSi in Milli-Q water were stirred at 300 rpm at room temperature, 37 °C, and 45 °C and 750 µL aliquots were removed for analysis with Zetasizer Nano ZS (Malvern Instruments Ltd., United Kingdom) at t= 0, 15, 30, 60, 120, and 180 min. Hydrolysis was also confirmed by the changing mass percentage of nitrogen on the NP surface using elemental analysis of dry samples (vario MICRO cube CHNS analyzer, Elementar AnalysenSystem). The nitrogen surface coverage determination was calculated from the nitrogen content. It was assumed that the silanization process was completed and that all nitrogen atoms were related to the surface terminating $-NH_2$ group.

PSi@Fe_3O_4 Magnetic Characterization and Specific Absorption Rate

The magnetic behavior and Fe content of APTESPSi@Fe_3O_4 was verified by a vibrating-sample magnetometer (MicroMag 3900 VSM; Lake Shore Cryotronics, Inc.). The sample was prepared by placing 0.56 mg of dry APTESPSi@Fe_3O_4 powder in a gelatin capsule. Magnetization curves were measured from -1.2 to 1.2 T at room temperature. The magnetic moment (A m^2) versus applied magnetic field (T) was normalized by the amount of Fe_3O_4 in the sample and corrected for dia/paramagnetic components to obtain the final magnetization value (A m^2 kg^{-1}).

SAR is an indicator for heating efficiency of Fe_3O_4 NPs in the presence of an AMF. The imaginary component of magnetic susceptibility is widely used to determine the Fe_3O_4 NP heat dissipation characteristics. When the particles are exposed to magnetic field frequencies with field direction reversals on a timescale less than the magnetic relaxation times of particles, heat is dissipated due to the delay in the magnetic moment relaxation, as previously discussed in Chapter 2. Thus, magnetic susceptibility is a valuable tool for determining heat dissipation values. Alternating current (AC) magnetic susceptibility measurements (SM-105 portable magnetic susceptibility meter, ZH Instruments, Czech Republic) were performed at frequencies 63, 129, 257, 511, 1026, 2055, 4001, 8093, and 16037 Hz at room temperature. Since the instrument only measures the real component of magnetic susceptibility, the imaginary component was determined from equations that consider the effective relaxation associated with Brownian and Neel relaxation.

Calorimetry experiments, where temperature changes with application of an AMF are recorded as a function of time, is another method for measuring SAR. The AMF was generated with a homemade magnetothermal setup consisting of a resonant RLC circuit and a 16 mm copper coil similarly used in previous reports [190]. The field amplitude was set at either 9 or 18 mT and the magnetic field frequency was fixed at 471 kHz. The temperature change was recorded for 200 µL of an APTESPSi@Fe_3O_4 and Fe_3O_4 solution with an infrared thermal imaging camera (FLIR SC7000, FLIR Systems, Inc.) at every second in a temperature range of 25 to 60 °C. All measurements were performed in water (C_{water} = 4185 J L^{-1} K^{-1}) and normalized by the amount of iron (g Fe/L) as determined by ICP. All reported SAR values and error bars were calculated from the mean and standard deviation of at least three experimental measurements.

Loading Degree (LD) and Drug Dissolution, Release Studies

We dissolved 18.33 mg SFN in 1mL acetone at 300 rpm, 37 °C (slightly elevated temperature used to ensure that drug was fully dissolved) for 10 min. Simultaneously, 2.1 mg of APTESPSi was centrifuged at 13,200 rpm for 5 min. The supernatant from the APTESPSi was removed, and the 1 mL SFN solution was added and mixed at 300 rpm, room temperature for 2 hours. The solution was then centrifuged at 13,200 rpm for 5 min and the supernatant was removed. A 1 mL 2.1 mg/mL Fe_3O_4 NP aqueous solution was added to the SFN-loaded APTESPSi and mixed at 300 rpm for 1 hour to cap the drug-loaded pores via electrostatic interactions. The mixing occurred in an aqueous solution to minimize the release of the loaded drug, which is highly hydrophobic and likely to stay in the pores. After capping the surface with Fe_3O_4 NPs, the solutions were separated into two aliquots: one for loading degree determination and the other for the drug dissolution studies. Loading degree and drug dissolution studies were also conducted for SFN loaded into APTESPSi without any capping agent.

Loading degree was determined by centrifuging the respective aliquot and redispersing it in 1 mL of ethanol. The solution was stirred at 300 rpm at room temperature for 3 hours and centrifuged at 13,200 rpm for 5 min to remove the PSi NPs. The supernatant was collected to assess the drug amount encapsulated inside using an Agilent 1200 series High Performance Liquid Chromatography (HPLC) system (Agilent Technologies, USA). The mobile phase was composed of 0.2% trifluoroacetic acid (TFA) and acetonitrile (ACN) at a 42:58 volume ratio and the stationary phase was a Gemini 3 µm NX-C18 110 Å column (Phenomenex, USA). An injection volume of 10 µL, flow rate of 1 mL min^{-1} and detection wavelength of 293 nm was used.

The loading degree was calculated as is shown in Eqn. 4.1

$$LD\ (\%) = \frac{Dissolved\ drug\ concentration\ detected\ by\ HLPC}{Total\ amount\ of\ nanoparticle}\ x\ 100\% \qquad (4.1)$$

The dissolution profiles of SFN from APTEPSi and APTESPSi@Fe_3O_4 were performed at room temperature, 37 °C, 45 °C, and 50 °C in sink conditions. The samples were dispersed in 20 mL Hank's Balanced Salt Solution (N-[2-hydroxyethyl]piperazine-N′-[2-ethanesulfonic acid]) (HBSS−HEPES, pH 7.4) 10% fetal bovine serum (FBS) and stirred at 300 rpm. At the respective timepoints a 200 µL aliquot was removed from the solution and replaced with the same volume of fresh solution. The analyte was centrifuged at 13,200 rpm and the supernatant was then collected for analysis by HPLC.

4.2. Temperature Accelerated Surface Hydrolysis of APTESPSi NP Surfaces

The hydrolysis reaction occurring on the APTESPi surface is crucial for having thermally responsive electrostatic degradation that removes the pore capping agent and promotes cargo release. During hydrolysis the propylsilane chain reacts with water and is removed from the PSi surface, leaving the surface with hydroxyl groups where the PSi now resembles TOPSi, which is associated with a negative zeta potential. A proposed mechanism for thermoresponsive cargo release is shown in Figure 3.19a and a reaction schematic describing this surface hydrolysis is shown in Figure 3.19b.

Because of the dramatic differences in zeta potential between APTESPSi and TOPSi, the ζ- potential was monitored as a function of temperature and time to indicate the ongoing hydrolysis. This hydrolysis reaction is accelerated at temperatures above room temperature, as shown by the decrease in zeta potential in Figure 4.1. At room temperature the zeta potential stays the same after 180 minutes, indicating that the amine surface functionalization remains intact. As the solution temperature increases to 37 °C and 45 °C the zeta potential decreased to

8.43 mV and-13 mV after 120 minutes, indicating a greater extent of hydroxyl group formation on the surface with increasing temperature.

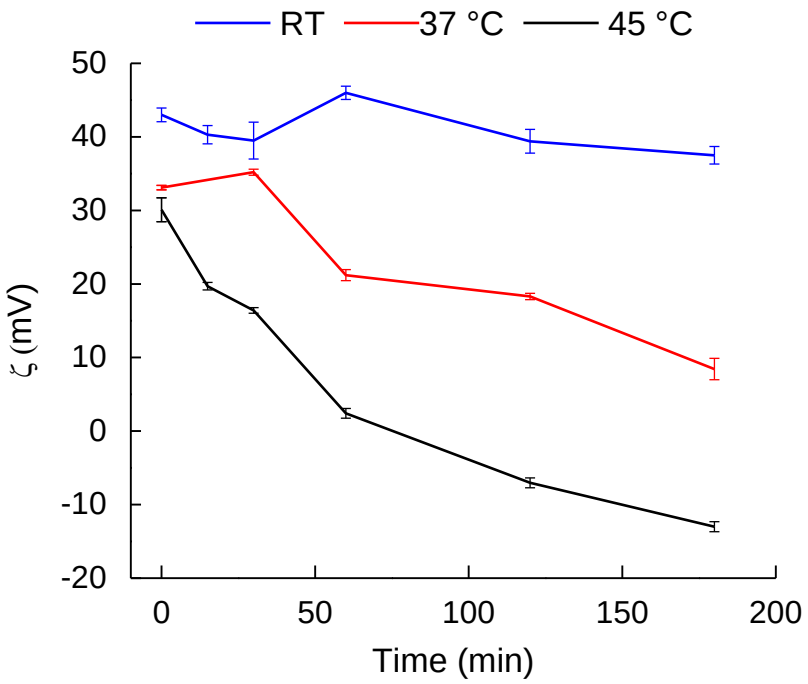

Figure 4.1 Zeta potential of APTESPSi at different times and temperatures. Decreasing zeta potentials indicates the hydrolysis of the alkoxy groups on the nanoparticle surface, and this reaction is accelerated at higher temperatures.

Elemental analysis determined the nitrogen surface coverage after 3 hours at room temperature, 37 °C, and 45 °C. The propylsilane chains are removed from the surface during hydrolysis the overall surface nitrogen content should decrease. Elemental analysis revealed a decrease in nitrogen content with increasing temperature, as shown in Table 4.1.

Table 4.1 Mass percentage of N element in APTESPSi determined by elemental analysis after 3 hours stirring in Milli-Q water at different temperatures. We assume that all nitrogen is related to amine groups during elemental analysis.

Temperature	mmol/g [a]	Surface Area (m^2/g)
RT	0.87	262
37 °C	0.66	199
45 °C	0.61	184

Considering that one aminopropylsilane covers approximately 50 $Å^2$ [244], the surface area for a surface coverage of 0.87 mmol/g was calculated as shown below.

$$(8.7 \times 10^{-4}\, mmol/g)(50 \times 10^{-20}\, m^2)(6.022 \times 10^{23}\, mol^{-1}) = 262\, m^2/g$$

As the nitrogen surface coverage decreases the surface area approaches that of TOPSi (173 m^2/g) as determined by N_2 adsorption according to the BET method (Chapter 3). The most dramatic decrease in nitrogen coverage occurs as the temperature is increased to 37 °C from room temperature, which does introduce some concern that hydrolysis of the silane groups may be occurring prematurely. This decrease in nitrogen coverage on the PSi surface further corroborates the hydrolysis reaction, where amount of nitrogen decreases as the NH^{3+} groups on the propylsilane are removed from the surface.

Hydrolysis is further confirmed by FTIR measurements of APTESPSi@Fe_3O_4 stirred in MilliQ water for 3 hours at room temperature and 45 °C. As the hydrolysis reaction proceeds, -OH groups are formed on the PSi surface. Figure 4.2 shows a broad absorbance band that appears at 3300 cm^{-1} when the particles are heated to 45 °C, which is assigned to -OH group formation.

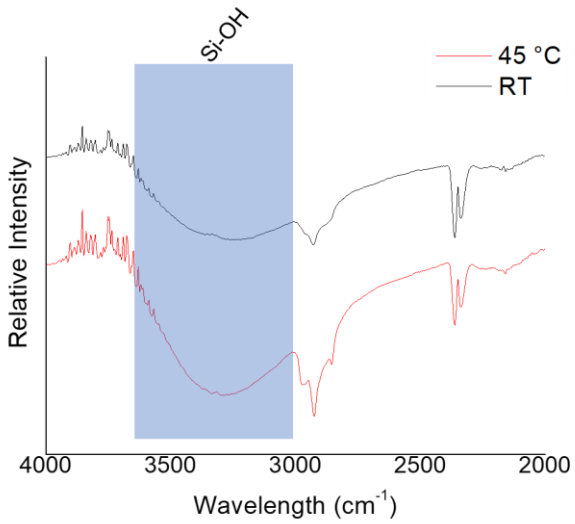

Figure 4.2 FTIR transmission spectra of APTESPSi particles stirred in Milli-Q water at room temperature and 45 °C after 3h.

Thus, the appearance of absorbance bands associated with -OH groups is an additional indicator that the hydrolysis reaction is occurring on the PSi NP surface.

Finally, as the hydrolysis reaction proceeds and the PSi surface charge becomes more negative, we anticipate electrostatic interactions between the PSi and Fe_3O_4 NPs to weaken, with repulsive forces eventually dominating. The changes in electrostatic interaction strength between the APTESPSi and Fe_3O_4 NPs were monitored with SEM/EDX. Figure 4.3 shows SEM images of APTESPSi@Fe_3O_4 dried in MilliQ water after stirring for 3 hours at room temperature (Figure 4.3a), 37 °C (Figure 4.3b), 45 °C (Figure 4.3c), and their corresponding EDX spectra (Figure 4.3d-f).

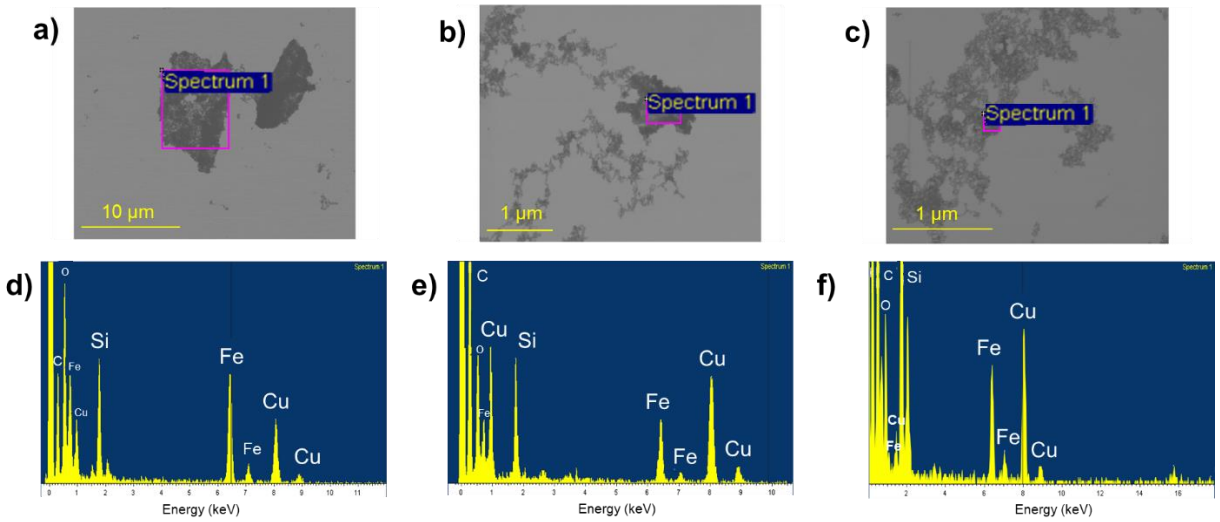

Figure 4.3 SEM images of APTESPSi@Fe_3O_4 nanoparticles dried in Milli-Q water after stirring at a) room temperature b) 37 °C and c) 45 °C to investigate the networks formed with varying electrostatic interaction strengths. Their corresponding EDX images in d- f) confirm the presence of both Si and Fe elements within the framework.

Before discussing the SEM images, it is important to note that these images are not a true depiction of how the nanocomposites are arranged in a colloidal solution, as DLS has previously indicated hydrodynamic sizes of 250.9 nm (Chapter 3). When the nanocomposite solution is dried during TEM grid preparation, the strong electrostatic interactions, or attractive inter-particle forces, cause the NPs to aggregate [245]. As electrostatic interactions weaken and Fe_3O_4 NPs are removed from the PSi NP surface less aggregation is observed (Figure 4.4). Instead, there is electrostatic repulsion between the Fe_3O_4 and PSi NPs due to their similar surface charges.

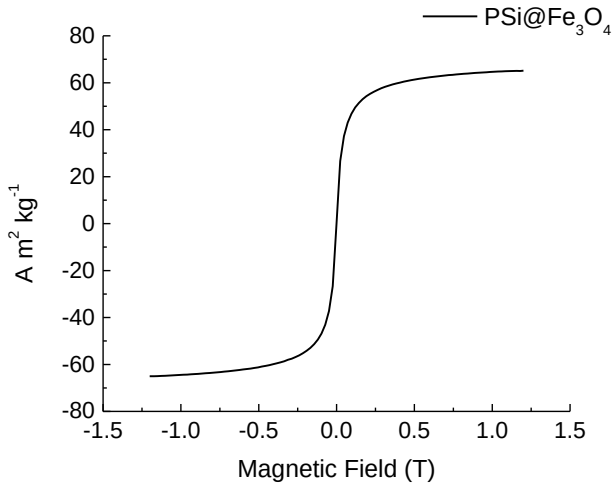

Figure 4.4 Magnetization of APTESPSi@Fe_3O_4 nanoparticles as a function of magnetic field as measured by VSM. The hysteresis loop confirmed superparamagnetic behavior and ~30% Fe content in the final formulation.

For the APTESPSi@Fe_3O_4 NPs that were stirred in aqueous solution at room temperature, an ~10 µm cluster (Figure 4.3a) was observed, indicating that the electrostatic interactions between the two components are strong enough to form a network of particles during the TEM drying process. At 37 °C and 45 °C the clusters do not form as a result of weakened electrostatic interactions between the components, which now exhibit repulsive interactions (Figure 4.3b-c). The corresponding EDX spectra (Figure 4.3d-f) show an overall decrease in the Fe K_α signal (6.398 eV) based on the decreasing full-scale counts as the temperature increases. The decreasing Fe signal indicates that the Fe_3O_4 NPs are not associated with the PSi NP surface at elevated temperatures because the two components face repulsive forces. Direct observation through SEM/EDX is an effective approach to understand electrostatic interactions between the two components with temperature changes, as one can observe how the distribution of both populations are changing rather than an average of the two, as would be observed in DLS. After confirming hydrolysis on the PSi NP surface, and how accelerating this hydrolysis at elevated temperatures could translate into a controlled release nanocarrier mediated by electrostatic degradation, the magnetic properties of this carrier with application of an AMF is investigated.

Nanocomposites with on-demand release by remote-controlled stimuli such as AMFs is attractive for achieving spatiotemporally controlled drug release that can be readily tuned from patient to patient.

4.3. Nanocomposite Localization and Heat Dissipation by Magnetic Field

This section focuses on the magnetic properties and heat dissipation capabilities of the APTESPSi@Fe_3O_4 nanocomposites to determine whether applying an AMF to the nanocarrier yields temperatures increases relevant in degrading the electrostatic interactions that promote carrier release. The SAR was determined for APTESPSi@Fe_3O_4 nanocomposites from magnetic susceptibility calculations and these results were compared with calorimetric heating measurements. Initial magnetic characterization was carried out by vibrating sample magnetometer (VSM) to determine magnetization as a function of magnetic field, as shown in Figure 4.4. The APTESPSi@Fe_3O_4 nanocomposite possessed superparamagnetic behavior, as demonstrated by the hysteresis curve and a saturation magnetization (M_s) of 66.2 A m^2 kg^{-1}. An Fe content of 28.4 wt%. was determined by dividing M_s of the APTESPSi@Fe_3O_4 nanocomposite by the M_s of pure Fe_3O_4 (M_s= 92.4 A m^2 kg^{-1}) [246]. This Fe content is in close agreement with ICP measurements of 27.9 wt%.

SAR of the APTESPSi@Fe_3O_4 nanocomposite was determined with application of an AMF. SAR measures the rate at which energy is absorbed per unit mass of the magnetic material, and has been used to quantify heat dissipation in MRI scanners[247], magnetic fluid hyperthermia (MFH) [83,248], and temperature-controlled drug release [249,250]. The SAR was determined for APTESPSi@Fe_3O_4 nanocomposites and Fe_3O_4 alone from magnetic susceptibility calculations with varying hydrodynamic volumes modelling the two systems (Eq. 2.2-2.4, 2.7, 4.2) and compared with calorimetric heating measurements. Previous research

efforts compared SAR values for Fe_3O_4 NPs determined by magnetic susceptibility and calorimetry experiments [161]. Research efforts have not compared SAR measurements between magnetic susceptibility and calorimetry for PSi@Fe_3O_4 nanocomposites to determine whether the electrostatic interactions between Fe_3O_4 and APTESPSi hinder the overall Brownian relaxation and, therefore, the heat dissipation.

The out-of-phase or imaginary component, χ", was used to calculate the heat dissipation of the magnetic particle. As shown in Chapter 2, Eqn. 2.7, the SAR is estimated as [82]

$$SAR = \frac{\mu_0 \pi \chi''}{\rho_{particle}} f H_{applied}^2 \qquad \text{Eq. 2.7}$$

The magnetic susceptibility of APTESPSi@Fe_3O_4 NPs is shown as a function of AMF in Figure 4.5a.

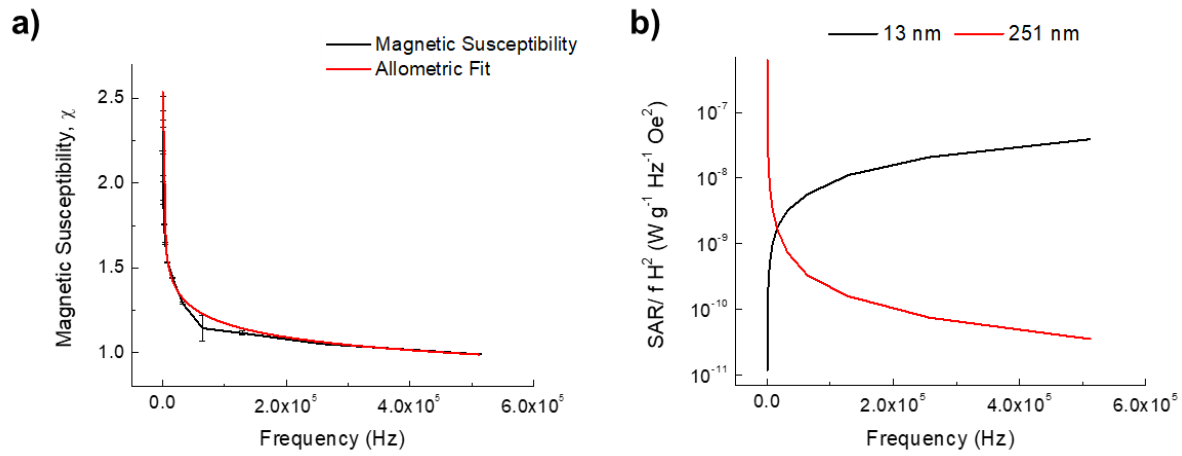

Figure 4.5 a) Magnetic susceptibility measurements as a function of frequency for APTESPSi@Fe_3O_4 nanoparticles and b) SAR values theoretically determined from magnetic susceptibility measurements at varying frequencies. Different particle sizes simulating Fe_3O_4 alone and APTESPSi@Fe_3O_4 were considered in calculating the Neel relaxation and Brown relaxation constants.

The magnetic susceptibility decreased with increasing frequency because the magnetization frequency of the nanocomposite cannot keep up with the AMF driving frequency. Because the

instrument used for measuring magnetization could not directly determine χ", we used Equation 4.2 to convert from the real into imaginary component [82]

$$\chi'' = \frac{2\pi f \tau \chi}{1+(2\pi f \tau)^2} \qquad \text{Eq. 4.2}$$

where χ is the measured susceptibility and τ is the effective relaxation associated with Brown and Neel, as shown in Equations 2.2 through 2.4 in Chapter 2. The effective relaxation constant was determined for each susceptibility measurement in Figure 4.5a and were then used to calculate χ" from Equation 4.2 for each respective frequency. The imaginary component was then used to determine SAR (Equation 2.7) at each frequency, and the final SAR value was normalized by $fH_{applied}^2$ to minimize the contributions from these experimental parameters, as was done in previous literature [161]. Moreover, the SAR was calculated with two different effective relaxation constants based on the hydrodynamic volumes representative of Fe_3O_4 NPs and the APTESPSi@Fe_3O_4 nanocomposite. The hydrodynamic diameter for each was determined from DLS while the particle diameter for Neel relaxation was determined via TEM. The ratios of $SAR/fH_{applied}^2$ as a function of AMF frequency for particles with diameters of 14 nm (Fe_3O_4) and 251 nm (APTESPSi@Fe_3O_4) are shown in Figure 4.5b. Using a diameter representative of Fe_3O_4 NPs yielded a normalized SAR value on the order of 10^{-8} W g^{-1} Hz^{-1} Oe^{-2} at high frequencies while using a diameter representative of the nanocomposite resulted in SAR values 3 orders of magnitude smaller. The hydrodynamic volume and particle volume increase the Brownian and Neel relaxation constants, and therefore the effective relaxation constant, τ, increases. Considering Equation 4.2, χ" decreases with higher τ, where χ" is proportional to $1/\tau$. Given that χ" is directly proportional to the SAR, as shown in Equation 2.7, increasing the particle size results in lower SARs, as shown in Figure 4.5b. Moreover, the SAR values calculated from magnetic susceptibility were compared with calorimetry experiments to

determine whether the electrostatic interactions between APTESPSi and Fe_3O_4 hinder the Brownian relaxation.

For calorimetry experiments, the sample was placed in a magnetic coil with a magnetic field frequency of 471 kHz and amplitude of 9 or 18 mT, as previously reported [190]. The temperature increase was recorded with a high-resolution infrared (IR) camera calibrated with a fluorescent temperature probe [190]. Figure 4.6 shows the temperature heating profile for Fe_3O_4 NPs (Figure 4.6a) and APTESPSi@ Fe_3O_4 (Figure 4.6b) at two different AMF amplitudes and a constant frequency of 471 kHz.

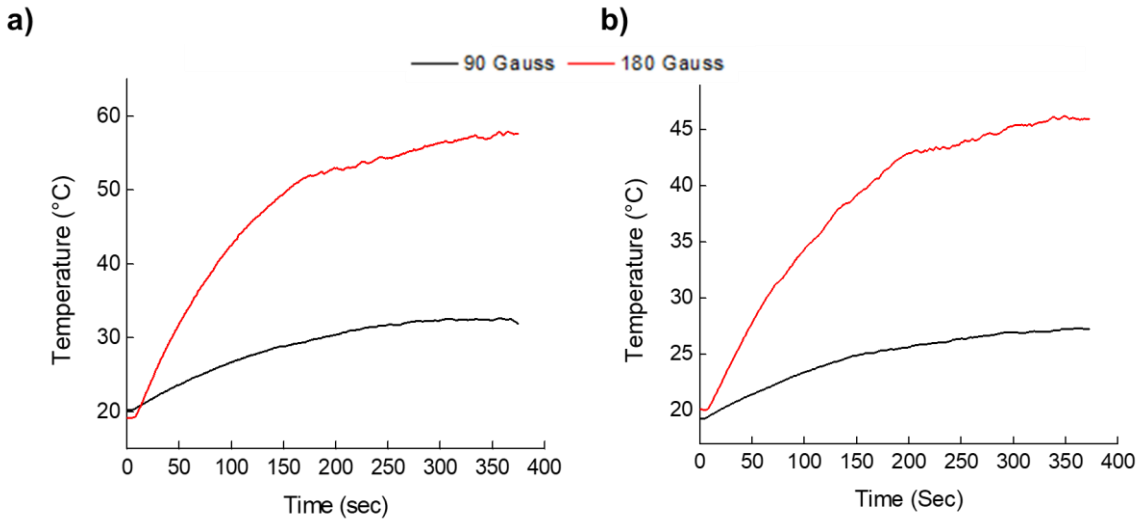

Figure 4.6 Temperature heating profiles with applied AC magnetic fields at different field amplitudes for a) Fe_3O_4 nanoparticles and b) APTESPSi@Fe_3O_4 nanoparticles.

With a field amplitude of 18 mT the Fe_3O_4 NPs see a temperature change of nearly 35 °C within 6 min while the APTESPSi@ Fe_3O_4 exhibit a temperature change of 25 °C within 6 min. When the field amplitude decreases to 9 mT the Fe_3O_4 NPs and APTESPSi@ Fe_3O_4 a 10 °C and 5°C temperature change within 6 minutes. In both particle systems exposed to an AMF with 18 mT field amplitude the temperature changes are relevant for hyperthermia and thermally responsive drug delivery. Moreover, while the temperature change is only 5 °C for APTESPSi@Fe_3O_4 with a field amplitude of 9 mT, the system would be within the proposed temperatures for controlled

release mediated by electrostatic interaction degradation if the measurements were started at 37 °C.

For calorimetry experiments the SAR is calculated from the initial linear slope (t≈30 s) of the temperature profile for particles exposed to an AMF. Equation 2.8 previously shown in Chapter 2) describes that SAR is obtained as follows

$$SAR = \frac{CV_s}{m}\frac{dT}{dt} \qquad \text{Eq. 2.8}$$

where m is the total mass of Fe in the sample, as previously determined by ICP, C is the specific heat capacity of the suspension water (C_{water} = 4185 J L^{-1} K^{-1}), V_s is the sample volume, and $\frac{dT}{dt}$ is the temperature profile slope. Each measurement was conducted in triplicates and an average was calculated for the SAR values. The SAR values calculated from Equation 2.8 at AMF amplitudes of 9 mT and 18 mT (with a field frequency of 471 kHz) are shown below in Table 4.2. The table also contains normalized SAR values determined from magnetic susceptibility measurements with calculations that model hydrodynamic volumes of Fe_3O_4 NPs (V_{Fe3O4}) alone and APTESPSi@Fe3O4 nanocomposites ($V_{APTESPSiFe3O4}$).

Table 4.2 SAR experimentally determined at varying magnetic field amplitudes and SAR values theoretically determined from magnetic susceptibility measurements with different particle sizes considered in calculating the Neel and Brownian relaxation constants.

SAR/fH^2 (Experimental) W g^{-1} Hz^{-1} Oe^{-2}		SAR/fH^2 (Theoretical) W g^{-1} Hz^{-1} Oe^{-2}	
H= 90 Gauss	3.00 x 10^{-8}	V_{Fe3O4}	3.59 x 10^{-8}
H= 180 Gauss	3.69 x 10^{-8}	$V_{APTESPSi@Fe3O4}$	3.86 x 10^{-11}

For the SAR values determined by magnetic susceptibility the magnetic susceptibility as a function of frequency was fit using an allometric fit (Figure 4.5a), and the susceptibility at f= 471 kHz was determined to match the frequency at which the calorimetry experiments were

conducted. The SAR values from the calorimetry experiment closely resemble the SAR determined by magnetic susceptibility which considered Fe_3O_4 NP volumes in calculating the effective relaxation constant. In comparison, the APTESPSi@Fe_3O_4 demonstrate normalized SAR values 3 orders of magnitude smaller than those determined by calorimetry experiments. Therefore, electrostatic interactions between the Fe_3O_4 and APTESPSi do not play hinder the Brownian relaxation and heat dissipation in APTESPSi@Fe3O4 nanocomposites. Instead, the behavior of these nanocomposites more closely resembles individual Fe_3O_4 NPs regarding changes in magnetization direction with field polarity changes.

The nanocomposite's ability to localize with a direct current (DC) magnetic field was also tested, since it is advantageous to have a system that possesses both thermoresponsive and spatiotemporal control. The magnet was placed at one end of a Petri (cell culture) dish and the nanocomposite was introduced at the other end of the dish, similar to previous experiments [200]. Figure 4.7 shows a sequence of photos after the nanocomposite is added to the dish, and within 10 minutes we observe the nanocomposite reaching the other side of the petri dish.

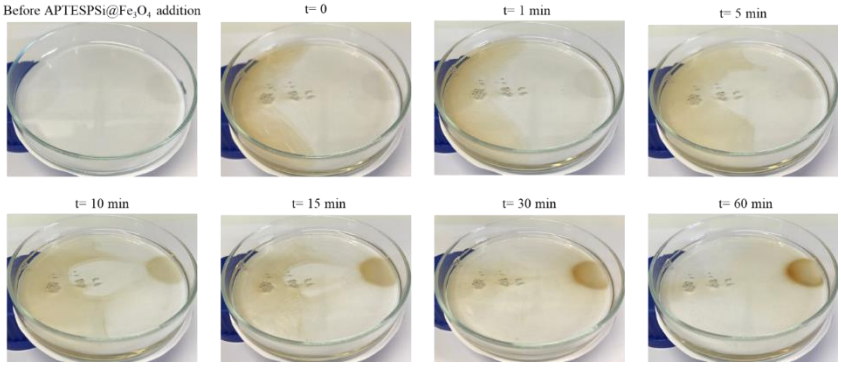

Figure 4.7 Optical images monitoring APTESPSi@Fe_3O_4 nanoparticles added into 20 mL of HBSS-HEPES and localized with a magnet at t= 0, 1, 5, 10, 15, 30, and 60 min.

A video (not shown) more clearly shows that the nanocomposite reaches the magnet on the other side of the dish within one minute. Thus, the nanocomposite is spatially controlled by the

application of an external DC magnet and can subsequently generate heating with application of an AMF to trigger the thermoresponsive capabilities of the system. After confirming that the APTESPSi NP surface undergoes accelerated hydrolysis at elevated temperatures, we investigated whether this phenomenon translates to the thermoresponsive release of a model drug.

4.4. Thermoresponsive Release of Model Drug from APTESPSi Nanocomposite

We investigated whether this thermoresponsive degradation translates into controlled release of the model drug Sorafenib (SFN, NEXAVAR®). SFN is a multi-kinase inhibitor that is indicated for treating unresectable hepatocellular carcinoma (HCC) and advanced renal cell carcinoma (RCC) [251,252]. Its clinical application has been limited, despite research demonstrating simultaneous targeting capabilities [253–256]. For example, the National Comprehensive Cancer Network (NCCN) guideline for treating kidney cancer patients lists SFN as "useful in some cases" for subsequent therapy in stage IV or relapsed cancer treatment [257]. This limited clinical application is probably due to the severe adverse effects and high variation between patients, which is caused by SFN's poor water solubility [258–260]. Thus, there is a need to encapsulate SFN in a nanocarrier to improve its solubility and therefore therapeutic efficacy.

To evaluate the thermal responsiveness of the magnetically capped PSi NPs, dissolution studies were performed at room temperature, 37 °C, 45 °C, and 50 °C in sink conditions. The bulk heating-triggered SFN dissolution studies were conducted in HBSS-HEPES supplemented with 10% FBS at pH 7.4. The release medium was supplemented with fetal bovine serum (FBS) to aid in the dissolution of SFN, where FBS was previously shown to improve SFN dissolution and release from the PSi matrix [261]. SFN was loaded into APTESPSi, and the Fe_3O_4 NP capping agents were subsequently adsorbed onto the porous surface in an aqueous solution to prevent any

SFN release. The loading degree is defined as the mass ratio of loaded SFN to the total drug-loaded NPs (Equation 4.1 in experimental section) and was calculated to be 13.2%. Dissolution studies were also performed for SFN loaded APTESPSi NPs without any capping agent at the same temperatures to confirm that increased dissolution at elevated temperatures is not a result of increased SFN solubility, and to assess the magnetic cap's efficiency in modulating SFN release.

Without a magnetic cap essentially all the SFN was released from the PSi matrix within 2 min, regardless of the release medium temperature (Figure 4.8a).

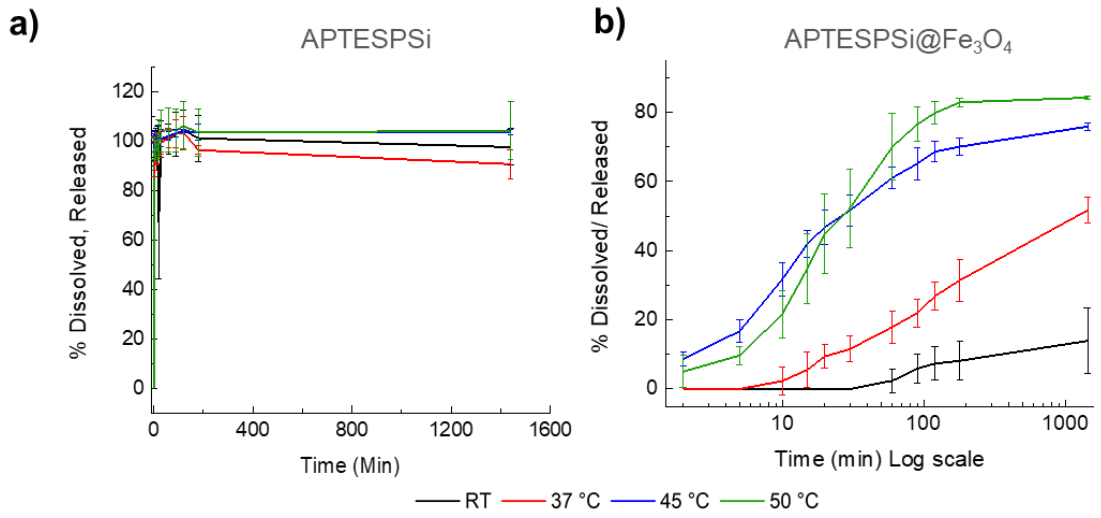

Figure 4.8 a) Sorafenib release profile from APTESPSi nanoparticles demonstrate a burst release at all solution temperatures when no capping agent is present b) A controlled release with temperature is exhibited in Sorafenib release profiles from APTESPSi@Fe_3O_4 nanoparticles due to Fe_3O_4 nanoparticles acting as a capping agent.

Therefore, a pore capping agent is fundamental for avoiding premature drug release. When the magnetic capping agent was present, a controlled, thermoresponsive release was observed (Figure 4.8b). Within 15 min there was a 15x difference in SFN release between 37 °C and 45 °C). After 1h the amount of SFN released at room temperature, 37 °C, 45 °C, and 50 °C was 0%, 11.6%, 51.7%, and 52.3%. After 4h these values increased to 5.9%, 22%, 65.2% and 76.6%. This thermoresponsive SFN release is due to the APTESPSi surface transforming into TOPSi via hydrolysis, where we showed changes in ζ- potential earlier in this chapter of 18.5% at room

temperature, 60% at 37 °C and 392% at 45 °C. Subsequently, the magnetic caps protecting the cargo inside the pores from premature release are removed from the surface as electrostatic interactions with the PSi NP surface are degraded.

The ability to minimize the amount of SFN released at physiological temperature while promoting release at elevated (but physiologically relevant) temperatures will prove useful in targeted, on-demand drug delivery applications. It is important to note, however, that some release is observed at 37 °C, which agrees with our previous work that observed some hydrolysis on the APTESPSi surface at this temperature, although far less notable than for release at 45 °C. While some hydrolysis is observed at 37 °C, which could potentially lead to premature drug release, growing thermally hydrocarbonized layers before the amine surface modification could increase amine stability, as was previously shown [262]. Moreover, given the slightly acidic conditions of tumor microenvironments (pH 5.5- 6.5)[67], higher release rates could potentially be observed for the magnetic nanocomposite. For example, paclitaxel release was promoted from rod-like iron oxide nanoparticles at a pH of 4.5 in comparison to pH 7.4[263]. Future studies will investigate the magnetic nanocomposite release kinetics in an environment with elevated temperature and slightly acidic pH.

For an *in vivo* scenario, the nanocarrier would initially be exposed to a normal physiological temperature of ~37 °C and once it has reached a site of interest the carrier would experience a temperature increase high enough to accelerate the therapeutic release (~45 °C) but not high enough to induce significant apoptosis. This temperature profile was modeled in dissolution studies with APTESPSi@Fe_3O_4 NPs by initiating the study at 37 °C and increasing the release medium temperature to 45 °C after 30 min or 1h. The release medium was maintained at 37 °C at these times to account for the time it takes for NPs to accumulate in tumor tissue.

Previous studies observing the biodistribution of chemotherapeutics, such as Paclitaxel, using positron emission tomography (PET) imaging found tumor uptake within 35 min [264,265]. However, other studies observed tumor uptake 6h post injection in head and neck squamous carcinoma-tumor bearing mice [266], which poses the problematic variation in uptake between different therapeutics, nanomedicine formulations, injection techniques, and imaging modalities. To more precisely decide when a therapeutic release should be probed, future studies could conjugate fluorinated probes or use the MRI contrast capabilities of Fe_3O_4 NPs to image tumor uptake, as this will vary from patient to patient.

Figure 4.9 shows SFN release from APTESPSi@Fe_3O_4 NPs with varying temperature release probing times (after 30 min and 1h).

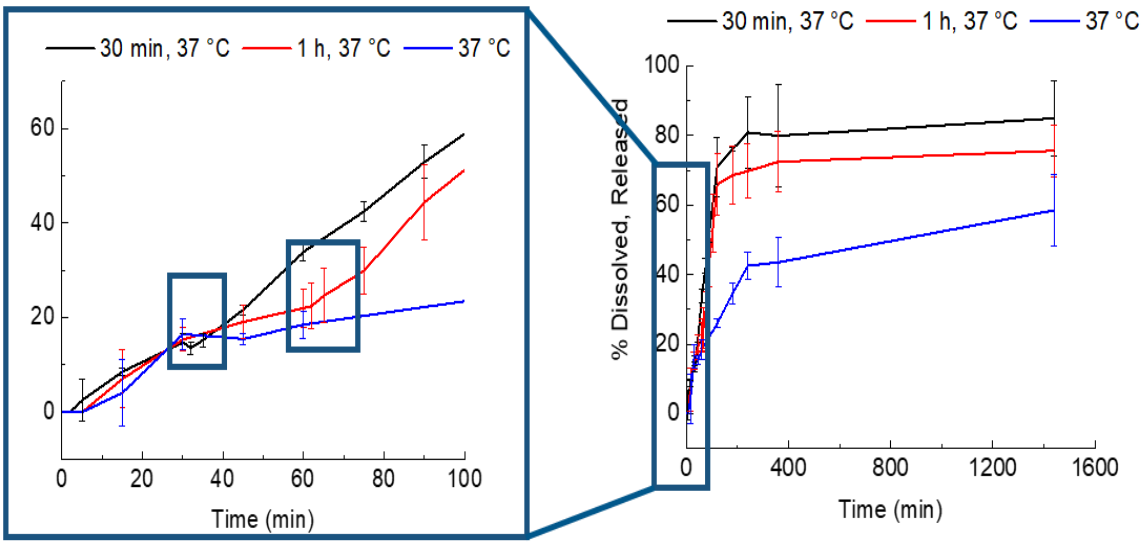

Figure 4.9 Sorafenib release from APTESPSi@Fe_3O_4 nanoparticles with the varying temperature profiles to promote release with sequential heating.

Once the temperature was raised to 45 °C an increased slope in the dissolution curve was observed after 30 min and 1h in comparison to the release medium which did not have a temperature increase. Moreover, the overall amount of SFN released increased by 12% at 24h

when heated to 45 °C after 30 min in comparison to when heating is applied after 1h. When compared to SFN release maintained at 37°C for 24h, there is a 45% and 23% increase when the release medium temperature is increased to 45 °C after 30 min and 1h. Thus, we demonstrated a system that can release a therapeutic on-demand, once it has reached a disease site. By minimizing the therapeutic release at normal physiological temperatures while promoting release on-demand once the local temperature is increased, this system is promising for increasing therapeutic efficacy and mitigating systemic toxicity.

4.5. Conclusion

Magnetic-capped PSi (APTESPSi@Fe_3O_4) NPs demonstrate temperature-mediated electrostatic degradation at physiologically relevant temperatures while overcoming the synthetic challenges typically associated with fabricating such drug delivery systems. The rate of hydrolysis on the APTESPSi NP surface was accelerated at temperatures slightly above physiological temperature. Further, these nanocarriers demonstrated heating with application of an AMF, with temperature changes that are relevant for promoting drug release as a result of electrostatic degradation. Magnetic susceptibility and calorimetry experiments yielded comparable SAR values when considering only Fe_3O_4 NPs into our calculations. Therefore, the electrostatic interactions do not hinder the heat dissipation with AMF application. Finally, dissolution studies of the model drug SFN under sink conditions from APTESPSi@Fe_3O_4 and APTESPSi without the magnetic cap revealed that the cap minimized the release at physiological temperature while promoting it at elevated temperatures (45 °C- 50 °C) that are within a physiologically relevant range. Within 15 min there was a 15x increase in the amount of SFN released when comparing dissolution studies conducted at 37 °C and 45 °C. Furthermore, the identical burst release kinetics for SFN dissolution studies from APTESPSi at various

temperatures confirmed that this increase in dissolution is not a result of increased solubility of the model drug at elevated temperatures. Inducing temperature changes in dissolution studies after stabilizing the release medium further corroborated the nanocomposite's ability to promote drug release "on-demand" with application of an external stimuli. Thus, this promising proof-of-concept on-command system may be of great interest for nanomedicine applications in oncological therapy. With establishing the APTESPSi@Fe_3O_4 NP thermoresponsive release kinetics, we continue with investigating the cytocompatibility of the nanocomposite and its components in four different cell lines in the subsequent Chapter.

Ch. 5 APTESPSi and Nanocomposite Interaction with Biological Systems

Assessing the magnetic nancomposite's interactions with biological systems is crucial for clinical translation considerations. In vitro studies are typically the first line of studies conducted to confirm a material's biocompatibility and cellular uptake. Investigating the biocompatibility is pertinent to ensure that the therapeutic, rather than the particles, are inducing localized toxicity. The particles are incubated with a respective cell line and he number of live are determined with an assay that measures the cell metabolic activity. The cell–NP interactions are qualitatively analyzed by confocal fluorescence microscopy, while quantitative assessment is conducted by flow cytometry.

RAW 246.7 macrophages were of interest, because this cell line is often used to initially screen products for bioactivity. Cytocompatibility with MCF-7 and MDA-MB-231 was assessed since these breast cancer cell lines typically take the form of a solid tumor where a therapeutic is localized using a magnetic field. Blood cancers such as leukemia and lymphoma, on the other hand, do not usually form solid tumors and, therefore, the therapeutic cannot be localized to the disease site. HepG2 cytocompatibility was investigated because Sorafenib's clinical indications include liver cancers such as hepatocellular carcinoma (HCC) and renal cell carcinoma (RCC). Therefore, any improvements to the drug's current efficacy could motivate its reformulation in the clinic.

This Chapter will initially assess the cytocompatibility of APTESPSi@Fe_3O_4 and its components after 24h incubation under physiological conditions with a macrophage, live cancer, and breast cancer cell lines (both triple negative and estrogen, progesterone receptor present). Cytocompatibility studies are conducted with incubation temperature increases typical of the nanocomposite's electrostatic mediated degradation as reported in Chapter 4. The anticancer

activity of SFN-loaded APTESPSi and APTESPSi@Fe_3O_4 in liver cancer and triple negative breast cancer is subsequently discussed. The Chapter concludes by investigating the cellular association of the particles at physiological and elevated temperatures through confocal fluorescence microscopy and flow cytometry.

5.1.Experimental

Cell Culturing

RAW 246.7 macrophages, MDA-MB-231 cells, HepG2, and MCF-7 cells were cultured in separate 75 cm^2 culture flasks (Corning Inc. Life Sciences). MDA-MB-231 cells were grown in Roswell Park Memorial Institute 1640 medium (RPMI, GE Life Sciences, USA). RAW246.7, HepG2 and MCF-7 cells were grown in HyClone Dulbecco's Modified Eagle Medium high glucose (DMEM, GE Life Sciences, USA) and HepG2 was supplemented with 1% sodium pyruvate. All mediums were supplemented with 10% heat inactivated fetal bovine serum (FBS), 1% of penicillin streptomycin (PEST), 1% of L- glutamine, 1% of non-essential amino acids (NEAA). All cells were cultured at 37 °C in a 95% humidified, 5% CO_2 atmosphere (BB 16 gas incubator, Heraeus Instruments GmbH). The growth medium was changed every other day and passaged to new flasks at >80% confluency. The cells were used for experiments at passage numbers between 20- 30.

Cytocompatibility Studies

Nanoparticle Cytotoxicity

APTESPSi, Fe_3O_4 and APTESPSi@Fe_3O_4 NP suspensions in medium at concentrations of 10, 25, 50, 100, and 200 µg/mL were incubated with RAW 246.7, MDA-MB-231, MCF-7, and HepG2 cells for 24h at 37 °C, for 6 hours at 37 °C, or 45 °C for 15 min followed by 37 °C for 5 h 45 min to assess the NPs' cytocompatibility and establish a toxicity profile. First, cells

were seeded at a density of 2×10^4 cells per well (100 µL volume in each well) in a 96-well plate and incubated overnight at 37 °C to allow the cells to attach. NPs were washed twice in HBSS−HEPES, pH 7.4 to remove ethanol, and suspensions were prepared in their respective medium (i.e. RPMI, DMEM, DMEM supplemented with 1% sodium pyruvate). NP suspensions were briefly bath sonicated before use to ensure homogeneous solutions. The 100 µL of medium was removed from the 96-well plates and replaced with 100 µL of particles with their respective concentrations. All experiments were performed in at least triplicates.

After the respective incubation time, the cell viability was assessed with CellTiter-Glo® Luminescent Cell Viability Assay (Promega Corporation, USA) according to the manufacturer's protocol. In this assay the amount of adenosine triphosphate (ATP) generation, which is correlated to the number of viable cells present in a culture, is proportional to the luminescent signal. This luminescent signal is generated by a luciferase reaction shown, as shown in Figure 5.1. Briefly, cell medium is removed from the wells and washed twice with 100 µL HBSS. Then, 50 µL HBSS and 50 µL of CellTiter-Glo® Reagent was added to the wells.

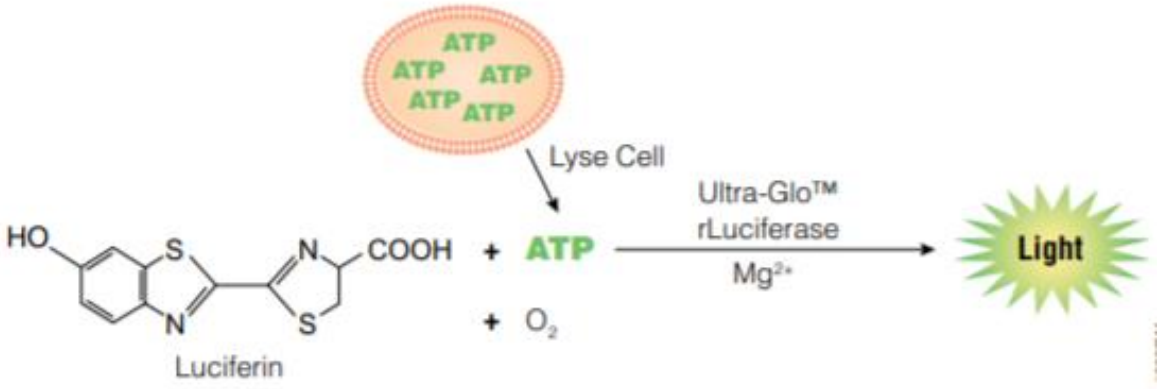

Figure 5.1 Overview of CellTiter-Glo® assay working principle. A luciferase reaction generates a "glow-type" luminescent signal that is proportional to the amount of ATP, and therefore the number of cells, present in a culture. Image reproduced from Promega Corporation [267].

The 96-well plate was shaken for 2 minutes on an orbital shaker to induce cell lysis and incubated at room temperature for 10 minutes to stabilize the luminescent signal before measuring the luminescence. ATP luminescence was measured with a Varioskan Flash Fluorometer (Thermo Fisher Scientific, USA, λ=490 nm).

Sorafenib and APTESPSi@Fe_3O_4-loaded Sorafenib Cytotoxicity

SFN was loaded into APTESPSi and subsequently capped with Fe_3O_4 NPs as previously described in Chapter 4's experimental section. The SFN concentration inside the final formulation was determined by multiplying the amount of APTESPSi@Fe_3O_4 particles (200 µg) by the loading degree (13.2%) and the SFN molar mas (464.8 g/mol). After loading SFN either into APTESPSi or APTESPSi@Fe_3O_4, the formulation was dispersed in the respective medium and diluted into 2.8, 7.1, 14.2, 28.4, and 56.7 µM solutions (equivalent to 10, 25, 50, 100, and 200 µg/mL of NPs). After allowing the cells to attach overnight in 96-well plates, the medium was removed and SFN-loaded APTESPSi and APTESPSi@Fe_3O_4 NPs were incubated at either 37 °C for 6 hours, or 45 °C for 15 min followed by 37 °C for 5 h 45 min. Cell viability was assessed by CellTiter-Glo® Luminescent Cell Viability Assay as discussed previously.

AlexaFluor 488 Conjugation

APTESPSi NPs were labeled with AlexaFluor 488 (Life Technologies, USA) by activating the particles with EDC/NHS chemistry (1-Ethyl-3-(3-dimethylaminopropyl)carbodiimide, N-hydroxysuccinimide) for 1 h and subsequently reacting them with AlexaFluor 488 for 2 h (400:1 AlexaFluor 488: APTESPSi). The reaction is shown below in Figure 5.2. First, 2 mg NHS, 4 µL EDC, and 10 mM 2-(N-morpholino)ethanesulfonic acid MES buffer were combined and brought to pH 5.5. The APTESPSi NPs (100 µg) were then added and activated by stirring at 300 rpm for 1 h. 2 µL of a 0.5 mg/mL AlexaFluor 488 solution

and 1.5 mL MES pH 6.5 was added to the solution and reacted for 2h to conjugate the activated APTESPSi and fluorescent marker.

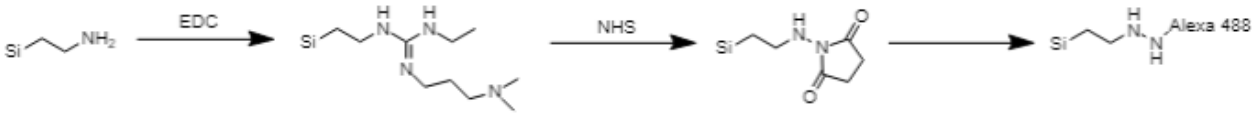

Figure 5.2 Reaction schematic for activating the APTESPSi surface with EDC/NHS chemistry and conjugating the fluorescent dye AlexaFluor 488 via amine linkage.

The Fe_3O_4 NPs were electrostatically bound after AlexaFluor 488 conjugation, since having the Fe_3O_4 NPs present before conjugation would block the amine groups that are crucial for activating the APTESPSi surface. The Fe_3O_4 NPs were expected to electrostatically bind to the amine groups available on the fluorescent dye. Moreover, the conjugated particles that were subsequently mixed with Fe_3O_4 NPs (versus fluorescent labeled APTESPSi) had double the amount of AlexaFluor 488 during conjugation to account for dye removal during Fe_3O_4 addition, and the lower amount of amine groups present on the surface to electrostatically bind to. The fluorescence intensities of AlexaFluor 488 labeled APTESPSi and APTESPSi@ Fe_3O_4 were verified and found to be similar. As a result, the variation in cellular uptake determined by fluorescence intensity is due to increased uptake and not fluorescence intensity differences within the particles.

In Vitro NP Internalization

NP Uptake Imaging by Confocal Microscopy

For confocal fluorescence imaging, MDA-MB-231 cells were seeded in Lab-Tek 8-chamber slides (Thermo Fisher Scientific, USA) at a cell density of 5×10^4 cells per well (200 µL) and allowed to attach overnight. After removal of the cell culture medium, 200 µL of 200 µg/mL Alexafluor 488-labeled APTESPSi and APTESPSi@Fe_3O_4 were added to the cells and incubated at 37 ºC for 6 h or 45 °C for 15 min followed by 37 °C for 5 h 45 min. After

incubation, the cells were washed once with fresh phosphate buffer solution (PBS). The plasma membrane were stained by adding 200 µL of CellMask deep red (5 µg/mL solution) and incubating for 10 min at 37 ºC. The excess staining solution was washed once with fresh phosphate buffer solution (PBS) and the cells were fixed using 4% Paraformaldehyde (PFA) for 15 min at 37 °C. Then, the cell nuclei were stained with 200µL of DAPI (4′,6-diamidino-2-phenylindole; 2.48µg/mL; Vector Laboratories) and incubated for 1-3min. The cells were finally washed twice with PBS and stored in the fridge until imaging by confocal fluorescence microscopy (Leica TCS SP5 II HCS-A, Germany). The LAS AF (2.6.0 build 7266) software was used to process the images.

Uptake Quantification by Fluorescence-activated cell sorting (FACS)

For quantifying NP internalization in MDA-MB-231, cells were seeded in 6 well plates (Corning, USA) at a density of $5x10^5$ cells per well (1.5 mL). After allowing the cells to attach overnight at 37 °C, the medium was removed and 1.5 mL of 200 µg/mL AlexaFluor 488-labeled APTESPSi and APTESPSi@ Fe_3O_4 was incubated at 37 ºC for 6 h or 45 °C for 15 min followed by 37 °C for 5 h 45 min. The cells were then washed three times with PBS-Ethylenediaminetetraacetic acid (EDTA) and collected with trypsinization (0.25% trypsin). Uptake measurements were performed using an LSRII flow cytometer (BD Biosciences, USA) with a laser excitation wavelength of 488 nm. To analyze NP internalization, the fluorescence of membrane-associated NPs was quenched by incubating the cells in 250 µL trypan blue (0.005% v/v) followed by centrifugation at 1200 rpm, 3 min and redispersing in 1 mL PBS-EDTA. Approximately 10,000 events were recorded per sample and the data was analyzed using the FlowJo X 10.0.7r2 software.

Flow cytometry is advantageous to other cellular uptake techniques such as TEM and inductively coupled plasma mass spectrometry, since it can analyze thousands of cells within seconds. In flow cytometry particles or cells flow in a flow chamber and intersect a light beam, causing light to scatter in various directions. Moreover, if fluorescent molecules are present, the light will cause fluorescence emission. Light that is scattered up to ~20 ° offset from the laser beam's axis is called forward scattered light (FS), and light scattered at an approximately 90 ° is known as side scattered light (SS). FS light provides information on the cell or particle size, while SS intensity is related to granular content within a cell or particle. The cellular uptake of a NP is determined by the increase in SS intensity without changes in FS intensity [268].

Statistical Analysis

All measurements were done in at least triplicates and were used for determining the mean and standard deviation. Statistical analyses were performed using one-way ANOVA with Tukey-Kramer post hoc test. The levels of significance were set at probabilities of * $p < 0.05$, ** $p < 0.01$, *** $p < 0.001$.

5.2.Particle Cytocompatibility at 24h

The cytocompatibility of the nanocomposite and its components was assessed with RAW 246.7 macrophages, MCF-7, MDA-MB-231, and HepG2 cell lines after 24h at 37 °C. APTEPSi, Fe_3O_4 NPs, and APTESPSi@Fe_3O_4 nanocomposites were incubated with RAW 246.7, MCF-7, and HepG2 (supplemented with 1% sodium pyruvate) in DMEM, and MDA-MB-231 was incubated in RPMI medium. The concentration of the incubated nanocomposite and its components ranged from 10 µg/mL to 200 µg/mL. Cell viability was assessed after incubating particles for 24h using CellTiter-Glo® assay per the manufacturer's protocols. Figure 5.3 and 5.4

shows the cell viability based on ATP content for RAW 246.7 (Figure 5.3a), MDA-MB-231 (Figure 5.3b), HepG2 (Figure 5.3c), and MCF-7 cells (Figure 5.4).

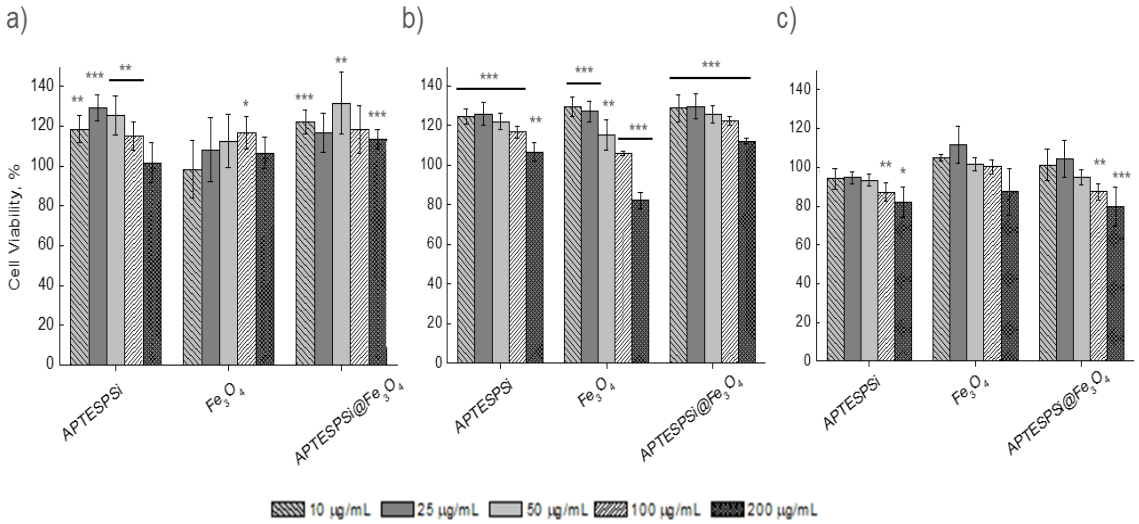

Figure 5.3 Cytotoxicity profiles for APTESPSi, Fe3O4, and APTESPSi@Fe3O4 NPs. Formulations were incubated with either RAW 246.7 macrophage (a) MDA-MB-231 (b) or HEPG-2 (c) cells for 24 h, and the percentage of viable cells was determined using a CellTiter-Glo® Luminescent Cell Viability Assay. Data is presented as mean ± S.D. ($n \geq 3$), and the level of significance was set at probabilities of $^{*}p < 0.05$, $^{**}p < 0.01$, and $^{***}p < 0.001$ compared to the control.

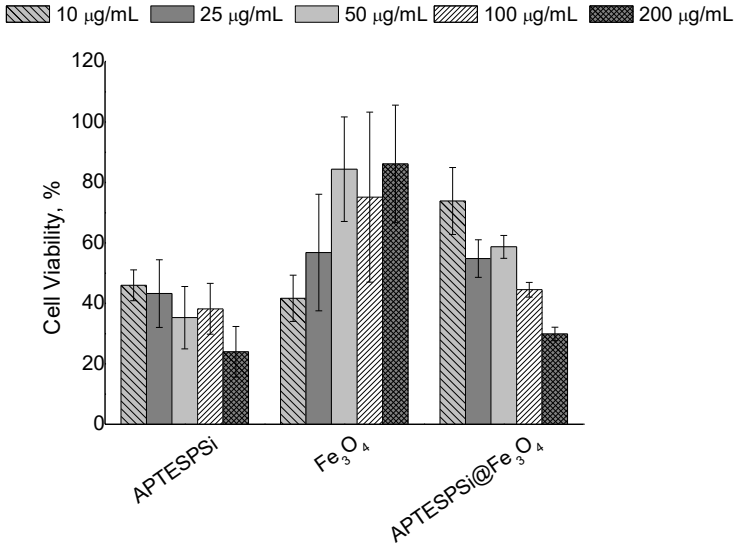

Figure 5.4 Cytotoxicity profiles for APTESPSi, Fe3O4, and APTESPSi@Fe3O4 NPs. Formulations were incubated with MCF-7cells for 24 h, and the percentage of viable cells was determined using a CellTiter-Glo® Luminescent Cell Viability Assay. Data is presented as mean ± S.D. ($n \geq 3$).

Overall, the nanocomposite and its components demonstrated high cytocompatibility with RAW 246.7 cells at all concentrations observed (up to 200 µg/mL) as shown in Figure 5.1a. Surface chemistry effects of PSi NPs on RAW 264.7 cells were previously investigated[269]. APTES-functionalized thermally carbonized PSi (APSTCPSi) NPs incubated with RAW 264.7 for 24h revelead cytotoxicity at concentrations as low 25 µg/mL (~50% viability), which contradicts our results of high cytocompatibility. However, it is important to note that these previous experiments were conducted in HBSS, which is for immediate survival purposes in comparison to DMEM that is used for prolonged survival. The DMEM used in this experiment was supplemented with serum that contains growth factors and hormones that stimulate cell growth and functions. The medium is also supplemented with non-essential amino acids, and essential amino acids such as L-glutamine, which promotes cell proliferation. Therefore, using medium containing supplements that promote cell proliferation and growth is perhaps one of the reasons for the discrepancy in cytotoxicity profiles.

Other research efforts have investigated the cytocompatibility of amine-modified mesoporous silica in RAW 246.7 cells in medium for 24h. Amine-modified mesoporous silica NPs with different aspect ratios induced limited toxicity (~64-85% viability) at a concentration of 500 µg/mL[125]. These higher viabilities are probably due to the cytotoxicity tests being conducted in DMEM rather than HBSS. Overall, the nanocomposites and its components demonstrate high cytocompatibility under physiological conditions within the concentration range studied with RAW 246.7 macrophages.

Further screening with MDA-MB-231 (Figure 5.3b), HepG2 (Figure 5.3c) and MCF-7 (Figure 5.4) cell lines showed high cytocompatibility of APTESPSi@Fe_3O_4 and its individual components in MDA-MB-231 and HepG2. Cytocompatibility results for HepG2 were

comparable to previous studies on similar magnetic PSi NPs [198]. Meanwhile, significant toxicity was observed for the nanocomposite and its components in MCF-7 cells, as shown in Figure 5.4. The APTESPSi NP viability decreases nearly in half from 46 ± 5% to 24 ± 8% over a concentration range of 10 µg/mL to 200 µg/mL. Higher toxicity has been previously explained in APTESPSi NPs by increased cellular uptake due to the strong interactions between the positively charged amine-modified particles and negatively charged cell membranes [270,271]. The positively charged particles can depolarize the membrane potential and increase the intracellular Ca^{2+} concentration [271]. Other explanations for disrupting the cellular membrane include increased membrane permeability and NP interaction with the intracellular mitochondria that leads to decreased ATP production as a result of reduced mitochondrial membrane potential [269,272].

However, the high biocompatibility of APTESPSi NPs with MDA-MB-231 and HepG2 cells questions whether the previous explanations for toxicity can be applied to all cell lines or whether a cell-type dependency on cell viability is simply observed. For example, MCF-7 and MDA-MB-231 cells present metabolic differences, where MDA-MB-231 cells possess higher glycolytic activity during normoxia, and exposure to hypoxic conditions resulted in only a modest increase in lactate production [273]. Contrarily, MCF-7 cells exhibit lower levels of glycolytic activity under normoxia and increased levels of lactate production under hypoxic conditions [273,274]. Fe-based NPs have previously demonstrated an increase in reactive oxygen species (ROS) production in MCF-7 cells after 24h incubation [275]. Thus, it is possible that the presence of Fe_3O_4 NPs in our nanocomposite is establishing hypoxic conditions, which are leading to higher levels of cytotoxicity in MCF-7 versus MDA-MB-231 cells. Overall, high biocompatibility was demonstrated in MDA-MB-231 and HepG2 cells, but not in MCF-7 after 24h incubation under normal physiological conditions.

5.3.Particle Cytocompatibility with Applied Heating

Because the therapeutic release from the nanocomposites is modulated by temperature increases, it was pivotal to also investigate particle cytocompatibility at temperatures above physiological condition (i.e. 37 °C) that are high enough to induce the electrostatic mediated degradation of APTESPSi@Fe_3O_4. Thus, we observed the compatibility of particles incubated with RAW 246.7 macrophages, HepG2, and MDA-MB-231 when exposed to an elevated temperature of 45 °C for 15 min, followed by 37 °C for 5 h 45 min. Cytocompatibility with heating was not investigated with MCF-7 cells, as 24h incubation times demonstrated significant toxicity. The particles and cells were exposed to this increase in temperature because temperature increases are anticipated with the application of an AMF, especially to promote the electrostatic mediated degradation that removes the Fe_3O_4 NP caps and induces cargo release. The RAW 246.7 controls were first compared when heated at 37 °C for 6 h versus 45 °C for 15 min, followed by 37 °C for 5 h 45 min (also for a total of 6h). A cell viability of 87 $\pm$ 5% was observed for control cells in the latter experiment. After confirming that the 15 min exposure to this elevated temperature did not significantly induce cytotoxic effects. Cell viability studies were conducted with particles. Toxicity was observed for Fe_3O_4 NP concentrations > 100 µg/mL (41.4 $\pm$ 3.2%) and for the APTESPSi@Fe_3O_4 nanocomposite at 200 µg/mL (59.7 $\pm$ 8.9%) . The nanocomposite toxicity at 200 µg/mL is between the cell viability values of the two individual components (18.4 $\pm$ 11.5% for Fe_3O_4 and 100 $\pm$ 27.3% for APTESPSi), indicating that having APTESPSi as part of the formulation contributes to higher cytocompatibility levels. Further studies on cytocompatibility with heating on MDA-MB-231 and HepG2 cell lines was motivated by the particles' applications in solid tumor cancer, where diseases are localized to a region where magnetic targeting and localized magnetic heating is possible.

The particles were incubated with HepG2 and MDA-MB-231 cells at elevated temperatures typical of promoting therapeutic release through electrostatic interaction degradation between APTESPSi and Fe_3O_4 NPs. The cells and particles were incubated for a total of 6h with the first 15 min at 45 °C and the remaining duration at 37 °C. We previously showed in Chapter 4 (Figure 4.9) a 15 time increase in SFN released at 45 °C in comparison to 37 °C within the first 15 min. First, the cell viability we determined for a temperature increase for 15 min in comparison to cells exposed to 37 °C for the entire 6h. Viabilities of 81 $\pm$ 1% and 90 $\pm$ 6% for MDA-MB-231 and HepG2 cells. After confirming that the temperature increases needed for a thermoresponsive release do not induce significant cytotoxicity on the control, the two cell lines were incubated with the APTESPSi@Fe_3O_4 nanocomposite and its components at 45 °C for 15 min followed by 37 °C for 5h 45 min (Figure 5.5).

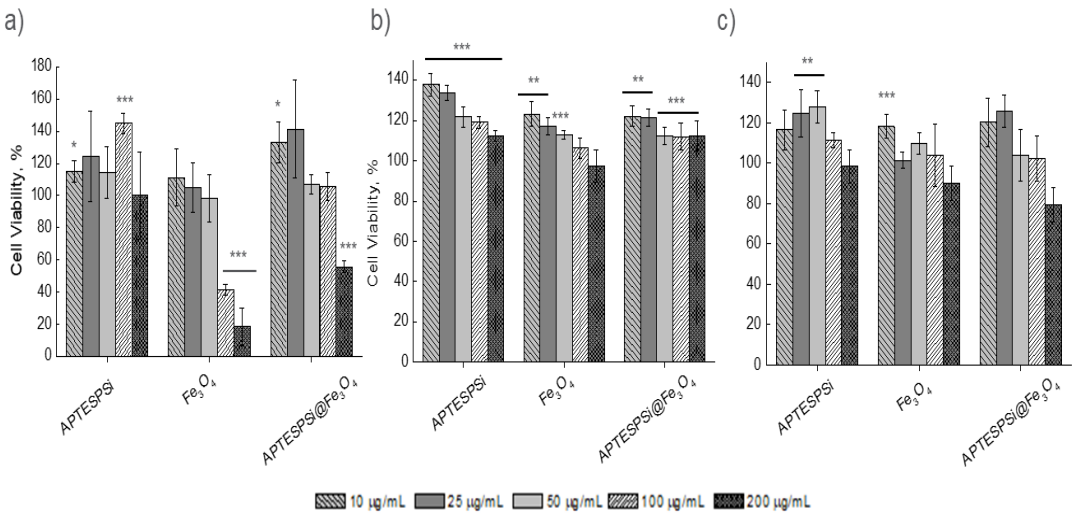

Figure 5.5 Cytotoxicity profiles for APTESPSi, Fe3O4, and APTESPSi@Fe3O4 NPs with elevated temperature Formulations were incubated with either RAW 246.7 macrophages (a) MDA-MB-231 (b) or HEPG-2 (c) cells for 15 min at 45 °C followed by 37 °C for 5 h, 45 min. The percentage of viable cells was determined using a CellTiter-Glo® Luminescent Cell Viability Assay. Significant cell death is observed in higher concentrations of the final formulation and Fe_3O_4 NPs. Data is presented as mean ± S.D. ($n \geq 3$), and the level of significance was set at probabilities of *$p < 0.05$, **$p < 0.01$, and ***$p < 0.001$ compared to the control.

The *in vitro* cytotoxicity measurements (Figure 5.5b-c) showed no statistically significant loss in cell viability for both cell types over the entire concentration range (10 µg/mL- 200 µg/mL). The data suggests that cancerous regions of the liver or triple negative breast tissue would not experience any localized toxicity from particle exposure.

5.4. Anticancer Activity of Therapeutic-Loaded PSi NPs

After confirming the biocompatibility of the APTESPSi@Fe_3O_4 nanocomposite and its components with application of temperature in macrophage and two cancer cell lines, the particles were loaded with SFN and assessed for its anti-cancer activity. As mentioned in Chapter 4, SFN has poor water solubility and its encapsulation in nanocarriers has improved anti-tumor activity [261]. Particles loaded with SFN were incubated with MDA-MB-231 (Figure 5.6) and HepG2 (Figure 5.7) cells at 37 °C for 6h or 45 °C for 15 min, followed by 37 °C for 5h 45 min. For MDA-MB-231 cells no toxicity was observed for the free drug with and without heating, probably due to SFN's poor water solubility. Another potential reason for the low cytotoxicity is a delay in downregulating Mcl-1, a gene encoding an anti-apoptotic protein that is required for the induction of apoptosis and has been implicated in resistance to anticancer drugs in several settings [276]. This Mcl-1 downregulation has resulted in < 25% cell death after one day of incubation with MDA-MB-231 cells, and therefore a 6h incubation time might have not been long enough to see the apoptotic effects of the free drug.

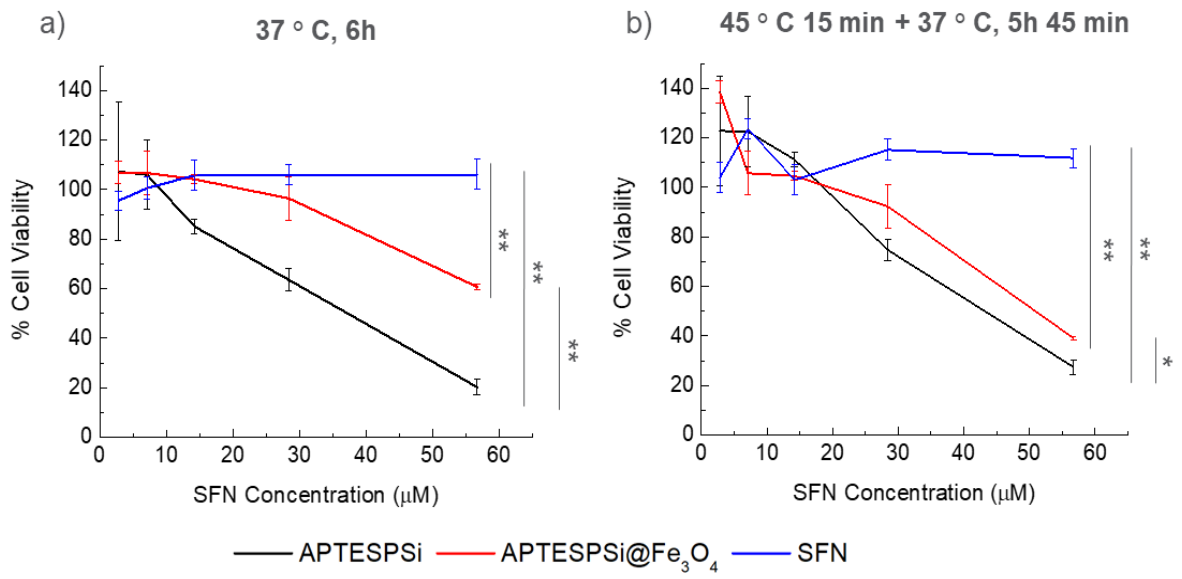

Figure 5.6 In vitro cell viability assays of APTESPSi and APTESPSi@Fe3O4 NPs loaded with Sorafenib, and Sorafenib as a free drug. Drug-loaded particles and free drug were incubated with MDA-MB-231 cells at 37 °C for 6 h (a) or exposed to an elevated temperature of 45 °C for 15 min followed by 37 °C for 5 h, 45 min (b). The percentage of viable cells was determined using a CellTiter-Glo® Luminescent Cell Viability Assay. Data is presented as mean ± S.D. ($n \geq 3$). One-way ANOVA, followed by the Tukey's post-test were performed and the level of significance was set at probabilities of *$p < 0.05$, **$p < 0.01$, and ***$p < 0.001$ compared to the control.

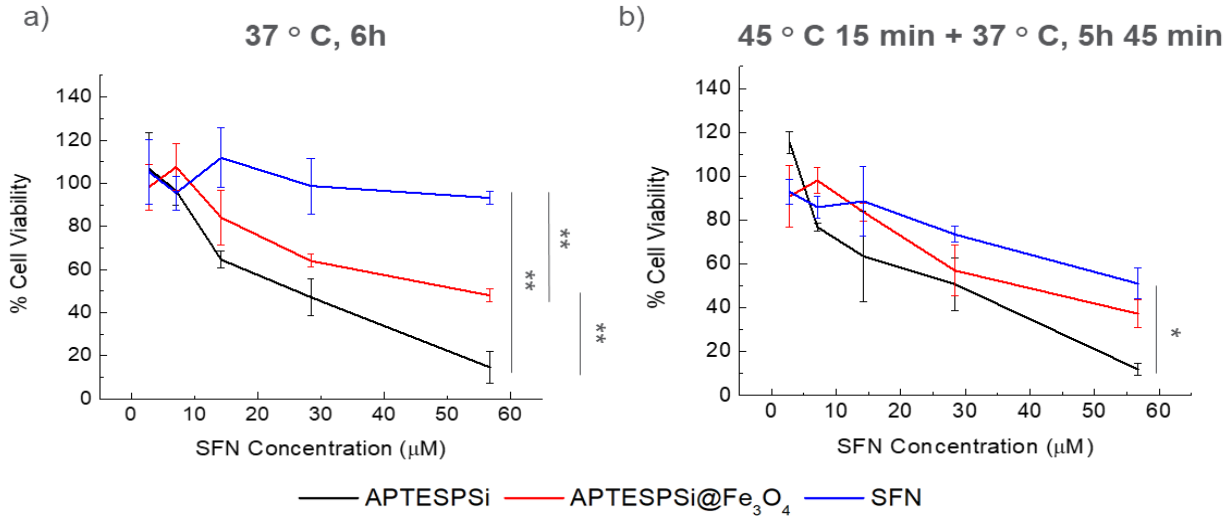

Figure 5.7 In vitro cell viability assays of APTESPSi and APTESPSi@Fe3O4 NPs loaded with Sorafenib, and Sorafenib as a free drug. Drug-loaded particles and free drug were incubated with HEPG-2 cells at 37 °C for 6 h (a) or exposed to an elevated temperature of 45 °C for 15 min followed by 37 °C for 5 h, 45 min (b). The percentage of viable cells was determined using a CellTiter-Glo® Luminescent Cell Viability Assay. Data is presented as mean ± S.D. ($n \geq 3$). One-way ANOVA, followed by the Tukey's post-test were performed and the level of significance was set at probabilities of *$p < 0.05$, **$p < 0.01$, and ***$p < 0.001$ compared to the control.

Loading SFN into APTESPSi and APTESPSi@Fe_3O_4 induced an increase in the vitro anticancer effect, with APTESPSi and APTESPSi@Fe_3O_4 inducing cell viabilities of 20 $\pm$ 3% and 61 $\pm$ 1% at the highest SFN concentration (56.7 µM). The higher toxicity induced by SFN-loaded APTESPSi in comparison to APTESPSi@Fe_3O_4 under both temperature profiles is perhaps due to the rapid release of SFN when no capping agent is present, as was shown in Chapter 4 (Figure 4.9a) where essentially all the drug is released within 5 min regardless of temperature. When the Fe_3O_4 capping agent is present, the amount of SFN released is controlled in a thermoresponsive manner, as shown in Chapter 4 (Figure 4.9b), and therefore less SFN released would induce less toxicity.

Moreover, higher levels of toxicity were observed with APTESPSi@Fe_3O_4 NPs that were initially heated at 45 °C for 15 min before going back to a typical incubation temperature of 37 °C for the remaining incubation duration. In fact, these toxicity levels (37 $\pm$ 1%) were comparable to that of APTESPSi (28 $\pm$ 3%) at the highest SFN concentration. A 40% decrease in the viability was observed in MDA-MB-231 cells treated with APTESPSi@Fe_3O_4 at 37 °C for the entire incubation time (61 $\pm$ 1%) in comparison to incubation at 45 °C for the first 15 min before returning to 37 °C (37 $\pm$ 1%). As previously mentioned, the amount of SFN released from APTESPSi@Fe_3O_4 increases around 15 times when the NPs are exposed to a temperature increase from 37 °C to 45 °C within the first 15 min as the electrostatic degradation mechanism is accelerated. Given that the MDA-MB-231 cells were compared to controls that were heated under the same respective temperature profile, the increase in cytotoxicity is not due to temperature application, but instead due to the increased SFN release with temperature. Thus, with MDA-MB-231 cells we demonstrate a system that can tune the amount of drug released to the cells and therefore the toxicity induced based on a temperature-responsive nanocarrier.

The same anti-cancer activity was assesed in HepG2 cells. At incubation conditions of 37 °C for 6h the cytotoxicity behavior was similar to that of MDA-MB-231, where SFN does not induce any significant toxicity, perhaps due to its poor water solubility, and APTESPSi exhibits the highest toxicity (15 $\pm$ 7% at 57 µM SFN), which is related to larger amounts of SFN being released. When the capping agent (Fe_3O_4) is electrostatically adsorbed onto the APTESPSi surface less drug is released and lower toxicity levels are induced (48 $\pm$ 3% at 57 µM SFN) at 37 °C. However, a synergistic effect is observed when free SFN is exposed to 45 °C for 15 min followed by 37 °C for the remaining incubation time. Additional interactions between drugs and hyperthermia have been described [277], known as 'thermal chemosensitization'. For example, pharmacodynamic features related to the kinetic changes of the drug's primary mode of action can contribute to drug–heat interactions. Moreover, most alkylating agents such as cyclophosphamide and platinum compounds possess linearly enhanced cytotoxicity effects when temperatures are increased above 40.5 °C [278]. Therefore, it is possible that free SFN exhibits a cytotoxic enhancing effect when combined with heat in HepG2 cells. Combining SFN with heat can potentially provide synergic antiangiogenic and proapoptotic effects in addition to the on-demand spatiotemporal control of the nanocarrier.

For HepG2 cells exposed to elevated temperatures there is no statistically significant difference between the free drug cytotoxicity (51 $\pm$ 7%) and that of SFN loaded APTESPSi@Fe_3O_4 NPs (37 $\pm$ 6%), which was unexpected given the cytotoxicity trend observed in MDA-MB-231 cells, yet plausible given the synergistic effect observed for the free drug with heating. Moreover, there is a smaller difference (23%) in toxicities between the APTESPSi@Fe_3O_4 nanocomposites incubated with the two temperature profiles (red lines in Figure 7) versus the difference observed in MDA-MB-231 cells (36%), which was unanticipated

assuming that higher amounts of SFN were released from the nanocomposite with heat that would induce more toxicity. Thus, we demonstrated the application of thermoresponsive APTESPSi@Fe_3O_4 nanocomposites as a promising tool for remotely controlling the anticancer activity in MDA-MB-231 and HepG2 cell lines.

5.5.Cellular Association of PSi NPs with MDA-MB-231 Cells

The cellular interaction of APTESPSiFe_3O_4 nanocomposites are anticipated to change as the surface charge varies with temperature mediated degradation of electrostatic interactions. Therefore, the cellular interactions of Alexafluor488-labeled APTESPSi and APTESPSi@Fe_3O_4 were investigated in MDA-MB-231 cells with and without heat application over 6h. Confocal imaging and flow cytometry assessed whether the Fe_3O_4 capping agent effected particle uptake by cells in comparison to nanocarriers without the cap (as Fe_3O_4 is associated with a negative surface charge of -38.3 $\pm$ 1.9 mV and APTESPSi exhibits a surface charge of +31.7 $\pm$ 1.4 mV). Moreover, the influence of temperature changes on cellular interaction were investigated. In all tests a particle concentration of 200 µg/mL was used, which corresponded to a safe dose of NPs administered as determined by earlier cytotoxicity assessments (Figure 5.5b).

Confocal fluorescence microscopy provided a quantitative, direct observation of Alexafluor488-labeled APTESPSi and APTESPSi@Fe_3O_4 NP uptake in MDA-MB-231 cells. The cellular association was more prominent for APTESPSi compared to the APTESPSi@Fe_3O_4 nanocomposites after incubating for 6h at 37 ° C (Figure 5.8). It is important to note that after Alexafluor488 labelling using EDC/NHS chemistry, the fluorescence intensities were verified to be the same. Therefore, reduced Alexafluor488 fluorescence for APTESPSi@Fe_3O_4 is due to the decrease in cellular association and not any differences in the amount of marker on the NP surface. This observation is related with the enhanced electrostatic interactions between the

positively charged APTESPSi NPs and the negatively charged cell membrane that results in a concentration- and time-dependent internalization of the APTESPSi.

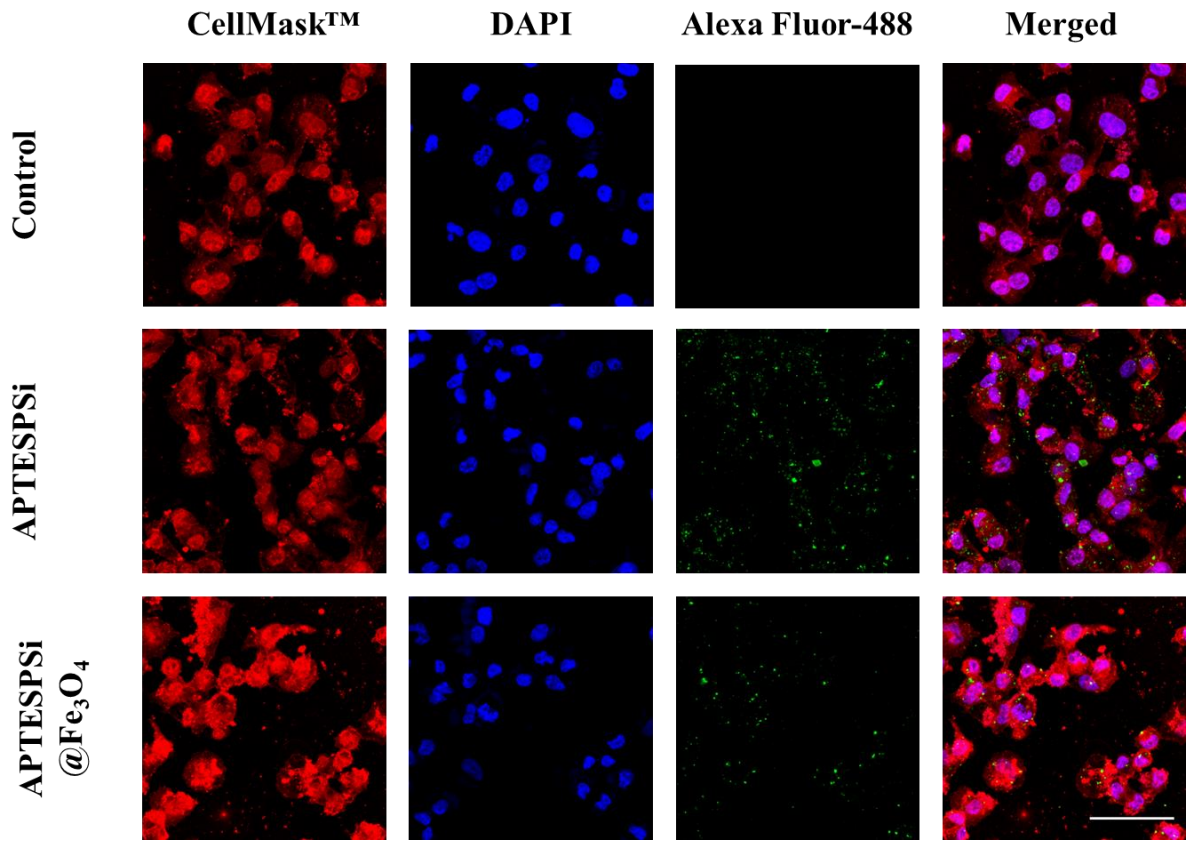

Figure 5.8 Confocal fluorescence microscopy images MDA-MB-231 cells incubated with 200 µg/mL APTESPsi and APTESPSi@Fe3O4 NPs conjugated with Alexa Fluor-488 at 37 °C for 6 h. The cell membranes and nuclei were stained with CellMask™ (red) and DAPI (blue). The scale bar in the lower right panel is the same for all images and corresponds to 100 µm.

In addition, the enhanced drug concentration around the nucleus (stained by DAPI) by positively charged NPs has been previously attributed to endosomal escape abilities after cell internalization [279] and by a phenomenon known as the 'proton-sponge' effect [270,280], where the lysosomal membrane is ruptured due to osmotic swelling that results from an influx of chloride ions into the lysosome to maintain a neutral charge. Moreover, the presence of a Fe_3O_4 NP cap decreased the positive surface charge, which to some extent reduced the cell uptake.

The qualitative differences in cellular association for the NPs incubated with a temperature increase (45 °C, 15 min followed by 37 ° C, 5h 45 min) are shown in Figure 5.9. From the confocal images (Figure 5.8-9) APTESPSi has higher cellular association in comparison to APTESPSi@Fe_3O_4 NPs.

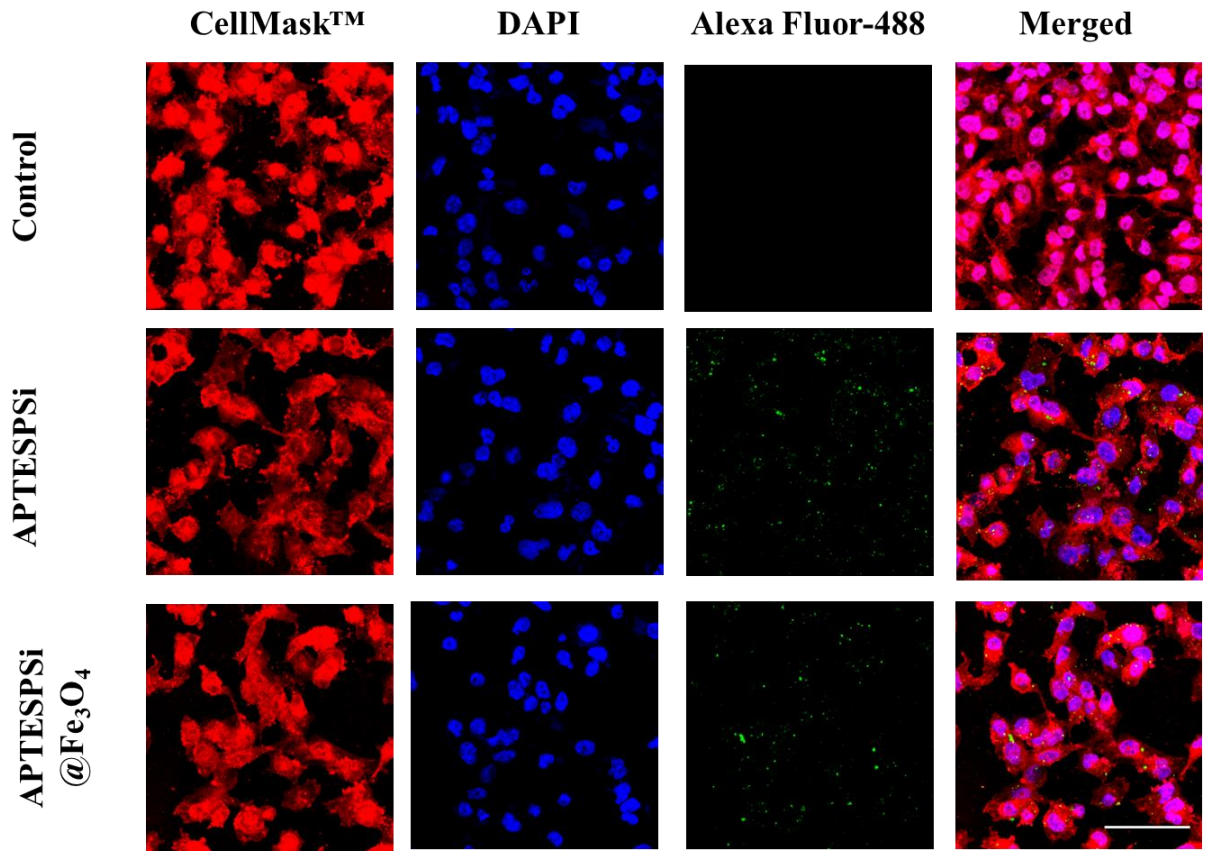

Figure 5.9 Confocal fluorescence microscopy images MDA-MB-231 cells incubated with 200 µg/mL APTESPsi and APTESPSi@Fe3O4 NPs conjugated with Alexa Fluor-488 at 45 °C for 15 min followed by 37 °C 5 h, 45 min. The cell membranes and nuclei were stained with CellMask™ (red) and DAPI (blue). The scale bar in the lower right panel is the same for all images and corresponds to 100 µm.

However, when comparing APTESPSi with and without the additional 45 °C heating a similiar cellular interaction was observed. This finding was unexpected, since previous findings reported an increase in therapeutic uptake in MDA-MB-231 cells with heating at 47 °C [281]. The increase in cellular association was attributed to enhanced cell perfusion that facilitated therapeutic agent diffusion into the cell membrane [282], an increase in membrane permeability that allowed more

therapeutic agents to enter through the cell membrane, and a morphological change in the cells that increased surface-area-to-volume ratio, thereby providing a higher possibility for the cells to adsorb more therapeutic. Confocal images are limited to observing the particle distribution throughout the cellular structure, such as whether the particles are within the nucleus or cytoplasm. However, this technique's quantitative assessment is limited and flow cytometry was used to quantitatively investigate the in vitro cellular interaction.

Cellular interactions were studied with flow cytometry for Alexafluor488-labeled APTESPSi and APTESPSi@Fe_3O_4 NPs incubated with MDA-MB-231cells at 37 °C for 6h (Figure 5.10a) and at 45 °C for 15 min followed by 37 ° C for 5h 45 min (Figure 5.10b).

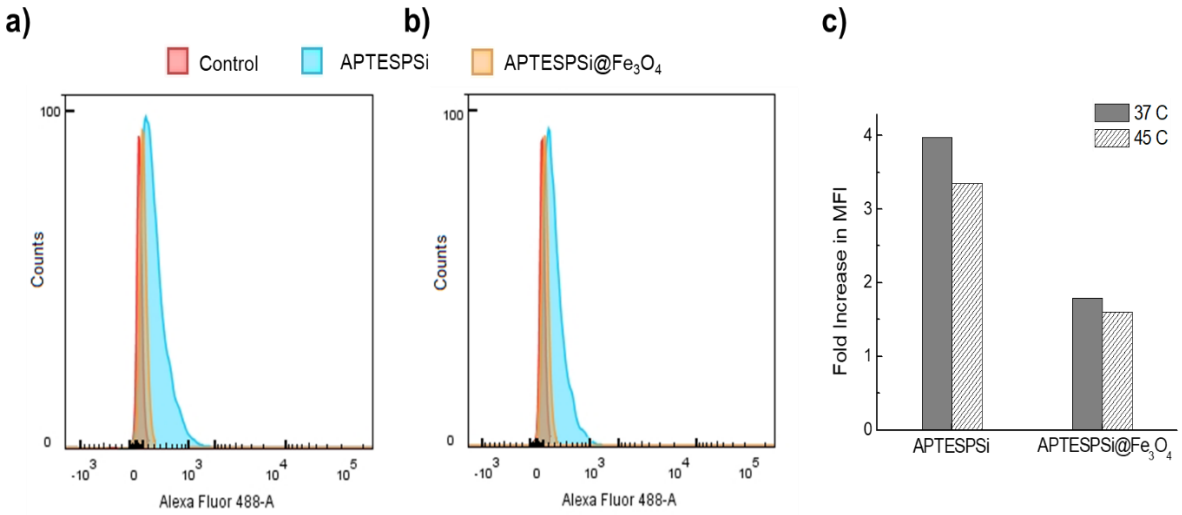

Figure 5.10 In vitro quantitative cellular interaction measured by flow cytometry of Alexa Fluor-488-labeled APTESPSi and APTESPSi@Fe3O4 NPs incubated with MDA-MB-231 cells at a) 37 °C for 6 h and at b) 45 °C for 15 min followed by 37 °C for 5 h 45 min. c) The fold increase in mean fluorescence intensity after 6 h was calculated. MDA-MB-231 cells incubated without any NPs served as a control to show the extent of cellular uptake by APTESPSi and APTESPSi@Fe_3O_4 at 37 °C for 6 h and at 45 °C for 15 min followed by 37 °C for 5 h 45 min.

The cellular association was quantified as the surface charge changed with the introduction of the Fe_3O_4 capping agent, and when temperature changes were introduced. The fluorescence was quenched to reduce fluorescence contributions from particles adsorbed on the external cell surface, thus analyzing the extent of internalized NPs with higher accuracy. In agreement with

confocal images for incubation at 37 °C, 6h (Figure 5.8) there was a 2-fold difference in the mean fluorescence intensity (MFI) for APTESPSi (4-fold increase) in comparison to APTESPSi@Fe_3O_4 NPs (2-fold increase). As previously mentioned, because of the APTESPSi's highly positive surface charge, the NPs more readily interact with the negatively charged cell membrane. Meanwhile, APTESPSi@Fe_3O_4 possesses a relatively less positive surface charge that could, to some extent, reduce the unspecific cell interactions and cell uptake. Moreover, as heat is applied during incubation (45 °C, 15 min) the cellular interaction with APTESPSi and APTESPSi@Fe_3O_4 decreased in comparison to no heating. However, this cellular interaction decrease is more pronounced for APTESPSi (almost 1-fold decrease) than for APTESPSi@Fe_3O_4 (~1/4-fold decrease) when compared to MFI values for incubation without any heating. These results were in agreement with the confocal images and recent work that observed increased cellular association of cisplatin and paclitaxel [281]. However, these small-molecule drugs are on the order of 1 nm while PSi-based NPs used in this study are on the order of ~220-250 nm. Thus, it would be interesting to repeat this study with drug-loaded Psi-based NPs to determine whether increasing the incubation temperature results in increased cellular association of the therapeutic.

5.6.Conclusion

In this Chapter the cytocompatibility and cellular association of magnetic-capped PSi (APTESPSi@Fe_3O_4) NPs and its components were investigated. High cytocompatibility was observed in RAW 246.7 macrophages that are typically used for initial bioactivity screening of particles, in HepG2 liver cancer cells where the model drug SFN has a clinical indication for liver-based cancers, and in MDA-MB-231 triple negative breast cancer cells, which are characterized as solid tumors that would be an ideal environment for localizing a therapeutic.

However, significant toxicity was induced in MCF-7 breast cancer cells, and therefore this nanocomposite formulation would not be suitable for such an application. The nanocomposite demonstrated high biocompatibility when incubated with RAW 246.7 macrophages, HepG2 and MDA-MB-231 cells that were heated to temperatures and times typical of promoting therapeutic release (45 °C, 15min) as observed in dissolution studies with SFN in Chapter 4. Some decrease in the cytocompatibility is observed for the nanocomposite at 200 µg/mL in HepG2 cells, although this decrease is not statistically significant. Moreover, heating MDA-MB-231 and HepG2 cells incubated with SFN-loaded APTESPSi and APTESPSi@Fe_3O_4 NPs showed a further decrease in cytocompatibility which was attributed to the increased dissolution of SFN from the nanocarrier with temperature.

Cellular association studies with MDA-MB-231 cells showed an overall higher uptake of APTESPSi NPs in comparison to APTESPSi@Fe_3O_4. This observation was explained by the positive surface charge of APTESPSi that binds to the negatively charged cell membrane via electrostatic interactions. Increasing the cell incubation temperature to 45 °C for 15 min followed by 37 °C for 5h 45 min caused a slight decrease in the particle uptake by MDA-MB-231 cells. Overall, the controlled release capabilities, biocompatibility and anticancer activity of APTESPSi@Fe_3O_4 nanocomposites were assesed. These nanocomposites demonstrated “on-demand” drug release, high biocompatibility, and high anticancer activity when combined with a model drug.

Chapter 6. Porous Silicon Nanoparticle Encapsulation of Thermoresponsive Polymers

6.1 Introduction

While Chapters 4 and 5 demonstrated a promising thermoresponsive Fe_3O_4 capping system, some SFN release observed at 37 °C may result in premature therapeutic degradation or therapeutic efficacy. PSi NPs coated with a thermoresponsive polymer can potentially reduce this unintended therapeutic release, where the polymer network more homogeneously covers the porous surface [216,283–285] in comparison to Fe_3O_4 NPs bound by electrostatic interactions. For example, PSi conjugated with a poly(N-isopropylacrylamide), PNIPAM, copolymer observed 18% release of doxorubicin after 24h at 37 °C [216] while our Fe_3O_4-capped formulation demonstrated a 50% release with SFN with the same experimental conditions.

PNIPAM is the most extensively investigated thermally responsive polymer for stimuli-responsive drug delivery carrier systems, because of its demonstrated biocompatibility [286–288] and phase transition near physiological temperature. The polymer undergoes a phase transition at a lower critical solution temperature (LCST) of 32 °C from a hydrophilic to hydrophobic state [289–292]. Above this temperature, the polymer chains which previously took up a larger volume due to hydrogen bonding with water, coil up and allow therapeutic release from the pores, as shown by the schematic in Figure 6.1[292].

The transition occurs below the physiological temperature of 37 °C, while a phase transition at a temperature a few degrees above physiological temperature is ideal. This phase transition temperature can be increased to slightly above 37 °C by copolymerization with other acrylic monomers such as acrylic acid (AA) [293].

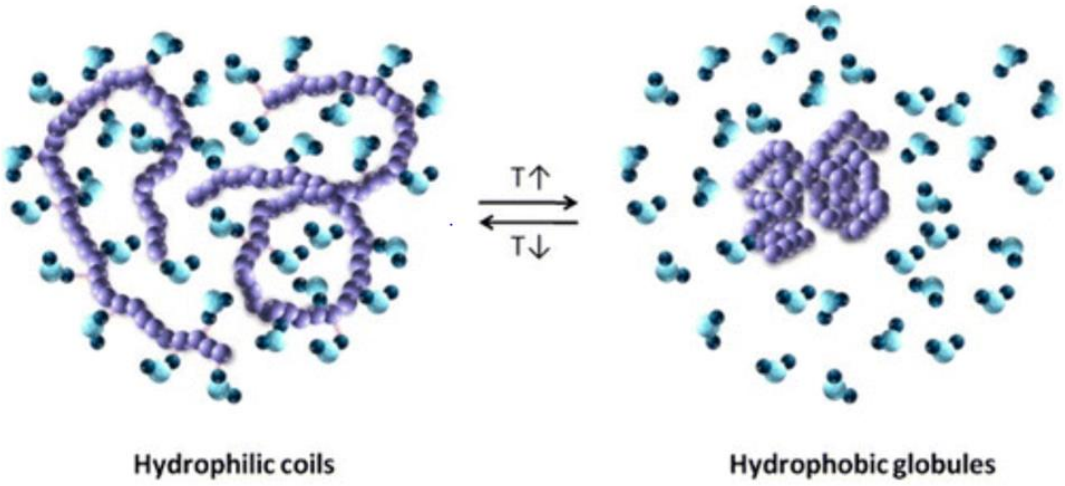

Figure 6.1 Schematic of thermoresponsive polymer undergoing a transition from its coil structure under soluble/expanded conditions to a globule structure (insoluble/collapsed) in an aqueous environment. Image adapted from ref 11.

Thermally responsive nanocarriers are fabricated either by chemical conjugation of the thermoresponsive polymer onto the nanocarrier surface or by physical encapsulation of the nanocarrier through solvent-switching precipitation methods. The chemical conjugation of PNIPAM and PNIPAM copolymers on PSi NP surfaces has been widely studied [215–217,283–285,294,295]. An α-bromoisobutyryl bromide (BIBB) was grafted onto a PSi NP surface to initiate the polymerization of a PNIPAM copolymer via a surface-initiated atom transfer radical polymerization (ATRP) approach[216]. The PNIPAM copolymer- grafted PSi NPs demonstrated a thermally modulated release, with less than 20% of doxorubicin released at 37 ° C and greater than 90% released at 45 ° C after 24 h. Vinyl groups have also been introduced on mesoporous silica and PSi NP surfaces for further for further PNIPAM polymerization [217,283]. However, these chemical conjugation steps are tedious and time consuming (~5-6 days). Moreover, numerous purification steps to eliminate side products further reduces the feasibility for scaling up this

method in clinical settings. An alternative to chemical conjugation is physically encapsulating the NP in a desired polymer.

Physical encapsulation techniques such as emulsion solvent evaporation, nanoprecipitation, and emulsion solvent diffusion are promising alternatives to chemical conjugation, as they are rapid, simple, and easy to scale up [296–298]. With nanoprecipitation, an amphipathic polymer is dissolved in a semi-polar water-miscible solvent. As an aqueous solution is introduced it displaces the semi-polar solvent and causes the polymer to precipitate into NPs [298–301]. The nonsolvent based precipitation process is comprised of four stages: generating a supersaturation state, nucleation, growth, and coagulation [236]. Supersaturation is achieved when the solution contains more dissolved solute than the equilibrium saturation value. When the nonsolvent (water) is introduced the system is put in a supersaturated state because the overall solvent potency to dissolve the solute decreases. The supersaturation ratio (Sr) is expressed as

$$S_r = \frac{C_s}{C_\infty} \quad \text{Eq. (6.1)}$$

Where C_s is the interfacial particle solubility ratio and C_∞. Typically, a higher supersaturation rate leads to smaller particle sizes. When the supersaturation reaches a critical level that is solvent/ non-solvent specific, the solution overcomes the activation energy barrier (ΔG) needed to assemble (i.e. homogeneous nucleation)

$$\Delta G = \frac{16\pi\sigma^3\nu^3}{3K^2T^2(\ln S_r)^2} \text{ Eq. (6.2)}$$

Where σ is the interfacial tension at the solution-precipitate interface, ν is the solute molar volume, K is the Boltzmann constant, and T is the temperature [236,302]. After primary nuclei formation due to solution supersaturation, solute molecules associate to the nuclei until reaching

a critical size that is stable against dissolution. Nucleation continues until the solution supersaturation is depleted by the growth of earlier nuclei. The nucleation rate (N_r) is expressed as

$$N_r = c\ exp\left[-\frac{16\pi\sigma^3\nu^2}{3K^3T^3(\ln S_r)^2}\right] \text{ Eq. (6.3)}$$

Where c is a constant [302]. As the solute concentration reduces below the critical supersaturation concentration the nuclei grow by condensation or coagulation. Condensation is dominated by diffusion-limited growth kinetics, where single molecules are added to the particle surface by 1) transporting solute from the bulk fluid through the solution boundary layer adjacent to the nuclei surface and 2) integrating the adsorbed solute molecules into the nuclei matrix via deposition [302]. Particle growth by condensation ceases when the solute concentration reaches the equilibrium saturation concentration. Coagulation, or the adhesion of particles, occurs when attractive forces are stronger than repulsive ones. The number of collisions that lead to coagulation, or collision frequency, is determined by the ratio between attractive and repulsive particle interaction.

Literature on NP synthesis by nanoprecipitation has demonstrated the importance of establishing a relationship between experimental parameters and controlling the nucleation and growth kinetics [299,301]. When NP sizes smaller than a few hundred nanometers are desired, nucleation is favored over growth [301]. High nucleation rates, N_r, result in higher nuclei densities and NP yield. An increase in supersaturation level leads to high N_r as predicted using Eq. (6.3). High local supersaturation and controlled nucleation rates can be achieved by rapid mixing, which will be discussed shortly. Moreover, growth is arrested when there is sufficient amphiphilic stabilizing material density on the particle surface to stop further aggregation [303].

When experimental conditions favor the growth regime over nucleation, few nuclei form and are likely to grow into micron-sized particles [236].

Nanoprecipitation has been primarily used to form biodegradable polymer NPs, including poly(lactic-co-glycolic acid) (PLGA) [304–306] and several amphiphilic block copolymers, for drug delivery of hydrophobic molecules [300,307–310]. A key requirement for NP self-assembly is having an amphiphilic polymer where the hydrophobic block adsorbs onto a particle surface through hydrophobic interactions while the hydrophilic block provides stability in the aqueous colloidal suspension. Table 6.1 shows several examples of amphiphilic block copolymers used to form NPs via nanoprecipitation and flash nanoprecipitation, which will be discussed later in this section. While most of these examples used nanoprecipitation to encapsulate hydrophobic molecules within a water-soluble vehicle for drug delivery applications [311–313], this method has also encapsulated MRI contrast agents and fluorescent molecules [314].

Table 6. 1 Summary of polymeric NPs formed by nanoprecipitation and their application.

Co-polymer	Precipitation Method	Application/ Encapsulant	Reference
PS-b-P4VP	Aerosel nanospheres	Solvent- morphology	Raula et al. (2013)
PS-b-PEG	Flash nanoprecipitation	pH response	Prud'homme et al. (2015)
		Fluorescent marker	Prud'homme et al. (2013), Clapp et al. (2014)
		Hydrophobic drug	Prud'homme et al. (2015)
PS-b-PVP	Flash nanoprecipitation	Metal nanocatalyst	Priestley et al. (2014)
PS-b-PEO	Flash nanoprecipitation	Hydrophobic drug	Prud'homme et al. (2009)
PLGA-b-PEG	Nanoprecipitation	Hydrophobic drug	Lamprecht et al. (2013)

		Controlled release	Préat et al. (2009), Feng et al. (2010), Puglisi et al. (2013)
	Flash nanoprecipitation	Hydrophobic drug	Zhu et al. (2013), Zhu et al. (2014)
PLA-b-PEG	Nanoprecipitation	Transmucosal transport	Alonso et al. (2004)
	Flash nanoprecipitation	MRI Contrast agent	Prud'homme et al. (2015)
		Stability, bioavailability	Moghe et al. (2012)
		Photosensitizer	Ju et al. (2011)
		Hydrophobic drug	Prud'homme et al. (2012), Chow et al. (2015)
PCL-b-PEG	Nanoprecipitation	Hydrophobic drug	Zhuo et al. (2005)
		Antimicrobial photoactivity	Nafee et al. (2013)
		Controlled release	Chau et al. (2013), Préat et al. (2009)
		Sensitive drug	Barreto et al. (2013), de Melo Cazal (2015)
PVP-b-PVOH	Flash nanoprecipitation	Hydrophobic drug	Prud'homme et al. (2008)

PS: polystyrene; P4VP: Poly(4-vinylpyridine); PEG: polyethylene glycol; PVP: Polyvinylpyrrolidone; PEO: Polyethylene oxide; PLGA: Poly Lactic-co-Glycolic Acid; PLA: Polylactic acid; PCL: Polycaprolactone; PVOH: Polyvinyl alcohol.

Table 6.2 Summary of PNIPAM block copolymer NPs.

Co-polymer	Precipitation Method	Application/ Encapsulant	Reference
PIL-PNIPAM	Temperature precipitation	Thermal, ionic strength responsive	Yuan et al. (2011)
PIL-PNIPAM-PIL	Aerosel nanospheres	Controlled release	Tenhu et al. (2015)
PS-b-P4VP pNIPAM surface conjugated	Solution processed films	Thermoresponsive molecular filters	Abetz et al. (2013)
PS-b-PNIPAM	Photoemulsion polymerization	Thermoresponsive	Ballauff et al. (2006)

PS-b-PNIPAM-b-PS	Aerosel nanospheres	Controlled release	Tenhu et al. (2010), Raula et al. (2012), Raula et al. (2015)
	Solution processed films	Thermoresponsive molecular filters	Tenhu et al. (2007)
	Temperature precipitation	Thermoresponsive micelles	Papadakis et al. (2010), Papadakis et al. (2012)

PS: polystyrene; P4VP: Poly(4-vinylpyridine); PNIPAm: Poly(N-isopropylacrylamide); PIL: Polymeric ionic liquids.

Moreover, tuning the morphology of polymeric NPs formed by nanoprecipitation resulted in controlled release profiles favorable for drug delivery. This work focuses on physical encapsulation with thermoresponsive polymers, such as PNIPAM. Extensive research has developed amphiphilic polymeric NPs based on polystyrene (PS) or polymer ionic liquids (PIL) and PNIPAM (PIL-PNIPAM, PS-PNIPAM), as shown in Table 6.2. NPs were formed either by temperature changes that induce hydrophobic characteristic and micellar collapse or by an aerosol technique where the polymer solution is atomized into small droplets in a gas-phase and the solvent is subsequently evaporated in an oven [315–317]. While these techniques have fabricated themoresponsive polymeric NPs with varying morphologies, the synthesis of these NPs via nanoprecipitation is limited [318,319]. Moreover, using flash nanoprecipitation to encapsulate hydrophobic PSi NPs with PNIPAM has the potential to rapidly form thermoresponsive PSi NPs with narrow size distribution at mass-scale production levels.

As previously mentioned, smaller NPs with narrow size distribution are formed using rapid mixing during nanoprecipitation that results in high local supersaturation and controlled nucleation rates. With flash nanoprecipitation, rapid mixing, on the order of milliseconds, produces solvent exchange between the good solvent and anti-solvent on time scales faster than the solute aggregation time [301,302]. The flash nanoprecipitation process is tuned through three time scales: (1) time to attain homogeneous mixing (τ_{mix}), (2) time for nucleation and growth of

hydrophobic block (τ_{ng}), and (3) time of block copolymer self-assembly (τ_{sa}) [320]. The NP size is controlled by having characteristic times on the order of τ_{mix} and τ_{ng}. These characteristic time scales on the order of milliseconds is achieved by using multi-inlet vortex mixers (MIVM) with mixing channels on the micron scale [310,321]. With these mixers, supersaturation levels are modified by varying the solvent and water stream flow rate, which results in varying solvent/ water ratios. Microfluidics is a widely used technique for the nanoprecipitation of polymeric NPs in microscale fluidic channels (tens to hundreds of micrometers) with continuous flows [49]. The small channel dimensions and large surface-to-volume ratio drastically reduce the mixing path of solvent and non-solvents to few tens of micrometers [322]. The short mixing path facilitates the microscale mixing process that results in nanoscale particles and narrow size distribution, as previously discussed. The fast and efficient mixing allows physicochemical features of the NPs to be controlled by tuning the flow rate ratios between the non-solvent and solvent or by changing the mixing patterns. The fluid patterns are predicted by two dimensionless parameters: Reynolds number (Re) and Péclet number (Pe). Reynolds number is calculated below in

$$R_e = \frac{\rho \nu L}{\mu} \quad \text{Eq. (6.4)}$$

where ρ is the fluid density, ν is the fluid velocity, L is a characteristic linear dimension, and μ is the fluid viscosity. A high Re (> 2300) possesses a turbulent flow pattern that is characterized by a chaotic pattern with no distinct streamlines[238]. At low Re values (<1800) the flow pattern is laminar with distinct streamlines which are parallel to the fluid direction[238]. The transition between turbulent and laminar flow occurs at a Re of 1800–2000. In droplet microfluidics for drug encapsulation laminar flow is typically favored, because the fluids and the molecules within the steady streamlines can be precisely manipulated to generate controllable and monodisperse droplets [238].

The Péclet number characterizes the diffusion or convection of molecules in the fluids [238,323] and is calculated using Eqn. 6.5

$$P_e = \frac{lu}{D} \qquad \text{Eq. (6.5)}$$

where, u is the local fluid velocity, l is the characteristic length, and D is the mass diffusion coefficient. The small volumes typical of microfluidics and laminar flow pattern result in slow molecular transfer through diffusion rather than convection.

Microfluidic devices used to form single emulsions are categorized into three different geometries: flow focusing, co-flow, and T-junction [237,323]. In flow focusing microfluidic devices, two immiscible fluids flow through at opposite sides of the system and meet at the inner capillary orifice, where the droplets are formed. With co-flow geometry the dispersed and continuous phases flow in parallel streams. For the T-junction configuration, two channels meet at a right angle, with one channel carrying the continuous phase and the orthogonal channel carrying the dispersed phase. Co-flow geometry has been extensively used to produce NPs via microfluidic nanoprecipitation [57,96,324–326]. Microfluidic synthesis of polymeric NPs is advantageous because it improves control over size, size distribution, and morphologies [327–329]. For example, PLGA NPs loaded with efavirenz (EFV) for treating HIV neuropathology were synthesized by microfluidics and bulk mixing [330]. NPs formed with microfluidics exhibited smaller sizes (73 nm *versus* 133 nm) and higher drug loading (10.8% *versus* 3.2%). Poly(lactic-co- glycolic acid)-polyethylene glycol (PLGA-PEG) NPs encapsulating the chemotherapeutic docetaxel (Dtxl) was also formed by microfluidics nanoprecipitation and demonstrated smaller NP sizes, narrower size distribution, and higher Dtxl encapsulation efficiency [331]. Similarly, chitosan NPs loaded with

dexamethasone (Dex) for enhanced osteogenic differentiation of stem cells were fabricated using nanoprecipitation in microfluidic devices [332].

Moreover, microfluidic nanoprecipitation has been used for the polymeric encapsulation of PSi NPs for applications such as diabetes, theranostics, nanovaccines and nanocarriers with dual hydrophilic and hydrophobic payloads [328,333]. Undecylenic acid-modified thermally hydrocarbonized PSi (UnPSi) NPs were encapsulated with the pH-sensitive hypromellose acetate succinate via microfluidics nanoprecipitation to investigate intestinal cells interaction and demonstrate the pH responsive release of the model antidiabetic drug glucagon-like peptide-1 (GLP-1) [334]. pH responsive delivery was also demonstrated with the anticancer drugs paclitaxel and sorafenib by encapsulating drug-loaded PSi NPs in acid- degradable acetalated dextran (AcDeX) matrix or polyethylene glycol- block-poly(L-histidine) PEG-b-PHIS through microfluidics nanoprecipitation [326]. In the first pH responsive case, an outer solution in the microfluidic device with an acidic pH (pH 3.7), forced the precipitation of hypromellose acetate succinate. For the anticancer drug-loaded PSi NPs, polymer precipitation was induced by its insolubility with the outer fluid. The glass-capillary microfluidics nanoprecipitation technique discussed in these last examples was also used to encapsulate PSi NPs and zinc-doped copper oxide (Zn–CuO) NPs with AcDex to formulate a nano- cancer vaccine [335] and cancerous tumor targeting NPs [336]. While extensive research has been dedicated to the forming pH responsive PSi NPs via nanoprecipitation in flow-focused microfluidic chips, this method has not been applied to the production of thermoresponsive PSi NPs.

This Chapter investigates whether nanoprecipitation provides a facile, improved route towards synthesizing thermoresponsive PSi NPs. We first confirmed whether PNIPAM NPs can precipitate and encapsulate PSi NPs in bulk and microfluidics via a co-nonsolvency method. We

then investigated whether the amphiphilic block copolymer PS-b-PNIPAM can encapsulate PSi NPs via bulk mixing nanoprecipitation. Preliminary results are then shown for thermoresponsive polymer encapsulated PSi NPs formed in flow-focused microfluidic chips. The chapter concludes with future studies that could further develop this facile approach to preparing thermoreponsive PSi NPs on a mass-commercialization level.

6.2 Experimental

PNIPAM Homopolymer Synthesis

A PNIPAM homopolymer was synthesized via free radical polymerization[287] to determine its ability to encapsulate PSi NPs. A 1.47 M solution of NIPAM monomer was formed by dissolving 0.33 mg of monomer in 8 mL of 1,4-dioxane. The solution was degassed with N_2 for 30 minutes and then heated to 70 ºC. Once the solution reached this temperature, 380 µL of 2,2′-Azobis(isobutyronitrile) AIBN (2.56 mM) was injected into the flask and the reaction occurred overnight under rapid stirring. The polymer was then precipitated out in diethyl ether and centrifuged at 6000 rpm for 5 min. The supernatant was decanted and the polymer was again washed with diethyl ether to precipitate. This procedure was repeated three times to remove any unreacted monomer or initiator. After removing leftover solvent with a rotary evaporator and drying under vacuum for 2 hours, 1.685 g of PNIPAM was collected as a white powder. Proton nuclear magnetic resonance (^{1}H-NMR) spectra was collected using a Bruker Ascend 400 MHz—Avance III HD NMR spectrometer (Bruker Corporation, Billerica, MA, USA) and confirmed the formation of PNIPAM. The ^{1}H-NMR measurement was conducted in deuterated water (D_2O).

PS-PNIPAM Block Copolymer Synthesis

PS-b-PNIPAM amphiphilic di-block copolymer was synthesized, as previously reported [317,337], via reversible addition-fragmentation chain transfer (RAFT) polymerization of NIPAM using a PS precursor as a macro-RAFT agent. First, the PS block was synthesized by dissolving styrene, S,S′-Bis(R,R′-dimethyl-R″-acetic acid) Trithio- carbonate (BDAT), and AIBN in 1,4-dioxane. The solution was degassed by three freeze-pump-thaw cycles (<1 mbar) and the vessel was sealed under vacuum and placed in a thermostatically controlled oil bath (70 °C) to allow polymerization during a well-defined predetermined time. After the PS polymerization, the polymer was precipitated in cold methanol and purified by repeated precipitations. The final product was dried in vacuum to yield yellow powders. The number average molecular weights (M_n), weight average molecular weights (M_w) and polydispersity index (M_w/M_n, PDI) of the PS-block were analyzed with size exclusion chromatography (SEC) against PS standards. Table 6.3 shows the respective molecular weights for two PS chains that were synthesized.

Table 6.3 PS polymer blocks and their respective lengths based on molecular weight.

Polymer	M_n[a] (g mol^{-1})	M_w (g mol^{-1})	M_w/M_n[a]
19PS1	4,400	5,100	1.19
19PS2	8,800	10,500	1.20

[a] Determined by SEC using calibration with PS standards, PS: polystyrene

To form the final block copolymer desired, PS yellow powder was then dissolved in 1,4-dioxane before adding NIPAM and AIBN. The mixture was stirred for 30 min at room temperature to dissolve all the components and then degassed by three successive freeze-pump-thaw cycles. The mixture was placed in an oil bath at 70 °C to start the polymerization reaction. The reaction was halted by cooling the solution to ambient temperature. The product was precipitated twice from tetrahydrofuran (THF) into diethyl ether and cold water for purification

purposes. The product was freed from the homopolymer PNIPAM by centrifugation at 29 °C (45 min, 5000 rpm). The block copolymer structure and purity was assessed by ^{1}H NMR spectroscopy (200 MHz Varian Gemini 2000 spectrometer) using deuterated chloroform ($CDCl_3$) as a solvent. The M_n of the diblocks were calculated using NMR data, namely the ratio between the signals 6.4-8.8 ppm (Ar-H and NH) and 3.7-4.3 ppm (N-CH). Other aliphatic protons were not used because they give ambiguous values (too high integral values). The PDI was determined by SEC using calibration with PS standards. The structural data shown in Table 6.4.

Table 6.4 PS-b-PNIPAM block copolymers with varying block lengths.

Polymer	M_n[a] (g mol^{-1})	M_w/M_n[b]	M_n[b] (g mol^{-1}) PS-block	M_n[c] (g mol^{-1}) PNIPAM-block
PS1PNIPA2	11,000	1.24	4,400	6,600
PS2PNIPA2	37,100	1.26	8,800	28,300
PS2PNIPA1	45,200	1.36	8,800	36,400

[a] M_n of the A-B block copolymer determined with ^{1}H NMR spectroscopy. [b] Determined by SEC using calibration with PS standards. [c] Determined with ^{1}H NMR spectroscopy. PS: polystyrene; PNIPAM: poly(N-isopropylacrylamide)

PNIPAM Nanoprecipitation by Co-Nonsolvency Method

While PNIPAM is soluble in pure water and pure ethanol, it has been previously shown to precipitate in water and ethanol mixtures over a certain mixture range [338], also known as co-nonsolvency. Precipitation was directly observed by comparing 1:1 mixtures of good solvent (10 mg/mL PNIPAM in ethanol) and bad solvent (Milli-Q water with 0.1 wt% or 1 wt% Pluronic® F-127) in bulk mixing. These mixtures were also compared with the good and bad solvents individually to confirm that precipitation is in fact due to the mixture. Pluronic® F-127 is a triblock copolymer consisting of a central hydrophobic block of polypropylene glycol and two outer hydrophilic blocks of polyethylene glycol (PEG). F-127 has previously been used as a

steric stabilizer in synthesizing PNIPAM microgels with increased biocompatibility for Doxorubicin release [286].

PS-PNIPAM Nanoprecipitation

PS-b-PNIPAM was dissolved in THF (good solvent) at varying concentrations. Around 500 µL of the block copolymer solution was introduced into 500 µL of Milli-Q water (antisolvent) under magnetic stirring at 300 pm either instantaneously or at 2 mL/hr, with the flow rate controlled by a syringe pump (PHD 2000, Harvard Apparatus, USA). The solution was stirred overnight to allow THF to evaporate before collecting the sample for washing and characterization.

Glass-Capillary Microfluidic Hydrodynamic Flow Focusing Device Fabrication

Microfluidic devices were fabricated on glass slides to which borosilicate glass capillaries with inner and outer diameters of 1100 and 1500 µm (World Precision Instruments, Inc.) were fixed with transparent epoxy resin (Epoxy, Devcon). Another borosilicate glass capillary with smaller diameters (inner and outer diameters of 560 and 1000 µm) was tapered using a micropipette puller (P-97, Sutter Instrument Co., USA) to a diameter of 10 µm. The diameter was then enlarged to 100 µm manually using fine sandpaper and confirmed with an optical microscope (EVOS XL, Life Technologies, Carlsbad, CA). The tapered capillary was inserted into the bigger capillary already glued to the glass slide and coaxially aligned with it. Figure 6.2 shows a schematic describing the coaxial geometry fabricated here. Then, the tapered capillary was fixed with epoxy. Injection needles were glued to the opening of the tapered glass capillary and to the entrance of the big glass capillary, such that the inner flow is introduced through the tapered capillary (good solvent) and the outer flow is introduced through the larger

capillary (antisolvent). Injection syringes (BD Luer-Lok syringe, 10 mL, and Terumo, 60cc Eccentric Luer Tip Syringe without Needle) and a syringe pump were used to introduce the flows to the channels at a constant flow rate. A MF-Millipore Membrane Filter, 1.2 µm pore size (Merck KGaA, Darmstadt, Germany) was used for the Terumo syringe to avoid micron-sized aggregates from flowing through the outer capillaries.

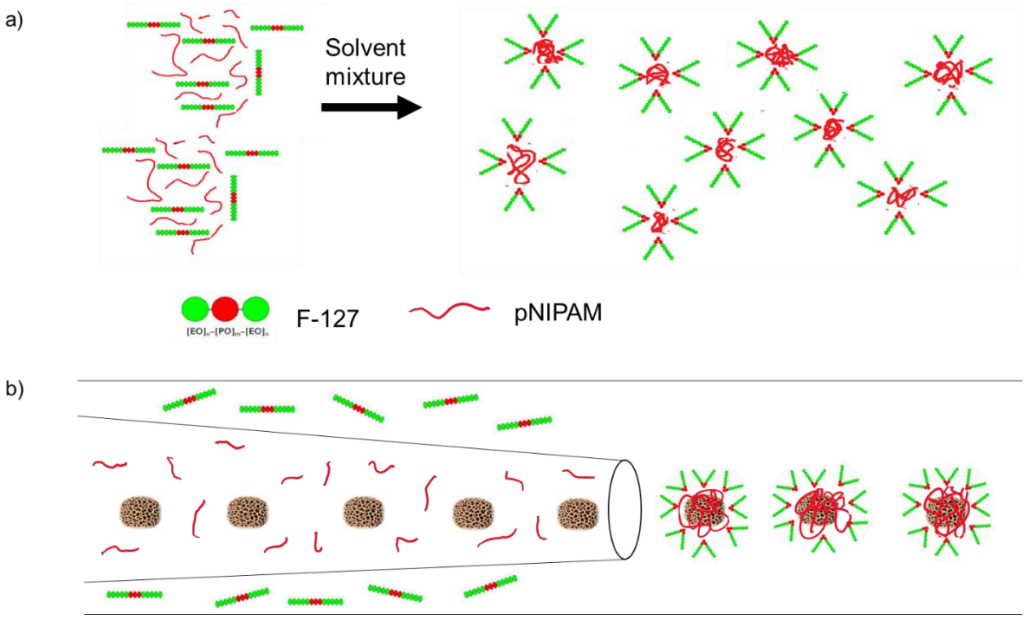

Figure 6.2 Schematic for pNIPAM nanoparticle formation by nanoprecipitation in bulk a) and pNIPAM encapsulation of PSi nanoparticles using microfluidics nanoprecipitation b). For both cases, the surfactant F-127 serves as a stabilizing agent in the water-ethanol solution mixture. *EtOH: Ethanol

Characterization

SEC of the PS-block was analyzed against PS standard to determine M_n, M_w and PDI. Measurements were performed with a Waters liquid chromatography system equipped with a Waters 2410 differential refractometer and a Waters 2487 UV as detectors. Three Styragel

columns (HR2, HR4, HR6) were used in series. HPLC-grade THF was used as an eluent with a flow rate of 0.8 mL/min at 35 °C. The NP size was measured in Milli-Q water using a Zetasizer Nano ZS (Malvern Instruments Ltd.). NP morphology and chemical analysis was confirmed by TEM (Jeol JEM-140, Jeol Ltd., Japan) and energy dispersive X-ray (EDX) spectroscopy. TEM samples were prepared by dropcasting 7 µL of a 100 µg/mL solution onto carbon-coated copper grids (300 mesh; Electron Microscopy Sciences, USA). Samples settled down for 5 min on the grid prior to removing excess liquid with filter paper.

Differential scanning calorimetry (DSC) thermograms were recorded using a calorimeter with an Indium reference for the temperature and heat flow rate (DSC 823e, Mettler Toledo, USA). A 40 µL volume of a 10 mg/mL solution of PNIPAM in Milli-Q water was pipetted into an aluminum pan and covered with an aluminum cover. Then the sample was heated from 25 to 50°C at 10°C/min linear heating rate with constant flow of nitrogen to create an inert environment. The data was evaluated by the STARe software.

6.3 Results

PNIPAM Synthesis and NP Formation

Initially, PNIPAM NPs were synthesized via nanoprecipitation. Figure 6.2 shows a schematic for the encapsulation of PSi nanoparticle with PNIPAM through nanoprecipitation with the co-nonsolvency method by bulk mixing (a) and microfluidics (b). Where PNIPAM precipitates in water and ethanol mixtures over a certain mixture range, the polymer chains were dispersed in ethanol and introduced to an aqueous solution containing 0.1 wt% Pluronic® F-127. The surfactant was expected to stabilize the PNIPAM NP structure. Specifically, upon precipitation the hydrophobic block of F-127 should interact with the PNIPAM and the

hydrophilic chains remain soluble in the aqueous solution through intermolecular forces such as hydrogen bonding.

A PNIPAM homopolymer was synthesized via free radical polymerization and purified by precipitating the polymer out in diethyl ether several times followed by centrifugation. The successful synthesis of the polymer was confirmed by NMR (Figure. 6.3a), DSC (Figure. 6.3b), and direct observation of the solution turbidity above the LCST (Figure. 6.3c). The broad peaks at chemical shifts δ= 1.5 ppm and 2 ppm correspond to the polymer backbone while at δ= 3.85 ppm there is a broad peak associated with the hydrogen adjacent to nitrogen. DSC (Figure 6.3b) confirmed a phase transition at 33 °C that is similar to what has been widely reported as the PNIPAM LCST (32 °C) [291], where the polymer chains begin to coil due to its increasing hydrophobicity.

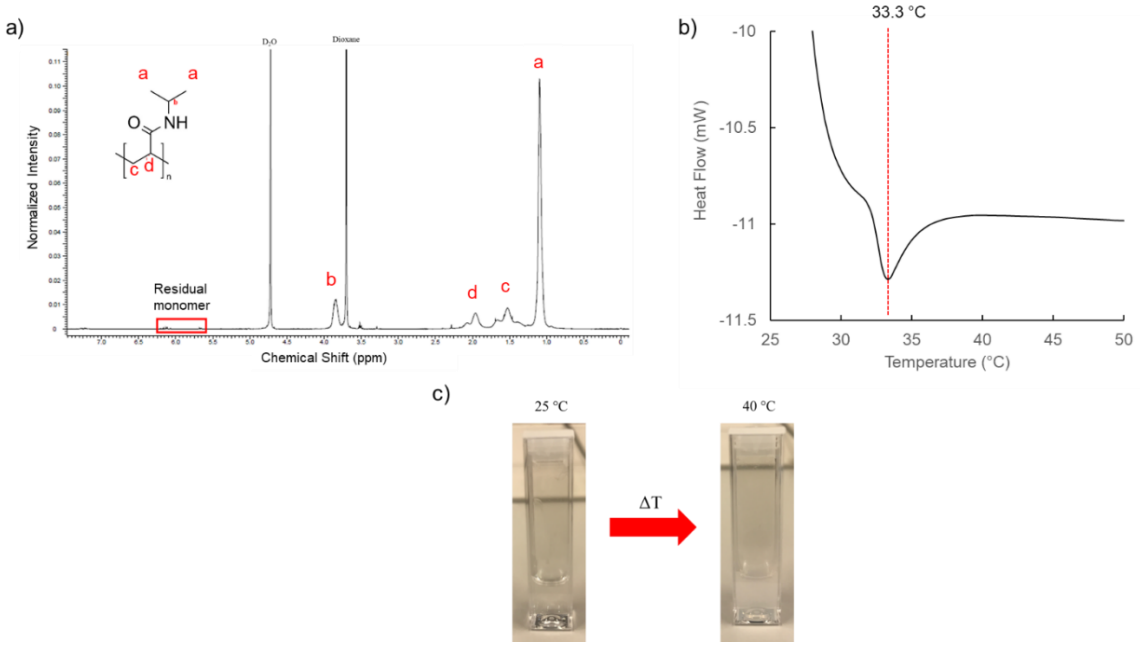

Figure 6.3 Characterization of pNIPAm formed by free radical polymerization with a) ^{1}H NMR and b) DSC. NMR clearly shows the chemical shifts associated with pNIPAM and DSC confirms the lower critical solution temperature of ~33 °C. c) Heating the polymer in water above the LCST shows a decrease in the polymer solubility.

The change in hydrophilicity is further corroborated by direct observation of the solution at temperatures below and above the LCST where changes in turbidity are evident. At room temperature the polymer is soluble in an aqueous solution and at 40 °C the solution appears turbid, which indicates the polymer's reduced solubility.

After synthesizing PNIPAM and demonstrating its thermoresponsive properties, the co-nonsolvency of PNIPAM with water, ethanol mixtures was confirmed (Figure 6.4b). PNIPAM was dissolved in ethanol and mixed with Milli-Q water, or an aqueous solution containing F-127 (0.1 or 1wt%) in a 1:1 ratio. Immediately upon mixing the two solutions, a white precipitate formed (Figure 6.4b) in comparison to pure ethanol mixed with a F-127 aqueous solution that did not form any precipitate.

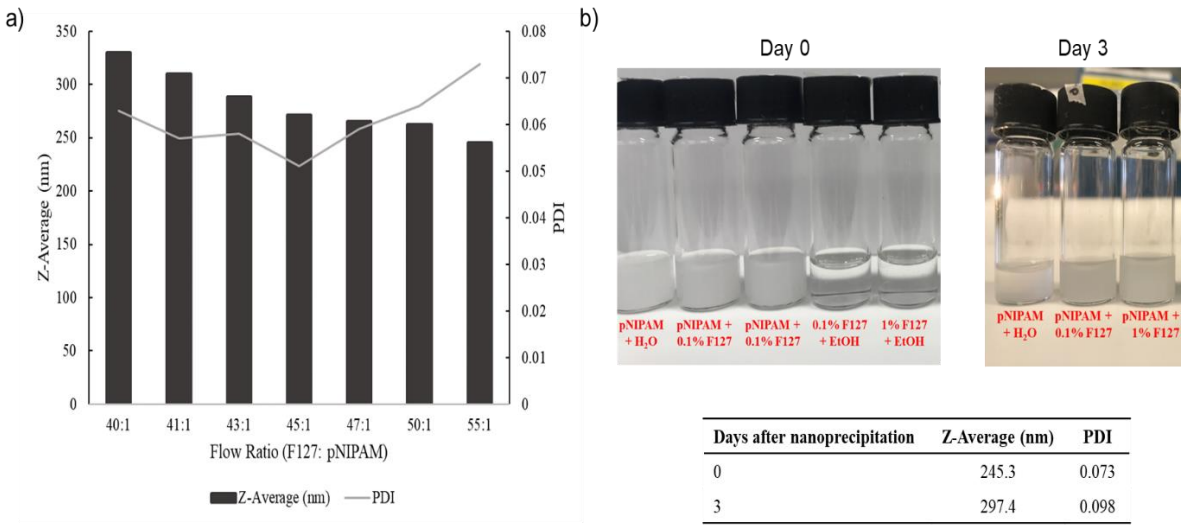

Days after nanoprecipitation	Z-Average (nm)	PDI
0	245.3	0.073
3	297.4	0.098

Figure 6.4 a) Z-average and PDI values for pNIPAM nanoparticles formed by microfluidics nanoprecipitation with aqueous F-127 as the outer solvent and varying outer: inner flow ratios. b) Stability of precipitation observed directly after mixing and 3 days after. Z-average and PDI of nanoparticles formed with an outer: inner flow ratio of 55:1 mL/h was assessed.

Thus, various mixtures confirm that F-127 is not required for the PNIPAM precipitation and that it is PNIPAM, rather than F-127, that precipitates out of these water-ethanol mixtures. After three days the PNIPAM mixture without F-127 surfactant had some phase separation while the

mixtures with surfactant remained homogeneous. PNIPAM precipitation by the co-nonsolvency method was applied to forming NPs via microfluidics in a similar manner shown in Figure 6.2 but without any PSi. The Z-average and PDI was assessed by DLS for NPs formed with varying outer: inner flow ratios (Figure 6.4a). As the flow ratio of the outer aqueous solution (0.1 wt% F-127) to the ethanol-containing polymer (2 mg/mL) increased from 40:1 to 55:1, the Z-average decreased by almost 100 nm. This observation agrees with previous reports that the particle size decreased with increasing Re [238]. Where Re is directly proportional to the fluid velocity, as the flow ratio increases the velocity and the Reynold's number increases. Therefore, the higher the Re, the faster the mixing rate between fluids, and consequently, the smaller the average particle size[339]. The NPs showed a slight increase in Z-average after 3 days, probably due to some aggregation but, overall, they possessed high stability (Figure 6.4b). The NP production reproducibility was investigated in different microfluidic chips with the same experimental parameters. The Z-average and PDIs were nearly identical. Therefore, the PNIPAM NP production is highly reproducible (Figure 6.5).

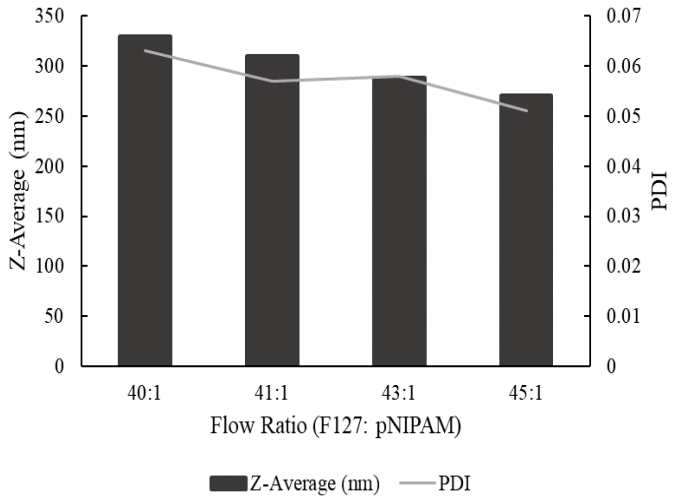

Figure 6.5 Reproducibility of Z-average and PDI values for pNIPAM nanoparticles with varying inner: outer flow ratios formed with a microfluidics chip fabricated on a different day.

TEM images assessed the morphology of PNIPAM NPs formed by microfluidics nanoprecipitation with a 55:1 flow rate (Figure 6.6). From n= 46 measurements using ImageJ the NPs had an average size of 107.8 ± 18.8 nm (Figure 6.6c). There is a discrepancy in average particle size between TEM and DLS (245.3 nm) measurements because DLS measures the hydrodynamic size, where swollen polymer chains in aqueous solution contribute to this size. We know that the NPs observed under TEM are not F-127 assembled into NPs because this copolymer tends to form micelles on the order of ~4-13 nm[340]. The single NP (Figure 6.6d) shows a ~10 nm outer layer, which is associated with the F-127 surfactant stabilizing the PNIPAM NP surface, as was proposed in Figure 6.2.

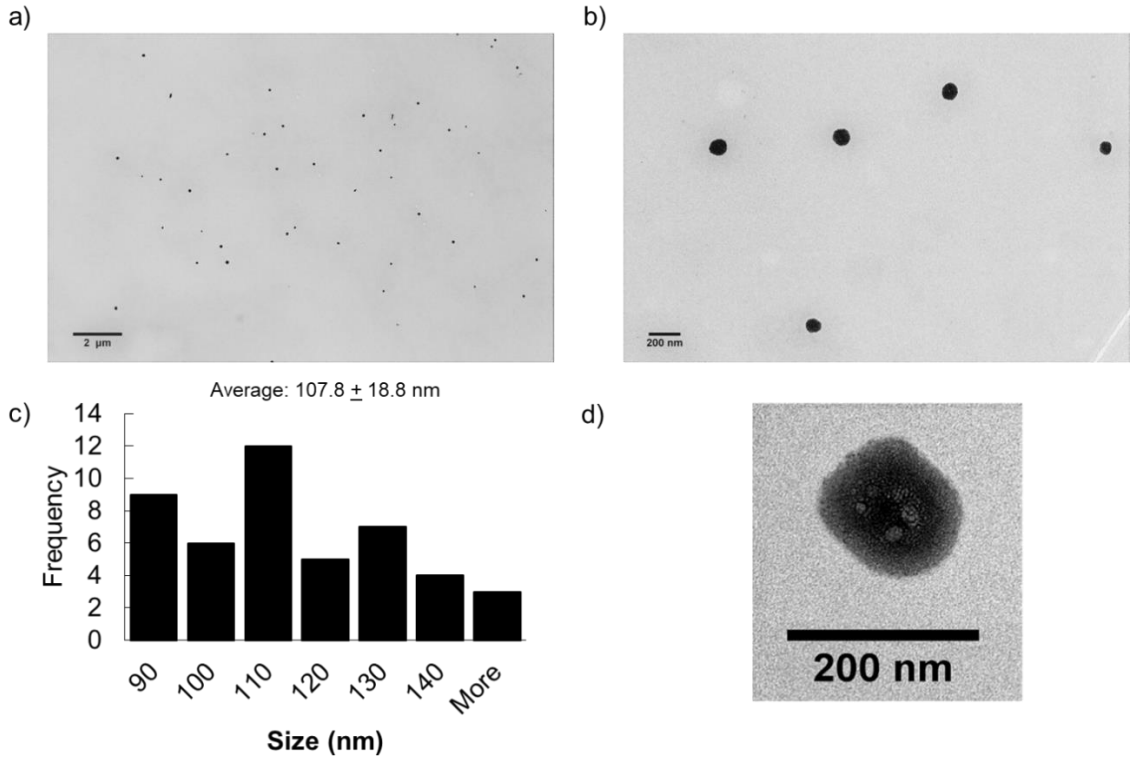

Figure 6.6 TEM images of pNIPAM nanoparticles stabilized by F-127 formed by microfluidics nanopreciptation with a 55:1 flow rate at lower a) and higher b) magnifications. c) Size distribution of the nanoparticles measured directly by TEM using ImageJ with n=46 measurements. d) Zoomed in TEM image of a pNIPAM nanoparticle showing an outer layer that is probably the F-127 stabilizer.

PSi Encapsulation by PNIPAM

After confirming the formation of PNIPAM NPs by microfluidics nanoprecipitation via the co-nonsolvency method, the precipitation was optimized, initially by bulk mixing, to encapsulate PSi NPs. TOPSi NPs were combined with PNIPAM in ethanol at various concentrations. The 'good solvent' solution was then added to a 0.1 wt% F-127 aqueous solution at an 8:2 ratio of bad solvent: good solvent. Figure 6.7a shows the Z-average and PDI measured by DLS for precipitated solutions with varying TOPSi and PNIPAM concentrations. Overall, the Z-average ranges between ~160- 200 nm. Given a diameter of 236 nm for TOPSi NPs alone, the Z-average of 160 nm for a PNIPAM: TOPSi ratio of 0.5: 0.5 mg/mL is perhaps a combined average of PNIPAM and TOPSi NPs, suggesting that encapsulation did not occur.

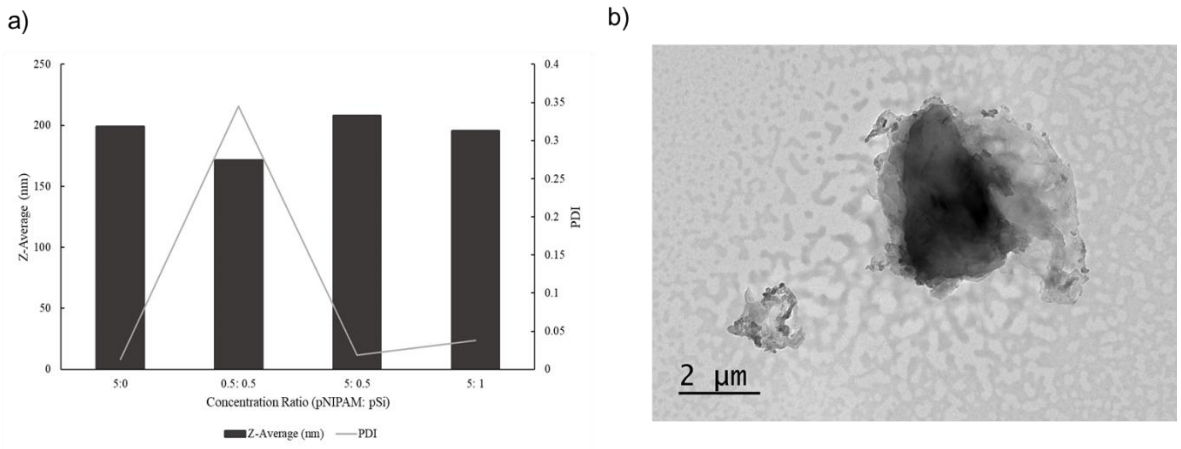

Figure 6.7 a) Z-average and PDIs for particles formed by precipitation via bulk mixing in a bad: good solvent ratio of 8: 2 with varying pNIPAM: PSi nanoparticle ratios in mg/mL. b) TEM images of bulk precipitation of 8:2 0.1 wt% $F127_{(aq)}$: 5 mg/mL pNIPAM, 0.5 mg/mL pSi.

The TOPSi NPs act as a seed for PNIPAM precipitation and encapsulation, and therefore we anticipate a Z-average slightly larger than the TOPSi NP size (236 nm, PDI 0.2). The solution with the largest Z-average and smallest PDI (5: 0.5 mg/mL PNIPAM: TOPSi) was further analyzed with TEM (Figure 6.7b), as DLS faces limitations of reporting an average of all NP population sizes and not discerning between PSi, PNIPAM, or encapsulated particles. The TEM

image shows micron-sized polymer clusters with TOPSi NPs embedded within the cluster. While encapsulation is occurring on a micron-level, well-defined encapsulated NPs are required for intravenous drug delivery applications. Moreover, dried free polymer is evident throughout the Formvar support film, indicating that either not all of the PNIPAM precipitates or as the solution evaporates on the Cu grid ethanol is evaporating faster which changes the overall solvent composition and may increase the solubility of PNIPAM during the drying process.

As previously mentioned, NP encapsulation with microfluidics tend to yield smaller NPs with lower PDI. Thus, we moved from bulk mixing to microfluidics to reduce the cluster size observed in bulk mixing (Figure 6.7b) and decrease the overall mixing time to promote TOPSi NP encapsulation. The inner flow 'good solvent' consisted of PNIPAM and TOPSi NPs with varying concentrations, while the outer flow contained 0.1 wt% F-127. Polymer precipitation onto the TOPSi surface was anticipated as the inner and outer solvents meet at the tapered end of the inner capillary. The Z-average and PDI of precipitated NPs with varying PNIPAM and TOPSi concentrations is shown in Figure 6.8, where the concentrations in Figure 6.8a and 6.8b vary from 10:1 to 1:1 mg/mL PNIPAM: TOPSi.

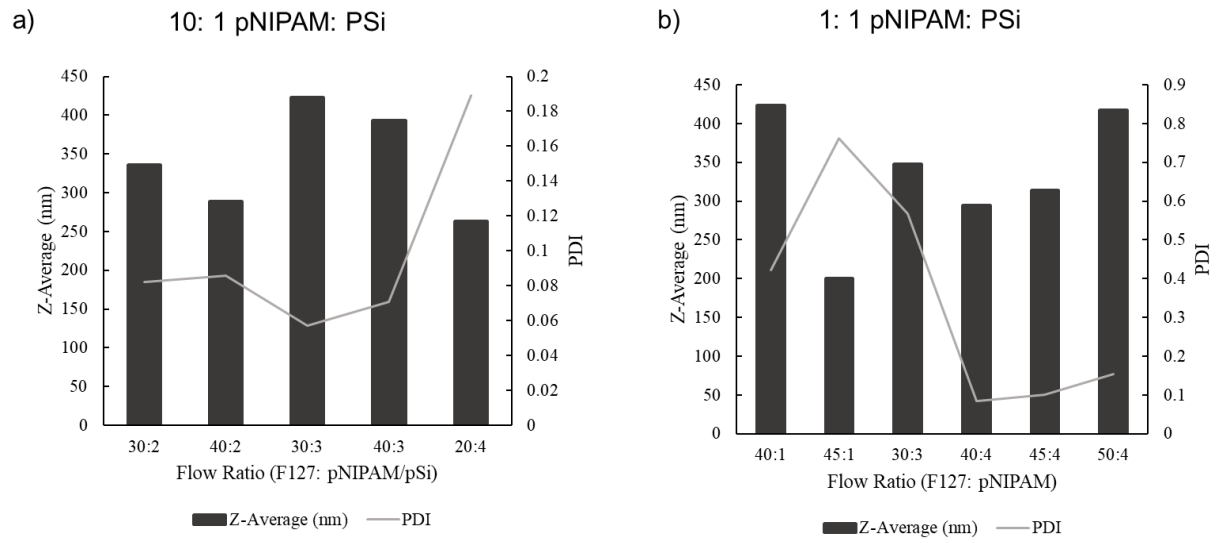

Figure 6.8 Z-average and PDI for pNIPAM encapsulation of PSi nanoparticles. The inner flow solution consisted of a a) 10:1 and b) 1:1 ratio of pNIPAM: PSi with a PSi concentration of 1 mg/mL. The outer flow solvent consisted of 0.1 wt% F-127 in Milli-Q water to stabilize the pNIPAM nanoparticle formation as it precipitates out of water-ethanol mixtures.

Higher outer flow rates observed in Figure 6.8a resulted in smaller Z-averages, which agrees with increasing Re. For example, as the inner: out flow ratio increases from 30:2 to 40:2 the Z-average decreased from 336 nm to 289 nm. Overall, it is difficult to determine a clear NP size trend as the PNIPAM concentration is decreased from 10 mg/mL to 1 mg/mL. When comparing NPs with the same outer: inner flow ratio (30:1) the Z-average decreased from 422 nm to 348 nm. This size decrease with decreasing polymer concentration has been previously observed with other polymer systems formed by nanoprecipitation. NPs with homopolymer cores (PS, polystyrene and PLA, polylactic acid) were stabilized with amphiphilic diblock copolymers (PS-b-PEG or PLA-b-PEG) by nanoprecipitation in microfluidic channels [299]. Smoluchowski diffusion-limited growth kinetics were used to describe the relationship between the homopolymer core and stabilizing block copolymer concentration, and the final NP radius. Moreover, this concept was also used to understand the encapsulation of inorganic colloids into polymeric NPs. Eqn. 6.6 is the average aggregate radius, R, as a function of time, t, for aggregates much larger than the starting material

$$R = \left(\frac{tk_bTc_{core}}{\pi\mu\rho}\right)^{1/3} \qquad \text{Eq. (6.6)}$$

where T is the absolute temperature, k_b is the Boltzmann constant, c_{core} is the mass concentration of the core material (homopolymer in this case), μ is the solvent viscosity, and ρ is the core material density[299]. Moreover, the time required for the formulation to reach the final radius, t_f, is also related to the concentration of the block copolymer (BCP) as shown in Eqn. 6.7.

$$t_f = K\frac{{c_{core}}^{2/3}}{c_{BCP}} \propto \frac{surface\ area\ of\ core}{surface\ area\ of\ BCP} \qquad \text{Eq. (6.7)}$$

where K is a single scaling constant value that is dependent on the material system being used. Combining Eqns. 6.6 and 6.7 yields

$$R = \left(\frac{tk_bT{c_{core}}^{5/3}}{\pi\mu\rho c_{BCP}}\right)^{1/3} \qquad \text{Eq. (6.8)}$$

The relationship between the block copolymer concentration and overall particle size in Eqn. 6.8 suggests that higher concentrations lead to smaller particle sizes. This relationship is due to the fact that particle growth is arrested by BCP coating the surface, so increasing the BCP concentration halts particle growth more quickly. However, this relationship is limited to systems where both the core and stabilizer are precipitated and undergoing assembly during mixing[299], while in this work, the PSi NP core does not undergo any assembly. Thus, if considering only the precipitating component (i.e. PNIPAM) and assuming that the core concentration is related to the precipitating polymer concentration, then the NP size will grow with increasing polymer concentration. TEM images (Figure 6.9) of PNIPAM and PSi with varying concentrations were taken to corroborate the relationship between PNIPAM concentration and particle size.

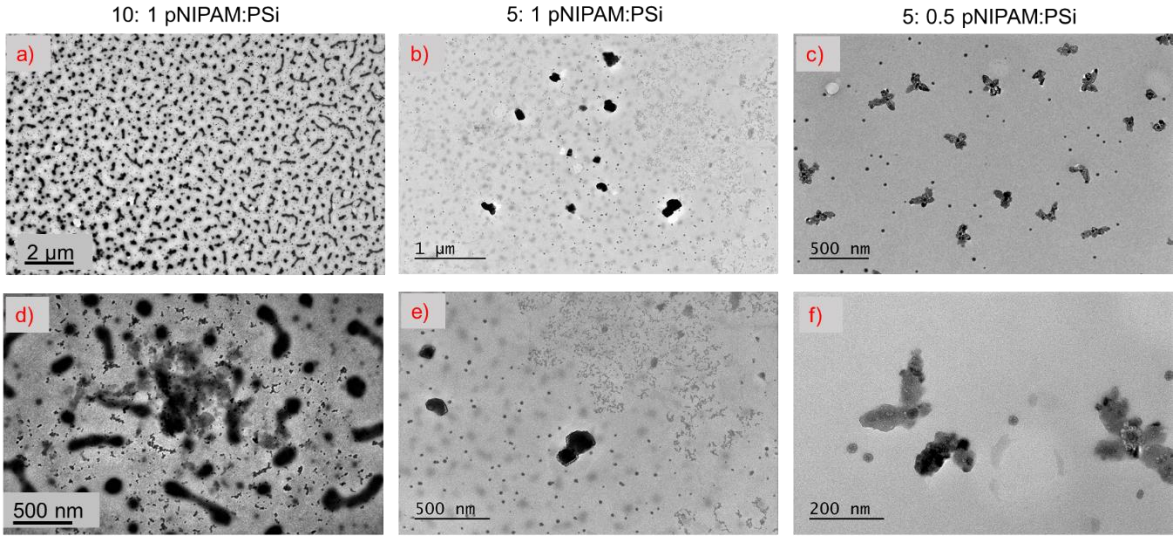

Figure 6.9 TEM images of pNIPAM nanoprecipitation by co-nonsolvency with microfluidics with a a,d) 10:1, b,e) 5:1, c,f) 5:0.5 pNIPAM: PSi ratio (with a PSi concentration of 1 mg/mL) and 40:2 outer: inner flow rate. The outer flow solvent consisted of 0.1 wt% F-127 in Milli-Q water to stabilize the pNIPAM nanoparticle formation as it precipitates out of water-ethanol mixtures.

The highest PNIPAM concentration (10 mg/mL, Figure 6.9a, d) had the largest particles, roughly ranging between 200 nm and 500 nm in diameter. These particles are ideal for encapsulating TOPSi NPs, but higher magnification images (Figure 6.9d) revealed TOPSi NPs outside the PNIPAM structures. Decreasing the PNIPAM concentration to 5 mg/mL (Figure 6.9b, e) showed an overall decrease in size and particle density on the surface. There is a combination of free polymer that has been dissolved during sample preparation drying for TEM, F-127 micelles, and several 200- 500 nm sized particles that could potentially have TOPSi inside granted there was no free TOPSi near these particles. Decreasing the TOPSi concentration from 1 mg/mL to 0.5 mg/mL (Figure 6.9c, f) revealed polymer nanostructures and F-127 micelles, but the TOPSi NPs were not encapsulated within the polymer. Given the promising TEM images shown in Figure 6.8b, this sample was analyzed by EDX (Figure 6.10) to confirm whether TOPSi was residing within the nanostructure.

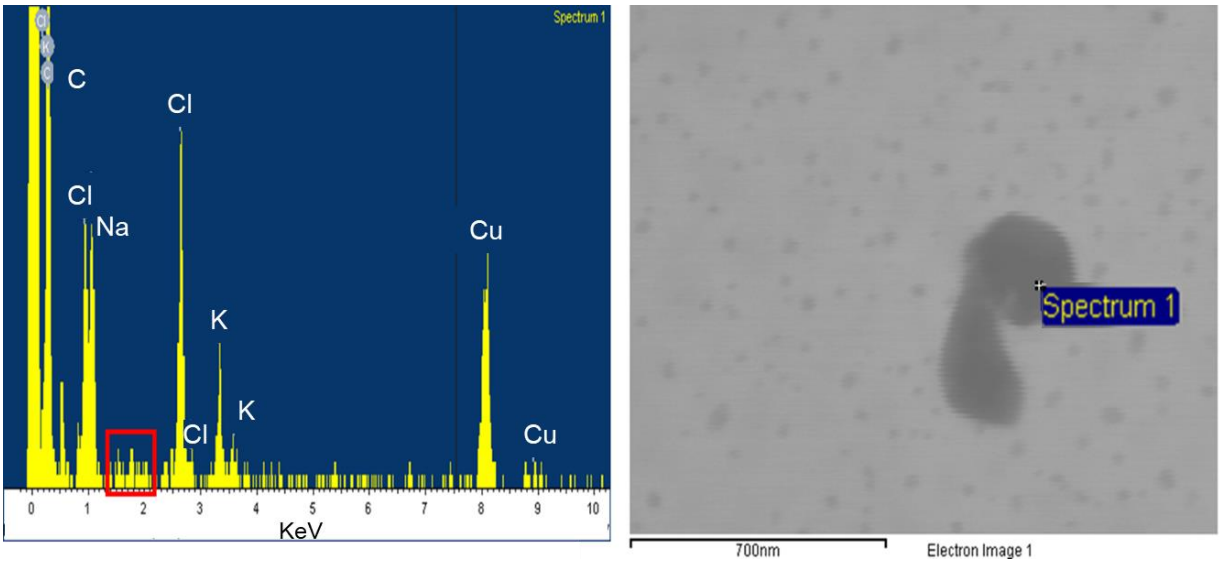

Figure 6.10 EDX spectrum and corresponding SEM image of nanoprecipitated pNIPAM to determine whether PSi is encapsulated inside. A 5:1 mg/mL pNIPAM: PSi ratio with 0.1 wt% F127 surfactant in the outer fluid and outer: inner fluid ratio of 40:2 was used.

An EDX spectrum corresponding to a point on one of these structures did not reveal any Si. The K_α Si peak did not appear for several point spectra, indicating that TOPSi NP encapsulation by PNIPAM was not successful. While it appears that the polymer is successfully precipitating out of the solution using the co-nonsolvency principle, we hypothesized that TOPSi encapsulation was not successful, because the polymer would precipitate onto a hydrophobic surface that acts as a seed. If the core material is hydrophilic and remains soluble after introducing the antisolvent then the polymer would not preferentially precipitate on the core surface [300–302]. In Chapter 3 the fabrication of hydrophobic PSi surfaces via a thermal carbonization treatment (THCPSi) was discussed. In the following section THCPSi was used for PNIPAM encapsulation via microfluidics nanoprecipitation.

THCPSi Encapsulation by PNIPAM

The varying THCPSi NP and PNIPAM concentrations determined whether the presence of a hydrophobic core promotes encapsulation and polymer precipitation onto PSi. The PNIPAM

concentration was decreased from 5 mg/mL to 0.5 mg/mL and the THCPSi concentration was decreased from 1 mg/mL to 0.5 mg/mL. Figure 6.11 shows the Z-average and PDI for a system with an inner flow solution of 5: 0.5 PNIPAM: THCPSi at varying outer: inner flow rates.

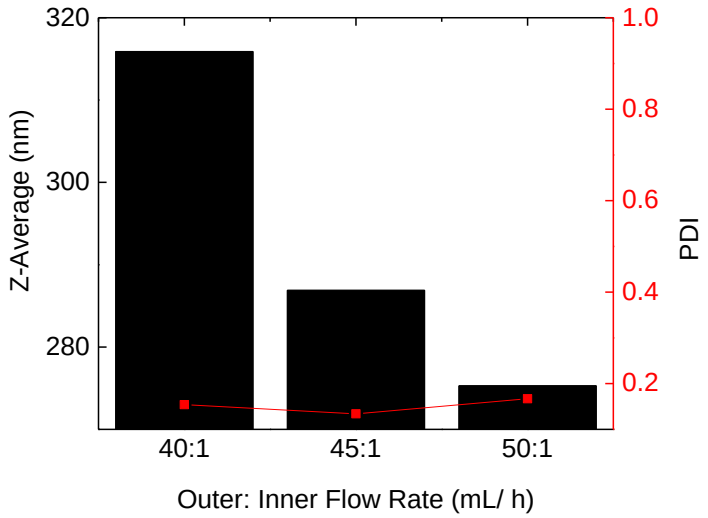

Figure 6.11 Z-average and PDI of THCPSi and pNIPAM nanoparticles precipitated by the co-nonsolvency with microfluidics with a 5:0.5 PNIPAM: THCPSi ratio (with a PSi concentration of mg/mL) and 40:2 outer: inner flow rate. The outer flow solvent consisted of 0.1 wt% F-127 in Milli-Q water to stabilize the pNIPAM nanoparticle formation as it precipitates out of water-ethanol mixtures.

As observed in previous outer: inner flow rate optimizations, the Z-average decreased from 316 nm to 275 nm as the ratio increased from 40:1 to 50:1. Overall, the Z-averages are comparable to those observed for encapsulation optimizations done with TOPSi (Fig. 6.8). Given a Z-average of 200 nm for the bare THCPSi NPs, the >200 nm Z-averages for all flow ratios is an indicator of encapsulation. The effect of PNIPAM on THCPSi concentration changes on the overall morphology and encapsulation was observed by TEM (Figure 6.12). All concentration variations in Figure 6.12 had a 40:2 outer: inner flow ratio.

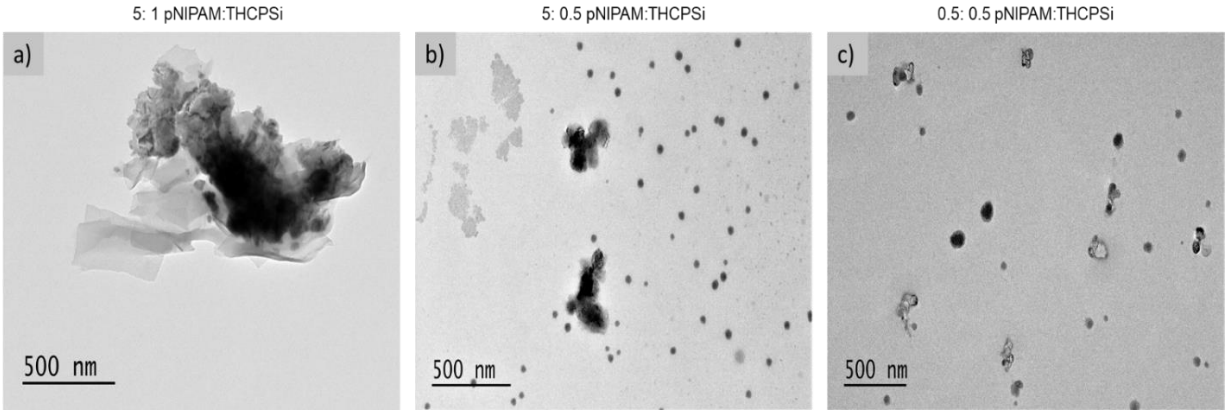

Figure 6.12 TEM images of pNIPAM nanoprecipitation by co-nonsolvency with microfluidics with a 5:1 a), 5:0.5 b), and 0.5:0.5 c) pNIPAM: THCPSi ratio (with a PSi concentration of mg/mL) and 40:2 outer: inner flow rate. The outer flow solvent consisted of 0.1 wt% F-127 in Milli-Q water to stabilize the pNIPAM nanoparticle formation as it precipitates out of water-ethanol mixtures.

At a concentration ratio of 5: 1 mg/mL PNIPAM: THCPSi (Fig. 6.12a) larger particles (~1 μm) were observed and based on the contrast difference in the particle center it appears that THCPSi NPs are encapsulated. Moreover, based on the size of this contrast difference (~550 nm) it could be that there is an aggregate of THCPSi NPs at the center. As the THCPSi concentration decreases from 1 mg/mL to 0.5 mg/mL (Fig. 6.12b) encapsulation is apparent based on the contrast difference within the particles. However, the overall particle size decreases (with sizes between ~250- 500 nm) probably since there are less THCPSi NPs to aggregate. The round NPs in Fig. 6.12b represent dimensions typical of F-127 micelles (~10 nm). As the PNIPAM concentration decreases from 5 mg/mL to 0.5 mg/mL (Fig. 6.12c) no encapsulation is observed, probably because as the PNIPAM concentration decreases 10-fold there is less polymer to precipitate on the THCPSi surface. Using Eqn. 6.8 the diffusion-limited growth kinetics from other systems can be applied to predict how the final radius varies with precipitating polymer concentration. Given the precipitated particle radius is proportional to $c^{2/9}$ (assuming that $c_{BCP}= c_{core}$), a 10-fold concentration decrease results in a 60% decrease in the radius. Thermodynamically, there PNIPAM concentration is high enough to produce a supersaturated

solution that results in precipitation, as F-127 stabilized PNIPAM nanostructures on the order of 100 nm are observed. Thus, at lower concentrations there is the preferential formation of PNIPAM NPs rather than precipitation on THCPSi NP surfaces. Overall, we observe that the presence of a hydrophobic NP surface is a crucial 'seed' that allows for encapsulation to occur. While encapsulation is more evident with the THCPSi NPs in comparison to TOPSi NPs, these encapsulated structures are not stable in aqueous solution once the ethanol is removed. When the nanostructures are dispersed in an aqueous-based solution the PNIPAM will dissolve into the solution (since ethanol is not present anymore to precipitate the polymer), leaving the PSi NPs exposed. Therefore, these nanostructures are not suitable for drug delivery applications where the encapsulant will dissolve upon exposure to aqueous-based biological fluids. One way to circumvent this dissolution is by encapsulating the THCPSi with a di-block copolymer chain with amphiphilic properties. Amphiphilic di-block copolymer chains have been extensively studied for the fabrication of polymeric NPs by nanoprecipitation[300,301,303,320]. However, using this principle to encapsulate PSi NPs with a thermoresponsive polymer has yet to be demonstrated.

THCPSi encapsulation was optimized with PS-PNIPAM di-block copolymers of varying molecular weights. A PS hydrophobic block was utilized, because of the extensive work reported on PS-based block co-polymers for polymer NP formation by nanoprecipitation[299,303,320]. Moreover, previous research on PS-PNIPAM di- and tri-block copolymers demonstrated films and polymeric NPs formed by an aerosol flow reactor [337,341–343]. In this reactor, the block copolymer self-assembly is induced by initial solvent evaporation and subsequent thermal annealing. Prud'homme's nanoprecipitation were combined with the aerosol reactor's solvent evaporation step to increase the antisolvent (water) concentration and promote the copolymer

self-assembly. We proposed a system where THCPSi and PS-b-PNIPAM were dissolved in the solvent tetrahydrofuran (THF), which is miscible with hydrophobic molecules. As water is added to the solution, the hydrophobic THCPSi and PS component of the block copolymer simultaneously precipitate while the hydrophilic PNIPAM remains stable in the aqueous portion. The relatively low boiling point of THF (65 °C) allows the solvent to readily evaporate when left overnight. As the solvent evaporates, the hydrophobic components further precipitate and the PS block self-assembles onto the THCPSi surface. Figure 6.13 shows a schematic of the THCPSi encapsulation with PS-b-PNIPAM by bulk mixing (Fig. 6.13a) and microfluidics (Fig 6.13b).

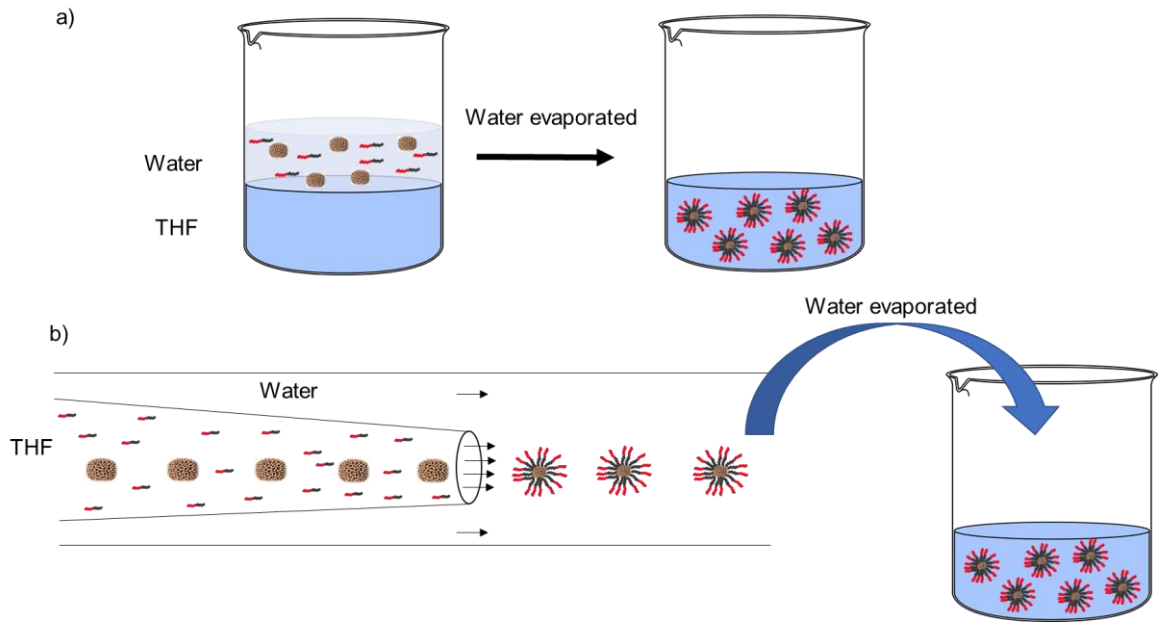

Figure 6.13 Schematics showing the formation of PSi-encapsulated PS-pNIPAM nanoparticles via nanoprecipitation in the bulk a) and using microfluidics b). After the antisolvent (water) induces nanoprecipitation, THF is evaporated from the solution to further decrease the solubility and maintain the stability of these nanoparticles.

Three block copolymers were synthesized with varying PS and PNIPAM block lengths, as shown in Table 6.4. 19PS1PNIPA2 has the short PS and PNIPAM blocks (based on molecular weight), 19PS2PNIPA2 has a longer PS and intermediate PNIPAM block, and 19PS2PNIPA1

has a long PS and long PNIPAM blocks. Table 6.5 summarizes the block copolymers synthesized and the relative block lengths.

Table 6.5 Summary of block copolymers and their relative block lengths.

Polymer	M_n PS-block	M_n PNIPAM-block
19PS1PNIPA2	Short	Short
19PS2PNIPA2	Long	Intermediate
19PS2PNIPA1	Long	Long

Optimizations were initially carried out in bulk mixing of varying block copolymer, THCPSi NP ratios, as shown in Figure 6.14.

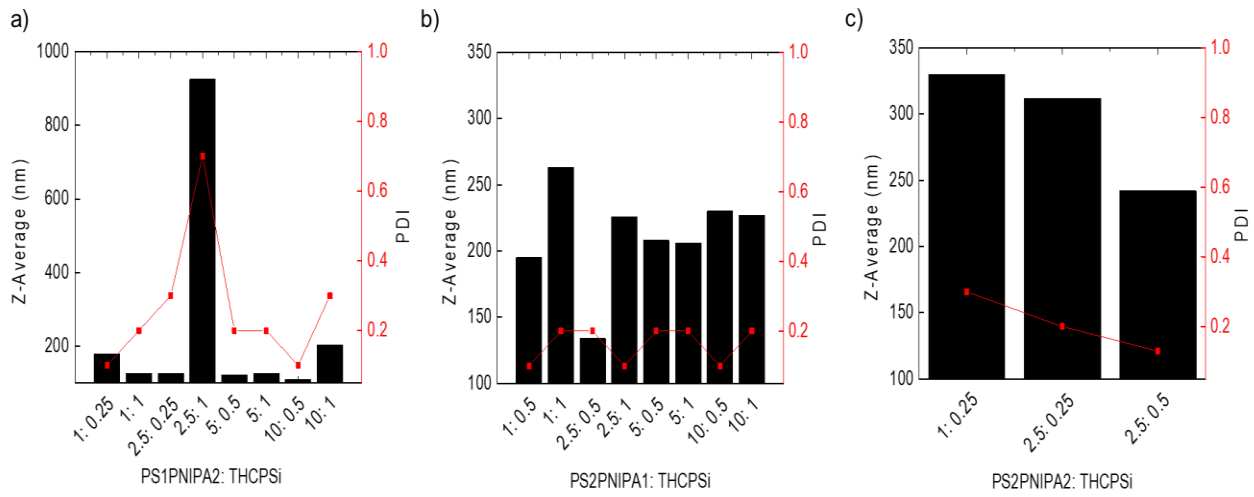

Figure 6.14 Z-average and PDI of THCPSi and PS-pNIPA nanoparticles mixed at different ratios and precipitated with bulk mixing. The PS-pNIPAM vary in molecular weights and the following samples are used: a) PS1PNIPA2, b) PS2PNIPA1, and c) PS2PNIPA2.

The 19PS1PNIPA2 (Figure 6.14a) and 19PS2PNIPA2 (Figure 6.14b) concentration was varied from 1 mg/mL to 10 mg/mL. The 19PS2PNIPA1 (Figure 6.14c) was varied from 1 mg/mL to 2.5 mg/mL. Overall, the PS2PNIPA2, THCPSi mixtures have the highest Z-averages, while 19PS1PNIPA2 mixtures have the lowest Z-averages. Prud'homme's model for nanoprecipitation of PS-b-PEG and PLA-b-PEG (Eq. 6.6-8) proposed that NP growth rate is independent of the molecular weight of the hydrophobic core. Moreover, PS-b-PNIPAM-b-PS tri-block copolymer

NPs observed that as the molecular weight and wt% PNIPAM increased, the mean NP diameter did as well. Given that Prud'homme's model holds for other PS block copolymer systems, we attribute the increase in Z-average to the increase in the PNIPAM molecular weight. Consequently, 19PS2PNIPA1should have the largest Z-averages, yet intermediate Z-averages are observed. A similar phenomenon was observed and attributed to variations in morphology (spherical versus gyroid-like), which can affect the extent of particle swelling[317,343]. Figure 6.15 shows TEM images of 2.5 mg/mL PS1PNIPA2 (Figure 6.15a) and PS2PNIPA1 (Figure 6.15b) precipitated with 0.5 mg/mL THCPSi via bulk mixing with the 'good' solvent addition to the antisolvent at a flow rate of 2 mL/h.

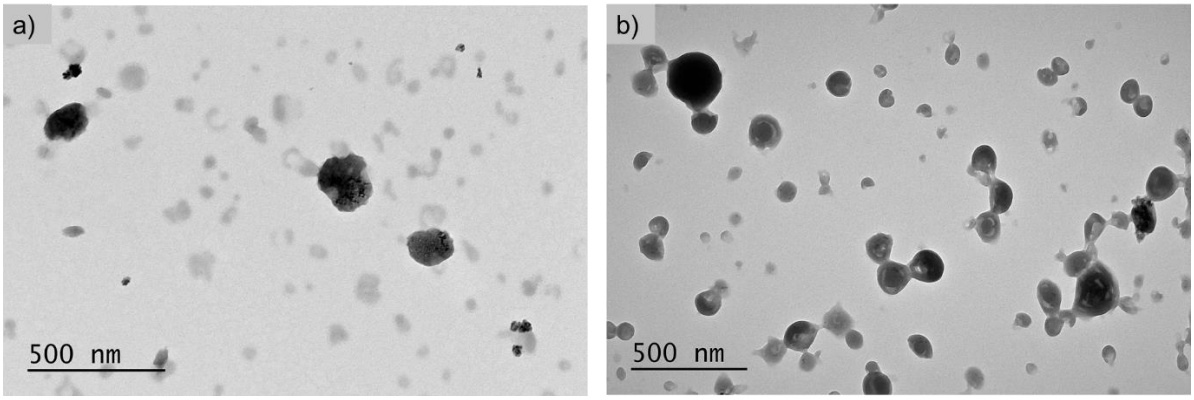

Figure 6.15 TEM images of nanoparticles formed by bulk mixing nanoprecipitation with a PS-pNIPAM: THCPSi ratio of 2.5: 0.5 (mg/mL) where the good solvent is introduced into the antisolvent at a rate of 2 mL/hr. The polymer chain molecular weight varies for precipitation with a) PS1PNIPA2 and b) PS2PNIPA1.

For encapsulation with PS1PNIPA2, less NPs were formed and more PNIPAM dissolved on the grid film. In contrast, the PS2PNIPA1 mixture, which has a diblock length twice the size, contained more well-defined spherical NPs and less dissolved polymer. These observations are in agreement with the di-block structure, which has a shorter hydrophobic block that results in a more hydrophilic block copolymer and, therefore, a nanostructure that is less stable in aqueous solution. The darker contrast inside the nanostructures in Figure 6.15 indicates THCPSi encapsulation. Moreover, Figure 6.15b demonstrates NPs that are both empty and encapsulated

with THCPSi based on the contrast differences, where darker contrast represents encapsulated NPs while lighter contrast particles do not contain any encapsulated material.

The Z-averages were then determined for particles that were left stirring overnight for THF to evaporate. The Z-average for a mixture containing PS1PNIPA2 at various concentrations was analyzed after THF evaporation. Overall, with THF evaporation the Z-average decreased (Figure 6.16a) in comparison to the size before THF evaporation (Figure 6.14b).

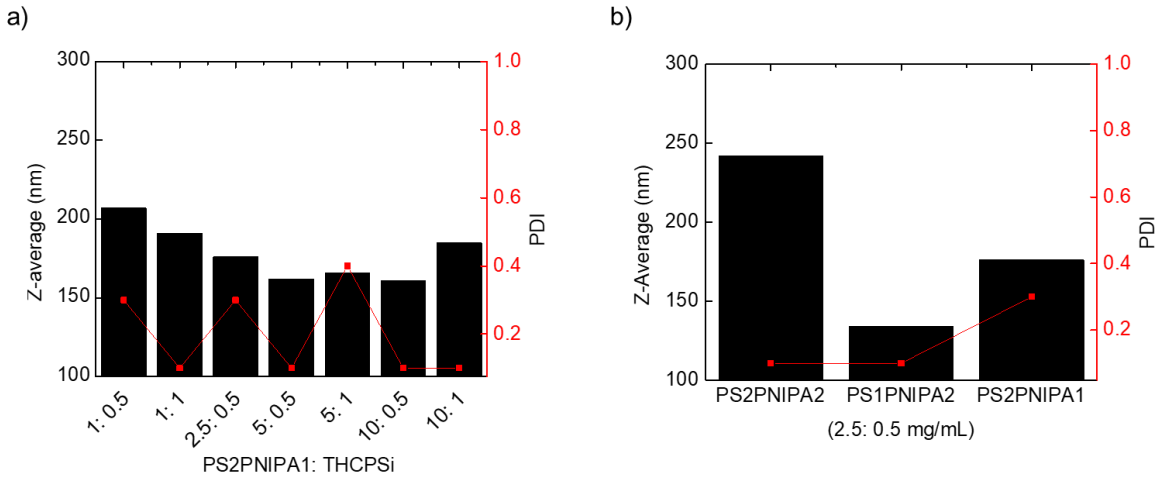

Figure 6.16 Z-average and PDI of THCPSi and PS-pNIPA nanoparticles a) mixed at different ratios or with polymers of varying molecular weights and b) precipitated with bulk mixing. The samples were left stirring overnight to evaporate any THF in the solution.

A decrease in particle size is anticipated, whereas the THF evaporates the PS block becomes less soluble and further precipitates out of the solution. Consequently, the copolymer undergoes further self-assembly and the particle swelling is expected to decrease. When comparing the block copolymers with varying PS- and PNIPAM- block lengths at a polymer: THCPSi concentration ratio of 2.5: 0.5 mg/mL (Figure 6.16b), the polymer with a ‘long’ PS block and ‘intermediate’ PNIPAM block (PS2PNIPA2) demonstrated the largest Z-average. PS2PNIPA1 (‘long’ PS- and PNIPAM blocks) had intermediate Z-averages and PS1PNIPA2 (‘short’ PS- and PNIPAM- blocks) had the smallest Z-averages. These size trends are similar to those observed

before THF evaporation. Overall, PS2PNIPA2 did not observe any significant size change before and after THF evaporation. While the PS-block is expected to self-assemble with THF evaporation, the longer PNIPAM chain (in comparison to PS2PNIPA1) becomes more soluble once the THF is evaporated and results in chains with increased swelling. TEM images of the particles formed by bulk mixing and THF evaporated are shown in Figure 6.17.

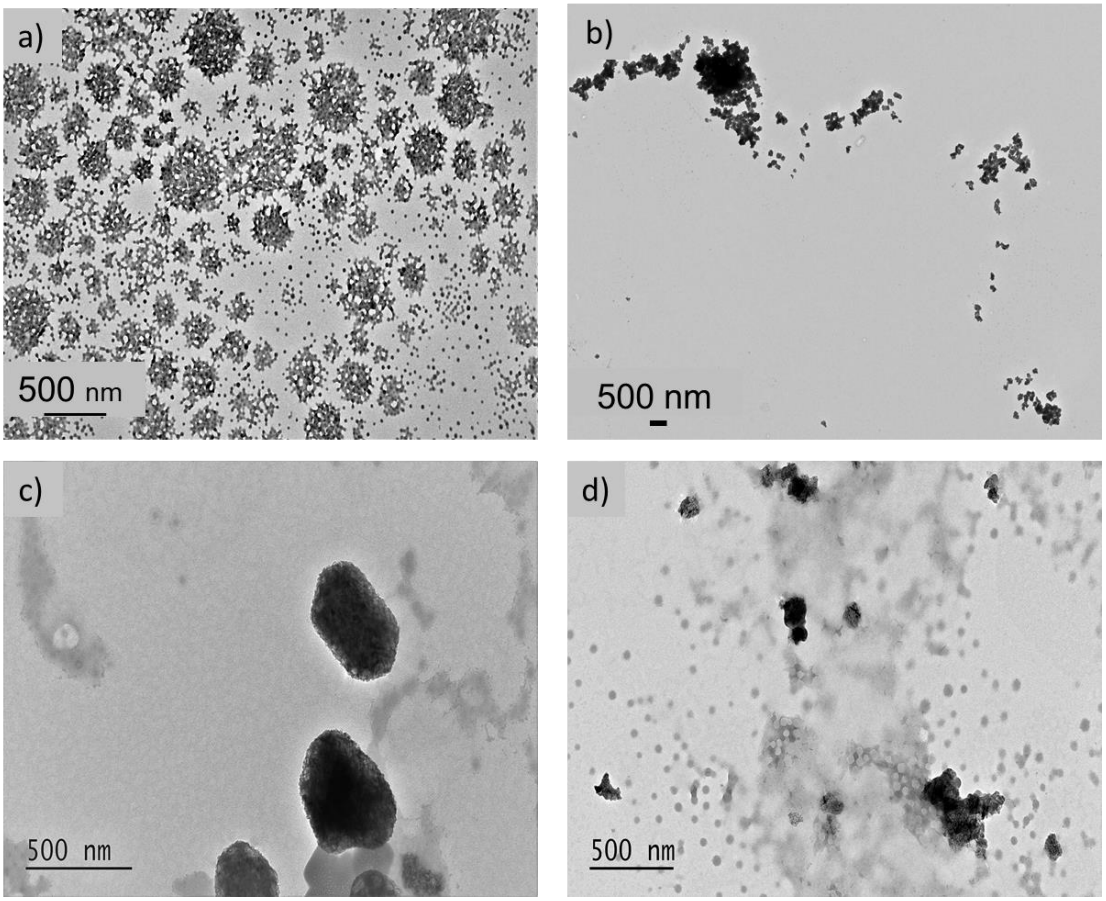

Figure 6.17 TEM images of THCPSi and PS-PNIPAM nanoparticles mixed at different ratios or with polymers of varying molecular weights and precipitated with bulk mixing. a) PS1PNIPA2: THCPSi 2.5: 0.5 mg/mL b) PS2PNIPA1: THCPSi 2.5: 0.5 mg/mL c) PS2PNIPA2: THCPSi 2.5: 0.5 mg/mL d) PS2PNIPA2: THCPSi 2.5: 1 mg/mL. The samples were left stirring overnight to evaporate any THF in the solution.

For particles formed with a 'short' PS- and PNIPAM-block (PS1PNIPA2) the NPs form a porous structure after THF evaporation, when compared to particles before THF evaporation (Figure 6.15a). For a 'long' PS- and 'intermediate' PNIPAM-block (PS2PNIPA2, Figure 6.17b) no

polymeric nanostructures or encapsulation was observed. Figures 6.17c and 6.17d show THF-evaporated nanostructures formed from ‘long’ PS- and ‘intermediate’ PNIPAM- block lengths (PS2PNIPA2) with varying THCPSi concentration (0.5, 1 mg/mL). With a THCPSi concentration of 0.5 mg/mL (Fig. 6.17c), self-assembled nanostructures were formed with THF evaporation. However, it is difficult to cconfirm whether THCPSi was encapsulated, and further chemical analysis by EDX is required. As the THCPSi concentration increases to 1 mg/mL, the overall NP size decreases by around half, and the morphology does not appear as rigid, or well-defined. Rather, the THCPSi NPs appear as partially encapsulated, and the amount of dissolved polymer is more evident. After confirming the formation PS-b-PNIPAM NPs and the ability to encapsulate THCPSi NPs with the polymer via bulk mixing, this nanoprecipitation technique was investigated with microfluidics.

Nanoprecipitation principles were applied to a microfluidics system for fabricating THCPSi NPs encapsulated by a PS-b-PNIPAM block copolymer. Figure 6.12b shows a schematic for the formation of polymer encapsulated NPs using a microfluidic chip. The inner capillary consists of THCPSi and the block copolymer dissolved in the ‘good solvent’, THF. The outer capillary contains the ‘antisolvent’, Milli-Q water. As the inner and outer solutions meet at the inner capillary tapered end, precipitation of the PS-block is expected on the THCPSi surface. Microfluidics is advantageous because the rapid mixing during nanoprecipitation results in controlled nucleation rates and, ultimately, a narrower size distribution. The three polymers previously used for optimizations with bulk mixing (PS1PNIPA2, PS2PNIPA1, PS2PNIPA2) were used for microfluidics optimization. The block copolymer and THCPSi concentrations in the inner capillary were varied, and the Z-average is shown for PS1PNIPA2 (Figure 6.18a), PS2PNIPA1 (Figure 6.18b), and PS2PNIPA2 (Figure 6.18c).

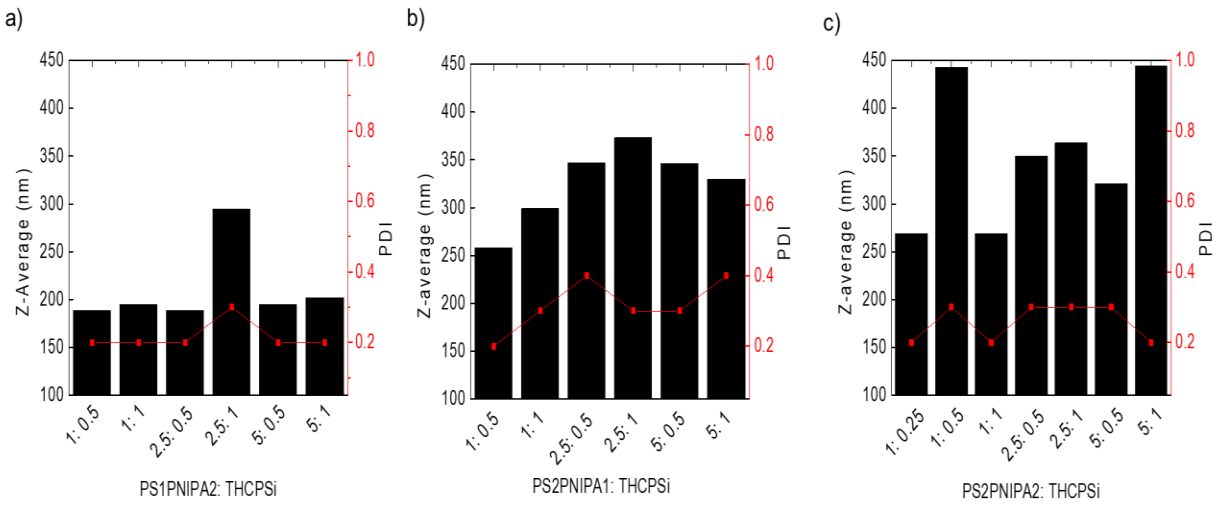

Figure 6.18 Z-average and PDI of THCPSi and PS-pNIPA nanoparticles mixed at different ratios and precipitated using microfluidics. The PS-pNIPAM vary in molecular weights and the following samples are used: a) PS1PNIPA2, b) PS2PNIPA1, and c) PS2PNIPA2.

Overall, the Z-averages for all solutions formed with microfluidics are higher than those formed with bulk mixing, which is surprising granted that microfluidics is expected to yield smaller particle sizes. However, the overall larger Z-averages could potentially indicate more efficient THCPSi encapsulation, but TEM images are needed to corroborate encapsulation. Overall, the 'long' PS- and 'intermediate' PNIPAM-block (PS2PNIPA2) demonstrated the highest Z-averages. The 'long' PS- and PNIPAM-block (PS2PNIPA1) demonstrated intermediate Z-averages and the 'short' PS- and PNIPAM- blocks exhibited the lowest Z-averages. This size trend for the different PS and PNIPAM block lengths is the same as that observed for bulk mixing. Therefore, there is a consistent trend in the overall NP size for the block copolymers with varying PS and PNIPAM block lengths in bulk mixing and microfluidics. TEM images of the samples formed by microfluidics need to confirm whether the higher Z-averages correspond to a higher THCPSi NP encapsulation efficiency. Moreover, TEM images will be crucial for observing any morphology changes as the PS and PNIPAM block lengths vary.

6.4 Conclusion

Physical encapsulation is a promising alternative to chemically conjugating stimuli-responsive polymers onto PSi NP surfaces for controlled drug delivery applications. Specifically, nanoprecipitation is a quick, reproducible solvent-switching method that can form stimuli-responsive encapsulated PSi on the order of seconds versus several days that are typical of chemical conjugation. The key requirements for NP formation by nanoprecipitation is that the polymer is initially dissolved in a compatible or 'good' solvent and upon introduction of an incompatible or 'bad' solvent the NP precipitates out of the solution. Moreover, in the presence of PSi NPs with similar solvent compatibilities as the precipitating polymer, the polymer will precipitate onto the PSi NP surface. F-127 stabilized PNIPAM NPs were formed with an average size of 107.8 $\pm$ 18.8 nm. The themoresponsive NPs were precipitated using the co-nonsolvency in a microfluidics system. Encapsulation of TOPSi NPs with PNIPAM using the same nanoprecipitation principles was unsuccessful because TOPSi is highly soluble in water (the 'bad' solvent in this case) and therefore the PNIPAM self-assembly was preferred over precipitating onto the dissolved TOPSi NP surface. PSi NPs with a hydrophobic surface (THCPSi) were then used for encapsulation optimizations to promote the PNIPAM precipitation onto the NP surface. Varying the surface hydrophilicity did result in the encapsulation of THCPSi NPs with PNIPAM. However, these particles are only stable in water-ethanol mixtures where the PNIPAM remains insoluble. Therefore, when this system is redispersed in an aqueous solution, the PNIPAM solubility increases and the encapsulant layer dissolves. Given the need for formulations with aqueous solution stability, the amphiphilic block copolymer PS-b-PNIPAM was applied to promote encapsulation and aqueous stability by precipitating the PS-block onto the THCPSi NP surface. While this simple and facile encapsulation technique was

demonstrated in bulk mixing, further characterization is required to determine whether a microfluidics fabrication approach yields improvements in PSi encapsulation efficiency and size distribution. Moreover, drug release studies at various temperatures and cell viability studies will need to be compared to PSi NPs chemically conjugated with PNIPAM. Overall, nanoprecipitation has the potential to overcome fabrication challenges typically associated with streamlined manufacturing towards the clinical translation of nanocomposites.

Chapter 7. Future Work and Conclusion

Overall, this dissertation developed a magnetic PSi nanocarrier system comprised of cost-effective, highly scalable materials to overcome fabrication and cost challenges in scale-up and manufacturing of nanomedicines. A thermoresponsive release was established by the electrostatic removal of Fe_3O_4 caps as the PSi surface is hydrolyzed. This thermoresponsive behavior was used to improve the delivery of the poorly water-soluble drug SFN. The biocompatibility and cellular interactions of the magnetic PSi nanocarrier system was confirmed with various cancer cell and macrophage lines. Moreover, the controlled, thermoresponsive release translated to an increase in anticancer activity in two cancer cell lines. Thus, by applying temperature to the magnetic nanocomposite the anticancer activity can be readily tuned.

First, this work broadly reviewed the current state of nanomedicine in research and the clinic. The theories of PSi fabrication by electrochemical etching and the relationship between experimental parameters and PSi morphology were surveyed. The synthesis and application of magnetic NPs in targeted drug delivery applications was discussed. This review provided a theoretical and experimental foundation for designing a magnetic thermoresponsive nanocarrier. In Chapter 3, the formation of a magnetic PSi nanocomposite with high efficiency and scalability is reported. PSi layers were fabrication via electrochemical etching, with a 3-step current density gradient formation. The layer size, and therefore amount of PSi produced, was readily tuned by the Si wafer exposed area. By increasing the exposed etching surface area, the amount of PSi fabricated was readily scaled by more than 30x (from ~13 mg to ~400 mg per run). PSi NPs were formed via a top-down approach, where PSi layers were either sonicated or ball milled. Moreover, the PSi layers were surface functionalized to demonstrate carriers with varying surface charge and hydrophilicities. Iron oxide NPs were synthesized by the co-precipitation

method, and varying NP sizes were most evident with varying Fe (III) concentration. Iron oxide NPs were infiltrated into the three-step gradient PSi layer with the guidance of a permanent magnet, but this infiltration approach yielded low efficiencies of magnetic PSi NP formation. Instead, the iron oxide NPs were physically mixed with APTESPSi NPs and bound to the surface via electrostatic interactions. This magnetic-capped PSi (APTESPSi@Fe3O4) NP system was fabricated with high efficiency while overcoming typical synthetic challenges associated with scaling up such drug delivery systems. We confirmed the electrostatic interactions between the APTEPSi and iron oxide NPs, and therefore developed a robust pore-block system for controlled drug delivery applications.

After successfully demonstrating the formation of magnetic-capped PSi (APTESPSi@Fe3O4) nanoparticles in Chapter 3, the temperature-mediated electrostatic degradation at physiologically relevant temperatures and magnetic heating capabilities was investigated in Chapter 4. The PSi NP hydrolysis rate was accelerated at temperatures slightly above physiological temperature (i.e. 45 °C). While some hydrolysis observed at 37 °C could potentially lead to premature drug release, future investigations could grow thermally hydrocarbonized layers before APTES modification to increase surface chemistry stability. We demonstrated that the APTESPSi@Fe_3O_4 nanocomposite does not induce any interparticle or secondary effects in during heat dissipation with AMF application. This observation was confirmed by comparing the SAR values determined directly via calorimetry experiments and with calculations using magnetic susceptibility, where both a nanocomposite or Fe_3O_4 NP system were considered in the calculations. Moreover, nanocomposite localization to a Petri dish end with a magnet was demonstrated. However, future experiments will need to better model

magnetic localization with the nanocomposite solution flowing through capillaries resembling vein dimensions (i.e. ~10 mm) at a typical blood flow rate (10 cm/s)[164].

Subsequently, the release profiles of SFN from APTESPSi@Fe_3O_4 at varying temperatures between room temperature and 50 °C revealed a temperature-dependent release behavior, with increasing drug release at increasing temperatures. Within 1h there was an almost 5 times increase in the amount of SFN released when comparing dissolution studies conducted at 37 °C and 45 °C. Furthermore, the identical burst release kinetics for SFN dissolution studies from APTESPSi at various temperatures confirmed that this increase in dissolution is not a result of increased solubility of the model drug at elevated temperatures. Therefore, the amount of drug released under normal physiological conditions is minimized and is accelerated upon increasing the system temperature. Inducing temperature changes in dissolution studies after stabilizing the release medium for 30 min and 1h further corroborated the nanocomposite's ability to promote drug release "on-demand" with application of an external stimuli. While we previously demonstrated the heating capabilities of these nanocomposites with application of an AMF to temperatures relevant to the dissolution studies, it will be pivotal to conduct future release studies under AMF application rather than an external heating source to determine whether the same release kinetics are observed, as it is anticipated that the heat will be more localized to the nanocomposite rather than homogeneously spread throughout the solution[183]. Furthermore, for dissolution studies which were monitored at 37 °C before introducing temperature changes it would be interesting to compare observe the release kinetics when the release medium is exposed to heat pulses (i.e. cycling between 45 ° C and 37 °C) to determine if the amount of SFN released is increased in comparison to no pulse at elevated temperature.

After confirming the thermoresponsive release properties of the APTESPSi@Fe_3O_4 nanocomposite in Chapter 4, the biocompatibility and cellular interaction of the nanocomposite were studied in Chapter 5. The APTESPSi@Fe_3O_4 nanocomposite demonstrated high biocompatibility in HepG2 liver cancer cells, MDA-MB-231 triple negative breast cancer cells, and RAW 246.7 macrophage cells. However, the nancomposite was not biocompatible with MCF-7 breast cancer cells, indicating that biocompatibility is cell-line dependent. The nanocomposite also demonstrated high biocompatibility when incubated with HepG2, MDA-MB-231, and RAW 246.7 cells that were heated to temperatures, times typical of promoting therapeutic release (45 °C, 15min) as observed in dissolution studies with SFN. For HepG2 cells, a decrease in the cytocompatibility was observed for the nanocomposite at 200 µg/mL, yet this decrease was not statistically significant. Further investigation will need to observe the cytocompatibility profile under application of an AMF, and how the cytocompatibility varies with AMF pulses. The *in vitro* cytocompatibility was further studied with SFN-loaded nanocomposites, and an increase in the anticancer activity was observed for nanocarrier encapsulated SFN in comparison to the free drug. Moreover, heating the cells incubated with SFN-loaded particles showed a further decrease in cytocompatibility which was attributed to the increased dissolution of SFN from the nanocarrier with increasing temperature.

Cellular association studies with MDA-MB-231 cells showed an overall higher uptake of APTESPSi nanoparticles in comparison to APTESPSi@Fe_3O_4. This observation was explained by the positive surface charge of APTESPSi that binds to the negatively charged cell membrane via electrostatic interactions. Increasing the cell incubation temperature to 45 °C for 15 min followed by 37 °C for 5h 45 min caused a slight decrease in the particle uptake by MDA-MB-231 cells, with APTESPSi@Fe_3O_4 demonstrating a larger decrease in the mean fluorescence

intensity. However, it is possible that that the accelerated hydrolysis at 45 °C is removing the Alexa Fluor 488 from the PSi surface so the fluorescent tag could simply not be tracked anymore. Future experiments could tag the loaded (or free) drug with a fluorescent molecule rather than the PSi particle, as there is greater interest in observing the therapeutic uptake. Tagging the therapeutic with a fluorescent marker would also increase understanding of the anticancer activity, especially in HepG2 cells where a synergistic effect was observed for the free drug with heating. Moreover, it would be worthwhile to further investigate the cellular morphology before and after heating to determine any changes in the cellular membrane permeability and whether this agrees with our observation of reduced cellular association with temperature application. Overall, we assessed the controlled release capabilities, biocompatibility and anticancer activity of APTESPSi@Fe_3O_4 nanocomposites. These nanocomposites demonstrated "on-demand" drug release, high biocompatibility, and high anticancer activity when combined with a model drug. Thus, this nanocomposite demonstrates a promising targeted delivery system comprised of a formulation that overcomes the synthetic challenges typically associated with fabricating such drug delivery systems. This promising proof-of-concept on-command system may be of great interest for improving the biopharmaceutical properties of current and emerging therapeutics.

After confirming the biocompatibility and thermoresponsive behavior of the APTESPSi@Fe_3O_4 nanocomposites in Chapters 4 and 5, a new thermoresponsive system was proposed and optimized in Chapter 6. PNIPAM is a thermally responsive polymer commonly used in stimuli-responsive drug delivery carrier systems, because of its phase transition near physiological temperature[289–291]. A physical encapsulation method was proposed as an alternative to chemically conjugating PNIPAM onto PSi NPs[216,217,283]. Physical encapsulation,

specifically nanoprecipitation, is a promising alternative because it can form stimuli-responsive encapsulated PSi on the order of seconds versus several days that are typical of chemical conjugation[302,344]. F-127 stabilized PNIPAM NPs with an average size of 107.8 $\pm$ 18.8 nm were initially precipitated using the co-nonsolvency[338] in a microfluidics system. The same co-nonsolvency principle was used to encapsulate TOPSi NPs with PNIPAM, but encapsulation was unsuccessful because TOPSi is highly soluble in water and therefore PNIPAM self-assembly occurred rather than precipitation onto the dissolved TOPSi NP surface. The PSi NP surface hydrophilicity was modified to a with a hydrophobic surface (THCPSi) to promote the PNIPAM precipitation onto the NP surface. A hydrophobic surface did result in the encapsulation of THCPSi NPs with PNIPAM, but these particles are only stable in water-ethanol mixtures where the PNIPAM remains insoluble which is undesirable for drug delivery applications where stability in aqueous solution is required. Given the requirement for nanocarriers with aqueous solution stability, the amphiphilic block copolymer PS-b-PNIPAM was used in nanoprecipitation studies to promote encapsulation and aqueous stability by precipitating the PS-block onto the THCPSi NP surface. This simple and facile encapsulation technique was demonstrated in bulk mixing, and preliminary optimizations were conducted in a microfluidics system. Further characterization by TEM is required to determine whether a microfluidics fabrication approach yields improvements in PSi encapsulation efficiency and size distribution. Moreover, changes in the LCST temperature need to be determined, particularly with the presence of the PS-block. Moreover, drug release studies at various temperatures and cell viability studies will need to be compared to PSi NPs chemically conjugated with PNIPAM. Overall, nanoprecipitation has the potential to overcome fabrication challenges typically associated with the clinical translation of nanocomposites. By developing a facile, streamlined manufacturing method for targeted drug

delivery apparatuses, its impact on patients' lives in the clinic can become a reality. This work has laid the groundwork for a promising nanocarrier completely comprised of cost-effective, highly scalable components with future applications in externally triggered drug delivery. Such a system bestows the clinician with the power to lessen the burden that millions of cancer patients face as they receive treatment; for it is the patient quality of life and treatment outcomes that drives these innovations.

Bibliography

1. Ferlay, J. *et al.* Cancer incidence and mortality worldwide: Sources, methods and major patterns in GLOBOCAN 2012. *Int. J. Cancer* **136**, E359–E386 (2015).
2. Ferlay, J. *et al.* GLOBOCAN 2012 v1. 0 Cancer Incidence and Mortality Worldwide: IARC CancerBase No. 11 [online] 2013.[cited on 2019 Apr 1. (2017).
3. Institute, N. C. Chemotherapy to Treat Cancer. https://www.cancer.gov/about-cancer/treatment/types/chemotherapy (2015).
4. Pearce, A. *et al.* Incidence and severity of self-reported chemotherapy side effects in routine care: A prospective cohort study. *PLoS One* **12**, 1–12 (2017).
5. Siddhartha Mukherjee. Cancer's Invasion Equation. *The New Yorker* (2017).
6. Kay, N. E., O'brien, S. M., Pettitt, A. R. & Stilgenbauer, S. The role of prognostic factors in assessing 'high-risk'subgroups of patients with chronic lymphocytic leukemia. *Leukemia* **21**, 1885–1891 (2007).
7. Döhner, H. *et al.* Genomic aberrations and survival in chronic lymphocytic leukemia. *N. Engl. J. Med.* **343**, 1910–1916 (2000).
8. Hare, J. I. *et al.* Challenges and strategies in anti-cancer nanomedicine development: An industry perspective. *Adv. Drug Deliv. Rev.* **108**, 25–38 (2017).
9. Celgene. *Abraxane Prescribing Information*. https://www.abraxane.com/wp-content/pi/prescribing-info.html.
10. Bristol-Myers Squibb Company. *Taxol Prescribing Information*. https://www.accessdata.fda.gov/drugsatfda_docs/label/2011/020262s049lbl.pdf.
11. Ragelle, H., Danhier, F., Préat, V., Langer, R. & Anderson, D. G. Nanoparticle-based drug delivery systems: a commercial and regulatory outlook as the field matures. *Expert Opin. Drug Deliv.* **14**, 851–864 (2017).
12. Damha, M. J. Exciting Times in the Field of Nucleic Acid Therapeutics. *Trends Mol. Med.* **25**, 1051–1052 (2019).
13. Whitehead, K. a, Langer, R. & Anderson, D. G. Knocking down barriers: advances in siRNA delivery. *Nat. Rev. Drug Discov.* **8**, 129–38 (2009).
14. Akinc, A. *et al.* The Onpattro story and the clinical translation of nanomedicines containing nucleic acid-based drugs. *Nat. Nanotechnol.* **14**, 1084–1087 (2019).
15. Rosenblum, D., Joshi, N., Tao, W., Karp, J. M. & Peer, D. Progress and challenges towards targeted delivery of cancer therapeutics. *Nat. Commun.* **9**, 1–12 (2018).
16. SLOWING, I., VIVEROESCOTO, J., WU, C. & LIN, V. Mesoporous silica nanoparticles as controlled release drug delivery and gene transfection carriers☆. *Adv. Drug Deliv. Rev.* **60**, 1278–1288 (2008).
17. Kalepu, S. & Nekkanti, V. Insoluble drug delivery strategies: Review of recent advances and business prospects. *Acta Pharm. Sin. B* **5**, 442–453 (2015).

18. Venditto, V. J. & Szoka, F. C. Cancer Nanomedicines: So Many Papers and So Few Drugs! Vincent. *Adv Drug Deliv Rev.* **65**, 80–88 (2013).

19. Sarker, D. & Workman, P. B. T.-A. in C. R. Pharmacodynamic Biomarkers for Molecular Cancer Therapeutics. in *Genomics in Cancer Drug Discovery and Development* vol. 96 213–268 (Academic Press, 2006).

20. Nanomedicine. *Nature Publishing Group* https://www.nature.com/subjects/nanomedicine.

21. Strebhardt, K. & Ullrich, A. Paul Ehrlich's magic bullet concept: 100 Years of progress. *Nat. Rev. Cancer* **8**, 473–480 (2008).

22. Feynman, R. P. There's plenty of room at the bottom. *Calif. Inst. Technol. Eng. Sci. Mag.* (1960).

23. Jones, A. A. D., Mi, G. & Webster, T. J. A Status Report on FDA Approval of Medical Devices Containing Nanostructured Materials. *Trends Biotechnol.* **37**, 117–120 (2019).

24. Bragazzi, N. L. Nanomedicine: Insights from a bibliometrics-based analysis of emerging publishing and research trends. *Medicina (B. Aires).* **55**, (2019).

25. Fargen, K. M. *et al.* The FDA approval process for medical devices: an inherently flawed system or a valuable pathway for innovation? *J. Neurointerv. Surg.* **5**, 269–275 (2013).

26. Farokhzad, O. C. & Langer, R. Impact of nanotechnology on drug delivery. *ACS Nano* **3**, 16–20 (2009).

27. Soutschek, J. *et al.* Therapeutic silencing of an endogenous gene by systemic administration of modified siRNAs. *Nature* **432**, 173–178 (2004).

28. The two directions of cancer nanomedicine. *Nat. Nanotechnol.* **14**, 1083 (2019).

29. Figueiredo, P. *et al.* Preparation and Characterization of Dentin Phosphophoryn-Derived Peptide-Functionalized Lignin Nanoparticles for Enhanced Cellular Uptake. *Small* **15**, 1–14 (2019).

30. Ferreira, M. P. A. *et al.* Dual-Drug Delivery Using Dextran-Functionalized Nanoparticles Targeting Cardiac Fibroblasts for Cellular Reprogramming. *Adv. Funct.* **28**, 1705134 (2018).

31. Torrieri, G. *et al.* Dual-peptide functionalized acetalated dextran-based nanoparticles for sequential targeting of macrophages during myocardial infarction. *Nanoscale* **12**, 2350–2358 (2020).

32. Charrois, G. J. R. & Allen, T. M. Drug release rate influences the pharmacokinetics , biodistribution , therapeutic activity , and toxicity of pegylated liposomal doxorubicin formulations in murine breast cancer. *Biochim. Biophys. Acta* **1663**, 167–177 (2004).

33. Barenholz, Y. C. Doxil ® — The fi rst FDA-approved nano-drug : Lessons learned. *J. Control. Release* **160**, 117–134 (2012).

34. Depalo, N. *et al.* Sorafenib delivery nanoplatform based on superparamagnetic iron oxide nanoparticles magnetically targets hepatocellular carcinoma. *Nano Res* **10**, 2431–2448 (2017).

35. Senapati, S., Mahanta, A. K., Kumar, S. & Maiti, P. Controlled drug delivery vehicles for cancer treatment and their performance. *Signal Transduct. Target. Ther.* **3**, 1–19 (2018).

36. Savjani, K. T., Gajjar, A. K. & Savjani, J. K. Drug Solubility: Importance and Enhancement Techniques. *ISRN Pharm.* **2012**, 1–10 (2012).

37. Curigliano, G. *et al.* Cardiovascular toxicity induced by chemotherapy, targeted agents and

radiotherapy: ESMO Clinical Practice Guidelines†. *Ann. Oncol.* **23**, vii155–vii166 (2012).

38. Staff, N. P., Grisold, A., Grisold, W. & Windebank, A. J. Chemotherapy-induced peripheral neuropathy: A current review. *Ann. Neurol.* **81**, 772–781 (2017).

39. Nurgalieva, Z., Liu, C.-C. & Du, X. L. Chemotherapy use and risk of bone marrow suppression in a large population-based cohort of older women with breast and ovarian cancer. *Med. Oncol.* **28**, 716–725 (2011).

40. Jin, J.-F. *et al.* The optimal choice of medication administration route regarding intravenous, intramuscular, and subcutaneous injection. *Patient Prefer. Adherence* **9**, 923–942 (2015).

41. Shi, J., Kantoff, P. W., Wooster, R. & Farokhzad, O. C. Cancer nanomedicine : progress , challenges and opportunities. *Nat. Rev. Cancer* **17**, 20–37 (2017).

42. Jiang, W. *et al.* Designing nanomedicine for immuno-oncology. *Nat. Biomed. Eng.* **1**, 1–11 (2017).

43. Tsoi, K. M. *et al.* Mechanism of hard-nanomaterial clearance by the liver. *Nat. Mater.* **15**, 1212–1221 (2016).

44. Wang, B., He, X., Zhang, Z., Zhao, Y. & Feng, W. Metabolism of Nanomaterials in Vivo: Blood Circulation and Organ Clearance. *Acc. Chem. Res.* **46**, 761–769 (2013).

45. Michelle Longmire, Peter L. Choyke, M.D., and Hisataka Kobayashi, M.D., P. . Clearance Properties of Nano-sized Particles and Molecules as Imagin Agents: Consideration and Caveats. *Nanomedicine* **3**, 703–717 (2012).

46. Choi, H. S. *et al.* Renal clearance of nanoparticles. *Nat. Biotechnol.* **25**, 1165–1170 (2007).

47. Yang, G., Zeng, S., Phua, F., Bindra, A. K. & Zhao, Y. Degradability and Clearance of Inorganic Nanoparticles for Biomedical Applications. *Adv. Mater.* **31**, 1805730–1805753 (2019).

48. Shen, H., Sun, T. & Ferrari, M. Nanovector delivery of siRNA for cancer therapy. **19**, 367–373 (2012).

49. Liu, D., Zhang, H., Fontana, F., Hirvonen, J. T. & Santos, H. A. Current developments and applications of microfluidic technology toward clinical translation of nanomedicines. *Adv. Drug Deliv. Rev.* **128**, 54–83 (2018).

50. Hobbs, S. K. *et al.* Regulation of transport pathways in tumor vessels: role of tumor type and microenvironment. *Proc. Natl. Acad. Sci.* **95**, 4607–4612 (1998).

51. Hashizume, H. *et al.* Openings between defective endothelial cells explain tumor vessel leakiness. *Am. J. Pathol.* **156**, 1363–1380 (2000).

52. Torchilin, V. Tumor delivery of macromolecular drugs based on the EPR effect. *Adv. Drug Deliv. Rev.* **63**, 131–135 (2011).

53. Maeda, H., Wu, J., Sawa, T., Matsumura, Y. & Hori, K. Tumor vascular permeability and the EPR effect in macromolecular therapeutics : a review. **65**, 271–284 (2000).

54. Fang, J., Nakamura, H. & Maeda, H. The EPR effect : Unique features of tumor blood vessels for drug delivery , factors involved , and limitations and augmentation of the effect ☆. *Adv. Drug Deliv. Rev.* **63**, 136–151 (2011).

55. Wang, F. *et al.* The biomolecular corona is retained during nanoparticle uptake and protects the cells from the damage induced by cationic nanoparticles until degraded in the lysosomes.

Nanomedicine Nanotechnology, Biol. Med. **9**, 1159–1168 (2013).

56. Park, J.-H. *et al.* Biodegradable luminescent porous silicon nanoparticles for in vivo applications. *Nat. Mater.* **8**, 331–336 (2009).

57. Herranz-Blanco, B. *et al.* pH-Switch Nanoprecipitation of Polymeric Nanoparticles for Multimodal Cancer Targeting and Intracellular Triggered Delivery of Doxorubicin. *Adv. Healthc. Mater.* **5**, 1904–1916 (2016).

58. Clinton, M., Frank, J., Gupta, M., Zhang, A. & Peppas, N. A. pH-responsive and enzymatically-responsive hydrogel microparticles for the oral delivery of therapeutic proteins : Effects of protein size , crosslinking density , and hydrogel degradation on protein delivery. *J. Control. Release* **221**, 18–25 (2016).

59. Naeem, M. *et al.* Colon-targeted delivery of budesonide using dual pH- and time-dependent polymeric nanoparticles for colitis therapy. *Drug Des. Devel. Ther.* **9**, 3789–3799 (2015).

60. Lee, H. L. *et al.* Redox- and pH-Responsive Nanoparticles Release Piperlongumine in a Stimuli-Sensitive Manner to Inhibit Pulmonary Metastasis of Colorectal Carcinoma Cells. *J. Pharm. Sci.* **107**, 2702–2712 (2018).

61. Ferris, D. P. *et al.* Light-operated mechanized nanoparticles. *J. Am. Chem. Soc.* **131**, 1686–1688 (2009).

62. Ji, J. *et al.* Light-Activatable Assembled Nanoparticles to Improve Tumor Penetration and Eradicate Metastasis in Triple Negative Breast Cancer. *Adv. Funct. Mater.* **28**, 1–14 (2018).

63. Croissant, J. & Zink, J. I. Nanovalve-controlled cargo release activated by plasmonic heating. *J. Am. Chem. Soc.* **134**, 7628–7631 (2012).

64. Zhu, Y. & Tao, C. DNA-capped Fe3O4/SiO2 magnetic mesoporous silica nanoparticles for potential controlled drug release and hyperthermia. *RSC Adv.* **5**, 22365–22372 (2015).

65. Dong, J. & Zink, J. I. Taking the temperature of the interiors of magnetically heated nanoparticles. *ACS Nano* **8**, 5199–5207 (2014).

66. Xu, H. *et al.* Polymer encapsulated upconversion nanoparticle/iron oxide nanocomposites for multimodal imaging and magnetic targeted drug delivery. *Biomaterials* **32**, 9364–9373 (2011).

67. Kato, Y. *et al.* Acidic extracellular microenvironment and cancer. *Cancer Cell Int.* **13**, 89 (2013).

68. Sablina, A. A. *et al.* The antioxidant function of the p53 tumor suppressor. *Nat. Med.* **11**, 1306–1313 (2005).

69. Kost, J. & Langer, R. Responsive polymeric delivery systems. *Advanced Drug Delivery Reviews* vol. 64 327–341 (2012).

70. Yoshida, T., Lai, T. C., Kwon, G. S. & Sako, K. pH- and ion-sensitive polymers for drug delivery. *Expert Opin. Drug Deliv.* **10**, 1497–1513 (2013).

71. Rahikkala, A. *et al.* Mesoporous Silica Nanoparticles for Targeted and Stimuli-Responsive Delivery of Chemotherapeutics: A Review. *Adv. Biosyst.* **2**, 1800020 (2018).

72. Lu, Y., Aimetti, A. A., Langer, R. & Gu, Z. Bioresponsive materials. *Nat. Rev. Mater.* **2**, (2016).

73. Castillo, R. R. *et al.* Expert Opinion on Drug Delivery Advances in mesoporous silica nanoparticles for targeted stimuli-responsive drug delivery : an update. *Expert Opin. Drug Deliv.*

16, 415–439 (2019).

74. Jiang, T., Mo, R., Bellotti, A., Zhou, J. & Gu, Z. Gel–liposome-mediated co-delivery of anticancer membrane-associated proteins and small-molecule drugs for enhanced therapeutic efficacy. *Adv. Funct. Mater.* **24**, 2295–2304 (2014).

75. Kuppusamy, P. *et al.* Noninvasive imaging of tumor redox status and its modification by tissue glutathione levels. *Cancer Res.* **62**, 307–312 (2002).

76. Meng, F., Hennink, W. E. & Zhong, Z. Reduction-sensitive polymers and bioconjugates for biomedical applications. *Biomaterials* **30**, 2180–2198 (2009).

77. Sarah A. Stanley, Jennifer E. Gagner, Shadi Damanpour, Mitsukuni Yoshida, Jonathan S. Dordick, J. M. F. Radio-Wave Heating of Iron Oxide Nanoparticles Can Regulate Plasma Glucose in Mice. *Science (80-.).* **336**, 604–608 (2012).

78. Schoellhammer, C. M. & Traverso, G. Low-frequency ultrasound for drug delivery in the gastrointestinal tract. *Expert Opinion on Drug Delivery* vol. 13 1045–1048 (2016).

79. Schoellhammer, C. M. *et al.* Ultrasound-Mediated Delivery of RNA to Colonic Mucosa of Live Mice. *Gastroenterology* **152**, 1151–1160 (2017).

80. Guardia, P. *et al.* Water-soluble iron oxide nanocubes with high values of specific absorption rate for cancer cell hyperthermia treatment. *ACS Nano* **6**, 3080–3091 (2012).

81. Guisasola, E., Baeza, A., Talelli, M., Arcos, D. & Vallet-Regí, M. Design of thermoresponsive polymeric gates with opposite controlled release behaviors. *RSC Adv.* **6**, 42510–42516 (2016).

82. Rosensweig, R. E. E. Heating magnetic fluid with alternating magnetic field. *J. Magn. Magn. Mater.* **252**, 370–374 (2002).

83. Suto, M. *et al.* Heat dissipation mechanism of magnetite nanoparticles in magnetic fluid hyperthermia. *J. Magn. Magn. Mater.* **321**, 1493–1496 (2009).

84. Fortin, J. *et al.* Size-Sorted Anionic Iron Oxide Nanomagnets as Colloidal Mediators for Magnetic Hyperthermia. 2628–2635 (2007) doi:10.1021/ja067457e.

85. Sershen, S. R., Westcott, S. L., Halas, N. J. & West, J. L. Temperature-sensitive polymer – nanoshell composites for photothermally modulated drug delivery. *J. Biomed. Mater. Res.* **51**, 293–298 (2000).

86. Canham, L. T. Bioactive Silicon Structure Fabrication Through Nanoetching Techniques. *Adv. Mater.* **12**, 1033–1037 (1995).

87. Canham, L. *et al.* Bioactive Polycrystalline Silicon. *Adv. Mater.* **8**, 850–852 (1996).

88. Uhlir Jr, A. Electrolytic shaping of germanium and silicon. *Bell Syst. Tech. J.* **35**, 333–347 (1956).

89. Canham, L. Handbook of Porous Silicon. *Handb. Porous Silicon* 1–1017 (2014) doi:10.1007/978-3-319-05744-6.

90. Cullis, A. G., Canham, L. T. & Calcott, P. D. J. The structural and luminescence properties of porous silicon. *J. Appl. Phys.* **82**, 909–965 (1997).

91. Low, S. P., Voelcker, N. H., Canham, L. T. & Williams, K. A. The biocompatibility of porous silicon in tissues of the eye. *Biomaterials* **30**, 2873–2880 (2009).

92. Tzur-Balter, A., Shatsberg, Z., Beckerman, M., Segal, E. & Artzi, N. Mechanism of erosion of

nanostructured porous silicon drug carriers in neoplastic tissues. *Nat. Commun.* **6**, 1–8 (2015).

93. Buriak, J. M. Silicon-Carbon Bonds on Porous Silicon Surfaces. *Adv. Mater.* **11**, 265–267 (1999).

94. Cullis, A. . G., Canham, L. T. & Calcott, P. D. J. The structural and luminescence properties of porous silicon. *J. Appl. Phys.* **82**, 909–965 (1997).

95. Shahbazi, M. *et al.* Nanostructured porous Si-based nanoparticles for targeted drug delivery Nanostructured porous Si-based nanoparticles for targeted drug delivery. *Biomatter* **2535**, 1–17 (2016).

96. Martins, J. P. *et al.* Microfluidic Nanoassembly of Bioengineered Chitosan-Modified FcRn-Targeted Porous Silicon Nanoparticles @ Hypromellose Acetate Succinate for Oral Delivery of Antidiabetic Peptides. *ACS Appl. Mater. Interfaces* **10**, 44354–44367 (2018).

97. Balasubramanian, V. *et al.* Engineered antibody-functionalized porous silicon nanoparticles for therapeutic targeting of pro-survival pathway in endogenous neuroblasts after stroke. *Biomaterials* **227**, 119556 (2020).

98. Almeida, P. V, Shahbazi, M., Kaasalainen, M., Salonen, J. & Hirvonen, J. Amine-modified hyaluronic acid-functionalized porous silicon nanoparticles for targting breast cancer tumors. *Nanoscale* **6**, 10377–10387 (2014).

99. Smith, R. L. & Collins, S. D. Porous silicon formation mechanisms. *J. Appl. Phys.* **71**, (1992).

100. Föll, H., Christophersen, M., Carstensen, J. & Hasse, G. Formation and application of porous silicon. *Mater. Sci. Eng. R Reports* **39**, 93–141 (2002).

101. Beale, M. I. J., Benjamin, J. D., Uren, M. J., Chew, N. G. & Cullis, A. G. An experimental and theoretical study of the formation and microstructure of porous silicon. *J. Cryst. Growth* **73**, 622–636 (1985).

102. Vaccari, L. *et al.* Porous silicon as drug carrier for controlled delivery of doxorubicin anticancer agent. *Microelectron. Eng.* **83**, 1598–1601 (2006).

103. Feng, Z. C. & Tsu, R. *Porous silicon*. vol. 17 (World Scientific, 1994).

104. Solanki, C. & Bilyalov, R. Self-standing porous silicon films by one-step anodizing. *J. Electrochem. Soc.* **151**, C307–C314 (2004).

105. Meade, S. O., Yoon, M. S., Ahn, K. H. & Sailor, M. J. Porous Silicon Photonic Crystals as Encoded Microcarriers. *Adv. Mater.* **16**, 1811–1814 (2004).

106. Meade, S. O. & Sailor, M. J. Microfabrication of freestanding porous silicon particles containing spectral barcodes. *Phys. Status Solidi - Rapid Res. Lett.* **1**, 71–73 (2007).

107. Hon, N. K., Shaposhnik, Z., Diebold, E. D., Tamanoi, F. & Jalali, B. Tailoring the biodegradability of porous silicon nanoparticles. *J. Biomed. Mater. Res. - Part A* **100 A**, 3416–3421 (2012).

108. Wang, F., Hui, H., Barnes, T. J., Barnett, C. & Prestidge, C. A. Oxidized mesoporous silicon microparticles for improved oral delivery of poorly soluble drugs. *Mol. Pharm.* **7**, 227–236 (2010).

109. Nidhi, K., Indrajeet, S., Khushboo, M., Gauri, K. & Sen, D. J. Mesoporous Silicon in Drug Delivery Applications. *J. Pharm. Sci.* **97**, 632–653 (2008).

110. Pacholski, C., Sartor, M., Sailor, M. J., Cunin, F. & Miskelly, G. M. Biosensing using porous

silicon double-layer interferometers: Reflective interferometric fourier transform spectroscopy. *J. Am. Chem. Soc.* **127**, 11636–11645 (2005).

111. Anglin, E. J., Schwartz, M. P., Ng, V. P., Perelman, L. A. & Sailor, M. J. Engineering the chemistry and nanostructure of porous silicon fabry-p??rot films for loading and release of a steroid. *Langmuir* **20**, 11264–11269 (2004).

112. Anglin, E. J., Cheng, L., Freeman, W. R. & Sailor, M. J. Porous silicon in drug delivery devices and materials. *Adv. Drug Deliv. Rev.* (2008) doi:10.1016/j.addr.2008.03.017.

113. Chiappini, C., Liu, X., Fakhoury, J. R. & Ferrari, M. Biodegradable porous silicon barcode nanowires with defined geometry. *Adv. Funct. Mater.* **20**, 2231–2239 (2010).

114. Park, J. *et al.* Biodegradable luminescent porous silicon nanoparticles for in vivo applications. *Natl. Institutes Heal.* **8**, 331–336 (2011).

115. Allongue, P., Costa-Kieling, V. & Gerischer, H. Etching of Silicon in NaOH Solutions: II. Electrochemical Studies of n-Si (111) and (100) and Mechanism of the Dissolution. *J. Electrochem. Soc.* **140**, 1018 (1993).

116. Foraker, A. B. *et al.* Microfabricated porous silicon particles enhance paracellular delivery of insulin across intestinal caco-2 cell monolayers. *Pharm. Res.* **20**, 110–116 (2003).

117. Silicon, O. N., Chin, B. V., Collins, B. E., Sailor, M. J. & Bhatia, S. N. Compatibility of Primary Hepatocytes with. 1999–2002 (2001).

118. Mayne, A. H., Bayliss, S. C., Barr, P., Tobin, M. & Buckberry, L. D. Biologically interfaced porous silicon devices. *Phys. Status Solidi Appl. Res.* **182**, 505–513 (2000).

119. Pattni, B. S. & Torchilin, V. P. *Targeted Drug Delivery : Concepts and Design*. *Targeted Drug Delivery: Concepts and Design* (2015). doi:10.1007/978-3-319-11355-5.

120. Kohane, D. S. Nanoparticles and microparticles for drug and vaccine delivery. *Biotechnol. Bioeng.* **96**, 203–209 (2007).

121. Singh, R. & W., L. J. Nanoparticle-based targeted drug delivery. *Exp. Mol .Pathol.* **86**, 215–223 (2009).

122. Beck, J. S. *et al.* A New Family of Mesoporous Molecular Sieves Prepared with Liquid Crystal Templates. *J. Am. Chem. Soc.* **114**, 10834–10843 (1992).

123. Zhang, J., Li, X., Rosenholm, J. M. & Gu, H. chen. Synthesis and characterization of pore size-tunable magnetic mesoporous silica nanoparticles. *J. Colloid Interface Sci.* **361**, 16–24 (2011).

124. Dongyuan Zhou, Jianglin Feng, Q. H., Nicholas Melosh, Glenn H. Fredrickson, B. F. C. & Stucky, G. D. Triblock Copolymer Syntheses of Mesoporous Silica with Periodic 50 to 300 Angstrom Pores. *Science (80-.).* **279**, 548–552 (1998).

125. Yu, T., Malugin, A. & Ghandehari, H. Impact of silica nanoparticle design on cellular toxicity and hemolytic activity. *ACS Nano* **5**, 5717–5728 (2011).

126. He, Q., Shi, J., Chen, F., Zhu, M. & Zhang, L. An anticancer drug delivery system based on surfactant-templated mesoporous silica nanoparticles. *Biomaterials* **31**, 3335–3346 (2010).

127. He, Q., Zhang, Z., Gao, Y., Shi, J. & Li, Y. Intracellular localization and cytotoxicity of spherical mesoporous silica nano-and microparticles. *Small* **5**, 2722–2729 (2009).

128. Li, X., Xie, Q. R., Zhang, J., Xia, W. & Gu, H. The packaging of siRNA within the mesoporous structure of silica nanoparticles. *Biomaterials* **32**, 9546–9556 (2011).

129. Andrew J Hamilton, D. C. B. A Species of Small Antisense RNA in Posttranscriptional Gene Silencing in Plants. *Science* **286**, 950–952 (1999).

130. Kim, H. J., Kim, A., Miyata, K. & Kataoka, K. Recent progress in development of siRNA delivery vehicles for cancer therapy. *Adv. Drug Deliv. Rev.* **104**, 61–77 (2016).

131. Meng, H. *et al.* Codelivery of an optimal drug/siRNA combination using mesoporous silica nanoparticles to overcome drug resistance in breast cancer in vitro and in vivo. *ACS Nano* **7**, 994–1005 (2013).

132. Meng, H. *et al.* Engineered design of mesoporous silica nanoparticles to deliver doxorubicin and Pgp siRNA to overcome drug resistance in a cancer cell line. *ACS Nano* **4**, 4539 (2010).

133. Shen, J. *et al.* Multi-step encapsulation of chemotherapy and gene silencing agents in functionalized mesoporous silica nanoparticles. *Nanoscale* **9**, 5329–5341 (2017).

134. Sun, L. *et al.* Core-shell hierarchical mesostructured silica nanoparticles for gene/chemo-synergetic stepwise therapy of multidrug-resistant cancer. *Biomaterials* **133**, 219–228 (2017).

135. Neeraj Prabhakar, Jixi Zhang, Diti Desai, Eudald Casals, Tina Gulin-Sarfraz, Tuomas Näreoja, Jukka Westermarck, J. M. R. Stimuli-responsive hybrid nanocarriers by controllable integration of hyperbranched PEI on mesoporous silica particles for sustained intracellular siRNA delivery. **11**, 6591–6608 (2016).

136. Liu, J. *et al.* Magnetic silica spheres with large nanopores for nucleic acid adsorption and cellular uptake. *Biomaterials* **33**, 970–978 (2012).

137. Kong, F. *et al.* Inhibition of multidrug resistance of cancer cells by CO-delivery of DNA nanostructures and drugs using porous silicon nanoparticles@giant liposomes. *Adv. Funct. Mater.* **25**, 3330–3340 (2015).

138. Joo, J. *et al.* Porous silicon–graphene oxide core–shell nanoparticles for targeted delivery of siRNA to the injured brain. *Nanoscale Horiz.* **1**, 407–414 (2016).

139. Kang, J. *et al.* Self-Sealing Porous Silicon-Calcium Silicate Core–Shell Nanoparticles for Targeted siRNA Delivery to the Injured Brain. *Adv. Mater.* **28**, 7962–7969 (2016).

140. Tanaka, T. *et al.* Sustained Small Interfering RNA Delivery by Mesoporous Silicon Particles. *Ther. Targets, Chem. Biol.* doi:10.1158/0008-5472.CAN-09-3931.

141. Babes, L., Denizot, B., Tanguy, G., Le Jeune, J. J. & Jallet, P. Synthesis of Iron Oxide Nanoparticles Used as MRI Contrast Agents: A Parametric Study. *J. Colloid Interface Sci.* **212**, 474–482 (1999).

142. Neuberger, T., Schof, B., Hofmann, H., Hofmann, M. & Von Rechenberg, B. Superparamagnetic nanoparticles for biomedical applications: Possibilities and limitations of a new drug delivery system. *J. Magn. Magn. Mater.* **293**, 483–496 (2005).

143. Corchero, J. L. & Villaverde, A. Biomedical applications of distally controlled magnetic nanoparticles. *Trends Biotechnol.* **27**, 468–476 (2009).

144. Klouda, L. Thermoresponsive hydrogels in biomedical applications A seven-year update. *Eur. J. Pharm. Biopharm.* **97**, 338–349 (2015).

145. van der Zee, J. Heating the patient: A promising approach? *Ann. Oncol.* **13**, 1173–1184 (2002).

146. Hergt, R., Dutz, S., Müller, R. & Zeisberger, M. Magnetic particle hyperthermia: nanoparticle magnetism and materials development for cancer therapy. *J. Phys. Condens. Matter* **18**, S2919–S2934 (2006).

147. Hergt, R. & Andrä, W. Magnetic Hyperthermia and Thermoablation. in *Magnetism in Medicine: A Handbook: Second Edition* 550–570 (2007). doi:10.1002/9783527610174.ch4f.

148. Bear, J. C. *et al.* Magnetic hyperthermia controlled drug release in the GI tract : solving the problem of detection. *Nat. Publ. Gr.* 1–11 (2016) doi:10.1038/srep34271.

149. Oliveira, H. *et al.* Magnetic field triggered drug release from polymersomes for cancer therapeutics. *J. Control. Release* **169**, 165–170 (2013).

150. Laurent, S. *et al.* Magnetic Iron Oxide Nanoparticles: Synthesis, Stabilization, Vectorization, Physicochemical Characterizations, and Biological Applications (vol 108, pg 2064, 2008). *Chem. Rev.* **108**, 2064–2110 (2008).

151. Gupta, A. K. & Gupta, M. Synthesis and surface engineering of iron oxide nanoparticles for biomedical applications. *Biomaterials* **26**, 3995–4021 (2005).

152. Anselmo, A. C. & Mitragotri, S. Nanoparticles in the clinic. *Bioeng. Transl. Med.* **1**, 10–29 (2016).

153. M.W. Freeman, A. Arrott, J. H. . W. Magnetism in Medicine. *J. Appl. Phys.* **31**, 404–405 (1960).

154. Mosbach, K. & Schroder, U. Preparation and application of magnetic polymers for targeting of drugs. *FEBS Lett.* **102**, 112–116 (1979).

155. Senyei, A., Widder, K. & Czerlinski, G. Magnetic guidance of drug-carrying microspheres. *J. Appl. Phys.* **49**, 3578–3583 (1978).

156. Alexiou, C. *et al.* Locoregional Cancer Treatment with Magnetic Drug Targeting Locoregional Cancer Treatment with Magnetic Drug Targeting 1. *Cancer Res.* 6641–6648 (2000).

157. Mahmoudi, M., Sant, S., Wang, B., Laurent, S. & Sen, T. Superparamagnetic iron oxide nanoparticles (SPIONs): Development, surface modification and applications in chemotherapy. *Adv. Drug Deliv. Rev.* **63**, 24–46 (2011).

158. Frenkel, Y. I. *Kinetic theory of liquids*. (Dover, 1955).

159. Brown, W. F. Thermal Fluctuations of a Single-Domain Particle. *Phys. Rev.* **130**, 1667–1686 (1963).

160. Hergt, R., Hiergeist, R., Hilger, I., Kaiser, W. A. & Lapatnikov, Y. Maghemite nanoparticles with very high AC-losses for application in RF-magnetic hyperthermia. *J. Magn. Magn. Mater.* **270**, 345–357 (2004).

161. Yuan, Y. & Tasciuc, D. B. Comparison between experimental and predicted specific absorption rate of functionalized iron oxide nanoparticle suspensions. *J. Magn. Magn. Mater.* **323**, 2463–2469 (2011).

162. Alev, M. *et al.* Targeting of drug-loaded nanoparticles to tumor sites increases cell death and release of danger signals. *J. Control. Release* **285**, 67–80 (2018).

163. Matuszak, J. *et al.* Drug delivery to atherosclerotic plaques using superparamagnetic iron oxide nanoparticles. *Int. J. Nanomedicine* **13**, 8443–8460 (2018).

164. Tartaj, P., del Puerto Morales, M., Veintemillas-Verdaguer, S., González-Carreño, T. & Serna, C. J. The preparation of magnetic nanoparticles for applications in biomedicine. *J. Phys. D. Appl. Phys.* **36**, R182 (2003).

165. Hennig, T. L., Unterweger, H., Lyer, S., Alexiou, C. & Cicha, I. Magnetic accumulation of spions under arterial flow conditions: Effect of serum and red blood cells. *Molecules* **24**, (2019).

166. Lübbe, A. S. *et al.* Clinical experiences with magnetic drug targeting: A phase I study with 4'-epidoxorubicin in 14 patients with advanced solid tumors. *Cancer Res.* **56**, 4686–4693 (1996).

167. Goodwin, S., Peterson, C., Hoh, C. & Bittner, C. Targeting and retention of magnetic targeted carriers (MTCs) enhancing intra-arterial chemotherapy. *J. Magn. Magn. Mater.* **194**, 132–139 (1999).

168. Janikowska, A. *et al.* A novel human artery model to assess the magnetic accumulation of SPIONs under flow conditions. *Sci. Rep.* **7**, 42314 (2017).

169. Viroonchatapan, E. *et al.* Preparation and Characterization of Dextran Magnetite-Incorporated Thermosensitive Liposomes: An on-line Flow System for Quantifying Magnetic Responsiveness. *Pharmaceutical Research: An Official Journal of the American Association of Pharmaceutical Scientists* vol. 12 1176–1183 (1995).

170. Pulfer, S. K. & Gallo, J. M. Targeting magnetic microspheres to brain tumors. in *Scientific and clinical applications of magnetic carriers* 445–455 (Springer, 1997).

171. Inada, Y. *et al.* Fibrinolysis by urokinase endowed with magnetic property. *Biochem. Biophys. Res. Commun.* **148**, 392–396 (1987).

172. Allen, L. M., Kent, T., Wolfe, C., Ficco, C. & Johnson, J. MTC TM. in *Scientific and clinical applications of magnetic carriers* 481–494 (Springer, 1997).

173. Cazares-Cortes, E. *et al.* Recent insights in magnetic hyperthermia: From the "hot-spot" effect for local delivery to combined magneto-photo-thermia using magneto-plasmonic hybrids. *Adv. Drug Deliv. Rev.* **138**, 233–246 (2019).

174. Qiu, Y. *et al.* Magnetic forces enable controlled drug delivery by disrupting endothelial cell-cell junctions. *Nat. Commun.* **8**, 1–10 (2017).

175. Zweifach, B. W. & Lipowsky, H. H. Pressure and flow distribution in microcirculation. *Handb. Physiol.* **11**, 251–307 (1985).

176. Regmi, R. *et al.* Hyperthermia controlled rapid drug release from thermosensitive magnetic microgels. *J. Mater. Chem.* **20**, 6158–6163 (2010).

177. Atkinson, W. J., Brezovich, I. A. & Chakraborty, D. P. Usable Frequencies in Hyperthermia with Thermal Seeds. *IEEE Trans. Biomed. Eng.* **BME-31**, 70–75 (1984).

178. Hergt, R. & Dutz, S. Magnetic particle hyperthermia-biophysical limitations of a visionary tumour therapy. *J. Magn. Magn. Mater.* **311**, 187–192 (2007).

179. Chinthaka P. Gooneratne, Adam Kurnicki, Sotoshi Yamada, Subhas C. Mukhopadhyay, J. K. Analysis of the Distribution of Magnetic Fluid inside Tumors by a Giant Magnetoresistance Probe Chinthaka. *PLoS One* **8**, 1–14 (2013).

180. Nanocubes, W. I. O., Values, H., Rate, A., Cell, C. & Treatment, H. Water-Soluble Iron Oxide Nanocubes with High Values of Speci fi \c Absorption Rate for Cancer Cell Hyperthermia Treatment. *ACS Nano* 3080–3091 (2012) doi:10.1021/nn2048137.

181. Albarqi, H. A. *et al.* Biocompatible Nanoclusters with High Heating Efficiency for Systemically Delivered Magnetic Hyperthermia. *ACS Nano* **13**, 6383–6395 (2019).

182. Kakwere, H. *et al.* Functionalization of strongly interacting magnetic nanocubes with (thermo)responsive coating and their application in hyperthermia and heat-triggered drug delivery. *ACS Appl. Mater. Interfaces* **7**, 10132–10145 (2015).

183. Cazares-Cortes, E. *et al.* Doxorubicin Intracellular Remote Release from Biocompatible Oligo(ethylene glycol) Methyl Ether Methacrylate-Based Magnetic Nanogels Triggered by Magnetic Hyperthermia. *ACS Appl. Mater. Interfaces* **9**, 25775–25788 (2017).

184. Hanini, A. *et al.* Zinc substituted ferrite nanoparticles with Zn0.9Fe2.1O4 formula used as heating agents for in vitro hyperthermia assay on glioma cells. *J. Magn. Magn. Mater.* **416**, 315–320 (2016).

185. Zhang, Z. Q. & Song, S. C. Multiple hyperthermia-mediated release of TRAIL/SPION nanocomplex from thermosensitive polymeric hydrogels for combination cancer therapy. *Biomaterials* **132**, 16–27 (2017).

186. Rebodos, R. L. & Vikesland, P. J. Effects of oxidation on the magnetization of nanoparticulate magnetite. *Langmuir* **26**, 16745–16753 (2010).

187. Jolivet, J. P., Belleville, P., Tronc, E. & Livage, J. Influence of Fe(II) on the Formation of the Spinel Iron Oxide in Alkaline Medium. *Clays Clay Miner.* **40**, 531–539 (1992).

188. D.K. Kim, Y. Zhang, K.V. Rao, M. M. Synthesis and Characterization of Iron Oxide Nanoparticles. *J. Magn. Magn. Mater.* **225**, 30–36 (2001).

189. Petcharoen, K. & Sirivat, A. Synthesis and characterization of magnetite nanoparticles via the chemical co-precipitation method. *Mater. Sci. Eng. B Solid-State Mater. Adv. Technol.* **177**, 421–427 (2012).

190. Espinosa, A. *et al.* Duality of Iron Oxide Nanoparticles in Cancer Therapy : Amplification of Heating Efficiency by Magnetic Hyperthermia and Photothermal Bimodal Treatment. *ACS N* **10**, 2436–2446 (2016).

191. Hugounenq, P. *et al.* Cooperative Organization in Iron Oxide Multi-Core Nanoparticles Potentiates Their E ffi ciency as Heating Mediators and MRI Contrast Agents. 10935–10949 (2012) doi:10.1021/nn304477s.

192. Plank, C., Schillinger, U., Bergemann, C., Anton, M. & Rosenecker, J. The Magnetofection Method: Using Magnetic Force to Enhance Gene Delivery. *Biol. Chem.* **384**, 737–747 (2003).

193. Chang, Y. *et al.* Novel water-soluble and pH-responsive anticancer drug nanocarriers : Doxorubicin – PAMAM dendrimer conjugates attached to superparamagnetic iron oxide nanoparticles (IONPs). *J. Colloid Interface Sci.* **363**, 403–409 (2011).

194. Yang, X. *et al.* Biomaterials oxide nanoparticles for targeted anticancer drug delivery and PET / MR imaging. *Biomaterials* **32**, 4151–4160 (2011).

195. Miao, L., Liu, C., Ge, J., Yang, W. & Liu, J. Antitumor Effect of TRAIL on Oral Squamous Cell Carcinoma using Magnetic Nanoparticle-Mediated Gene Expression. *Cell Biochem Biophys* **69**, 663–672 (2014).

196. Kinsella, J. *et al.* Enhanced magnetic resonance contrast of iron oxide nanoparticles embedded in a porous silicon nanoparticle host. 859409 (2013) doi:10.1117/12.2009784.

197. Park, J.-H. *et al.* Local Heating of Discrete Droplets Using Magnetic Porous Silicon-Based Photonic Crystals. *J. Am. Chem. Soc.* **128**, 7938–7946 (2006).

198. Kinsella, J. M. *et al.* Enhanced magnetic resonance contrast of Fe 3O 4 nanoparticles trapped in a porous silicon nanoparticle host. *Adv. Healthc. Mater.* **23**, 248–253 (2011).

199. Dorvee, J. R., Derfus, A. M., Bhatia, S. N. & Sailor, M. J. Manipulation of liquid droplets using amphiphilic, magnetic one-dimensional photonic crystal chaperones. *Nat. Mater.* **3**, 896–899 (2004).

200. Gu, L., Park, J. H., Duong, K. H., Ruoslahti, E. & Sailor, M. J. Magnetic luminescent porous silicon microparticles for localized delivery of molecular drug payloads. *Small* **6**, 2546–2552 (2010).

201. Rumpf, K., Granitzer, P., Poelt, P. & Reissner, M. Magnetic properties of an iron oxide/porous silicon system controlled by magnetic interactions. *ECS Trans.* **50**, 83–86 (2012).

202. P. Granitzer, K. Rumpf, A.G. Roca, M.P. Morales, P. P. Porous silicon/Fe3O4-nanoparticle composite and its magnetic behaviour P. *ECS Trans.* **16**, 1–2 (2016).

203. Granitzer, P. *et al.* Fe3O4-nanoparticles within porous silicon: Magnetic and cytotoxicity characterization. *Appl. Phys. Lett.* **102**, 1–5 (2013).

204. Granitzer, P., Rumpf, K., Reissner, M. & Poelt, P. Control of the magnetic properties of a magnetic field guidable biocompatible nanovehicle. *ECS Trans.* **75**, 51–55 (2016).

205. Granitzer, P. *et al.* Magnetic Study of Fe3O4 Nanoparticles Incorporated within Mesoporous Silicon. *J. Electrochem. Soc.* **157**, K145 (2010).

206. Granitzer, P. *et al.* A porous silicon/iron oxide nanocomposite with superparamagnetic and ferromagnetic behaviour. *ECS Trans.* **33**, 95–99 (2011).

207. Granitzer, P., Rumpf, K., Gonzalez-Rodriguez, R., Coffer, J. L. & Reissner, M. The effect of nanocrystalline silicon host on magnetic properties of encapsulated iron oxide nanoparticles. *Nanoscale* **7**, 20220–20226 (2015).

208. Granitzer, P. *et al.* Assessment of cytocompatibility and magnetic properties of nanostructured silicon loaded with superparamagnetic iron oxide nanoparticles. *ECS Trans.* **64**, 1–7 (2014).

209. Harraz, F. a. Synthesis and surface properties of magnetite (Fe3O4) nanoparticles infiltrated into porous silicon template. *Appl. Surf. Sci.* **287**, 203–210 (2013).

210. Saint-Cricq, P., Deshayes, S., Zink, J. I. & Kasko, A. M. Magnetic field activated drug delivery using thermodegradable azo-functionalised PEG-coated core-shell mesoporous silica nanoparticles. *Nanoscale* **7**, 13168–72 (2015).

211. Rühle, B., Datz, S., Argyo, C., Bein, T. & Zink, J. I. A molecular nanocap activated by superparamagnetic heating for externally stimulated cargo release. *Chem. Commun.* **52**, 1843–1846 (2015).

212. Chen, W., Cheng, C.-A. & Zink, J. I. Spatial , Temporal , and Dose Control of Drug Delivery using Non-Invasive Magnetic Stimulation. *ACS Nano* (2019) doi:10.1021/acsnano.8b06655.

213. Meng, H., Xue, M., Xia, T., Zhao, Y. & Tamanoi, F. Autonomous in Vitro Anticancer Drug Release from Mesoporous Silica Nanoparticles by pH-Sensitive Nanovalves. *Jacs* **132**, 12690–12697 (2010).

214. Xia, T. *et al.* Polyethyleneimine Coating Enhances the Cellular Uptake of Mesoporous Silica Nanoparticles and Allows Safe Delivery of siRNA and DNA Constructs. *ACS Nano* **3**, 3273–3286 (2009).

215. Manivannan, K., Huang, Y. S., Huang, B. R., Huang, C. F. & Chen, J. K. Real-time packing behavior of core-shell silica@poly(N-isopropylacrylamide) microspheres as photonic crystals for visualizing in thermal sensing. *Polymers (Basel).* **8**, (2016).

216. Tamarov, K. *et al.* Temperature responsive porous silicon nanoparticles for cancer therapy – spatiotemporal triggering through infrared and radiofrequency electromagnetic heating. *J. Control. Release* **241**, 220–228 (2016).

217. Zúñiga, E. *et al.* Rhodamine-loaded surface modified mesoporous silica particles embedded into a thermoresponsive composite hydrogel for prolonged release. *Eur. Polym. J.* **95**, 358–367 (2017).

218. Li, Z. *et al.* Measurement of Uptake and Release Capacities of Mesoporous Silica Nanoparticles Enabled by Nanovalve Gates. *J. Phys. Chem. C Nanomater. Interfaces* **115**, 19496–19506 (2011).

219. Thomas, C. R. *et al.* Noninvasive remote-controlled release of drug molecules in vitro using magnetic actuation of mechanized nanoparticles. *J. Am. Chem. Soc.* **132**, 10623–10625 (2010).

220. Ngamcherdtrakul, W. *et al.* Cationic Polymer Modified Mesoporous Silica Nanoparticles for Targeted SiRNA Delivery to HER2+ Breast Cancer. *Adv. Funct. Mater.* **25**, 2646–2659 (2015).

221. Ma, X., Zhao, Y., Ng, K. W. & Zhao, Y. Integrated hollow mesoporous silica nanoparticles for target drug/siRNA co-delivery. *Chem. - A Eur. J.* **19**, 15593–15603 (2013).

222. Finlay, J. *et al.* Mesoporous silica nanoparticle delivery of chemically modified siRNA against TWIST1 leads to reduced tumor burden. *Nanomedicine Nanotechnology, Biol. Med.* **11**, 1657–1666 (2015).

223. Marcazzan, S., Varoni, E. M., Blanco, E., Lodi, G. & Ferrari, M. Nanomedicine , an emerging therapeutic strategy for oral cancer therapy. *Oral Oncol.* **76**, 1–7 (2018).

224. Segal, E., Perelman, L. A., Moore, T., Kesselman, E. & Sailor, M. J. Grafting stimuli-responsive polymer brushes to freshly-etched porous silicon. *Phys. Status Solidi Curr. Top. Solid State Phys.* **6**, 1717–1720 (2009).

225. Xia, B. *et al.* Biodegradable and Magnetic-Fluorescent Porous Silicon @ Iron Oxide Nanocomposites for Fluorescence / Magnetic Resonance Bimodal Imaging of Tumor in Vivo. (2017) doi:10.1021/acsbiomaterials.7b00467.

226. Gan, Q. *et al.* Endosomal pH-activatable magnetic nanoparticle-capped mesoporous silica for intracellular controlled release †. *J. Mater. Chem.* **22**, 15960–15968 (2012).

227. Vivero-Escoto, J. L., Slowing, I. I., Wu, C.-W. & Lin, V. S.-Y. Photoinduced intracellular controlled release drug delivery in human cells by gold-capped mesoporous silica nanosphere. *J. Am. Chem. Soc.* **131**, 3462–3463 (2009).

228. Giri, S., Trewyn, B. G., Stellmaker, M. P. & Lin, S.-Y. V. Stimuli-Responsive Controlled-Release Delivery System Based on Mesoporous Silica Nanorods Capped with Magnetic Nanoparticles. *Angew. Chem. Int. Ed.* **44**, 5038–5044 (2005).

229. Berger, P. *et al.* Preparation and Properties of an Aqueous Ferrofluid. **76**, (1999).

230. Gervasoni, M., Machness, A. & Goorsky, M. Decreased Surface Porosity and Roughness of InP for Epitaxially Grown Thin-Film Devices: A Path to Integration of High Performance Electronics.

ECS Trans. **75**, 241–245 (2016).

231. Hare, R. W. & Hill, R. M. Space charge in insulators with needle-plane geometry. *J. Phys. D. Appl. Phys.* **24**, 398–406 (1991).

232. Herino, R., Barla, K., Bertrand, C. & Ginoux, J. L. Porosity and Pore Size Distributions of Porous Silicon Layers. *J. Electrochem. Soc.* **134**, 1994–2000 (1987).

233. Kim, J., Seidler, P., Fill, C. & Wan, L. S. Surface Science Investigations of the effect of curing conditions on the structure and stability of amino-functionalized organic films on silicon substrates by Fourier transform infrared spectroscopy , ellipsometry , and fluorescence microscopy. *Surf. Sci.* **602**, 3323–3330 (2008).

234. Pasternack, R. M., Amy, S. R. & Chabal, Y. J. Attachment of 3- (Aminopropyl) triethoxysilane on Silicon Oxide Surfaces : Dependence on Solution Temperature. **7**, 12963–12971 (2008).

235. Boukherroub, R., Wojtyk, J. T. C., Wayner, D. D. M. & Lockwood, D. J. Thermal Hydrosilylation of Undecylenic Acid with Porous Silicon. *J. Electrochem. Soc.* **149**, H59–H63 (2002).

236. Janeth, C. *et al.* Nanoprecipitation process : From encapsulation to drug delivery. *Int. J. Pharm.* **532**, 66–81 (2017).

237. Duncanson, W. J. *et al.* Microfluidic synthesis of advanced microparticles for encapsulation and controlled release. *Lab Chip* **12**, 2135–2145 (2012).

238. Liu, D. *et al.* Core/Shell Nanocomposites Produced by Superfast Sequential Microfluidic Nanoprecipitation. *Nano Lett.* **17**, 606–614 (2017).

239. Thanh, N. T. K., Maclean, N. & Mahiddine, S. Mechanisms of Nucleation and Growth of Nanoparticles in Solution. *Chem. Res. Toxicol.* **3**, (2014).

240. Guozhong, C. *Nanostructures and nanomaterials: synthesis, properties and applications*. (World scientific, 2004).

241. Jolivet, J.-P., Chanéac, C. & Tronc, E. Iron oxide chemistry. From molecular clusters to extended solid networks. *Chem. Commun.* 477–483 (2004) doi:10.1039/B304532N.

242. Patterson, A. L. The Scherrer Formula for X-Ray Particle Size Determination. *Phys. Rev.* **56**, 978–982 (1939).

243. Park, J.-H. *et al.* Local Heating of Discrete Droplets Using Magnetic Porous Silicon-Based Photonic Crystals. doi:10.1021/ja0612854.

244. Etienne, M. & Walcarius, A. Analytical investigation of the chemical reactivity and stability of aminopropyl-grafted silica in aqueous medium. *Talanta* **59**, 1173–1188 (2003).

245. Balog, S. & Petri-fink, A. Avoiding drying-artifacts in transmission electron microscopy : Characterizing the size and colloidal state of nanoparticles. *Sci. Rep.* **5**, 9793 (2015).

246. Lin, H., Shaohong, C. & Chaoping, Z. Protein-Fe MR Fluid and its Properties. *Int. J. Mod. Phys. B* **16**, 2399–2404 (2002).

247. Seo, Y. & Wang, Z. J. MRI scanner-independent specific absorption rate measurements using diffusion coefficients. *J. Appl. Clin. Med. Imaging* **18**, 224–229 (2017).

248. Jordan, A., Scholz, R., Wust, P., Fa, H. & Felix, R. Magnetic Fluid hyperthermia (MFH): Cancer treatment with AC magnetic field induced excitation of biocompatible superparamagnetic

nanoparticles. *J. Magn. Magn. Mater.* **201**, 413–419 (1999).

249. Zhu, Y. & Tao, C. DNA-Capped Fe3O4/SiO2 Magnetic Mesoporous Silica Nanoparticles for Potential Controlled Drug Release and Hyperthermia. *RSC Adv.* **5**, 22365–22372 (2015).

250. Hayashi, K., Nakamura, M., Miki, H., Ozaki, S. & Abe, M. Magnetically Responsive Smart Nanoparticles for Cancer Treatment with a Combination of Magnetic Hyperthermia and Remote-Control Drug Release. *Theranostics* **4**, 834–844 (2014).

251. Bayer & Inc., H. P. NEXAVAR Prescribing Information. (2010).

252. Hilgard, P. *et al.* Sorafenib in Advanced Hepatocellular Carcinoma. *N. Engl. J. Med.* **359**, 378–390 (2008).

253. Wilhelm, S. M. *et al.* BAY 43-9006 Exhibits Broad Spectrum Oral Antitumor Activity and Targets the RAF / MEK / ERK Pathway and Receptor Tyrosine Kinases Involved in Tumor Progression and Angiogenesis. *Cancer Res* **64**, 7099–7109 (2004).

254. Auclair, D. *et al.* Antitumor activity of sorafenib in FLT3-driven leukemic cells. *Leukemia* **21**, 439–445 (2007).

255. Adnane, L., Trail, P. A., Taylor, I. & Wilhelm, S. M. Sorafenib (BAY 43-9006, Nexavarw), a Dual-Action Inhibitor That Targets RAF/MEK/ERK Pathway in Tumor Cells and Tyrosine Kinases VEGFR/PDGFR in Tumor Vasculature. *Methods Enzymol.* **407**, 457–459 (2006).

256. Wilhelm, S. M. *et al.* Preclinical overview of sorafenib, a multikinase inhibitor that targets both Raf and VEGF and PDGF receptor tyrosine kinase signaling. *Mol Cancer Ther* **7**, 3129–3141 (2008).

257. Network, N. C. C. NCCN Guildelines for Patients: Kidney Cancer. (2020).

258. Jain, L. *et al.* Population pharmacokinetic analysis of sorafenib in patients with solid tumours. *Br. J. Clin. Pharmacol.* **72**, 294–305 (2011).

259. Golmard, J. L. *et al.* Early Sorafenib-Induced Toxicity Is Associated with Drug Exposure and UGTIA9 Genetic Polymorphism in Patients with Solid Tumors : A Preliminary Study. *PLoS One* **7**, 1–9 (2012).

260. Ravandi, F. *et al.* Phase I/II Study of Combination Therapy With Sorafenib, Idarubicin, and Cytarabine in Younger Patients With Acute Myeloid Leukemia. *J. Clin. Oncol.* **28**, 1856–1862 (2010).

261. Wang, C.-F. C.-F. *et al.* Multifunctional porous silicon nanoparticles for cancer theranostics. *Biomaterials* **48**, 108–118 (2015).

262. Mäkilä, E. *et al.* Amine modification of thermally carbonized porous silicon with silane coupling chemistry. *Langmuir* **28**, 14045–14054 (2012).

263. Yue, Z. G. *et al.* Iron oxide nanotubes for magnetically guided delivery and pH-activated release of insoluble anticancer drugs. *Adv. Funct. Mater.* **21**, 3446–3453 (2011).

264. Gangloff, A. *et al.* Estimation of Paclitaxel Biodistribution and Uptake in Human-Derived Xenografts In Vivo. *J. Nucl. Med.* **46**, 1866–1872 (2005).

265. Chen, Y., Zhang, W., Huang, Y., Gao, F. & Fang, X. In Vivo Biodistribution and Anti-Tumor Efficacy Evaluation of Doxorubicin and Paclitaxel-Loaded Pluronic Micelles Decorated with c (RGDyK) Peptide. *PLoS One* 1–18 (2016) doi:10.1371/journal.pone.0149952.

266. Hu, S. *et al.* Longitudinal PET Imaging of Doxorubicin Induced Cell Death with 18 F-Annexin V Shuo. *Mol Imaging Biol.* **14**, 762–770 (2012).

267. Promega Corporation. CellTiter-Glo(R) 2.0 Assay Technical Manual TM403. 0–16 (2018).

268. Reineke, J. *Nanotoxicity: Methods and Protocols*. (Humana Press, 2012).

269. Shahbazi, M. A. *et al.* The mechanisms of surface chemistry effects of mesoporous silicon nanoparticles on immunotoxicity and biocompatibility. *Biomaterials* **34**, 7776–7789 (2013).

270. Fröhlich, E. The role of surface charge in cellular uptake and cytotoxicity of medical nanoparticles. *Int. J. Nanomedicine* **7**, 5577–5591 (2012).

271. Tae Kim, S., Saha, K., Kim, C. & Rotello, V. M. The Role of Surface Functionality in Determining Nanoparticle Cytotoxicity. *Acc. Chem. Res.* **46**, 681–691 (2013).

272. Bhattacharjee, S. *et al.* Cytotoxicity and cellular uptake of tri-block copolymer nanoparticles with different size and surface characteristics. *Part. Fibre Toxicol.* **9**, 1 (2012).

273. Theodossiou, T. A. *et al.* Simultaneous defeat of MCF7 and MDA-MB-231 resistances by a hypericin PDT – tamoxifen hybrid therapy. *npj Breast Cancer* (2019) doi:10.1038/s41523-019-0108-8.

274. Sakamoto, T., Niiya, D. & Seiki, M. Targeting the Warburg Effect That Arises in Tumor Cells Expressing Membrane Type-1 Matrix Metalloproteinase. *J. Biol. Chem.* **286**, 14691–14704 (2011).

275. Figueiredo, P., Lintinen, K., Kiriazis, A., Hynninen, V. & Liu, Z. Biomaterials In vitro evaluation of biodegradable lignin-based nanoparticles for drug delivery and enhanced antiproliferation effect in cancer cells. **121**, 97–108 (2017).

276. Yu, C. *et al.* The role of Mcl-1 downregulation in the proapoptotic activity of the multikinase inhibitor BAY 43-9006. *Oncogene* **24**, 6861–6869 (2005).

277. Hildebrandt, B. *et al.* The cellular and molecular basis of hyperthermia. *Crit. Rev. Oncol. Hematol.* **43**, 33–56 (2002).

278. Caldarola, G. G. *et al.* Sorafenib and locoregional deep electro - hyperthermia in advanced hepatocellular carcinoma : A phase II study. *Oncol. Lett.* **8**, 1783–1787 (2014).

279. Tu, J. *et al.* Biomaterials Multifunctional ZnPc-loaded mesoporous silica nanoparticles for enhancement of photodynamic therapy ef fi cacy by endolysosomal escape. *Biomaterials* **33**, 7903–7914 (2012).

280. Shahbazi, M. *et al.* Augmented cellular trafficking and endosomal escape of porous silicon nanoparticles via zwitterionic bilayer polymer surface engineering. *Biomaterials* **35**, 7488–7500 (2014).

281. Lee, T. H. *et al.* Sub-lethal hyperthermia promotes epithelial-to- mesenchymal-like transition of breast cancer cells: implication of the synergy between hyperthermia and chemotherapy. *RSC Adv.* **9**, 52–57 (2019).

282. Jha, S., Sharma, P. K. & Malviya, R. Hyperthermia : Role and Risk Factor for Cancer Treatment. *Achiev. Life Sci.* **10**, 161–167 (2016).

283. Tanjim, M. *et al.* Mesoporous magnetic silica particles modified with stimuli-responsive P(NIPAM-DMA) valve for controlled loading and release of biologically active molecules. *Soft*

Matter **14**, 5469–5479 (2018).

284. Li, A., Zhang, J., Xu, Y., Liu, J. & Feng, S. Thermoresponsive copolymer/SiO2 nanoparticles with dual functions of thermally controlled drug release and simultaneous carrier decomposition. *Chem. - A Eur. J.* **20**, 12945–12953 (2014).

285. Liu, C. *et al.* Magnetic mesoporous silica microspheres with thermo-sensitive polymer shell for controlled drug release. *J. Mater. Chem.* **19**, 4764–4770 (2009).

286. Chastek, T. T., Wadajkar, A., Nguyen, K. T., Hudson, S. D. & Chastek, T. Q. Polyglycol-templated synthesis of poly(N-isopropyl acrylamide) microgels with improved biocompatibility. *Colloid Polym. Sci.* **288**, 105–114 (2010).

287. Vihola, H., Laukkanen, A., Valtola, L., Tenhu, H. & Hirvonen, J. Cytotoxicity of thermosensitive polymers poly(N-isopropylacrylamide), poly(N-vinylcaprolactam) and amphiphilically modified poly(N-vinylcaprolactam). *Biomaterials* **26**, 3055–3064 (2005).

288. Guo, Z. *et al.* Biocompatibility and cellular uptake mechanisms of poly(N -isopropylacrylamide) in different cells. *J. Bioact. Compat. Polym.* **32**, 17–31 (2017).

289. Alarcón, C. de las H., Pennadam, S. & Alexander, C. Stimuli responsive polymers for biomedical applications. *Chem. Soc. Rev.* **34**, 276–285 (2005).

290. Hoogenboom, R. *et al.* Tuning the LCST of poly(2-oxazoline)s by varying composition and molecular weight: Alternatives to poly(N-isopropylacrylamide)? *Chem. Commun.* 5758–5760 (2008) doi:10.1039/b813140f.

291. Roy, D., Brooks, W. L. A. & Sumerlin, B. S. New directions in thermoresponsive polymers. *Chem. Soc. Rev.* **42**, 7214–7243 (2013).

292. Weber, C., Hoogenboom, R. & Schubert, U. S. Temperature responsive bio-compatible polymers based on poly(ethylene oxide) and poly(2-oxazoline)s. *Prog. Polym. Sci.* **37**, 686–714 (2012).

293. Bergueiro, J. & Calderon, M. Thermoresponsive nanodevices in biomedical applications. *Macromol. Biosci.* **15**, 183–199 (2015).

294. Stroeve, P. *et al.* Poly (N -isopropylacrylamide) -gated Fe 3 O 4 / SiO 2 core shell nanoparticles with expanded mesoporous structures for the temperature triggered release of lysozyme. *Colloids Surfaces B Biointerfaces* **135**, 652–660 (2015).

295. Yang, M. Y., Tan, L., Wu, H. X., Liu, C. J. & Zhuo, R. X. Dual-stimuli-responsive polymer-coated mesoporous silica nanoparticles used for controlled drug delivery. *J. Appl. Polym. Sci.* **132**, 1–9 (2015).

296. Li, W. *et al.* Tailoring Porous Silicon for Biomedical Applications: From Drug Delivery to Cancer Immunotherapy. *Adv. Mater.* **30**, (2018).

297. Kumar, V., Wang, L., Riebe, M., Tung, H. & Prud, R. K. Formulation and Stability of Itraconazole and Odanacatib Nanoparticles : Governing Physical Parameters. *Mol. Pharm.* **6**, 1118–1124 (2009).

298. Gindy, M. E., Panagiotopoulos, A. Z. & Prud, R. K. Composite Block Copolymer Stabilized Nanoparticles : Simultaneous Encapsulation of Organic Actives and Inorganic Nanostructures. *Langmuir* **23**, 83–90 (2008).

299. Pagels, R. F., Edelstein, J., Tang, C. & Prud, R. K. Controlling and Predicting Nanoparticle Formation by Block Copolymer Directed Rapid Precipitations. *Nano Lett.* **18**, 1139–1144 (2018).

300. Zhang, C., Pansare, V. J., Prud'Homme, R. K. & Priestley, R. D. Flash nanoprecipitation of polystyrene nanoparticles. *Soft Matter* **8**, 86–93 (2012).

301. Saad, W. S. & Prud'Homme, R. K. Principles of nanoparticle formation by flash nanoprecipitation. *Nano Today* **11**, 212–227 (2016).

302. D'Addio, S. M. & Prud'homme, R. K. Controlling drug nanoparticle formation by rapid precipitation. *Adv. Drug Deliv. Rev.* **63**, 417–426 (2011).

303. Shen, H., Hong, S., Prud'Homme, R. K. & Liu, Y. Self-assembling process of flash nanoprecipitation in a multi-inlet vortex mixer to produce drug-loaded polymeric nanoparticles. *J. Nanoparticle Res.* **13**, 4109–4120 (2011).

304. Pustulka, K. M. *et al.* Flash nanoprecipitation: Particle structure and stability. *Mol. Pharm.* **10**, 4367–4377 (2013).

305. Zhu, Z. Biomaterials Effects of amphiphilic diblock copolymer on drug nanoparticle formation and stability. *Biomaterials* **34**, 10238–10248 (2013).

306. Zhu, Z. Flash Nanoprecipitation: Prediction and Enhancement of Particle Stability via Drug Structure. *Mol. Pharm.* **11**, 776–786 (2014).

307. Zhang, Y. & Clapp, A. R. Preparation of quantum dot-embedded polymeric nanoparticles using fl ash nanoprecipitation. *RSC Adv.* **4**, 48399–48410 (2014).

308. York, A. W. *et al.* Kinetically Assembled Nanoparticles of Bioactive Macromolecules Exhibit Enhanced Stability and Cell-Targeted Biological Efficacy. *Adv. Mater.* **24**, 733–739 (2012).

309. Nafee, N., Youssef, A., El-gowelli, H., Asem, H. & Kandil, S. Antibiotic-free nanotherapeutics : Hypericin nanoparticles thereof for improved in vitro and in vivo antimicrobial photodynamic therapy and wound healing. *Int. J. Pharm.* **454**, 249–258 (2013).

310. Liu, Y., Cheng, C., Liu, Y., Prud'homme, R. K. & Fox, R. O. Mixing in a multi-inlet vortex mixer (MIVM) for flash nano-precipitation. *Chem. Eng. Sci.* **63**, 2829–2842 (2008).

311. Ehab, M. & Lamprecht, A. Polyethylene glycol as an alternative polymer solvent for nanoparticle preparation. *Int. J. Pharm.* **456**, 135–142 (2013).

312. Zhang, Y. & Zhuo, R. Synthesis and in vitro drug release behavior of amphiphilic triblock copolymer nanoparticles based on poly (ethylene glycol) and polycaprolactone. *Biomaterials* **26**, 6736–6742 (2005).

313. Fung, S. *et al.* European Journal of Pharmaceutics and Biopharmaceutics Development of highly stabilized curcumin nanoparticles by flash nanoprecipitation and lyophilization. *Eur. J. Pharm. Biopharm.* **94**, 436–449 (2015).

314. Pansare, V. J., Bruzek, M. J., Adamson, D. H., Anthony, J. & Prud'homme, R. K. Composite Fluorescent Nanoparticles for Biomedical Imaging. *Mol. Imaging Biol.* **16**, 180–188 (2014).

315. Rahikkala, A., Aseyev, V., Tenhu, H., Kauppinen, E. I. & Raula, J. Thermoresponsive Nanoparticles of Self-Assembled Block Copolymers as Potential Carriers for Drug Delivery and Diagnostics. *Biomacromolecules* **16**, 2750–2756 (2015).

316. Rahikkala, A. *et al.* Self-assembly of PS-b-P4VP block copolymers of varying architectures in aerosol nanospheres. *Soft Matter* **9**, 1492–1499 (2013).

317. Nykänen, A. *et al.* Thermally sensitive block copolymer particles prepared via aerosol flow reactor

method: Morphological characterization and behavior in water. *Macromolecules* **45**, 8401–8411 (2012).

318. Michailova, V. *et al.* Nanoparticles formed from PNIPAM- g -PEO copolymers in the presence of indomethacin. **384**, 154–164 (2010).

319. Turner, J. R. Intestinal mucosal barrier function in health and disease. *Nat. Rev. Immunol.* **9**, 799 (2009).

320. Johnson, B. K. & Prud'homme, R. K. Flash NanoPrecipitation of Organic Actives and Block Copolymers using a Confined Impinging Jets Mixer. *Aust. J. Chem.* **56**, 1021–1024 (2003).

321. Chow, S. F., Sun, C. C. & Chow, A. H. L. Assessment of the relative performance of a confined impinging jets mixer and a multi-inlet vortex mixer for curcumin nanoparticle production. *Eur. J. Pharm. Biopharm.* **88**, 462–471 (2014).

322. Serra, C. A. & Chang, Z. Microfluidic-assisted synthesis of polymer particles. *Chem. Eng. Technol.* **31**, 1099–1115 (2008).

323. Liu, D., Zhang, H., Fontana, F., Hirvonen, J. T. & Santos, H. A. Microfluidic-assisted fabrication of carriers for controlled drug delivery. *Lab Chip* **17**, 1856–1883 (2017).

324. Bertoni, S. *et al.* pH and Reactive Oxygen Species-Sequential Responsive Nano-in-Micro Composite for Targeted Therapy of Inflammatory Bowel Disease. *Adv. Funct. Mater.* **28**, (2018).

325. Liu, Z. *et al.* Multifunctional Nanohybrid Based on Porous Silicon Nanoparticles, Gold Nanoparticles, and Acetalated Dextran for Liver Regeneration and Acute Liver Failure Theranostics. *Adv. Mater.* **30**, 1–10 (2018).

326. Herranz-Blanco, B. *et al.* On-chip self-assembly of a smart hybrid nanocomposite for antitumoral applications. *Adv. Funct. Mater.* **25**, 1488–1497 (2015).

327. Zhang, Y., Liu, D., Zhang, H. & Santos, H. A. Microfluidic mixing and devices for preparing nanoparticulate drug delivery systems. *Microfluid. Pharm. Appl.* 155–177 (2019) doi:10.1016/B978-0-12-812659-2.00007-7.

328. Liu, D. *et al.* Microfluidic assisted one-step fabrication of porous silicon@acetalated dextran nanocomposites for precisely controlled combination chemotherapy. *Biomaterials* **39**, 249–259 (2015).

329. Martins, J. P., Torrieri, G. & Santos, H. A. The importance of microfluidics for the preparation of nanoparticles as advanced drug delivery systems. *Expert Opin. Drug Deliv.* **15**, 469–479 (2018).

330. Martins, C. *et al.* Using microfluidic platforms to develop CNS-targeted polymeric nanoparticles for HIV therapy. *Eur. J. Pharm. Biopharm. Off. J. Arbeitsgemeinschaft fur Pharm. Verfahrenstechnik e.V* **138**, 111–124 (2019).

331. Karnik, R. *et al.* Microfluidic Platform for Controlled Synthesis of Polymeric Nanoparticles 2008. (2008).

332. Hasani-Sadrabadi, M. M. *et al.* Enhanced osteogenic differentiation of stem cells via microfluidics synthesized nanoparticles. *Nanomedicine Nanotechnology, Biol. Med.* **11**, 1809–1819 (2015).

333. Almeida, P. V. *et al.* Amine-modified hyaluronic acid-functionalized porous silicon nanoparticles for targeting breast cancer tumors. *Nanoscale* **6**, 10377–10387 (2014).

334. Martins, J. P. *et al.* Micro fl uidic Nanoassembly of Bioengineered Chitosan-Modified FcRn-

Targeted Porous Silicon Nanoparticles @ Hypromellose Acetate Succinate for Oral Delivery of Antidiabetic Peptides. *ACS Appl. Mater. Interfaces* **10**, 44354–44367 (2018).

335. Fontana, F. *et al.* Multistaged Nanovaccines Based on Porous Silicon@Acetalated Dextran@Cancer Cell Membrane for Cancer Immunotherapy. *Adv. Mater.* **29**, (2017).

336. Zhang, H. *et al.* Microfluidic Encapsulation of Prickly Zinc-Doped Copper Oxide Nanoparticles with VD1142 Modified Spermine Acetalated Dextran for Efficient Cancer Therapy. *Adv. Healthc. Mater.* **6**, (2017).

337. Nykänen, A. *et al.* Phase behavior and temperature-responsive molecular filters based on self-assembly of polystyrene-block-poly(N-isopropylacrylamide)-block-polystyrene. *Macromolecules* **40**, 5827–5834 (2007).

338. Bischofberger, I., Calzolari, D. C. E. & Trappe, V. Co-nonsolvency of PNiPAM at the transition between solvation mechanisms. *Soft Matter* **10**, 8288–8295 (2014).

339. Shi, J., Votruba, A. R., Farokhzad, O. C. & Langer, R. Nanotechnology in drug delivery and tissue engineering: From discovery to applications. *Nano Lett.* **10**, 3223–3230 (2010).

340. Sharma, P. K. & Bhatia, S. R. Effect of anti-inflammatories on Pluronic® F127: Micellar assembly, gelation and partitioning. *Int. J. Pharm.* **278**, 361–377 (2004).

341. Karjalainen, E. *et al.* Complex interactions in aqueous PIL-PNIPAm-PIL triblock copolymer solutions. *Polymer (Guildf).* **58**, 180–188 (2015).

342. MARKUS NUOPPONEN, KATRIINA KALLIOMA¨ KI, ANTTI LAUKKANEN, SAMI HIETALA, H. T. A–B–A Stereoblock Copolymers of N-Isopropylacrylamide. *Polymer (Guildf).* **48**, 1973–1978 (2010).

343. Ruokolainen, J. *et al.* Temperature controlled release from polystyrene-block-poly(N-isopropylacrylamide-block-polystyrene block copolymer hydrogel. *J. Control. Release* **148**, e53–e54 (2010).

344. Zhu, Z. Flash nanoprecipitation: Prediction and enhancement of particle stability via drug structure. *Mol. Pharm.* **11**, 776–786 (2014).